

©Copyright 2012

Joshua Jacobs



Vortex Dynamics of Geostrophically Adjusted Density  
Perturbations in Triply-Periodic Models of Stratified  
Incompressible Fluids

Joshua Jacobs

A dissertation  
submitted in partial fulfillment of the  
requirements for the degree of

Doctor of Philosophy

University of Washington

2012

Reading Committee:

Randall J. LeVeque, Chair

Marie-Pascale Lelong

Bernard Deconinck

James J Riley

Miles A. Sundermeyer

Program Authorized to Offer Degree:  
University of Washington  
Applied Mathematics



University of Washington

**Abstract**

Vortex Dynamics of Geostrophically Adjusted Density Perturbations in  
Triply-Periodic Models of Stratified Incompressible Fluids

Joshua Jacobs

Chair of the Supervisory Committee:  
Professor of Applied Mathematics Randall J. LeVeque  
Department of Applied Mathematics

A model exploring contributions to lateral dispersion in the oceanic submesoscale is presented. Well-mixed patches of fluid, produced by turbulent mixing events, are geostrophically adjusted to create compound vortices. The dynamics of these vortices are investigated for their contributions to inverse cascades of kinetic energy and to the lateral dispersion of a passive tracer in numerical simulations. When perturbed by the proximity of another vortex, these vortices break down into propagating dipole forms, contributing to the dispersion of tracers. A memory effect for the locations of well-mixed patches is explored for its effect on dispersion dynamics. The vertical periodicity of triply-periodic numeric domains is found to be a source of weakly dissipated, slowly accumulated, barotropic mode kinetic energy and increased tracer dispersion. The two dimensionality of the barotropic mode is found to be the source for observed inverse cascades of kinetic energy in viscous simulations of anisotropic domains. Signatures of inverse cascades in nearly equilibrated simulations are found to strongly contribute to the lateral dispersion of a passive tracer. Additional techniques are proposed to evaluate lateral dispersion relevant to the ocean.



# TABLE OF CONTENTS

	Page
List of Figures . . . . .	iv
Chapter 1: Introduction . . . . .	1
Chapter 2: Background . . . . .	9
2.1 Internal Waves . . . . .	9
2.2 Geostrophic Adjustment . . . . .	13
2.3 Numerical Model . . . . .	14
2.3.1 Model Setup . . . . .	17
2.3.2 Diffusive Forcing . . . . .	17
2.3.3 N/f Scaling . . . . .	19
2.3.4 Hyper-viscosity . . . . .	20
2.3.5 Effective Diffusivity . . . . .	21
2.4 Wave-Vortex Decomposition . . . . .	23
Chapter 3: Pairwise Interaction of Adjustment Vortices . . . . .	25
3.1 Introduction . . . . .	25
3.2 Model and Methods . . . . .	28
3.2.1 Measuring Pairwise Interactions . . . . .	28
3.3 Results . . . . .	33
3.3.1 Induced Azimuthal Instabilities . . . . .	34
3.3.2 Dipole Pairing . . . . .	40
3.3.3 Merging Cores . . . . .	44
3.3.4 Overlapping Mixed Patches . . . . .	47
3.4 Discussion . . . . .	48
3.5 Conclusion . . . . .	53
Chapter 4: Clustering Parameterized Wave-Breaking Events and the Ef- fect on Lateral Dispersion . . . . .	54
4.1 Introduction . . . . .	54

4.2	Model and Methods . . . . .	56
4.2.1	Energetics and Energy Spectra . . . . .	56
4.2.2	Inferring Effective Diffusivity . . . . .	57
4.2.3	Poisson Process with Gaussian Clusters . . . . .	58
4.2.4	Barotropic Dynamics . . . . .	60
4.3	Results . . . . .	61
4.3.1	Unclustered Cases . . . . .	61
4.3.2	Clustered Cases . . . . .	65
4.3.3	Influence of the Barotropic Mode . . . . .	76
4.4	Discussion . . . . .	82
4.5	Conclusions . . . . .	88
Chapter 5: Inverse Cascades of Kinetic Energy in Anisotropic, Rotating, Stratified Domains . . . . .		90
5.1	Introduction . . . . .	90
5.2	Methods . . . . .	92
5.2.1	Anisotropic Scaling for Boussinesq Equations of Motion with Laplacian Viscosity . . . . .	93
5.2.2	Hyperviscosity . . . . .	99
5.2.3	Barotropic Dissipation . . . . .	101
5.3	Results . . . . .	101
5.3.1	Single Adjustment Vortex . . . . .	102
5.3.2	Persistent Periodic Forcing . . . . .	102
5.4	Discussion . . . . .	114
5.5	Conclusion . . . . .	121
Chapter 6: Conclusions . . . . .		123
Appendix A: Nonlinearity of Diffusive Forcing . . . . .		136
A.1	Introduction . . . . .	136
A.2	Method . . . . .	137
A.3	Consequences of Diffusive Forcing in a Numeric Domain . . . . .	140
A.4	Detecting Differences in Diffusive Forcing . . . . .	143
A.5	Conclusion . . . . .	144
Appendix B: Stability of Adjustment Vortices . . . . .		147
B.1	Introduction . . . . .	147

B.2	The Stability of Two-Dimensional Vortices . . . . .	150
B.3	An Eigenvalue Problem for an Approximated Adjustment Vortex . . . . .	155
B.4	Evolution of a Single Adjustment Vortex . . . . .	159
B.5	Proposed Numerical Study . . . . .	168
Appendix C: Hyperviscosity Simplified . . . . .		171
C.1	Introduction . . . . .	171
C.2	Dissipation Time Scales . . . . .	172
C.3	Defining the Higher-Order Dissipation Range . . . . .	176
C.4	Conclusion . . . . .	181
C.4.1	Research Experience . . . . .	185
C.4.2	Teaching Experience . . . . .	185
C.4.3	Work Experience . . . . .	186

## LIST OF FIGURES

Figure Number	Page
1.1 Development of an adjustment vortex. . . . .	5
2.1 Phase and group velocity of an internal wave . . . . .	13
2.2 Wave-vortex decomposition of domain energy . . . . .	24
3.1 Interactions between proximal pairs of adjustment vortices . . . . .	30
3.2 Depiction of two adjustment vortex simulations . . . . .	31
3.3 Dipole structures . . . . .	33
3.4 Development of vortex instabilities for (8.0, 0.0). . . . .	36
3.5 Azimuthal instabilities of adjustment vortex in (8.0, 0.0) . . . . .	37
3.6 Wave-vortex decomposition of vortex instability in (8.0, 0.0) . . . . .	38
3.7 Azimuthal instabilities of adjustment vortex in (4.0, 0.0) . . . . .	39
3.8 Dipole coupling of vertically offset adjustment vortices . . . . .	41
3.9 Strain and vertical vorticity in dipole coupling of $(\Delta r, 1.0)$ . . . . .	42
3.10 Extended simulation showing vortex merging for (3.5, 1.0) . . . . .	43
3.11 Transient merging of anti-cyclonic cores in (2.0, 0.0) . . . . .	45
3.12 Strain and vertical vorticity for $(\Delta r, 0.0)$ . . . . .	46
3.13 Times until instability for $(\Delta r, \Delta z)$ . . . . .	48
4.1 Evolution of kinetic energy for $\tau \in \{4.0, 2.0, 1.0\} T_{ip}$ . . . . .	62
4.2 Diffusive forcing statistics for $\tau \in \{4.0, 2.0, 1.0\} T_{ip}$ , and $\tau = 1.0 T_{ip}$ . . . . .	63
4.3 Horizontal kinetic energy spectrum for $\tau \in \{4.0, 2.0, 1.0\} T_{ip}$ . . . . .	64
4.4 Evolution of tracer variance for $\tau \in \{4.0, 2.0, 1.0\} T_{ip}$ . . . . .	66
4.5 Logarithmic evolution of tracer variance for $\tau \in \{4.0, 2.0, 1.0\} T_{ip}$ . . . . .	67
4.6 Evolution of tracer variance exponent for $\tau \in \{4.0, 2.0, 1.0\} T_{ip}$ . . . . .	68
4.7 Diffusive forcing statistics for $\tau = 4.0 T_{ip}$ by varying $\sigma$ and $N$ . . . . .	70
4.8 Horiz. KE Spectra for $\tau = 1.0 T_{ip}$ with varying $\sigma$ , $N = 5$ , $t = 10 T_{ip}$ . . . . .	72
4.9 Horiz. KE Spectra for $\tau = 1.0 T_{ip}$ with varying $\sigma$ , $N = 5$ , $t = 50 T_{ip}$ . . . . .	73
4.10 Horiz. KE Spectra for $\tau = 1.0 T_{ip}$ with varying $\sigma$ , $N = 5$ , $t = 250 T_{ip}$ . . . . .	74
4.11 Horiz. KE Spectra for $\tau = 1.0 T_{ip}$ with varying $\sigma$ , $N = 5$ , $t = 750 T_{ip}$ . . . . .	75
4.12 Loglog of tracer variance, $\tau = 4.0 T_{ip}$ , $N = 5$ , and varied $\sigma$ . . . . .	76

4.13	Loglog of tracer variance, $\tau = 2.0 T_{ip}$ , $N = 5$ , and varied $\sigma$ . . . . .	77
4.14	Loglog of tracer variance, $\tau = 1.0 T_{ip}$ , $N = 5$ , and varied $\sigma$ . . . . .	78
4.15	Evolution vertical kinetic energy spectrum for $\tau = 1.0 T_{ip}$ . . . . .	80
4.16	Evolution horizontal kinetic energy spectrum for $\tau = 1.0 T_{ip}$ . . . . .	81
4.17	Horizontal kinetic energy spectrum for $\tau = 1.0 T_{ip}$ . . . . .	82
4.18	Evolution of tracer variance for $\tau \in \{4.0, 2.0, 1.0\} T_{ip}$ with barotropic damping . . . . .	83
4.19	Evolution of tracer variance exponent for $\tau \in \{4.0, 2.0, 1.0\} T_{ip}$ with barotropic damping . . . . .	84
4.20	Tracer distributions at $800 T_{ip}$ for $\tau = 1.0 T_{ip}$ . . . . .	84
5.1	E-folding dissipation time scales . . . . .	100
5.2	Evolution of kinetic energy spectrum for adjustment vortex . . . . .	103
5.3	Vorticity evolution of a single adjustment vortex in viscous domain	104
5.4	Kinetic energy evolution for $\tau = 1.0 T_{ip}$ . . . . .	105
5.5	Evolution of kinetic energy spectrum for $\tau = 1.0 T_{ip}$ . . . . .	105
5.6	Barotropic mode vorticity for $\tau = 1.0 T_{ip}$ . . . . .	106
5.7	Horizontal spectrum of barotropic mode kinetic energy for $\tau = 1.0 T_{ip}$	107
5.8	Horiz. spectrum of first baroclinic mode kinetic, $\tau = 1.0 T_{ip}$ . . . . .	108
5.9	Kinetic energy evolution for $\tau = 0.025 T_{ip}$ . . . . .	109
5.10	Evolution of kinetic energy in the first seven horizontal and vertical wavenumbers for $\tau = 0.025 T_{ip}$ . . . . .	110
5.11	Plan views of vorticity for $\tau = 0.025 T_{ip}$ . . . . .	110
5.12	Horizontal spectrum of barotropic mode kinetic energy for $\tau = 0.025 T_{ip}$ . . . . .	111
5.13	Horiz. spectrum of first baroclinic mode kinetic, $\tau = 0.025 T_{ip}$ . . . . .	112
5.14	Evolution of kinetic energy in the first seven horizontal and vertical wavenumbers for $\tau = 1.0 T_{ip}$ with barotropic dissipation . . . . .	113
5.15	Kinetic energy evolution for $\tau = 0.025 T_{ip}$ with barotropic dissipation	114
5.16	Evolution of kinetic energy spectrum in the first seven horizontal and vertical wavenumbers for $\tau = 0.025 T_{ip}$ with barotropic dissipation	115
5.17	Evolution of kinetic energy in seven horizontal, vertical wavenumbers for $\tau = 1.0 T_{ip}$ , $\nu = 2.5 \times 10^{-6}$ . . . . .	118
5.18	Horiz. spectrum of barotropic mode kinetic, $\tau = 1.0 T_{ip}$ , $\nu = 2.5 \times 10^{-6}$ . . . . .	119
5.19	Horiz. spectrum of first baroclinic mode kinetic, $\tau = 1.0 T_{ip}$ , $\nu = 2.5 \times 10^{-6}$ . . . . .	120
A.1	Density perturbation and destratification ratio . . . . .	141

A.2	Available potetial energy for continuous forcing . . . . .	142
A.3	Detail of diffusive forcing effect on changes to total energy . . . . .	144
A.4	Energy of multiple diffusive forcings over time . . . . .	145
B.1	Comparison of analytic and simulated adjustment vortices velocity fields . . . . .	157
B.2	Comparison of analytic and simulated adjustment vortices vorticity fields . . . . .	158
B.3	Comparison of analytic and simulated adjustment vortices density fields . . . . .	158
B.4	Instability evolution of adjustment vortex . . . . .	161
B.5	Polar coordinate evolution of instabilities in adjustment vortex . . .	162
B.6	Cylindrical evolution of instabilities in adjustment vortex . . . . .	163
B.7	Azimuthal instability growth of adjustment vortex . . . . .	165
B.8	Wave-vortex energy decomposition for the evolution of an adjustment vortex . . . . .	166
B.9	Evolution of horizontal and vertical mode kinetic energy for an adjustment vortex . . . . .	167
B.10	Azimuthal instability growth in adjustment vortex derived from elliptically perturbed mixed-patch . . . . .	169
C.1	Dissipation time scales for $p = 6$ , $\nu = 2.5 \times 10^{-5} m^2 s^{-1}$ , and $\nu'_6 = 48 s^{-1}$ . . . . .	178
C.2	Dissipation time scales for $p = 26$ , $\nu = 2.5 \times 10^{-5} m^2 s^{-1}$ , and $\nu'_{26} = 48 s^{-1}$ . . . . .	179
C.3	Dissipation time scales for $p = 30$ , $\nu = 0 m^2 s^{-1}$ , and $\nu'_{30} = 48 s^{-1}$ . .	180

## ACKNOWLEDGMENTS

This dissertation represents six years of in depth personal investigation and the refinement of techniques. Though personally executed, it was not done alone. I would like to take this opportunity to express my appreciation to many of those that made this journey possible. It is impossible to acknowledge everybody in the vast and interconnected community that makes doing this work possible. It is deeply humbling to know that I have been helped by so many.

First, I would like to acknowledge sources of financial support that have made it possible to write a dissertation. I am grateful for grants from the National Science Foundation (OCE-0623620) and the Office of Naval Research (N00014-09-M-0214, N00014-10-C-0080) that supported me from the summer of 2007 through the spring of 2011. Opportunities to be an instructor and a teaching assistant for classes in the departments of Mathematics and Applied Mathematics supported me from the fall of 2006 through the spring of 2007 and from the summer of 2011 through the winter of 2012. I am thankful for the research assistantship provided by the Kristin Swanson Cancer Research Lab in the spring of 2012. It was indeed an inspiration to explore interests that I never knew I had. I am also grateful for the financial assistance from the chair of my committee, Randall J. LeVeque (NSF grant DMS-0914942), over the last few months of my dissertaion work.

Next, I would like to express my gratitude to the professional support that I have gotten from my committee and beyond. To my advisor, M. Pascale Lelong, I am humbled by your dedication and patience in guiding your first student through this process. I would not have been able to proceed without both the grants you secured above nor the steadfast manner that you encouraged me to find something simple and relevant from the sea of interesting details. To collaborator and

committee member, Miles Sundermeyer, I am grateful the manner with which you continued to bring me back to the relevance of the physical ocean. To committee members Bernard Deconinck, James Riley, Parker MacCready, and Robert Breidenthal, I am grateful for all of the intense conversations of both professional and private in nature. The patience and experience of the committee chair, Randall LeVeque, has been invaluable in the face of many difficulties. Beyond members of my dissertation committee have been others that have been instrumental in my progress and understanding. One of Bernard Deconinck's students, Vishal Visan, has been both a good friend and an excellent source of knowledge. Anne-Marie Brunner-Suzuki and Debbie Debiegun, students of Miles Sundermeyer, worked on similar projects and were also a source of understanding and inspiration.

## **DEDICATION**

to my dear wife, Sharon



## Chapter 1

### INTRODUCTION

The stirring and mixing of physical and biological quantities in the ocean is one of the most fundamental, yet least understood, of oceanic processes. Processes of both lateral and vertical mixing are essential to distribute carbon dioxide, plankton, nutrients, and pollutants throughout the depth and breadth of the ocean. Anthropogenic carbon dioxide is broadly accepted by the scientific community to be the primary green house gas responsible for warming our climate (Hansen et al., 2010). The ocean is responsible for absorbing 25% of the annual emissions of anthropogenic carbon dioxide (Sallée et al., 2012). Whereas a large portion of this carbon dioxide is subducted into deeper layers of the ocean, another portion is integrated into the oceanic food chain starting with phytoplankton. The ability of phytoplankton to absorb and convert carbon dioxide into organic carbon is dependent on the availability of macro-nutrients (e.g. nitrates, phosphates) and micro-nutrients (e.g. iron, zinc, cobalt). When any of these nutrients are in limited supply the populations of various phytoplankton are limited in their growth (Martin, 2003, 2012). These nutrients must be dispersed from some source to be used by the phytoplankton. The sources of effective nutrients can be from rivers, dust, the vertical mixing of nutrient-rich deep water in the ocean, or intentionally adding a missing nutrient. A recent experiment in the Southern Ocean involved adding iron to otherwise nutrient rich waters (Smetacek et al., 2012). They concluded that at least half of the resultant bloom sank below 1,000 meters, effectively sequestering the absorbed carbon for centuries. In addition, the capacity of the ocean to transport or disperse concentrated pollutants can either extend or ameliorate their effects. For example, numerical models of radioactive water from the Fukushima Dai-ichi power plant present concern that eddy-trapped radioactive isotopes may

be harmful to organisms in its locality (Prants et al., 2011). However, they indicate a small likelihood that these radioactive isotopes would be transported large distances without thorough mixing.

The distribution of carbon dioxide, phytoplankton, nutrients, and pollution in the ocean all depend on stirring and mixing on multiple scales. The ocean contains a broad range of energetic scales that transport and mix these various quantities. On one extreme, large scale motions are responsible for transporting Gulf Stream waters thousands of kilometers from the tip of Florida towards Europe. The presence of Gulf Stream water provides a more moderate climate for Western Europe than would otherwise be granted by its latitude. On the other extreme, the small scales of turbulent surf quickly mix small quantities of dye beyond recognition. In placid conditions this same mixing would take months to achieve through molecular diffusion. Though the processes of large scale transport and small-scale turbulent mixing are well characterized, there exists a lack of understanding how the scales between contribute to mixing and dispersal in the ocean.

A large portion of the ocean's energy enters through predominantly large scales from tidal and wind forcing (Thorpe, 2005). Balancing the large scale forcing of energy is dissipation at small scales. The process of large scale energy being successively broken down into smaller, dissipative scales is known as a forward energy cascade (Pope, 2000). In this process, large vortices are broken into successively smaller vortices until dissipated by viscosity. Forward energy cascades are characteristic of the oceanic microscales, up to 1 km. However, this is not the only way that energy can be transferred. In the oceanic mesoscales, between 10 km to 100 km, the coalescence of vortices can produce an inverse energy cascade. With forward cascades dominating the microscale and inverse energy cascades occupying the mesoscales, the mechanisms transferring energy through the submesoscales, 100 m to 10 km, have yet to be fully characterized McWilliams (2008). Of specific interest are the contributions to mixing that is made by submesoscale processes in the ocean.

A five-year directed research initiative, Scalable Lateral Mixing and Coherent Turbulence, is underway to evaluate three major hypotheses that contribute to lateral dispersion unaccounted for by known models (Paluszkiwicz et al., 2008). Those three hypotheses are: Vortical stirring from the adjustment of mixed regions generated by turbulent internal wave breaking, submesoscale instabilities of mesoscale oceanic fronts, and large scale straining of conserved quantities down to the submesoscale. Understanding submesoscale processes will provide a means to parameterize mixing for global models that cannot resolve small scales.

It is the purpose of this dissertation to investigate the mechanisms involved in the first hypothesis above. Of particular interest is the capacity of vortices at the submesoscale to participate in an inverse cascade of kinetic energy. An inverse cascade of vortical mode kinetic energy may provide a mechanism that accounts for the observed lateral dispersion at the submesoscale. A process of vortex creation is presented below and the non-linear interactions responsible for observed inverse energy cascades are examined in the core chapters of this dissertation.

As noted above, submesoscales connect the large energetic scales of the ocean to the small dissipative scales. Submesoscale processes contribute to ecosystem dynamics, such as predator-prey relationships and primary production, which have their foundation in the dispersal rates of nutrients and plankton that require them (Martin, 2003). Models of the submesoscale show that strong horizontal shear can bring nutrients up into the euphotic zone, where phytoplankton can utilize them. However, these processes can also disperse nutrients too quickly to support high rates of productivity (Thomas et al., 2008). Variability in nutrient transport, primary production, and gas exchange make submesoscales an essential element of the global carbon cycle (Doney et al., 2003) and an unevaluated contributor to our changing climate.

The submesoscale process under consideration is the geostrophic adjustment of well-mixed patches of water in the thermocline of the ocean. In Gregg et al. (1986), micro-structure and current profilers detect patches of well-mixed water in the thermocline of the California Current. The turbulent events that gave

rise to these mixed patches are hypothesized to be the result of breaking internal waves. These well-mixed patches of water, 1 – 10 m in height and 0.1 – 1 km in diameter, have also been observed as variations in the stratification over the continental shelf of Northwest Africa using salinity-temperature-density profilers (Barton and Hughes, 1982). Other field experiments have confirmed that breaking internal waves can lead to the development of mixed patches (Alford and Pinkel, 2000). Furthermore, numerical simulations have shown breaking internal waves can lead to the conversion of kinetic energy of small scale turbulence to the potential energy embodied by the mixed patches (Winters, 1994; Birch and Sundermeyer, 2010). Current instabilities (Thorpe, 2005) and hydrothermal plumes (Helfrich and Battisti, 1991) have also been shown to be able to create well-mixed patches of fluid in the stratified ocean. Analysis of the Coastal Mixing and Optics experiment showed that current models of lateral dispersion could not account for what was observed in the data (Sundermeyer and Ledwell, 2001). It hypothesized that vortical motions caused by the geostrophic adjustment of well-mixed patches of fluid may contribute to observed rates of lateral dispersion for a passive tracer unaccounted for by current models (Sundermeyer, 1998).

After the completion of a turbulent mixing event, a well-mixed region goes through a period of gravitational slumping. This is characterized by the fluid at the vertical extents, being heavier (top) or lighter (bottom) than the surrounding ambient fluid, moving towards the vertical center of the mixed patch. Due to the conservation of mass, fluid is pulled inward at the vertical extremes of the mixed patch. Likewise, the vertical convergence of fluid induces a radially symmetric horizontal flow away from the vertical and horizontal center of the patch. In less than one inertial period, should the mixed patch be large enough, the Coriolis effect induces an anticyclonic flow in the vertical center flanked above and below by two weaker cyclones. An inertial period is denoted  $T_{ip} = \frac{2\pi}{f}$ , where  $f$  is the Coriolis parameter. An inertial period is approximately 18 hours at mid-latitudes. In the Northern Hemisphere, cyclonic flow is counter-clockwise and anti-cyclonic flow is clockwise in rotation. This compound structure is referred to as an *adjustment*

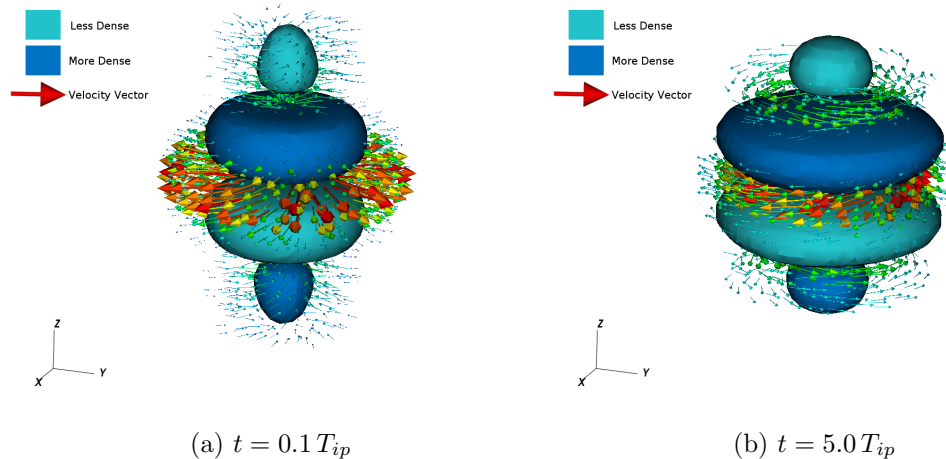


Figure 1.1: Earlier (a) and later times (b) in the development of an adjustment vortex. Contours of perturbation density reflect the outward slumping and the downward pull of fluid from the vertical extents. Arrows of velocity show the geostrophic adjustment of the fluid velocity into three vortices. The center anti-cyclone rotates clockwise while the top and bottom cyclones rotate anti-clockwise (b).

*vortex* throughout this dissertation. Oscillations of the mixed patch due to the slumping process and its rebound emit internal waves until the oscillations subside. The structure of a numerically simulated adjustment vortex can be seen in Figure 1.1.

The geostrophic adjustment of a well-mixed lens within a rotating, stratified, and incompressible fluid was first explored by McWilliams (1988). The existence of vortices created from the gravitational flattening (or slumping) and geostrophic adjustment of a well-mixed lens was shown through Lagrangian conservation relations of potential vorticity, mass, and angular momentum. More recently, geostrophic adjustment of well-mixed patches were numerically examined (Lelong and Sundermeyer, 2005). Mixed patches that convert most of their initial potential energy to the kinetic energy of a vortex have lateral radius equal to the internal deformation radius of the fluid. The deformation radius is defined by the scale at which a phe-

nomenon is influenced by the Coriolis effect. The adjustment of the mixed patch converts the initial potential energy approximately to 10% the kinetic energy of internal waves, 25% to the available potential energy of internal waves, and 20% to the kinetic energy of the vortex while 45% remains as available potential energy of the vortex. For a mixed patch with radius smaller than the deformation radius, more of the initial energy is converted into internal waves. However, when a mixed patch has a radius greater than the deformation radius, the geostrophic adjustment process arrests before much of the initial available potential energy is converted to either internal waves or vortex kinetic energy. Some of these observations have been confirmed by rotating table experiments in which perturbed linear stratification is allowed to adjust under the influence of rotation (Stuart, 2011). Periodic introduction of adjusted mixed patches, that are uniformly distributed in a numeric domain, were used to investigate contributions to the lateral mixing of a passive tracer at the submesoscale (Sundermeyer and Lelong, 2005). When the mixed patches are introduced at a rate of 10 per inertial period, an inverse cascade of kinetic energy is observed. Non-linear interactions between adjustment vortices were hypothesized to be the source of the inverse cascade of kinetic energy and the lack of statistical equilibration.

The presence of the inverse cascades of kinetic energy are not without precedence. In the quasi-geostrophic limit, with strong rotation and stratification, it is predicted that incompressible fluids, with negligible viscosity, will exhibit inverse cascades of kinetic energy (Charney, 1971). As the Taylor-Proudman effect reduces vertical gradients in fluids of constant density and strong stratification reduces vertical velocity outright, layers of fluid are decoupled into two-dimensional slabs. Scaling arguments of Kraichnan (1967) predicted the inverse kinetic energy cascades and the forward cascade of enstrophy of two-dimensional turbulence. Many numerical simulations and rotating table experiments confirm the inverse cascade of kinetic energy in two dimensional fluids. Recent arguments present an analytic foundation for both dipolar and bar end states in randomly forced, periodic, two-dimensional flows with small viscosity (Beck and Wayne, 2012). The

dipolar end state of two-dimensional flows consists of two counter-rotating vortices that dominate the domain. The bar end state consists of a jet that encircles the toroidal domain with another jet in the opposite direction. Many studies of rotating, stratified fluids have used these arguments as a foundation for the inverse energy cascades observed on planetary scales. Examples of these are seen in the merging of Gulf Stream rings (Cresswell, 1982) and the large spot on Jupiter.

Numerical studies of quasi-geostrophic and Boussinesq fluids have demonstrated inverse energy cascades in anisotropic, triply-periodic models of rotating stratified fluids. McWilliams and Weiss (1994) and McWilliams et al. (1994) demonstrate triply-periodic, anisotropic models exhibiting large coherent vortices emerging from random initial conditions. Triply-periodic numerical simulations of rotating stratified flows that were spectrally forced around a mean scale with kinetic energy also resulted in inverse cascades (Métais et al., 1996). Using a similar forcing in a Boussinesq fluid, inverse cascades of kinetic energy were also observed (Smith and Waleffe, 1999, 2002). However, there is a concern that vertically periodic boundary conditions may strongly contribute to these inverse cascades. Dritschel and Macaskill (2000) show that changing the aspect ratio of the domain in relation to the number and aspect ratio of initial vortices considerably affects the capacity to form coherent two-dimensional vortices.

This dissertation is divided into six chapters and three appendices. The present introduction chapter has outlined the phenomenon of interest and the context in which it resides. Concepts and elements of the numerical model that are employed throughout the rest of the dissertation are presented in Chapter 2. In Chapter 3, two vortices of geostrophic adjustment are introduced into a rotating, stratified, numerical domain with small viscosity. The proximal interactions of the two compound vortices are described with respect to the type of stable form that results. Using a clustering assumption of continually forced simulations in Chapter 4 a spatial Poisson process is used to cluster mixing events and examine the effect upon lateral dispersion. It is expected that the non-linear interactions will drive greater dispersion of a passive tracer in the numerical model representative

of an oceanic context. The results of this chapter, along with the next, reveal the nature of the inverse energy cascade and the effects on the dispersion of the passive tracer. The non-dimensionalization of the spectral Boussinesq equations in Chapter 5, reveal that comparatively weak barotropic damping in anisotropic, triply-periodic numerical models contribute to inverse cascades of kinetic energy. Numerical simulations confirm that the undamped accumulation of barotropic mode kinetic energy is strongly associated with an inverse cascade of kinetic energy for the model, parameters, and forcing used. In the Conclusions chapter, the results from each of the core chapters are summarized in terms of contributions that they make to the understanding of modeling the submesoscale ocean.

The three appendices present supporting and unpublished studies that contribute to the dissertation as a whole. In Appendix A, the technique of diffusively forcing density stratified domains is presented in depth. It is shown that introducing diffusive forcings in close proximity to previously destratified regions introduces varying amounts of energy. In Appendix B, what is known about the stability properties of an adjustment vortex is presented. Finally, in Appendix C, a simple technique for incorporating higher-order dissipative terms is developed.

## Chapter 2

### BACKGROUND

In this chapter, concepts relevant to the modeling of processes in the oceanic submesoscale are presented. First, the theory of internal waves is given a cursory review. Next, elements of geostrophic adjustment of mixed patches unaddressed in the Introduction are presented. Finally, the numerical model used for simulations of this dissertation is presented. When a technique used in the numerical model has consequences relevant to material presented in specific chapters, the reader is referred to the chapter of interest.

#### 2.1 *Internal Waves*

Internal waves come in a few simple varieties. The first is seen at the interface of fluids of two different densities. These interfacial waves behave much like the waves I know that form at the interface between air and water. The propagation speed of interfacial waves are dependent on the difference in the densities of the two fluids. Otherwise, the energy of these waves are transferred only in horizontal directions. The second variety, internal waves propagating through a continuously stratified fluid, transfer energy vertically as well as horizontally. To see this, the Boussinesq equations of motion are simplified. The Boussinesq equations of motion are

$$\frac{\partial \mathbf{u}}{\partial t} + \mathbf{u} \cdot \nabla \mathbf{u} + f \mathbf{e}_3 \times \mathbf{u} = -\frac{1}{\rho_0} \nabla p' - g \mathbf{e}_3 \frac{\rho'}{\rho_0} + \nu \nabla^2 \mathbf{u}, \quad (2.1)$$

$$\nabla \cdot \mathbf{u} = 0, \quad (2.2)$$

$$\frac{\partial \rho'}{\partial t} + \mathbf{u} \cdot \nabla \rho' + w \frac{\partial \bar{\rho}}{\partial z} = \kappa \nabla^2 \rho', \quad (2.3)$$

where the velocity vector  $\mathbf{u} = [u, v, w]^T$ , perturbation pressure  $p'$ , and perturbation density  $\rho'$  are the solution variables. The remaining parameters are the vertical density gradient  $d\bar{\rho}/dz$ , background density  $\rho_0$ , vertical unit vector  $\mathbf{e}_3 = [0, 0, 1]^T$ , Coriolis parameter  $f$ , gravitational acceleration  $g$ , Laplacian viscosity  $\nu$ , and Laplacian diffusivity  $\kappa$ . These three equations are the momentum equations (2.1), incompressibility constraint (2.2), and the density evolution equation (2.3). The full density is in a Reynolds decomposition of background with linearly varying vertical density profile and a perturbation from the previous two,  $\rho = \rho_0 + \bar{\rho}(z) + \rho'$ . Taking the inviscid form of these equations, assuming the vertical density profile remains constant ( $d^2\bar{\rho}/dz^2 = 0$ ), removing the Coriolis term, assuming that the physical quantities are perturbations from rest, and removing the squares of these perturbations, (2.1)-(2.3) are simplified to

$$\frac{\partial u}{\partial t} = -\frac{1}{\rho_0} \frac{\partial p}{\partial x} \quad (2.4)$$

$$\frac{\partial v}{\partial t} = -\frac{1}{\rho_0} \frac{\partial p}{\partial y} \quad (2.5)$$

$$\frac{\partial w}{\partial t} = -\frac{1}{\rho_0} \frac{\partial p}{\partial z} - g \frac{\rho}{\rho_0}, \quad (2.6)$$

$$\frac{\partial \rho}{\partial t} + w \frac{\partial \bar{\rho}}{\partial z} = 0, \quad (2.7)$$

where all lower case variables are assumed to be perturbations from a rest state.

The equations (2.4)-(2.7) can be simplified to an equation only in  $w$  as follows. From (2.4) and (2.5),

$$\frac{\partial^2 u}{\partial x \partial t} + \frac{\partial^2 v}{\partial y \partial t} = -\frac{1}{\rho_0} \left[ \frac{\partial^2 p}{\partial x^2} + \frac{\partial^2 p}{\partial y^2} \right]. \quad (2.8)$$

Using (2.2),

$$\frac{\partial^2 w}{\partial z \partial t} = \frac{1}{\rho_0} \left[ \frac{\partial^2}{\partial x^2} + \frac{\partial^2}{\partial y^2} \right] p. \quad (2.9)$$

Eliminating  $\rho$  from (2.9) requires another relation. This is accomplished by taking

a time derivative of (2.6), solving for  $\frac{\partial \rho}{\partial t}$ , and equating with (2.7),

$$\frac{\partial^2 w}{\partial t^2} + N^2 w = -\frac{1}{\rho_0} \frac{\partial^2 p}{\partial z \partial t}, \quad (2.10)$$

where  $N^2 = -\frac{g}{\rho_0} \frac{d\bar{\rho}}{dz}$  is the Brunt-Väisälä frequency, or *buoyancy frequency*, squared. The Brunt-Väisälä frequency is the frequency with which a disturbed parcel of fluid will oscillate vertically around its preferred location in a density stratified fluid. The restoring force that produces the oscillation is the buoyancy force of the fluid parcel being out of equilibrium with its surroundings.

The final step is to construct an equation involving only  $w$ , eliminating the pressure variable  $p$ . This is accomplished by applying the operator  $(\partial^2/\partial x^2 + \partial^2/\partial y^2)$  to (2.10), applying the operator  $\partial^2/\partial z \partial t$  to (2.9), and adding. This results in,

$$\frac{\partial^2}{\partial t^2} \left[ \frac{\partial^2}{\partial x^2} + \frac{\partial^2}{\partial y^2} + \frac{\partial^2}{\partial z^2} \right] w + N^2 \left[ \frac{\partial^2}{\partial x^2} + \frac{\partial^2}{\partial y^2} \right] w = 0. \quad (2.11)$$

This differential equation for  $w$  has traveling wave solutions

$$w = \text{Re} \{ W \exp [\mathbf{i}(\mathbf{k} \cdot \mathbf{x} - \omega(\mathbf{k})t)] \}, \quad (2.12)$$

where  $W$ ,  $\omega(\mathbf{k})$ ,  $\mathbf{x} = [x, y, z]^T$ , and  $\mathbf{k} = [k, l, m]^T$  are the wave amplitude, dispersion relation, position vector, and wavenumber vectors respectively. The dispersion relation,  $\omega(\mathbf{k})$ , satisfies

$$\omega^2(\mathbf{k}) = \frac{(k^2 + l^2)N^2}{k^2 + l^2 + m^2}, \quad (2.13)$$

or

$$\omega^2(\mathbf{k}) = \frac{k_h^2 N^2}{k_h^2 + m^2}, \quad (2.14)$$

where  $k_h^2 = k^2 + l^2$ . The other components of velocity and the density have similar solutions that can be inferred by conservation of mass (2.2) and the evolution of density (2.3).

Another expression for the above dispersion relation is  $\omega(\mathbf{k}) = N \cos \theta$ , where  $\theta = \cos^{-1}[(k_h)/\sqrt{k_h^2 + m^2}]$  is the angle between the horizontal plane and the wave

vector  $\mathbf{k}$ . With the inclusion of the Coriolis terms into equations (2.4)-(2.7), and following a similar process, the dispersion relation becomes,

$$\omega^2(\mathbf{k}) = \frac{(k^2 + l^2)N^2 + m^2 f^2}{k^2 + l^2 + m^2}. \quad (2.15)$$

One interesting consequence of the dispersion relation is that the phase velocity

$$\mathbf{c}_p = \omega(\mathbf{k}) \cdot \frac{\mathbf{k}}{|\mathbf{k}|^2} \quad (2.16)$$

and the group velocity

$$\mathbf{c}_g = \nabla_{\mathbf{k}}\omega(\mathbf{k}) \quad (2.17)$$

are orthogonal,  $\mathbf{c}_p \cdot \mathbf{c}_g = 0$  (Figure 2.1). The energy of the internal wave is transferred in the direction of the group velocity. As with surface waves, internal waves can reflect when they encounter a boundary to their propagation. In this way internal waves can transport energy from the boundaries of the ocean (surface, bottom, and continental shelves) to the interior. The above derivations for solutions of internal waves can be found in many texts on fluid dynamics (Acheson, 1990; Lighthill, 1996; Cohen and Kundu, 2007).

When the conditions allow for the steepening of internal waves, they can break, create turbulence, and deposit energy in a localized region by turbulent mixing. The turbulent mixing increases the local available potential energy by reducing the stratification of that region. When the amplitude of an internal wave exceeds the wavelength, overturning and breaking can occur. This sensitivity to overturning is encoded in the Richardson Number  $Ri = N^2/(du/dz)^2$ . One of the necessary conditions for the breaking of internal waves is for the Richardson Number to be sufficiently small,  $Ri < 1/4$ . Resonant interactions with other internal waves, reflective focusing off a boundary, or instabilities inherent in wave shear are other means through which internal wave breaking can occur (Staquet and Sommeria, 2002).

In this dissertation, the turbulent mixing of an internal wave breaking event

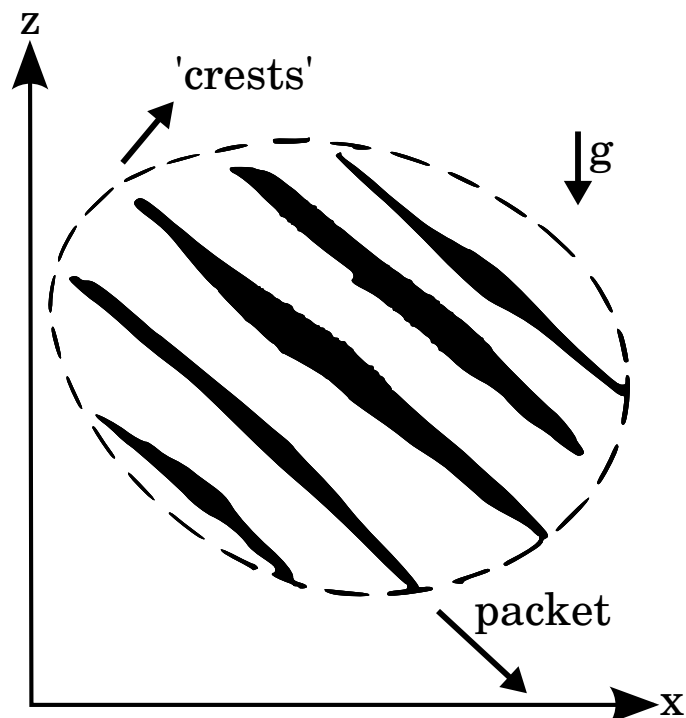


Figure 2.1: Phase and group velocity of an internal wave (Acheson, 1990)

itself is not directly modeled (see Section 2.3.2), the conditions required for the breaking of internal waves are considered in constructing a probability model (see Chapter 4). The localized mixing generated by parameterized internal wave breaking provides potential energy in the form of a locally destratified lens. Modeling the adjustment of this destratified lens into a vortex is the starting point for the numerical model employed.

## 2.2 Geostrophic Adjustment

Geostrophic adjustment is the process by which a disturbed fluid attains a balance between the horizontal pressure gradient and the Coriolis force. As reviewed in the introduction, a well-mixed region in a stably stratified fluid is geostrophically adjusted. This mixed region is generated by a turbulent mixing event. These turbulent mixing events can be caused by the breaking of an internal wave as well as shear instabilities and other processes.

The above balance adjustment process is not completely in the linear geostrophic regime. At the scales and velocities that are being investigated, effects of the non-linear term have some influence. The significance of the non-linear term puts the flow in the gradient wind regime. This is also known as the non-linear geostrophic regime (Lelong and Sundermeyer, 2005).

In the numerical study of Lelong and Sundermeyer (2005), it is shown that mixed patches convert the most available potential energy to balanced, or vortex, kinetic energy when their radial extent is equal to the internal Rossby radius of deformation,

$$R = \frac{\Delta N h}{f}, \quad (2.18)$$

where  $h$  is the height of the mixed patch,  $f$  is the Coriolis parameter, and  $\Delta N$  is the change in buoyancy frequency. The change in buoyancy frequency is derived from comparing the square buoyancy frequency at a location,  $N^2 = -g/\rho_0 \partial \rho / \partial z$ , with its linear component,  $\bar{N}^2 = -g/\rho_0 \partial \bar{\rho} / \partial z$ , or  $N^2 = \bar{N}^2 - \Delta N^2$ , with  $0 \leq \Delta N^2 \leq N^2$ . For  $\Delta N^2 = N^2$  the mixed patch is totally destratified. The remainder of the energy resides in the potential energy of the balanced flow or the internal wave field generated by the adjustment process.

### 2.3 Numerical Model

As in previous studies (Lelong and Sundermeyer, 2005; Sundermeyer and Lelong, 2005), the pseudo-spectral numerical model of Winters et al. (2004) is used. This code solves the three dimensional Boussinesq equations, with a constant Coriolis parameter, coupled with advection/diffusion equations for fluid density and the evolution of a passive tracer on a triply-periodic domain. Spatial derivatives are approximated with Fourier transforms. Time stepping is implemented with a third-order Adams-Bashforth method.

Table 2.1: Model Parameters for base run (Sundermeyer and Lelong, 2005)

Variable	Symbol	Model Value	Scaled Value
Horizontal and vertical domain size	$L_x = L_y, L_z$	500 m, 12.5 m	5 km, 12.5 m
Coriolis parameter	$f$	$9.5 \times 10^{-4} \text{ s}^{-1}$	$9.5 \times 10^{-5} \text{ s}^{-1}$
Background stratification	$\frac{\partial \rho}{\partial z}$	$0.037 \text{ kg m}^{-4}$	$0.037 \text{ kg m}^{-4}$
Interval between anomalies	$\tau = 1/\phi$	$3 \frac{2\pi}{f}$	$3 \frac{2\pi}{f}$
Anomaly amplitude	$\Delta N^2/N^2$	1.0	1.0
Anomaly horizontal scale	$L = 2\sigma_x, 2\sigma_y$	50 m	500 m
Anomaly vertical scale	$h = 2\sigma_z$	1.25 m	1.25 m
$\nabla_2$ viscosity	$\nu_2$	$2.5 \times 10^{-5} \text{ m}^2 \text{ s}^{-1}$	$2.5 \times 10^{-6} \text{ m}^2 \text{ s}^{-1}$
$\nabla_2$ diffusivity	$\kappa_2$	$2.5 \times 10^{-6} \text{ m}^2 \text{ s}^{-1}$	$2.5 \times 10^{-7} \text{ m}^2 \text{ s}^{-1}$
$\nabla_6$ viscosity (horizontal)	$\nu_6$	$48 \text{ m}^6 \text{ s}^{-1}$	—
$\nabla_6$ diffusivity (horizontal)	$\kappa_6$	$48 \text{ m}^6 \text{ s}^{-1}$	—
$\nabla_6$ viscosity (vertical)	$\nu_6$	$1.8 \times 10^{-10} \text{ m}^6 \text{ s}^{-1}$	—
$\nabla_6$ diffusivity (vertical)	$\kappa_6$	$1.8 \times 10^{-10} \text{ m}^6 \text{ s}^{-1}$	—
Model time step	$\Delta t$	30 s	30 s
Total model run time	—	$800 \times \frac{2\pi}{f}$	$800 \times \frac{2\pi}{f}$
Tracer injection time	—	$100 \times \frac{2\pi}{f}$	$100 \times \frac{2\pi}{f}$

The governing equations are,

$$\frac{\partial \mathbf{u}}{\partial t} + \mathbf{u} \cdot \nabla \mathbf{u} + f \mathbf{e}_3 \times \mathbf{u} = -\frac{1}{\rho_0} \nabla p' - g \mathbf{e}_3 \frac{\rho'}{\rho_0} + \nu_2 \nabla^2 \mathbf{u} + \nu_6 \nabla^6 \mathbf{u}, \quad (2.19)$$

$$\nabla \cdot \mathbf{u} = 0, \quad (2.20)$$

$$\frac{\partial \rho'}{\partial t} + \mathbf{u} \cdot \nabla \rho' + w \frac{d\bar{\rho}}{dz} = \kappa_2 \nabla^2 \rho' + \kappa_6 \nabla^6 \rho', \quad (2.21)$$

$$\frac{\partial C}{\partial t} + \mathbf{u} \cdot \nabla C = \kappa_2 \nabla^2 C + \kappa_6 \nabla^6 C, \quad (2.22)$$

where, as in (2.1)-(2.3), the velocity vector  $\mathbf{u}$ , pressure perturbation  $p'$ , and density perturbation  $\rho'$  are the solution variables. The remaining parameters are the linear density gradient  $d\bar{\rho}/dz$ , the background density  $\rho_0$ , the Coriolis parameter  $f$ , the gravitational acceleration  $g$ , Laplacian viscosity  $\nu_2$ , sixth-order viscosity  $\nu_6$ , Laplacian diffusivity  $\kappa_2$ , sixth-order diffusivity  $\kappa_6$ , and unit vector in the vertical  $\mathbf{e}_3 = [0, 0, 1]^T$ . These four equations represent evolution of momentum (2.19), incompressibility constraint (2.20), evolution of density (2.21), and the evolution

of tracer (2.22). Terms referring to linearly varying vertical gradients of pressure and density,  $\bar{p}$  and  $\bar{\rho}$ , have been removed from (2.19) with use of hydrostatic balance. This leaves perturbation variables that are periodic and can be treated with Fourier methods. The higher-order viscosity and diffusion terms for momentum (2.19), density (2.21), and tracer (2.22) equations remove steep gradients of velocity, density, and tracer at the smallest resolved scales. Without higher-order terms, steep gradients may cause Gibbs phenomenon and numerical errors to accumulate.

The numerical model of Winters et al. (2004) uses Fourier transforms to convert the above equations to spectral equivalents. Derivatives of quantities involved in non-linear terms (i.e.  $u du/dx$ ) are taken in spectral space, brought back to physical space through inverse transforms, combined with associated quantities, and transformed back to spectral space. This method avoids aliasing of wavenumbers in the non-linear terms (Orszag, 1972). The Fourier transform of (2.19) is

$$\frac{\partial \hat{\mathbf{u}}_k}{\partial t} - T_k + f \mathbf{e}_3 \times \hat{\mathbf{u}}_k = -\frac{i\mathbf{k}}{\rho_0} \hat{p}'_k - \mathbf{e}_3 \frac{g}{\rho_0} \hat{\rho}'_k - \frac{1}{2} \mathbb{D}_k \hat{\mathbf{u}}_k, \quad (2.23)$$

with all hatted variables being Fourier transforms at wavenumber  $\mathbf{k}$  and

$$T_k = -(\widehat{\mathbf{u} \cdot \nabla \mathbf{u}})_k, \quad (2.24)$$

$$\mathbb{D}_k = 2\nu_2 |\mathbf{k}|^2 + 2\nu_6 |\mathbf{k}|^6, \quad (2.25)$$

where  $T_k$  is the Fourier transform of the non-linear term and  $\mathbb{D}_k$  is the spectral dissipation operator. Using the spectral form of the incompressibility constraint ( $\mathbf{k} \cdot \hat{\mathbf{u}}_k = 0$ ) on (2.23), the pressure variable is solved for in terms of the other variables,

$$\hat{p}'_k = \frac{i\mathbf{k}}{|\mathbf{k}|^2} \cdot \left( f \mathbf{e}_3 \times \hat{\mathbf{u}}_k - \frac{g}{\rho_0} \hat{\rho}'_k \mathbf{e}_3 - T_k \right). \quad (2.26)$$

The spectral momentum equation can now be expressed as,

$$\frac{\partial \hat{\mathbf{u}}_k}{\partial t} = \mathbf{F}(\hat{\mathbf{u}}_k, \hat{\rho}'_k, \mathbf{k}) - \frac{1}{2} \mathbb{D}_k \hat{\mathbf{u}}_k, \quad (2.27)$$

where  $\mathbf{F}$  is the collection of all other terms not shown. Using an integrating factor  $\exp\{-\frac{1}{2}\mathbb{D}_k t\}$ , (2.27) is expressed as,

$$\frac{\partial}{\partial t} \left[ \hat{\mathbf{u}}_k e^{-\frac{1}{2}\mathbb{D}_k t} \right] = e^{-\frac{1}{2}\mathbb{D}_k t} \mathbf{F}. \quad (2.28)$$

The quantity  $\hat{\mathbf{u}}_k e^{-\frac{1}{2}\mathbb{D}_k t}$  is integrated discretely in time using a third-order, Adams-Bashforth, finite-difference method. Each time step for the remaining evolved quantities is accomplished using the same integrating factor technique. The method is bootstrapped by using lower-order techniques until a sufficient number of snapshots are available for the third-order method.

In this dissertation, and in related work, additional settings and techniques are used. The techniques in the following subsections are used for computational tractability and numerical stability. Where pertinent, the reader is referred to relevant chapters and appendices that present important considerations to the techniques presented.

### 2.3.1 Model Setup

The scales represented by the horizontal and vertical resolution reflect the scaling between the Brunt-Väisälä and Coriolis frequencies ( $L/H \sim N/f$ ). The modeled domain width, 500 m, has a resolution of 128 grid points, while the vertical extent, 12.5 m, has a resolution of 64 grid points. The extent of the domain is chosen to allow ten mixing events to occur in the domain without overlapping. Baroclinic vortices in a rotating stratified flow are known to have aspect ratios that reflect these considerations (Thorpe, 2005). Values for other parameters (background vertical density gradient, viscosity, diffusivity, and mixed patch dimensions) are listed in Table 2.1.

### 2.3.2 Diffusive Forcing

The diapycnal mixing of a fluid is brought about by a turbulent mixing event, such as a breaking internal wave packet. Simultaneously modeling the wave break-

ing, turbulent mixing, and geostrophic adjustment of a fluid is a computationally prohibitive process. Modeling turbulent mixing on small physical scales would require increased spatial resolution and a comparative refinement in time stepping for numeric stability. To avoid numerically modeling both large and small scales a technique of a parameterized diffusive forcing is employed. This technique is applied while the rest of the Navier-Stokes model is in between time steps.

Parameterized diapycnal mixing events are introduced by temporarily imposing a vertical diffusivity of the form

$$\kappa^*(\mathbf{x}, t) = \frac{1}{\Delta t} \frac{\Delta N^2}{N^2} \sigma_z^2 \exp\left(-\left[\frac{(x-x_0)^2 + (y-y_0)^2}{2\sigma_r^2} + \frac{(z-z_0)^2}{2\sigma_z^2}\right]\right) \quad (2.29)$$

centered at a chosen location,  $(x_0, y_0, z_0)$ , in the density stratified domain, where  $\Delta N^2/N^2 \in [0.0, 1.0]$  represents the extent of destratification that is desired for the mixed region. Complete destratification,  $\Delta N^2/N^2 = 1.0$ , is used for all simulations. The horizontal and vertical extent,  $\sigma_r = 12.5 m$  and  $\sigma_z = 0.625 m$ , are used in conjunction with  $\Delta N^2/N^2 = 1.0$  to ensure the most conversion of initial potential energy to vortex kinetic energy as in Lelong and Sundermeyer (2005). The density perturbation of the code is combined with a shifted linear density profile  $\bar{\rho}(z - z_0)$ , where  $z_0$  is the center of the mixed patch. This places the center of the mixed patch,  $(x_0, y_0, z_0)$ , at the center of a shifted linear density profile. The full density of the fluid is updated by solving a diffusivity equation,  $\rho_t = (\kappa^* \rho_z)_z$ , with vertically varying diffusivity parameter (2.29), for a fixed amount of time. After completion, the shifted linear density profile is removed, leaving a density perturbation at the desired location. Application of this off-line diffusive forcing has the effect of creating a well mixed region that introduces available potential energy into the domain. The resulting mixed patch is the initial condition for the geostrophic adjustment described above.

In practice, the above process produces a destratification ratio of only  $\Delta N^2/N^2 = 0.5$  for a single mixing event. This, coincidentally, is close to what is found in comparative oceanic settings, see Gregg et al. (1986). Attempts to increase this ratio

through changes in (2.29) or extending the length of time it is imposed, create density gradients too sharp for the Fourier method to accurately resolve for the resolution used. In simulations where adjustment is allowed to occur for an inertial period between adding five mixing events in close proximity, the destratification ratio can be as high as  $\Delta N^2/N^2 = 0.7$ . This occurs in conjunction with a doubling in the radius of the mixed patch created and a 10% increase in mixed patch height. A more complete review and other consequences of diffusive forcing are outlined in Appendix A.

### 2.3.3 $N/f$ Scaling

The range of temporal and spatial scales necessary for modeling the range of dynamics typical of mid-latitude, oceanic submesoscales are computationally prohibitive. While internal waves require scales of seconds and meters to be well resolved, turnover times and horizontal scales for submesoscale vortices are on the order of days and kilometers. Numerically modeling one vortex turnover time would require thousands of time steps with high spatial resolution. Artificially increasing the Coriolis parameter by a factor of ten decreases the ratio of inertial to buoyancy time scales from  $N/f \approx 100$  to  $N/f \approx 10$  and reduces the internal deformation radius by the same amount. To maintain dynamic similarity to an unscaled domain, the radius of the vortices  $L$  is reduced by a factor of ten, the viscosity  $\nu_2$  is increased by the same factor, and the vortex height  $h$  is held constant. This ensures that the Burger ( $Bu = (\Delta N h / f L)^2 = (R/L)^2$ ), Ekman ( $Ek = h^2 f / \nu_2$ ), and Rossby ( $Ro = U / f L$ ) numbers are preserved along with their implied dynamics. Using the  $N/f$  scaling technique, as in Lelong and Dunkerton (1998), enables a thousand fold increase in computational efficiency, but is not without additional considerations.

Although the Burger, Ekman, and Rossby numbers are preserved by the  $N/f$  scaling, the Reynolds number is not. For consistent velocity scale  $U$  the above adjustments in vortex radius  $L$  and viscosity  $\nu$  scale the Reynolds number two orders of magnitude lower than in the unscaled domain,  $Re = U(L_0/10)/(\nu_0 \cdot 10) =$

$Re_0/100$ , with  $L_0$ ,  $\nu_0$ , and  $Re_0$  being the unscaled vortex radius, Laplacian viscosity, and Reynolds number. With the dissipation times for vertical gradients of velocity the Reynolds number scales as  $Re = Ro/Ek(f/N)^2$ . For simulations where viscosity is sufficiently small, Reynolds numbers will remain in a turbulent range ( $Re > 10,000$ ). However, when Reynolds number is scaled through transitional Reynolds numbers, the behavior of the scaled domain will no longer be representative of unscaled dynamics. It can also be seen in the above spectral diffusion operator (2.25) that the Reynolds number is directionally different depending on the anisotropy of the domain. When the velocity gradients are strongest in the vertical direction, it is the vertical Reynolds number that is important. Likewise, if the velocity gradients are primarily in the horizontal direction, it is the horizontal Reynolds number that takes precedence. These observations are also made in Chapters 4 and 5. The numerical simulations of Chapter 3 are in a high Reynolds number regime and are unaffected by this adjustment.

#### 2.3.4 *Hyper-viscosity*

The hyper-viscosity (as hyper-diffusion) provides a strong dissipation at the smallest scales in the simulation. This, in turn, extends the inertial subrange of the flow, where the fluid is effectively described by the inviscid equations (Borue and Orszag, 1995b). In the anisotropic domain used for all simulations, the hyper-viscosity and hyper-diffusion ensure numerical stability in the horizontal direction while the Laplacian terms, with lower Reynolds numbers ( $Re = UL/\nu_2$ ), represent the physical background viscosity and diffusion that act primarily on small vertical scales. For the high Reynolds numbers of the presented simulations, the hyper-viscosity removes enstrophy at small scales in all directions.

Hyperviscosity is used in conjunction with the 8/9 wavenumber truncation number of Orszag and Patterson (1971) such that the dissipation timescale, or e-folding timescale, is constant on the surface of an ellipsoid defined by

$$\left(\frac{k}{k_{max}}\right)^2 + \left(\frac{l}{l_{max}}\right)^2 + \left(\frac{m}{m_{max}}\right)^2 \approx 1,$$

where  $\mathbf{k} = [k, l, m]^T$  is the wavenumber vector and  $\mathbf{k}_{max} = [k_{max}, l_{max}, m_{max}]^T$  is the maximum retained wavenumber in each direction, defined by truncating the largest 1/9 of the wavenumbers in each direction. Therefore, the dissipation and diffusion time-scales for the above parameters is  $T_{max} = 1/\nu_6$  on the wavenumber ellipsoid defined above.

Further insights and motivations are provided in both Chapter 5 and in Appendix C. Chapter 5 provides a comparison of the above hyper-viscosity representation to one directly derived from the non-dimensionalization of the Boussinesq equations of motion. For anisotropic domains, the above representation gives a near isotropic dissipation in spectral space. Appendix C further develops techniques concerning hyper-viscosity. Appropriate settings for parameters of hyper-dissipation can provide desired dynamics for specified ranges of wavenumbers.

### 2.3.5 Effective Diffusivity

Sundermeyer and Lelong (2005) presented a parameterization of the effective lateral diffusivity for the weakly non-linear regime:

$$\kappa_H \propto \left(\frac{1}{2}\right) \left(\frac{h^2 \Delta N^2}{L f^2}\right)^2 \phi \left(\frac{h^2/\nu_B}{1/f}\right). \quad (2.30)$$

This parameterization is derived from a random walk. The step size is the geostrophic velocity,  $U = \frac{h^2 \Delta N^2}{L f^2}$ , multiplied by the adjustment time scale,  $T = 1/f$ , or  $S = \frac{h^2 \Delta N^2}{L f^2}$ . Taken with the frequency of events,  $\phi$ , gives an estimate of a diffusivity,  $\kappa_e = \frac{1}{2} S^2 \phi$ . The last element of the parameterization represents the lifetime of the vortices in relation to the inertial time scale, or inverse Ekman number ( $Ek^{-1} = \frac{h^2/\nu_B}{1/f}$ ).

This parameterization is consistent with statistics taken from multiple runs in the following manner:

$$\kappa_H = \frac{1}{2} \frac{\partial \sigma_x^2}{\partial t}, \quad (2.31)$$

where

$$\sigma_x^2 = \int_V x^2 \hat{C}(\mathbf{x}) dV - \mu_x^2, \quad (2.32)$$

$$\hat{C}(\mathbf{x}) = \frac{C(\mathbf{x})}{\int_V C(\mathbf{x}) dV}, \quad (2.33)$$

$$\mu_x = \int_V x \hat{C}(\mathbf{x}) dV, \quad (2.34)$$

where the effective diffusivity  $\kappa_H$  is calculated from the horizontal variance of the tracer  $\sigma_x^2$ , the horizontal mean of the tracer  $\mu_x$ , the concentration of the tracer  $C$ , and the normalized concentration of the tracer  $\hat{C}$  at selected times during the simulations.

The parameterization above is found to be consistent for a weakly non-linear regime. In this regime, the adjusted mixed patches dissipate away before another mixed patch is able to interact with them. However, when the recurrence frequency  $\phi$  of the density anomalies is too high, or the Laplacian viscosity  $\nu_2$  is too low, a strongly non-linear and energetic regime is entered. In this regime the parameterization of  $\kappa_H$  is no longer representative. The recurrence and persistence of mixed regions is strong enough to induce interactions between the vortices of adjustment. In this non-linear regime the numerical simulation no longer balances the addition of potential energy with the dissipation of kinetic energy. The inverse energy cascade results in the build up of kinetic energy at large scales and the loss of a statistically stationary flow. Without a statistically stationary flow the current method of calculating effective diffusivity from simulation data can no longer be used.

Select simulations that were used to produce these results are revisited in Chapter 4. Additionally, a clustering assumption is used to investigate the effect of non-linear interactions between adjustment vortices. Inverse cascades of kinetic energy occurring largely in the barotropic mode are found to contribute to the lateral dispersion of a passive tracer. The mechanisms for this inverse energy

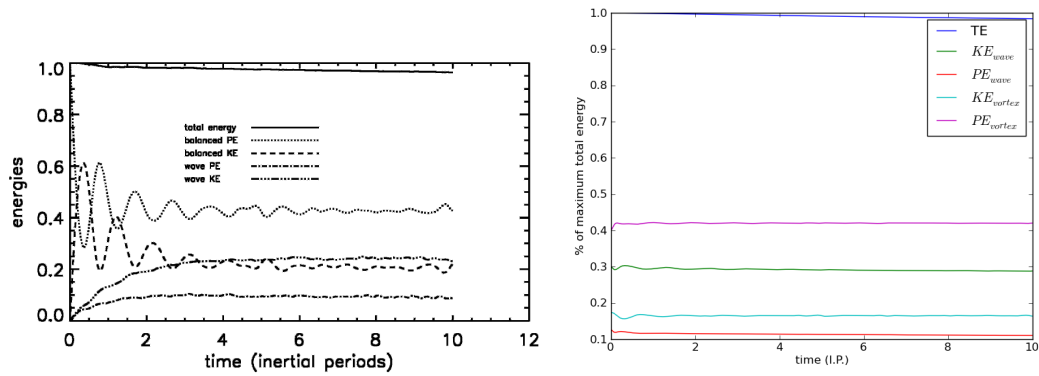
cascade are evaluated in Chapter 5.

#### **2.4 Wave-Vortex Decomposition**

The wave-vortex decomposition of Bartello (1995) is used to divide the energy into wave and vortical modes. It uses a normal mode decomposition of the inviscid, linearized Navier-Stokes Equations in Fourier space. This decomposition uses the fact that internal waves have no potential vorticity and the rest of the energy must be in the vortical mode. These energies are further divided into potential and kinetic energy components using known ratios between kinetic and potential energies for the wave and vortical modes (Gill, 1982; Polzin et al., 2003). This decomposition is compared to the decomposition used in Lelong and Sundermeyer (2005). Lelong and Sundermeyer (2005) consider the energy within the volume of a single, isolated mixed patch to be vortex energy and that outside to be the wave energy. The normal mode decomposition captures the linear, rather than non-linear, behavior of the vortices. As a consequence, the normal mode decomposition does not capture the initial slumping behavior of the adjustment process. However, the longer term behavior ( $t > 4 IP$ ) of the two methods is comparable (Figure 2.2).

The normal mode decomposition is tested on a domain with a forced mode 1 internal wave. As expected, the wave energy is sharply peaked at the mode 1 wavenumber. The vortex energy is also peaked at the mode 1 wavenumber, though five orders of magnitude less. If the Coriolis parameter is increased, decreasing the Rossby number, the effect upon the vortex energies is significantly decreased. Though this normal mode decomposition is more accurate for smaller Rossby numbers, it provides a good estimate of the energies in the wave and vortex fields.

The wave-vortex decomposition is used in Chapter 3 and Appendix B to investigate transfers of energy between the available potential energy of an adjustment vortex and its kinetic energy during the evolution of an instability. It is found that for the scale of vortices investigated, baroclinic instabilities draw kinetic energy from the conversion of available potential energy.



(a)  $R/L = 1.0$  from Lelong and Sundermeyer (2005).

(b) Single Mixing Event

Figure 2.2: Comparison between the wave-vortex decompositions from (a) a volume decomposition and (b) a normal mode decomposition. Differences can be accounted for by the linearity of the normal mode decomposition and the superposition of waves and vortices in the volume decomposition.

## Chapter 3

# PAIRWISE INTERACTION OF ADJUSTMENT VORTICES

In this chapter, I explore the interactions of two adjustment vortices in a near inviscid domain (very high Reynolds number or low Ekman number). Although stable merging of adjustment vortices are seen, overlapping diffusive forcing can create larger adjustment vortices with more energy. Instabilities, dipole pairing, and partial merger is seen to play a role in the formation of stable structures. The resultant stable structures are seen to interact, merge, and vertically couple with the assistance of associated dipole pairs.

### **3.1 Introduction**

In recent years much interest has been given to submesoscale processes and their contributions to a range of oceanic processes. One area of investigation has been how kinetic energy is able to cascade from geostrophic, largely two-dimensional, flows through the submesoscale to small dissipative scales. McWilliams (2008) proposed the straining of large fronts in the ocean as one possible mechanism in this energy cascade. Field experiments by D'Asaro et al. (2011) observed enhanced turbulence on the boundaries of large fronts in support of this theory.

Furthermore, the amount of energy available to drive lateral dispersion at submesoscales has a direct impact on the dispersal of the nutrients necessary for the growth of plankton (Levy, 2008; Thomas et al., 2008). In addition, variations in the rate of gas exchange between the ocean and atmosphere make submesoscale processes important contributors to the global carbon cycle (Doney et al., 2003). Intense variability in rates of submesoscale lateral dispersion are currently not accounted for in global models of the ocean and atmosphere.

The submesoscale process presently investigated is the geostrophic adjustment

of well-mixed patches in the oceanic thermocline. The majority of these mixed patches are thought to be generated by turbulent mixing driven by the episodic breaking of internal waves (Gregg et al., 1986). These well-mixed patches of water, 1-10 m in height and 0.1-1 km in diameter, have been observed as variations in the stratification over the continental shelf of Northwest Alaska (Barton and Hughes, 1982), off the coast of California (Gregg et al., 1986), and on the New England shelf (Sundermeyer et al., 2005). Indeed, field and numerical experiments have confirmed that breaking internal waves can lead to the development of mixed patches (Alford and Pinkel, 2000), and to the conversion of kinetic energy of small scale turbulence to the potential energy embodied by the mixed patches (Winters, 1994; Birch and Sundermeyer, 2010). Current instabilities (Thorpe, 2005) and hydrothermal plumes (Helfrich and Battisti, 1991) have also been shown to be able to create well-mixed patches of fluid in the stratified ocean. Although the breaking of internal waves is not the only process that can lead to the mixing of a localized patch of fluid, it will serve to describe what leads to and is left behind by a turbulent mixing event.

Despite being studied in numerical simulations and laboratory settings, adjustment vortices have yet to be observed in the ocean. One factor contributing to this may be the disparity in horizontal and vertical scales that need to be sampled to resolve an adjustment vortex. Another factor may be the shorter lifetimes of the vortices due to their stability properties. Whether unstable perturbations are introduced by varying the shape of the mixing event (see Appendix B), by numerical noise, or by the presence of internal waves (Brunner-Suzuki et al., 2012), the instabilities result in the eventual breakdown of the adjustment vortex structure.

The evolution of the instabilities seen in an adjustment vortex involves two-dimensional instabilities of each vortex core and interactions between counter-rotating, adjacent cores. Instabilities of two-dimensional isolated vortices have been identified by Carton and Legras (1994). For these two-dimensional vortices, initialized with a vertical vorticity profile of  $\zeta = (1 - \frac{1}{2}\alpha r^\alpha) \exp(-r^\alpha)$ , with steepness parameter  $\alpha$ , a mode two azimuthal instability has the fastest growth

for  $1.85 < \alpha < 6.0$ . The instabilities of these vortices portray linear growth, non-linear amplification, and non-linear saturation phases resulting in a stable, two-dimensional tripole structure. In two-layer simulations of baroclinic, quasi-geostrophic vortices, the number of split-propagating dipoles (hetons) that a vortex evolved into depended on the initially perturbed azimuthal modes (Helfrich and Send, 1988). As will be shown, the instabilities that evolve in adjustment vortices show similar behavior to the above vortices.

The introduction of episodic mixed patches into a viscous, rotating, and stratified domain has been used to study the influence of adjustment vortices on the lateral dispersion of a passive tracer at the submesoscale (Sundermeyer and Leong, 2005). As the rate of mixed patch introduction is increased, an accumulation of energy is observed at large scales. The interactions between adjustment vortices that contribute to an inverse energy cascade have yet to be explored. Being in a regime influenced by dynamics of both large and small scales, the details of how submesoscale vortices of geostrophic adjustment interact with one another are unknown. In this study, the interactions of two vortices of geostrophic adjustment are numerically investigated as well as their potential contributions to an inverse energy cascade.

Two shielded and isolated mono-polar vortices have been shown to stably merge in two-dimensional simulations when the separation distance between respective cores is in an appropriate range (Carton, 1992). This effect remains when taken to a two-layer, quasi-geostrophic framework (Valcke and Verron, 1997). The success and final structure of this merger has recently been shown to depend on Reynolds number ( $Re = \frac{UL}{\nu}$ , with velocity scale  $U$ , length scale  $L$ , and viscosity  $\nu$ ) as well as initial separation distance (Tóth and HÁzi, 2010). Three-dimensional, quasi-geostrophic simulations of the pairwise interactions between piecewise, ellipsoidal vortices show robust merging with both horizontal and vertical separation distances (Reinaud and Dritschel, 2002; Bambrey et al., 2007; Ozugurlu et al., 2008). Conversely, in three-dimensional, non-rotating, linearly stratified laboratory experiments and numerical simulations, co-rotating mono-polar shielded vortices do

not merge (Beckers et al., 2002).

Just as the merging of co-rotating cores from two different adjustment vortices is a possibility, the dipole association of counter-rotating cores is also a potential interaction. Dipole pairings of co-rotating vortices have been explored with two-dimensional shielded vortices (Schmidt et al., 1998) as well as with single three dimensional shielded baroclinic vortices (Beckers et al., 2002).

It is anticipated that the shear and strain of proximal adjustment vortices will have multiple effects. First, it is expected that instabilities that lead to the breakdown of a single vortex will occur more readily. Next, it is expected that the merging of co-rotating cores will be observed along with the pairing of counter-rotating cores. Furthermore, I hope to identify the interactions between adjustment vortices that contribute to an inverse energy cascade.

The numerical algorithm and methods of analysis for the interactions between two adjustment vortices are presented in Section 2.3. The results, Section 3, show that proximal adjustment vortices evolve into different stable forms depending on relative position. The results are summarized in the discussion, Section 4, and variations of experiments are considered. Contributions to an inverse energy cascade are presented in the conclusions of Section 5.

## **3.2 Model and Methods**

As in previous studies (Lelong and Sundermeyer, 2005; Sundermeyer and Lelong, 2005), the pseudo-spectral numerical model developed by Winters et al. (2004) is used. Section 2.3 addresses this numerical model and the techniques of potential energy forcing,  $N/f$ -Scaling, and hyper-viscosity used. The following sub-section quantifies the pairwise interactions between adjustment vortices.

### *3.2.1 Measuring Pairwise Interactions*

In this study, two mixed patches of the same dimensions and destratification are sequentially introduced with varied relative position into a domain . The dimensions of the mixed patches are chosen such that the resultant adjustment vortices

have the highest possible ratio of vortex kinetic energy to initial potential energy. The relative position of each mixed patch with respect to the other is given by the ordered pair  $(\Delta r, \Delta z)$  (Figure 3.1). The horizontal separation  $\Delta r$  is scaled by the internal Rossby radius of deformation, while the vertical separation  $\Delta z$  is scaled by the separation between the vorticity extrema of a single adjustment vortex. The scaling of the vertical separation is a convenience to denote which cores of respective adjustment vortices are interacting and is helpful in understanding the types of interactions that can occur. The mixed patches are introduced into the domain one inertial period apart, the first being introduced at the beginning of each simulation. This is intended to represent the episodic nature of mixed patches in the ocean. The 66 numerical simulations performed are represented in Figure 3.2.

It is noted by Flierl (1988) that external shears and strains provide a means to excite the natural modes of oscillation of a vortex. The external shear and strain of one vortex proximal to another is measured by the total strain rate,

$$s = \left[ \left( \frac{\partial u}{\partial x} - \frac{\partial v}{\partial y} \right)^2 + \left( \frac{\partial u}{\partial y} + \frac{\partial v}{\partial x} \right)^2 \right]^{1/2}, \quad (3.1)$$

and compared to the vorticity at  $5 T_{ip}$  for each simulation. For weak but axially asymmetric strain rates, it is expected that each adjustment vortex will be subject to evolving instabilities. For stronger strain rates between counter-rotating and co-rotating vortex cores it is expected that dipole pairing or merger of respective cores will occur. The strain between pairs of counter-rotating vortices is known to pull vortices together into propagating pairs (Schmidt et al., 1998; Beckers et al., 2002). The jet between the counter-rotating vortices is both the source of their propulsion and their attraction to one another. For pairs of co-rotating vortices it is the the strong, mutual shearing and integration of vorticity provide the mechanism for merging (Valcke and Verron, 1997). However, there is a point when the strain rates are too weak and the evolution of instabilities dominates the capacity to pair or merge.

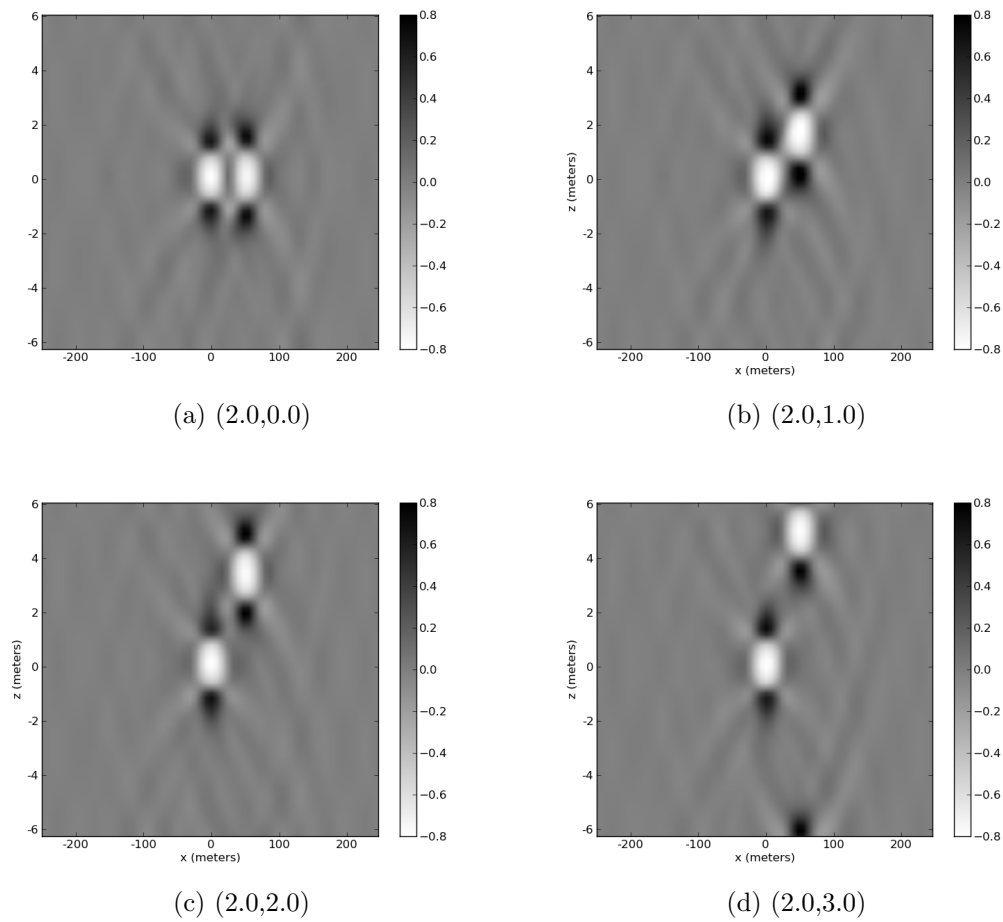


Figure 3.1: Mixed regions are introduced an inertial period apart and spaced by  $(\Delta r, \Delta z)$ . Shown above are vertical cross sections of vertical vorticity for interactions between co-rotating vortices that result in merging (a,c,d) and counter-rotating vortices that result in dipole pairing (b). The gray scale represents scaled vertical vorticity  $(\zeta/f = (dv/dx - du/dy)/f)$ .

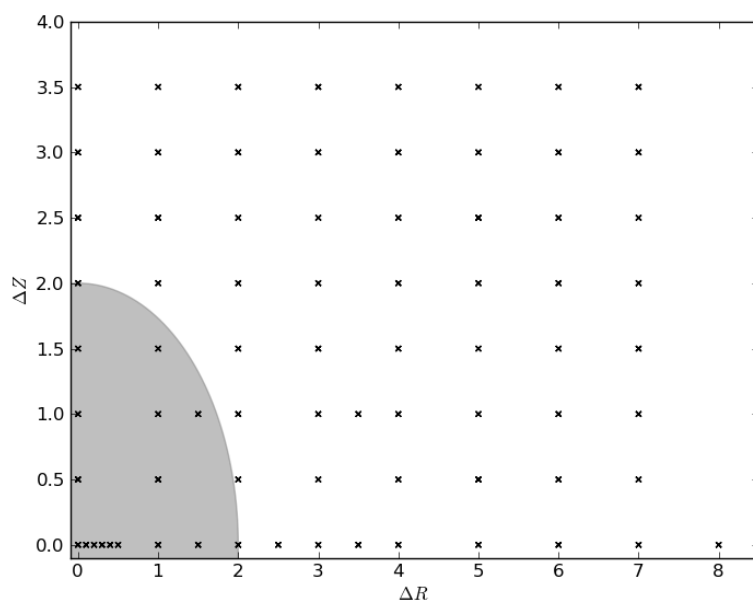


Figure 3.2: The numerical simulations performed are shown in  $(\Delta r, \Delta z)$  space. The horizontal separation  $\Delta r$  is scaled by the internal Rossby radius of the mixed patch. The vertical separation  $\Delta z$  is scaled by the distance between the respective cores of an adjustment vortex. Cases of overlapping mixing events are depicted in the shaded region.

The vertical vorticity,  $\zeta = dv/dx - du/dy$ , is the dominant component of the vorticity vector,  $\omega = \nabla \times \mathbf{u}$ , for adjustment vortices. The structure and behavior of vertical vorticity in adjustment vortices is consistent with two-dimensional counterparts. The vertical vorticity of each core of an adjustment vortex possesses a horizontal profile most closely resembling those with steepness parameter  $\alpha = 2.0$  as in Carton and Legras (1994). As with the shielded vortices of Carton and Legras (1994), the instabilities of any core in the adjustment vortex goes through a linear growth phase and a non-linear amplification phase. Similar to the two-layer, counter-rotating baroclinic vortices of Helfrich and Send (1988), the developing instabilities of adjustment vortices are out of phase in vertically adjacent cores. As an elliptical (azimuthal mode two) instability develops in a core, the shield is displaced and intensifies in regions where the cores have become narrow. These regions of increased vorticity interact with the cores in the non-linear amplification phase, resulting in shields that focus vorticity into two discrete centers. In the present study, unlike in Carton and Legras (1994), the tripoles formed by each original core with its fragmented shield do not stabilize. Rather, the out-of-phase cores strongly associate and exchange vorticity with the divided shields on adjacent layers. The strain of the divided and strengthened shields is enough to split the three cores into two split dipoles (Figure 3.3a). These split dipoles are a three-layer analog to the two-layer propagation seen in Helfrich and Send (1988), where two vortex cores are associated with one another across the boundary of two layers of fluid. The split dipoles are composed of a central core flanked above and below by cores of opposite vorticity connected to each other through the weaker asymmetric shield of the central core.

The instabilities that develop on individual adjustment vortices are identified by taking the volume averaged, azimuthal fast Fourier transform of horizontal cross sections of vorticity through the individual cores. The development of azimuthal modes in vortices has been used to study vortex stability and evolution in other numerical studies (Helfrich and Send, 1988; Carton and Legras, 1994). With assumptions of symmetry and for the sake of simplicity, I investigate the azimuthal

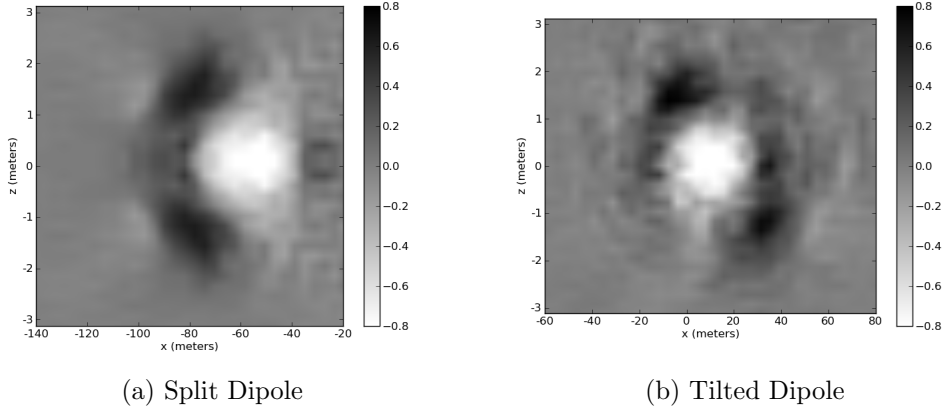


Figure 3.3: Two major kinds of dipoles resulting from adjustment vortex interactions. Split dipoles (a) have cyclonic cores vertically aligned, while tilted dipoles (b) have cyclonic cores vertically offset with one being dominant. The gray scale represents scaled vertical vorticity ( $\zeta/f = (dv/dx - du/dy)/f$ ), where  $f$  is the Coriolis parameter.

instabilities in the region of the initial vortex introduced into the domain.

Depending on the kind of interaction expected (instabilities, dipole pairing, or merging) the amount of time until the adjustment vortices attain a stable form will vary. Where azimuthal instabilities dominate, it is the time it takes for the split-dipoles to form. Where interactions between counter-rotating cores dominate, it is the time until the dipole pairing is complete. As in (Schmidt et al., 1998), the dipole pairing process is considered to be complete when the maximum propagation velocity is reached, which also corresponds to the closest distance between the counter-rotating cores. Finally, the time until a merger is considered complete is identified by the amount of time it takes for the individual cores to stably merge or evolve into other stable forms.

### 3.3 Results

The interactions of two sequential adjusted mixing events fall into three broad categories: Those that result in the destructive instabilities of individual adjustment vortices, those that result in the dipole pairing of counter-rotating vortex

cores of respective structures, and those that result in transient merging of co-rotating cores of respective adjustment vortices. Although there are simulations beyond the representative subset presented, all interactions have been found to be influenced by vortex stability, dipole pairing, or merging. Additionally, when the mixed patches are introduced in an overlapping fashion, strong variations in total energy may occur.

The following results address each of the above broad categories and the additional concern of overlapping diffusive forcings in turn. First, the causes and consequences of the azimuthal instabilities of an adjustment vortex are examined. Proceeding, the interactions of counter-rotating vortices that result in propagating dipole pairs are investigated. Next, the effect of the transient merging of like signed vortex cores is considered. Finally, the consequences of the volume of a diffusive forcing event overlapping with an already existing adjustment vortex are presented.

### *3.3.1 Induced Azimuthal Instabilities*

Azimuthal instabilities for both adjustment vortices are induced by the background noise in the domain or the shear and strain they exert on one another. This background noise can be seen as a combination of numerical noise introduced in the equations and the adjustment driven internal waves superimposing with themselves via the triply-periodic boundary conditions. For instabilities induced exclusively by background noise, the time for the strongest instability to evolve is virtually identical (around  $100 T_{ip}$ ) from one simulation to the next. A single adjustment vortex in the same numerical domain takes twice as long to develop the same instabilities. Furthermore, the time until the identifiable onset of instability is inversely related to the amount of axially asymmetric strain of the interacting vortices.

For two sequential mixed patches placed into the domain at  $(8.0, 0.0)$ , evolution of instabilities into two split dipoles each progresses as with a single, isolated adjustment vortex (Figure 3.4). The second azimuthal mode of the initial adjust-

ment vortex becomes dominant around  $68 T_{ip}$  and grows exponentially until  $101 T_{ip}$  (Figure 3.5), yielding an e-folding time of  $\tau = 10.8 T_{ip}$ . After  $101 T_{ip}$ , non-linear amplification ensues, concluding with the breakdown into two propagating split dipoles for each adjustment vortex at around  $150 T_{ip}$ . The other modes presented are the mean vorticity (mode 0), vortex core displacement (mode 1), and a three-lobed mode (mode 3). All higher modes are seen to grow at slower rates and are not displayed. As the unstable modes are developing, the potential energy of the vortex is being converted into the kinetic energy of those azimuthal modes. This is especially noticeable using a wave-vortex decomposition of the energy (Bartello, 1995). This linear decomposition of the energy portrays energy associated with Ertel potential vorticity (vortex mode) and the energy associated with the absence of Ertel potential vorticity (wave mode). After the onset of the non-linear amplification phase, around  $100 T_{ip}$  (Figure 3.6), the exchange of vortex potential to vortex kinetic energy is observed. All cases that evolve from adjustment vortices into stable forms exhibit this conversion of vortex potential energy to vortex kinetic energy.

As the two adjustment vortices are placed closer, the proximal strain of the two vortices can be enough to induce instabilities that precipitate the breakdown of those structures. In contrast to the (8.0,0.0) case above, the (4.0,0.0) case shows a dominant azimuthal mode one instability by  $3 T_{ip}$ . This mode grows linearly until  $10 T_{ip}$ , with an e-folding time scale of  $\tau = 11.6 T_{ip}$ , before non-linear amplification and breakdown (Figure 3.7). The azimuthal mode one is primarily a lateral displacement of one of the cores in relation to the others, precipitating the interactions of cores with the shields in adjacent layers. In this case, each adjustment vortex breaks down into a single split dipole form. Increasing the horizontal distance weakens the induced first azimuthal mode, but it is still able to facilitate the asymmetry in the pairs of split dipoles for each adjustment vortex until  $\Delta r \geq 6.0$ .

The azimuthal instabilities induced by the shear and strain of a proximal vortex, being stronger than the ones driven by the background noise of the domain,

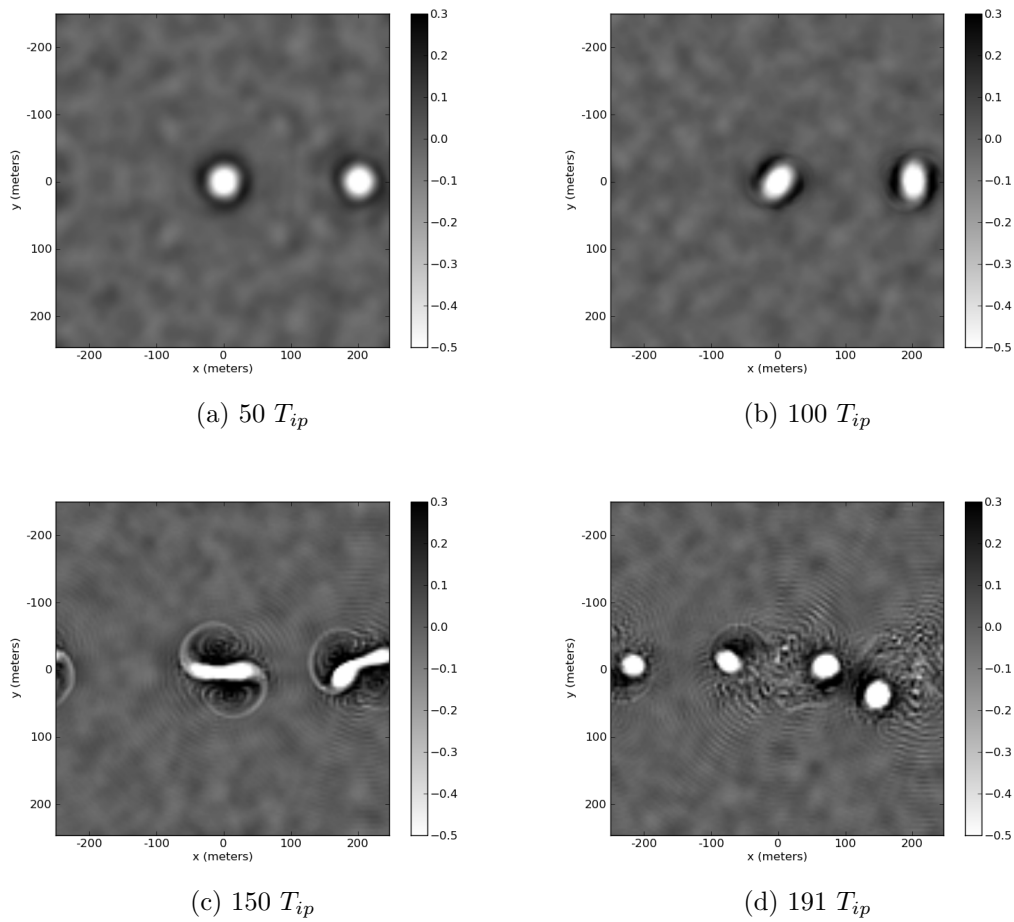


Figure 3.4: The instabilities of distant vortices  $(8.0, 0.0)$  are seen to develop into split dipoles. The instability is visible by (b)  $100 T_{ip}$ , develops a tri-polar structure by (c)  $150 T_{ip}$ , and evolves into propagating split dipoles by (d)  $191 T_{ip}$ . The gray scale represents scaled vertical vorticity  $(\zeta/f = (dv/dx - du/dy)/f)$ . The “waves” around vortices in (d) are the result of the bottle-necking of kinetic energy described in Appendix C.

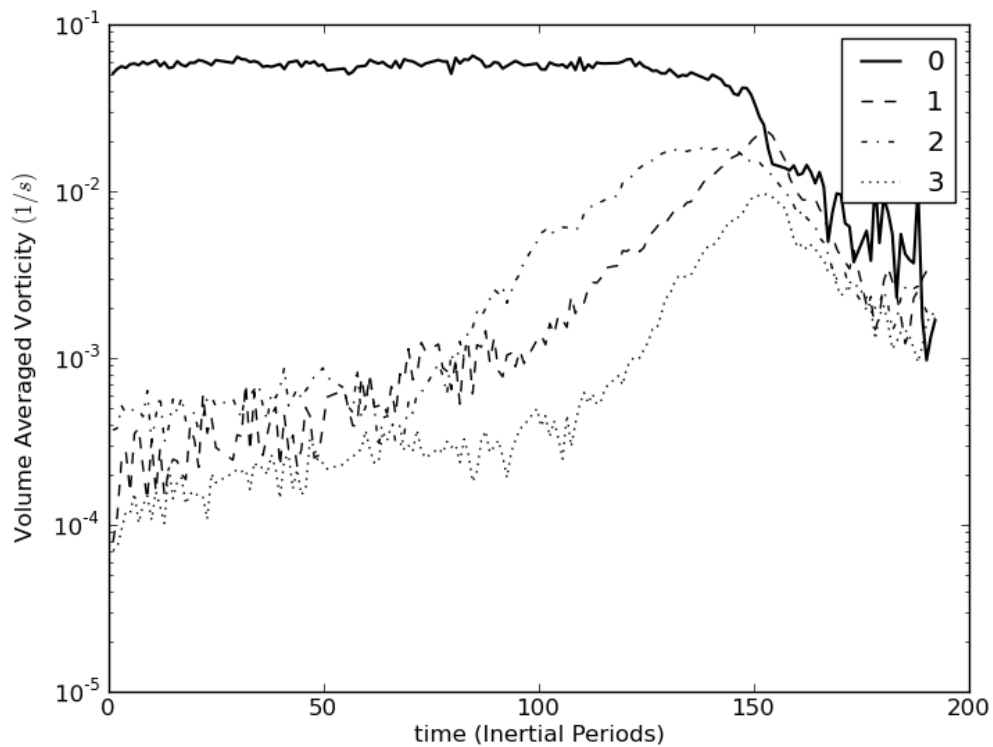


Figure 3.5: Evolution of the first three azimuthal modes for the central anticyclone of the  $(8.0, 0.0)$  case. The second azimuthal mode grows from  $68 T_{ip}$  until  $140 T_{ip}$ , after which the vortex breaks into two propagating pairs. The azimuthal mode zero represents the mean vorticity in the sample frame and declines when the split dipoles propagate out of the sampling frame. The first azimuthal mode represents the mean lateral displacement of the vortex cores. The third azimuthal mode is a tri-lobed undulation. All higher modes are seen to grow at slower rates and are not displayed.

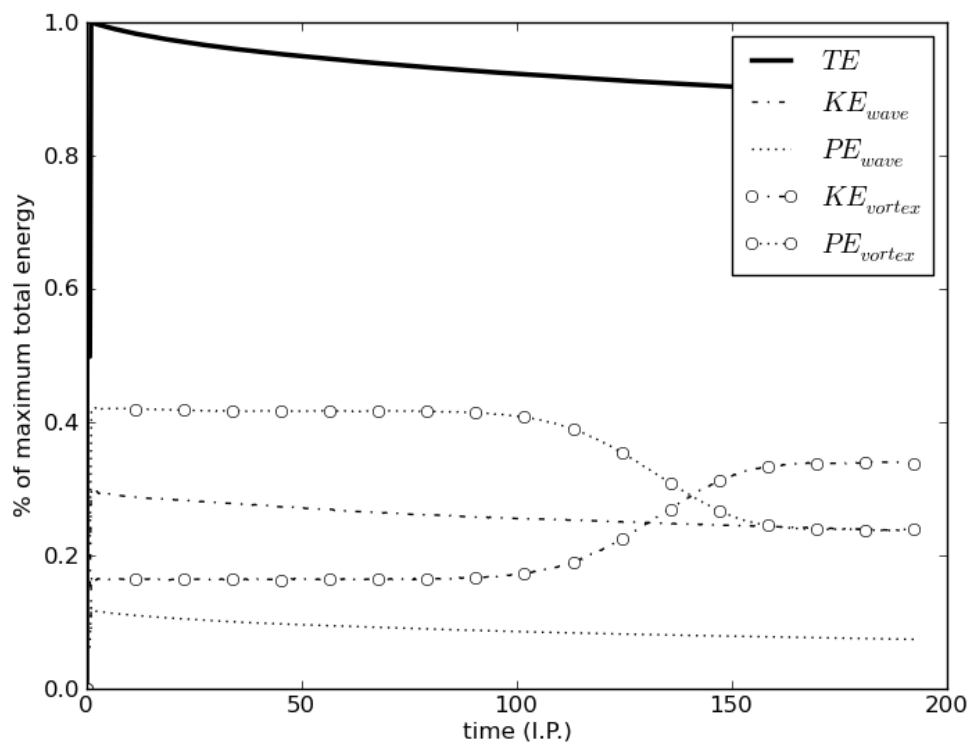


Figure 3.6: A wave-vortex energy decomposition for the (8.0,0.0) case. The evolution of the total energy (solid line) of two adjustment vortices decomposed into kinetic (dashed) and available potential (dotted) energy in both wave (non-circled) and vortex (circled). The onset of the non-linear amplification phase is correlated with the exchange of vortex potential to kinetic energy.

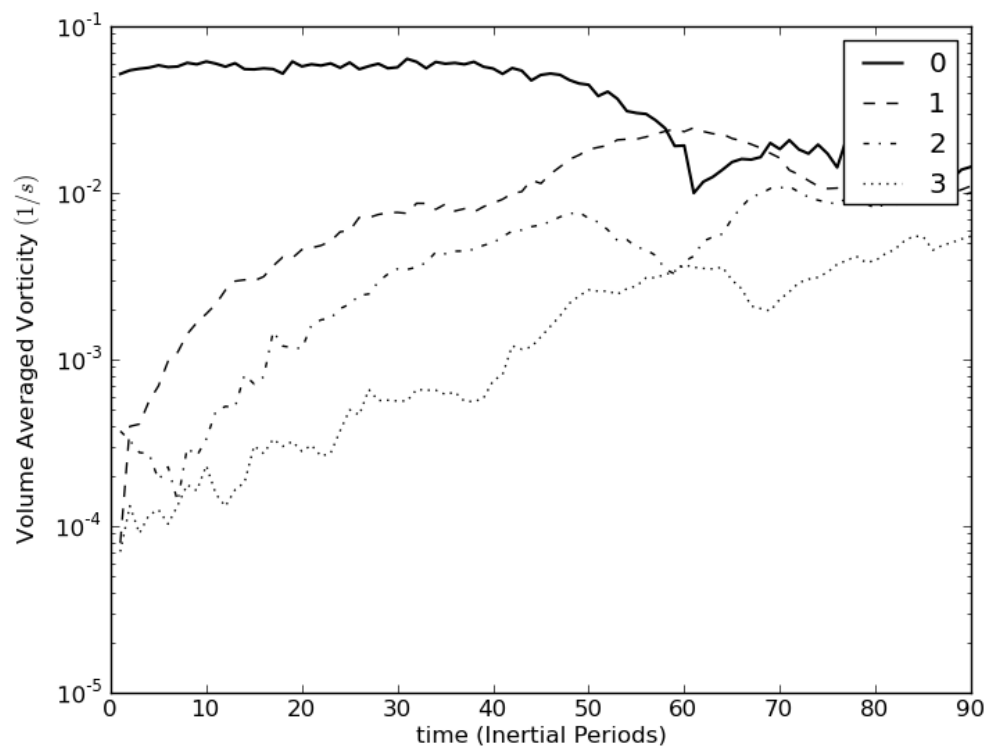


Figure 3.7: Evolution of the first three azimuthal modes for the central anticyclone of the (4.0,0.0) case. The first azimuthal mode, displacement of an adjustment vortex's cores relative to one another, governs the conversion into one split dipole for each adjustment vortex.

take less time to evolve into the stable dipole forms.

### 3.3.2 Dipole Pairing

When the adjustment vortices are placed even closer, counter-rotating cores of the respective vortices can couple to form asymmetric dipole pairs that propagate in circles. This process occurs most strongly for the  $\Delta z = 1.0$  cases, where respective vortex cores are vertically aligned with matching, counter-rotating pairs (Figure 3.1b). Direct dipole pairing also occurs for other cases ( $\Delta z \neq 1.0$ ), but only the  $\Delta z = 1.0$  cases are presented. The evolution of the dipole pairing for the (2.0,1.0) case is shown in Figure 3.8. Time until complete pairing, defined by maximum dipole propagation speed, varies from  $5 T_{ip}$  to  $80 T_{ip}$  for the simulations from (1.0,1.0) to (3.5,1.0). The time until pairing is closely fit with an exponential relationship to the horizontal distance between the counter-rotating cores (not shown). Beyond  $\Delta r = 3.5$ , azimuthal instabilities result in the breakdown of each structure before dipole pairing can occur.

The strain rate (3.1) necessary for dipole pairing to dominate over azimuthal instabilities is observed to be at least  $s = 0.47 f$ . Contours of strain rate,  $s$ , are overlaid upon color gradients of vorticity in Figure 3.9. For the two simulations shown,  $\Delta r = 2.0, 3.0$  with  $\Delta z = 1.0$  (Figure 3.9a,b), dipole pairing occurs when the strain rate is above this limit. Contours of strain can also be seen to include both vortices. For the other two simulations shown,  $\Delta r = 4.0, 6.0$  with  $\Delta z = 1.0$  (Figure 3.9c,d), the contours of strain no longer surround both vortices, and strain is insufficient to create dipole pairing. In one of these latter cases, (4.0, 1.0) (Figure 3.9c), the strain perturbs the azimuthal instabilities of the vortices before pairing can occur.

In some extended simulations, the resulting propagating dipoles exchange partners with other dipole pairs and exhibit the horizontal merger and vertical coupling of like signed vortex cores. Paired anticyclonic cores are observed to capture an additional partner and facilitate the merger between the new cyclone and its original partner. When the cyclones of respective pairs come in close vertical proximity,

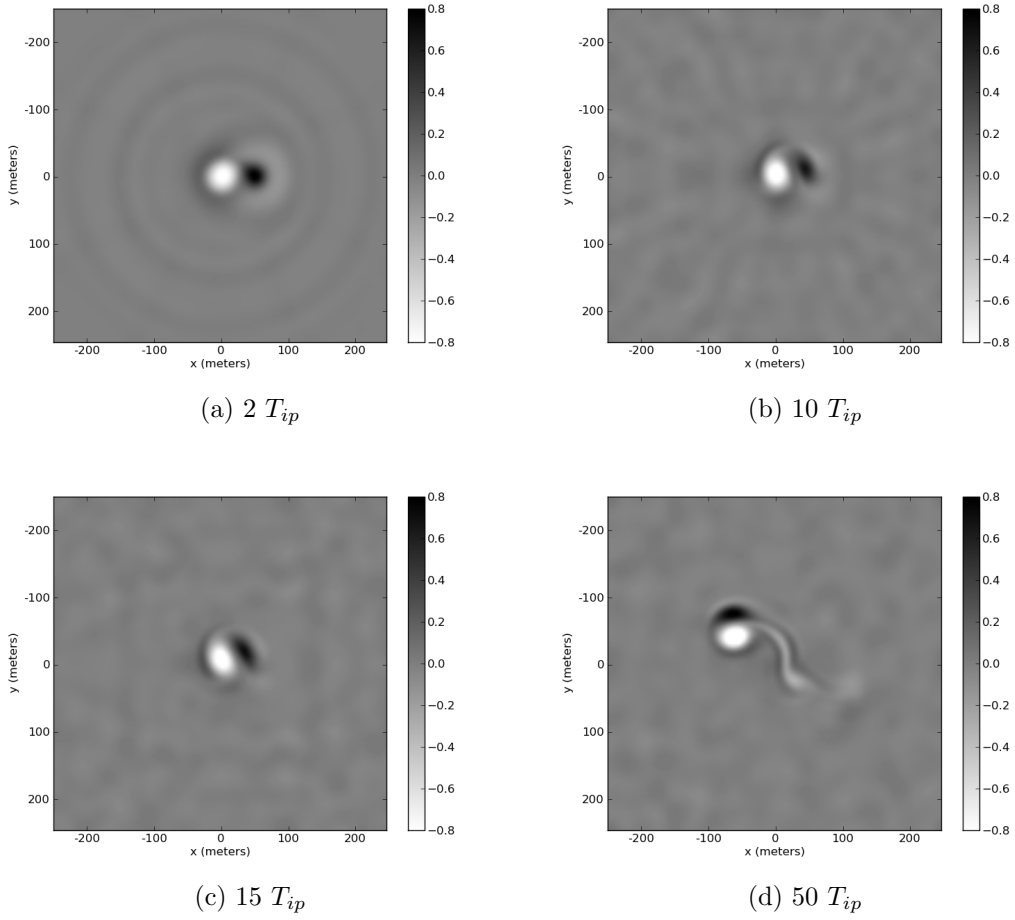


Figure 3.8: The interaction of counter-rotating cores of different adjustment vortices are observed to form an asymmetric, propagating dipole. Dipole pairing, with initial conditions  $(2.0, 1.0)$ , is completed by  $15 T_{ip}$  (c) and propagates in a circle. Filaments of the shields are seen to stretch out behind the dipole by (d)  $50 T_{ip}$ . Presented is a plan-view of vertical vorticity scaled by the Coriolis parameter ( $\zeta/f = (dv/dx - du/dy)/f$ ) through vertical center of initial mixed patch.

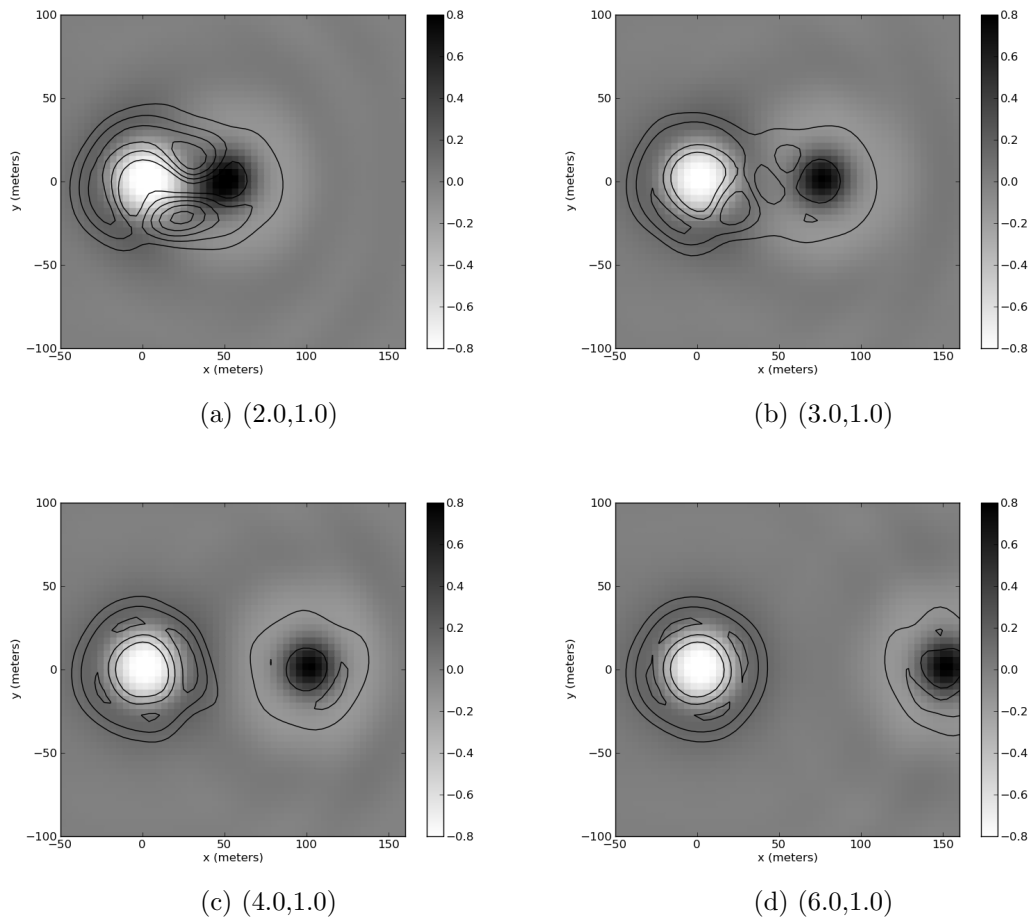


Figure 3.9: The vertical vorticity distribution at  $2 T_{ip}$  for  $\Delta z = 1.0$  simulations with varied radial spacing,  $\Delta r \in \{2.0, 3.0, 4.0, 6.0\}$ . Overlaid are contours of the total strain. Both vertical vorticity and strain are scaled by  $1/f$ . The contour spacing is 0.2.

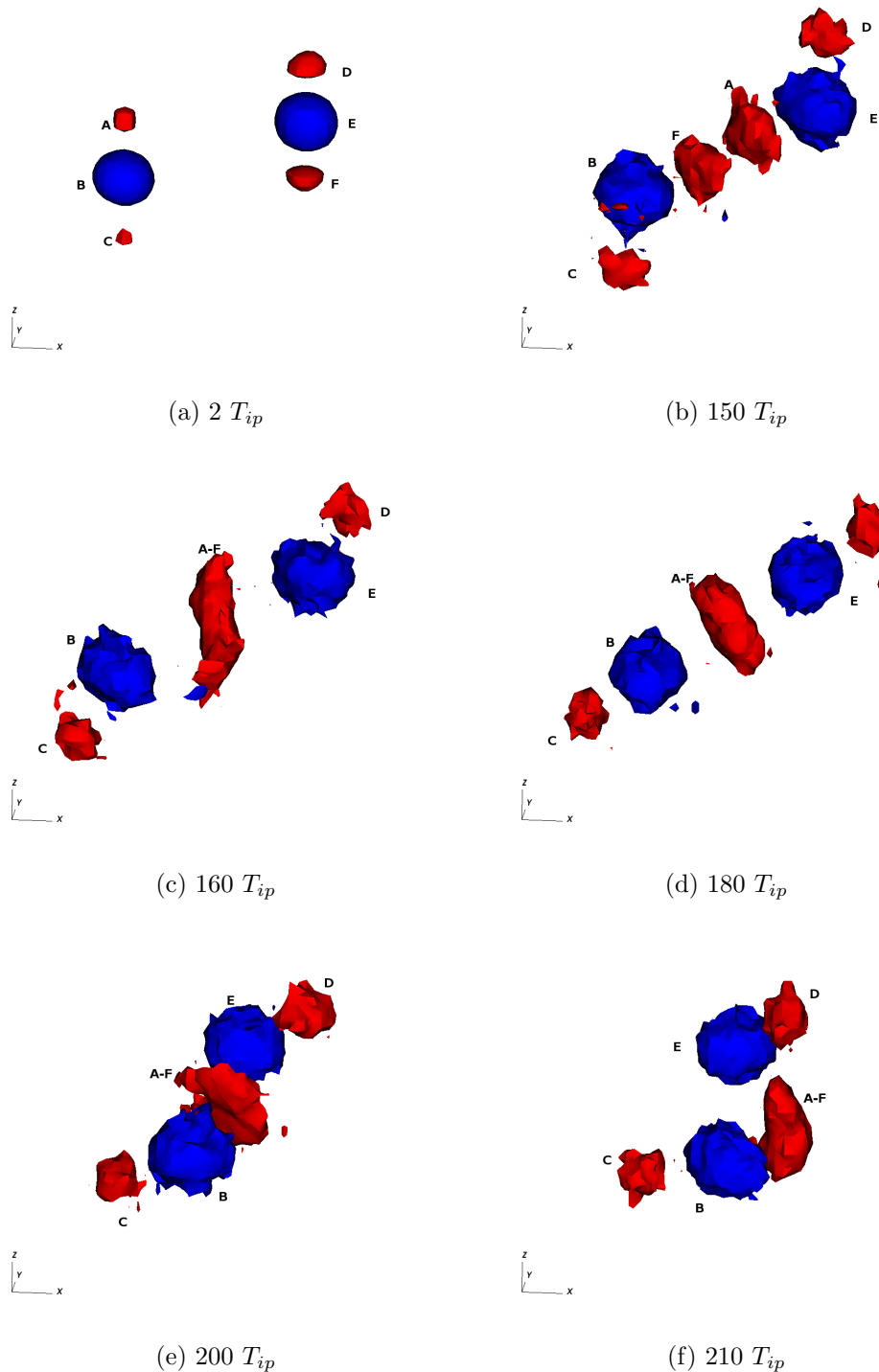


Figure 3.10: An extended simulation for (3.5, 1.0) case. Interacting dipole pairs can be seen to display merging (c) and exchanging partners (f). The vortices are labeled from top to bottom, left to right (A to F). The B+F dipole is meeting up with the A+E dipole by  $150 T_{ip}$ . Although the A and F cyclones started on different levels they can be seen to vertically couple by  $160 T_{ip}$ . All five vortices form a compound structure that is pulled together. By  $220 T_{ip}$  anti-cyclonic core B has become associated with the merged A-F cyclone and the propagating structure assumes a different trajectory than the remaining vortex cores.

they have a strong tendency to vertically couple, forming a taller and stronger vortex.

For the (3.5,1.0) case the asymmetric dipole pairs propagate on circular paths, resulting in respective cyclones meeting up (Figure 3.10). The vortices are labeled from top to bottom left to right (A to F). The B+F dipole is meeting up with the A+E dipole by  $150 T_{ip}$ . Although the A and F cyclones started on different levels they can be seen to vertically couple by  $160 T_{ip}$ . All five vortices form a compound structure that is pulled together. By  $220 T_{ip}$  anti-cyclonic core B has become associated with the vertically coupled A-F cyclone and the propagating structure assumes a different trajectory than the remaining vortex cores.

### 3.3.3 Merging Cores

The cases that lead to the most apparent, although unstable, merging are where the mixed patches are introduced on the same plane ( $\Delta z = 0.0$ ). A critical distance for merging to take place is observed at  $\Delta r = 2.5$ . In the (2.0,0.0) case (Figure 3.11), the anti-cyclonic cores coalesce into a single structure by  $15 T_{ip}$ . However, the cyclonic cores of the adjustment vortices of these cases do not merge. Rather, they vertically associate with strengthened portions of the cyclonic shield of central, merging anti-cyclones. This can be seen starting at  $2 T_{ip}$  (Figure 3.11a) above and below the point of closest contact between the two anti-cyclones. By  $15 T_{ip}$  these two regions have not only accumulated more of the cyclonic vorticity in the shield, but they have become strongly associated with the cyclonic cores above and below the merged anti-cyclonic cores seen in Figure 3.11. The strain of the combined strength of the associated cyclones is enough to pull the anti-cyclonic cores apart into two split dipoles.

The value of strain rate that is necessary to drive the merging for these vortices is  $s \geq 0.80 f$ . The shear-strain  $(\frac{\partial u}{\partial y} + \frac{\partial v}{\partial x})^2$  is the dominant component of the strain parameter (3.1) for co-rotating vortices. When the shear-strain is in this range, the vortices are stretched and pulled into one another to merge (Figure 3.12).

The (2.0,0.0) case exhibits the minimum merging time of  $15 T_{ip}$ , with the

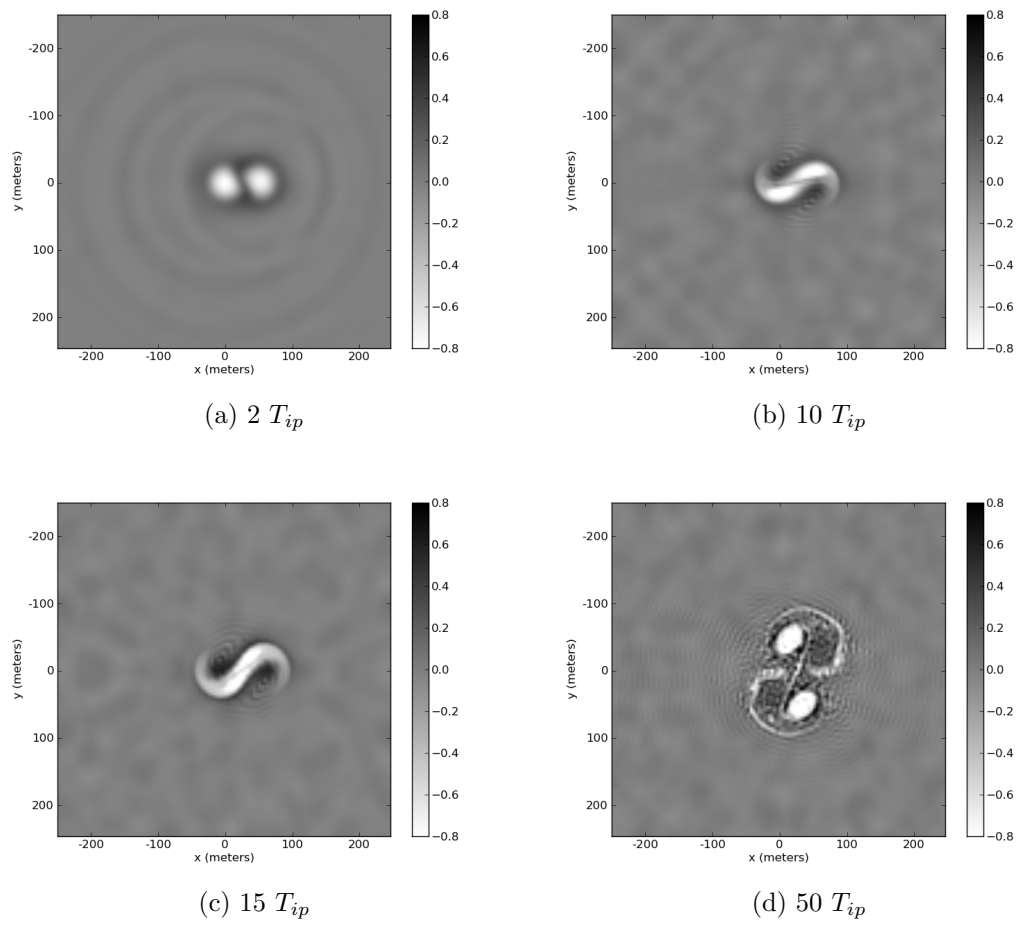


Figure 3.11: The  $(2.0,0.0)$  case showing the merging of anti-cyclonic cores (b,c) and the development of two split dipoles (d).

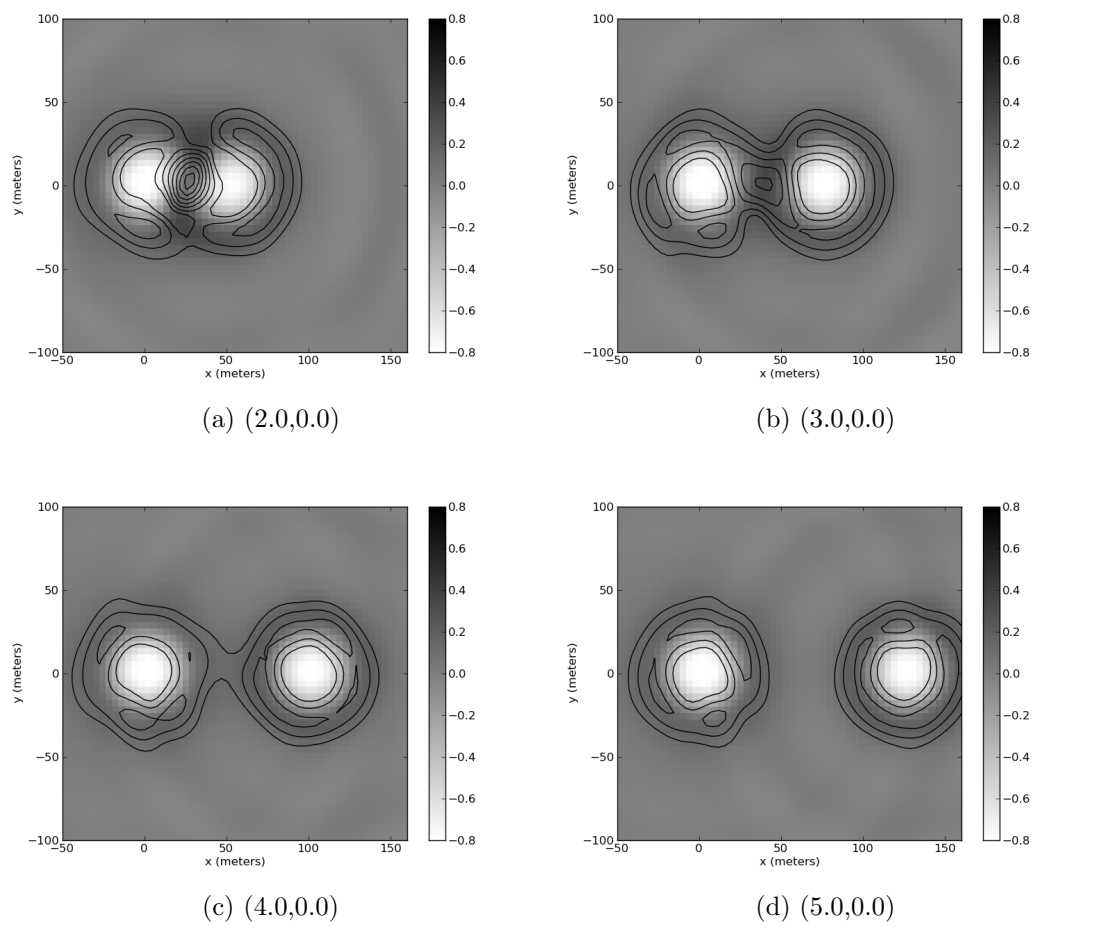


Figure 3.12: The same as Figure 3.9, but with vertical separation of mixed patches at  $\Delta z = 0.0$  (Figure 1a).

maximum strain rate in the first five inertial periods of  $s = 0.84 f$ . Complete split into propagating dipoles is achieved by  $45 T_{ip}$ . The  $(2.5, 0.0)$  case has the maximum time until merging of  $25 T_{ip}$ , with propagating split dipoles by  $32 T_{ip}$ . Similar merging is found for interacting cyclones of the adjustment vortices when  $\Delta z \geq 2.0$  (Figure 3.1cd). The top cyclonic core of the initial adjustment vortex merges with the bottom cyclonic core of the second adjustment vortex. Merging occurs for  $\Delta r \leq 1.0$ , but is a by-product of the proximal placement of the mixed patches. The inward flow of fluid that draws the respective cores together is an effect of the adjustment process. The merged cyclones create the strain necessary to pull both anticyclonic cores out of place to form a large compound tilted dipole (multi-pole) by  $15 T_{ip}$ . A tilted dipole is a structure in which one of the cyclonic cores strongly associates with a mode one azimuthal asymmetry in the cyclonic shield of the anti-cyclonic core (Figure 3.3b). The other cyclonic core becomes out of phase from the dominant one, becoming associated with a weaker mode two azimuthal asymmetry of the shield. The compound tilted dipole is unstable, collapsing when the larger cyclone associates with only one of the anticyclones (see Figure 3.10). These tilted dipoles and multi-poles have been observed in earlier numerical simulations of isolated vortices in the ocean (Morel and McWilliams, 1997).

### 3.3.4 *Overlapping Mixed Patches*

The Gaussian profile of a mixed patch extends the density perturbation beyond two standard deviations of the patch. If a subsequent mixed patch is placed far enough from the initial, they will not interfere with each other's adjustment. However, when a subsequent mixed patch is introduced into the domain such that its density perturbation overlaps the initial patch, the energy introduced by the second mixed patch can vary by up to 40%. Introducing the second, overlapping, mixed patch on the same plane as the first ( $\Delta z = 0$ ) produces a single, larger, although asymmetric vortex with more total energy than otherwise. Conversely, introducing the subsequent mixing event at  $\Delta z = 1.0$  results in less energy. Both

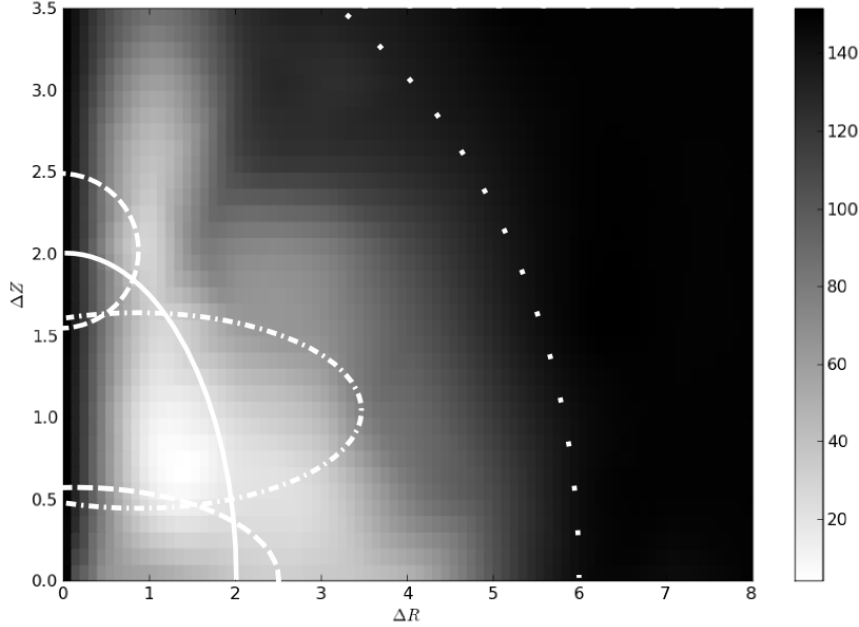


Figure 3.13: Time in inertial periods until a stable form evolves. Symmetric overlaps,  $\Delta r = 0$ , as well as distant runs are the most stable, with the longest times to reach a stable form. The region where internal waves induce azimuthal instabilities are outside the dotted line. Regions of co-rotating core merging are within the dashed lines. Regions influenced by dipole pairing are within the dashed-dotted lines. The region where overlapping effects are seen is within the solid line. The remainder is influenced by azimuthal modes one and two due to shear and strain. Curves are estimated from observations of all simulations.

of these effects are the byproduct of using the diffusive forcing method on fluid that is no longer linearly stratified after the initial parameterized mixing event.

Each of the above simulations has an observed time until the stable forms are achieved. These times are represented in Figure 3.13 for all simulations. The outlining ovals estimate regions where the specified behavior is observed to dominate.

### 3.4 Discussion

The above simulations show interactions between adjustment vortices can result in different types of propagating dipoles. Background noise or the proximal strain from nearby vortices induce instabilities that result in split or tilted dipoles, de-

pending on the azimuthal modes that are excited. Counter-rotating cores of respective vortices form asymmetric dipole pairs that propagate in circles when the adjustment vortices are within a certain range of distances ( $\Delta r < 3.5$ ) and vertical alignment ( $0.7 \leq \Delta z \leq 1.3$ ). The anti-cyclonic cores of respective adjustment vortices temporarily merge and continue to evolve as one unstable vortex before breaking into two split dipoles, while the merging of cyclonic cores results in tilted dipoles. Overlapping a subsequent mixing event with an existing mixed patch results in varied amounts of induced potential energy and a redistribution of the potential energy of the initial mixed patch.

Adjustment vortices are unstable to perturbations by azimuthal modes. When there are two distant adjustment vortices in the domain, noticeable instabilities develop by  $68 T_{ip}$ , at least  $100 T_{ip}$  earlier than a single adjustment vortex in the same domain. Adjustment vortices are unstable to perturbations caused by the shear and strain of an internal wave field (Brunner-Suzuki et al., 2012). Each adjustment vortex produces an internal wave field during adjustment. In near inviscid simulations in a triply-periodic domain, these internal waves persist and interact with each other and the vortices. It is thought that the internal waves provide the largest component of the background noise that drives the instability of distant vortices. The periodic Cartesian boundary conditions, as in Melander et al. (1991), create small perturbations of azimuthal modes that may lead to instabilities seen here. Shear and strain of proximal vortices displace the vortex cores relative to one another. This is represented on an azimuthal Fourier transform by a mode one perturbation. Depending on the influence of the displacement mode, the adjustment vortices evolve into one to two dipole forms each. For adjustment vortices that evolve into two split dipoles, the displacement mode can influence the size of each.

For adjustment vortices that may form in the ocean, it is expected that the shear and strain fields within the ocean will excite the natural modes of oscillation in the vortices (Flierl, 1988). This may be one reason that adjustment vortices have yet to be observed in the ocean. The tendency to evolve into propagating

forms would contribute to rates of dispersion observed in field studies unaccounted for by established theories Sundermeyer and Ledwell (2001).

Dipole pairing and unstable merging of cores of this study occur within established critical distances for mono-polar forms of vortices observed in previous studies. Dipole pairing of counter-rotating cores of adjustment vortices is observed for  $\Delta r \leq 3.5$ . This compares well to the dipole pairing distance of  $\Delta r \leq 4.0$  (as a ratio of vortex radius) observed in two-dimensional, counter-rotating vortices by Schmidt et al. (1998). Likewise, our critical merging distance is found to be  $\Delta r \leq 2.5$  for the co-rotating anti-cyclones. This is consistent with the critical merging distances Valcke and Verron (1997) reported with two-dimensional vortices ( $\Delta r = 2.3$ ). Sufficient proximal strain rates are necessary for the pairing and merging processes to compete with the azimuthal instabilities of individual adjustment vortices.

Although the primary interactions of proximal adjustment vortices do not result in stable merger, the merger and vertical coupling of co-rotating vortex cores is still observed. The stable merger and vertical coupling of co-rotating cores is only observed after the breakdown of adjustment vortices. Each dipole type consists of a large anticyclone associated with one or two smaller cyclones. The dominant anti-cyclones of the dipole forms exchange and exhibit the merger of peripheral cyclones. Though the exchange of cores in dipole collisions are not new (Dubosq and Viúdez, 2007), this is the first study that I am aware of that investigates the three-dimensional exchange of cores in vortices of this type. Additionally, the merging of multiple like-signed cores associated with a stronger counter-rotating vortex has been reported in oceanic observations and numerical simulations (Rodríguez-Marroyo et al., 2011). The stability properties of each compound vortex type determine the capacity to stably merge or vertically couple. As is noted above and in Appendix B, adjustment vortices are inherently unstable. Criteria for the interactions of dipoles resulting from the breakdown of adjustment vortices has yet to be developed.

Interactions of subsequent diffusive forcings overlapping with the density per-

turbations of prior vortices introduce vortices with varying sizes, shapes, and energy content. This particular effect is a result of the non-linearity of the density field and is not produced by an inverse energy cascade. The extremes of this particular effect are unlikely to occur in an oceanic setting. The mixed patches introduced into the numerical domain are a parameterization of the turbulent mixing of breaking internal waves. Internal waves have been shown to be less likely to break within regions of decreased stratification in a Boussinesq fluid (Brown et al., 2008). This makes the more energetic cases of overlapping,  $\Delta z = 0.0$ , unlikely for subsequent, internal wave driven mixing events of the same size in the ocean. Nevertheless, superpositions of incident and reflected internal waves off of a destratified region have been shown to lead to breaking. Although parameterizing of mixing events is intended to introduce a particular energetic scale into the domain, variability in the forcing emulates some of the natural variability of such mixed patches in the ocean.

Interactions between the end products of adjustment vortex instability, dipole pairing, or transient merging are shown to result in vortex core merging or vertical coupling. The merging of vortex cores is the fundamental process through which the inverse cascade of kinetic energy occurs. The merging of the vortex cores results in an increase in horizontal and vertical scales, whereas the vertical coupling increases the vertical scale without a corresponding increase in horizontal scale. Determining the relative dominance between horizontal merging and vertical coupling in numerical simulations with multiple forcings may be important in evaluating the existence of an inverse cascade from similar oceanic submesoscale processes. With predominantly horizontal mergers, an inverse cascade of kinetic energy is consistent with what is predicted by quasi-geostrophic theory (Charney, 1971). However, if vertical coupling is dominant, vertically periodic boundary conditions will drive a two-dimensional inverse cascade, as is seen in Chapter 5. In the ocean, compounded vertical coupling may eventually result in further instabilities such as seen by Billant and Chomaz (2000).

Ripples in the vorticity field of Figure 3.4 show the consequence of stretching

and thinning of vorticity filaments. This represents a forward cascade of enstrophy. However, it may also be associated with a bottle-necking effect discussed in Appendix C. The bottle-necking effect represents a build up of kinetic energy at the smallest scales before dissipation by higher order viscosity. Though a forward cascade of kinetic energy is usually associated with fully three-dimensional fluids, the quasigeostrophic approximation does not prohibit a forward cascade of kinetic energy as do two-dimensional flows (Tung and Orlando, 2003). Furthermore, the Boussinesq approximation also allows for forward cascades of kinetic energy.

There are several questions encountered that are left unexplored. First, the evolution time of most interactions presented above are longer than the dissipation time,  $T_D = h^2/\nu_2 = 10 T_{ip}$ , for adjustment vortices in viscous simulations of previous work Sundermeyer and Lelong (2005). This disparity is explored more in Chapter 4 and Chapter 5. It is unknown if the interactions between two vortices would yield similar results in these domains or, as in Tóth and HÁzi (2010) and Dubosq and Viúdez (2007), whether they would result in a stable merger between adjustment vortices. Numerical simulations in Chapter 4 and Chapter 5, along with the stability analysis of Appendix B, indicate the former. Furthermore, the varying scale and energy that the diffusive forcing introduces points to the need to explore interactions between adjustment vortices of varying size, scale, and destratification. Also open for investigation is the manner in which an adjustment vortex interacts with and affect the breaking of internal waves. Contributions to lateral dispersion from the evolution of adjustment vortices into propagating dipoles has yet to be considered. In the turbulent oceanic context, bolus transfer of tracer by propagating dipoles could contribute to the observed lateral dispersion. Although criteria for vortex merger in oceanic tripoles have been explored for mesoscale vortices (Rodríguez-Marroyo et al., 2011), criteria for the exchange and merger of components of the stable dipoles has yet to be established. The multi-mixing event simulations of following chapters suggest that the vertical coupling of multiple co-rotating cores may be one of the driving mechanism that creates an increasingly two-dimensional flow.

### **3.5 Conclusion**

Two vortices produced by the geostrophic adjustment of sequential parameterized mixing events in a linearly stratified fluid show a variety of interactions resulting in one of three stable forms. Azimuthal instabilities, dipole pairing, or unstable merging of component vortex cores result in propagating dipoles, split dipoles, or tilted dipoles. Although the direct, stable merging of two adjustment vortices is not observed, the evolution into and interactions between stable forms exhibit the exchange and coalescence of like signed vortex cores. The unstable interactions between adjustment vortices, resulting in propagating dipoles, present another mechanism contributing to lateral dispersion in the ocean. The interaction of resultant dipole pairings portray a mechanism capable of participating in both forward and inverse energy cascades at the submesoscale.

## Chapter 4

# CLUSTERING PARAMETERIZED WAVE-BREAKING EVENTS AND THE EFFECT ON LATERAL DISPERSION

Proximal adjustment vortices are created by clustered mixing events. The clustering of adjustment vortices is performed using the assumption that the adjustment vortices themselves increase the likelihood of other mixing events in their proximity. In this manner, non-linear interactions between adjustment vortices may be used to increase the lateral dispersion of a tracer. It is found that increases in scale of resultant vortices can account for much of the increase in lateral dispersion of a tracer beyond the diffusive regime limit. For simulations with high rate densities of mixing event introduction, passive tracer dispersion dynamics fall into a non-linear regime. This behavior is explained mostly from the scales of kinetic energy that are persistently at or greater than the scale of the tracer, with a portion of this kinetic energy from barotropic mode energy that is accumulating due to the unphysical dissipation at that mode.

### **4.1 Introduction**

The introduction of episodic mixed patches into a viscous, rotating, and stratified domain has been used to study the influence of adjustment vortices on the lateral dispersion of a passive tracer at the submesoscale (Sundermeyer and Lelong, 2005). Characteristics consistent with an inverse energy cascade were observed in the numerical domains as the frequency of introduced mixed patches was increased. It was hypothesized that the non-linear interactions between adjustment vortices precipitated the inverse energy cascade and prevented statistical equilibration of the velocity fields. In the present study, a clustering assumption is used to locally increase the rate of mixing event introduction while keeping the global rate of

mixing events constant. From this local increase, I hope to be able to accomplish two things. First, to investigate the increase in the rates of lateral dispersion of a passive tracer due to the clustering assumption and the dynamics therein. These results are compared to the parameterization of lateral dispersion presented by Sundermeyer and Lelong (2005). Second, the nature of the non-linear interactions that lead to the inverse energy cascades observed in previous work is investigated. Although the relationship between the model configuration and the inverse energy cascade are covered in more detail in Chapter 5, it has an effect upon the results presented here.

The clustering assumption is supported as follows. Firstly, it has been proposed that rotating stratified fluids possess a turbulent memory effect (Vanneste and Haynes, 2000), that turbulence is more likely in regions that have experienced turbulence in the recent past. Next, for the modeled process, internal waves are more likely to break in regions of increased vertical shear Winters (1994). Furthermore, internal waves are known to amplify and break when moving through decreasing stratification in the atmosphere (Staquet and Sommeria, 2002). Finally, although internal waves are less likely to break within a destratified region, superpositions of internal waves, incident and reflected from a destratified region, can lead to breaking and turbulence (Brown et al., 2008). From the clustering assumption, a time varying, spatial Poisson process is utilized to localize an increase in rate of mixing events.

The presentation of the paper is as follows. The numerical model, spatial Poisson process, use of a barotropic damping, and methods for analysis are presented in Section 2. In the results, Section 3, the effects of clustering on dynamics of the flow and a passive tracer field are presented. These results are compared to simulations without clustering, but at the same global rate. Furthermore, these unclustered cases are compared to simulations performed with barotropic damping. In the discussion, Section 4, the findings and their implications for simulations of anisotropic, rotating, stratified flow are reviewed. Further investigations are proposed to address outstanding issues discovered. Finally, in the conclusion,

Section 4, the effects of clustering on lateral dispersion and the barotropic mode are summarized.

## 4.2 *Model and Methods*

As in previous studies (Lelong and Sundermeyer, 2005; Sundermeyer and Lelong, 2005), the pseudo-spectral numerical model developed by Winters et al. (2004) is employed in this chapter. In addition to the numerical model and the techniques described in Section 2.3, a few more techniques are introduced and reviewed.

### 4.2.1 *Energetics and Energy Spectra*

Both kinetic and available potential energy are needed to detect statistical equilibrium in the domain. Statistical equilibrium occurs when there is a balance between the energy forced into the domain and the energy dissipated out of the domain. The globally averaged kinetic energy is calculated as  $\frac{1}{2} \frac{1}{V} \int_V \mathbf{u} \cdot \mathbf{u} dV$ . The domain averaged potential energy is calculated as  $\frac{1}{2} \frac{1}{V} \int_V \left( \frac{g}{N\rho_0} \rho' \right)^2 dV$ . Both kinetic energy and available potential energy are in units of Joules per kilogram J/kg. For domains without isopycnal overturns this approximation of available potential energy is considered accurate (Gill, 1982). The total available energy in the domain is the sum of the kinetic and available potential energy.

Depending on the background stratification present in the domain, diffusive forcings can introduce varying amounts of available potential energy. For a more complete review of how this occurs, see Appendix A. The sampling rate of the energetics is fine enough to capture these differences. Comparing the total energy in the domain just before a diffusive forcing event to that just after allows us to calculate statistics on the energy delivered by a diffusive forcing event. Likewise, comparing the total energy just after a diffusive forcing event to the level of energy just before the next allows us to measure the dissipation of energy between events and calculate statistics on those as well.

The two kinds of energy spectra presented here are the vertically averaged, horizontally isotropic spectrum of kinetic energy and the horizontally averaged,

vertical spectrum of kinetic energy. The first allows us to determine the distribution of kinetic energy at different horizontal scales. The second allows us to determine the distribution of kinetic energy at different vertical scales. The distribution of the vertical kinetic energy spectrum between barotropic and baroclinic modes (wavenumber vectors with zero and non-zero vertical components respectively) is critical in understanding the effect of vertical periodic boundary conditions on the dynamics of rotating, stratified flows.

#### 4.2.2 *Inferring Effective Diffusivity*

The domain is allowed to reach apparent statistical equilibrium before a streak of passive tracer is injected into the numerical domain. For most simulations, statistical equilibrium is achieved after  $100 T_{ip}$  and the passive tracer is injected in a Gaussian streak parallel to the  $y$  direction in the middle of the domain. The horizontal and vertical variance of the injected tracer is initially the same as the radial and vertical variance of the diffusively forced mixed patch. The method for estimating effective (or eddy) diffusivity from the numerical domain is described in Section 2.3.5. When the evolution of a passive tracer variance is linear with respect to time it is possible to infer a constant diffusivity parameter. However, when the variance of the dye is in a near-linear regime, such an estimate is no longer accurate. To depict this both the log-log plots and the slope of the log-log plot of variance with respect to time are taken. The slope-log-log plots are derived as follows,

$$\frac{\partial(\log \sigma_T^2)}{\partial(\log t)} = \frac{\partial \sigma_T^2}{\partial t} \cdot \frac{t}{\sigma_T^2}. \quad (4.1)$$

For a tracer variance defined by  $\sigma_T^2 = C_0 t^{p(t)}$ ,

$$\frac{\partial(\log \sigma_T^2)}{\partial(\log t)} = p(t), \quad (4.2)$$

or the power with which the tracer is being dispersed.

### 4.2.3 Poisson Process with Gaussian Clusters

A continuous Poisson process is a stochastic process in which events occur continually and independently. In the simplest sense, it is a process that counts the number of events that occur in a given time interval. The number of events in a time interval,  $N(t)$ , are Poisson distributed,

$$P[N(t) = n] = e^{-\lambda t} \frac{(\lambda t)^n}{n!}, \quad n \in \{1, 2, 3, \dots\}, \quad (4.3)$$

$$E[N(t)] = \lambda t, \quad (4.4)$$

if they are independent of events occurring in any other time interval, and are never simultaneous ( $N(0) = 0$ ). The parameter  $\lambda$  represents the frequency of occurring events. For a Poisson process, the waiting time between events is always finite, non-zero, and exponentially distributed (with mean  $1/\lambda$ ) (Ross, 2009).

Extending the above process to include spatial variations of a recurrence rate in the domain, a spatial Poisson process is considered. The rate parameter is generalized to include these spatial variations,  $\lambda(\mathbf{x}, t)$  such that  $\int_V \lambda(\mathbf{x}, t) dV = \lambda_c$ , where  $\lambda_c$  is the domain level recurrence frequency. It is simplified further by making the temporal and spatial components separable,  $\lambda(\mathbf{x}, t) = \lambda_c f(\mathbf{x})$ , where  $f(\mathbf{x})$  is a probability density function. This separation enables the separate selection and control of the global rate parameter  $\lambda_c$  and the spatial probability density function  $f(\mathbf{x})$ . This generalized rate parameter  $\lambda(\mathbf{x}, t)$  can be seen to be a rate density function for each point in the domain or as a recurrence frequency per unit volume.

In a departure from a traditional Poisson process, waiting times between mixing events are held constant, instead of being exponentially distributed with a global rate parameter. This is done, in part, to be consistent with the methods of previous research (Sundermeyer and Lelong, 2005), but it also lends itself to certain aspects of data analysis. Though this change makes the probability model Markovian instead of Poisson, statistics taken from long simulations are seen to be negligibly different.

The numerical study of Sundermeyer and Lelong (2005) uses a spatial distribution that is uniformly random in space,  $f(\mathbf{x}) = 1/V$ , with fixed waiting times between events,  $\tau = 1/\lambda_c$ . The rate density function,  $\lambda(\mathbf{x}, t) = \lambda_c f(\mathbf{x})$ , is constant for the entire domain. By varying the rate density function in space, regions are created where mixing events occur with increased frequency. This allows for the dynamics of these mixing events to interact in the strongly non-linear regime of Sundermeyer and Lelong (2005), without increasing the global rate of mixing event occurrence.

However, care must be taken to preserve the ergodicity of the domain. If the rate density function is varying throughout the domain, but remains constant for the entire simulation, then the activity experienced by each subset of the domain is not representative of any other subset (on average). That is, some regions will experience more energy and dye dispersion than others because of the probability density function of mixing events being fixed in time. To address this, the following technique is employed such that the effects of proximity can be examined while still maintaining the ergodicity of the domain.

Mixing events are clustered by using a Gaussian probability density function, with given dimensions, around a randomly chosen center for a set number of waiting times. After the set number of waiting times, chosen to preserve ergodicity, the mean of the Gaussian probability density function is moved and the process started over again. The scale of the Gaussian probability density function, represented by  $\sigma$ , is a scaling of the radial and vertical dimensions of well-mixed region introduced by a diffusive forcing,  $diag(\Sigma) = \sigma[\sigma_r^2, \sigma_r^2, \sigma_z^2]$ , where  $\Sigma$  is the covariance matrix for the Gaussian and  $\sigma_r$  and  $\sigma_z$  are the radial and vertical standard deviation for the individual well-mixed regions. The numerical simulations presented are evaluated from varying the waiting times between mixing events  $\tau$ , the size of the Gaussian cluster  $\sigma$ , and the number of mixing events in each cluster  $N$  before moving the center to another location. For the simulations presented here, the waiting times between events are  $\tau = 4.0 T_{ip}$ ,  $\tau = 2.0 T_{ip}$ , and  $\tau = 1.0 T_{ip}$ . The scaling of the Gaussian clusters are  $\sigma = 5.0$ ,  $\sigma = 2.5$ , and  $\sigma = 0.5$  times the

original dimensions of a mixed patch. The volume of the Gaussians, determined by the selection of  $\sigma$ , within one standard deviation are thus successively smaller than the volume of the domain by factors of 4.8, 8.0, and 125. Together,  $\tau$  and  $\sigma$  indicate the increase of rate density in the locale of the cluster until a new center is introduced. Within the volume of one standard deviation around the mean of the Gaussian probability density function, the average rate density is  $\lambda = \frac{1}{\tau V_a}$ , where  $V_a$  is this volume. Instead of calculating and presenting the numeric rate densities, the values of waiting times  $\tau$  and scalings  $\sigma$  are presented in decreasing increments or increasing rate density.

Note, the smallest cluster sizes are an extreme from which to measure the potential effects of overlapping diffusive forcing. The effects of these tightly clustered cases upon the size of the resultant mixed patches are explored in the results.

#### 4.2.4 *Barotropic Dynamics*

Investigated in Chapter 5 is the discrepancy in dissipation timescales between the barotropic and baroclinic modes of kinetic energy in anisotropic domains with Laplacian viscosity. In numerical simulations that have a high frequency of the diffusive forcing in relation to the volume and dissipation timescales, it is found that accumulated, undissipated, barotropic mode kinetic energy makes the largest contribution to an inverse energy cascade. This occurs after the barotropic mode kinetic energy has started to dominate all levels of baroclinic mode kinetic energy. It is found that by applying a scaled dissipation to the barotropic mode kinetic energy this inverse cascade was arrested, without noticeable effect on the baroclinic modes. To this end, the contribution of barotropic mode kinetic energy to the lateral dispersion of a tracer is accounted for. The levels of barotropic mode kinetic energy are determined in numerical simulations without clustering effects. A scaled barotropic damping is applied to these simulations to determine the effect of the barotropic mode on the dispersal of a passive tracer. Finally, the consequences of clustering on the equilibration of simulations, the barotropic mode kinetic energy, and the dispersion of the passive tracer are speculated upon.

### 4.3 Results

The results are presented as follows. First, the variations of forcing, kinetic energy, spectra, and passive tracer dispersion for the unclustered, base cases are presented. Each base case is of increasing frequency, with decreasing waiting times ( $\tau = 4.0 T_{ip}$ ,  $\tau = 2.0 T_{ip}$ , and  $\tau = 1.0 T_{ip}$ ) between each forcing. Data and statistics for all results are presented in order of increasing frequency (decreasing waiting times). Next, I will present the effects of clustering on each of the base cases in turn. Finally, considerations on the relationship between the presence of the barotropic mode kinetic energy and the lateral dispersion of a passive tracer are reviewed.

#### 4.3.1 Unclustered Cases

To begin, I investigate the energetics and dispersion rates of the unclustered base cases,  $\tau = 4.0 T_{ip}$ ,  $\tau = 2.0 T_{ip}$ , and  $\tau = 1.0 T_{ip}$ . Each of these base cases approximately equilibrates after  $100 T_{ip}$ , showing only a 2.84%, 1.76%, and 4.32% additional growth in mean kinetic energy (taken in a  $50 T_{ip}$  frame) by the end of the simulations (Figure 4.1). The mean quantity of available potential energy, per mixing event, introduced by the diffusive forcing for each the base cases,  $7.89 \times 10^{-9}$  J/kg,  $7.83 \times 10^{-9}$  J/kg, and  $7.79 \times 10^{-9}$  J/kg respectively, show little difference, being only 1.27% smaller for the highest frequency of forcing. Alternatively, the standard deviation from the mean of the diffusive forcing increases with frequency,  $2.2 \times 10^{-10}$  J/kg,  $3.2 \times 10^{-10}$  J/kg, and  $4.9 \times 10^{-10}$  J/kg respectively. This amounts to 2.75%, 4.14%, and 6.25% percent variation from the mean forcing for each case (Figure 4.2). The variability of the diffusive forcing is compounded by the increase in forcing frequency when viewed in terms of the rate of energy introduction per unit time. At later times, there is an easily discernible difference in the horizontal scale of the kinetic energy in the domain between these base runs (Figure 4.3). When the dominant scale of energy is larger than the scale of the dye, the rate of dye dispersion increases.

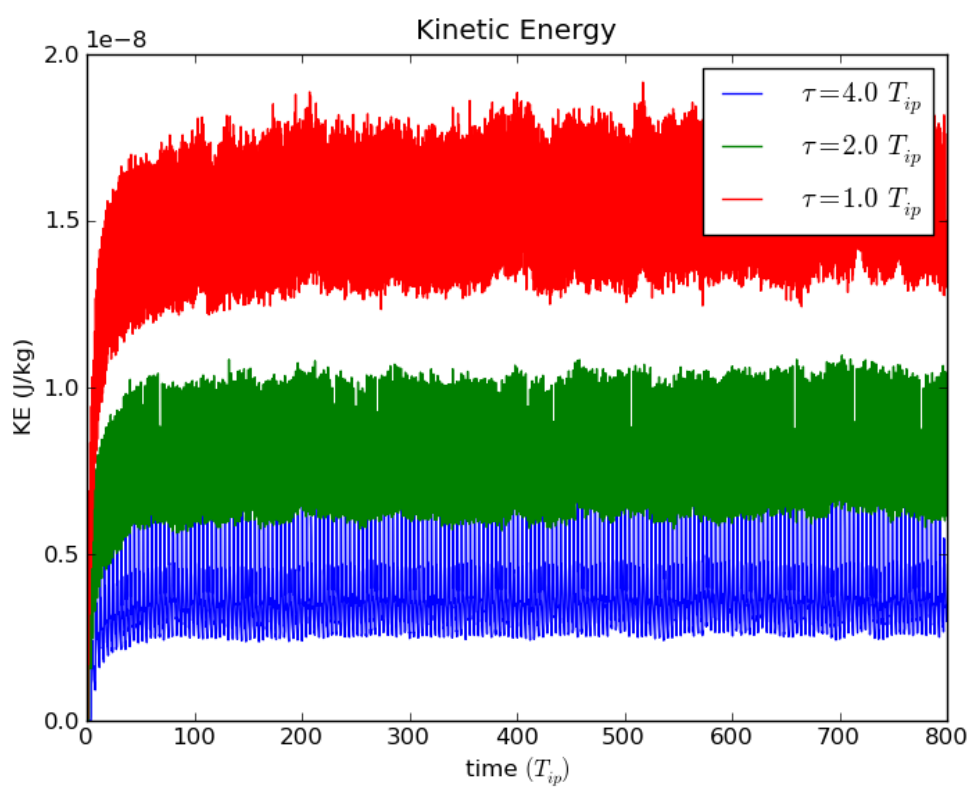


Figure 4.1: Evolution of the domain averaged kinetic energy for unclustered simulations.

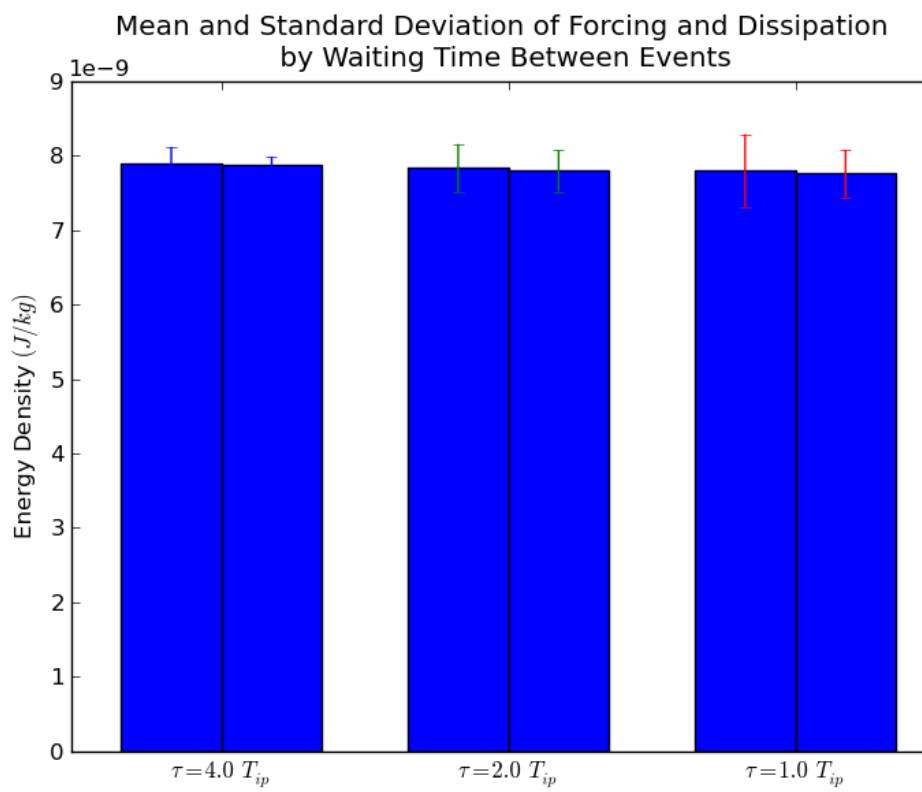


Figure 4.2: Mean and standard deviation of the diffusive forcing and dissipation for base runs.

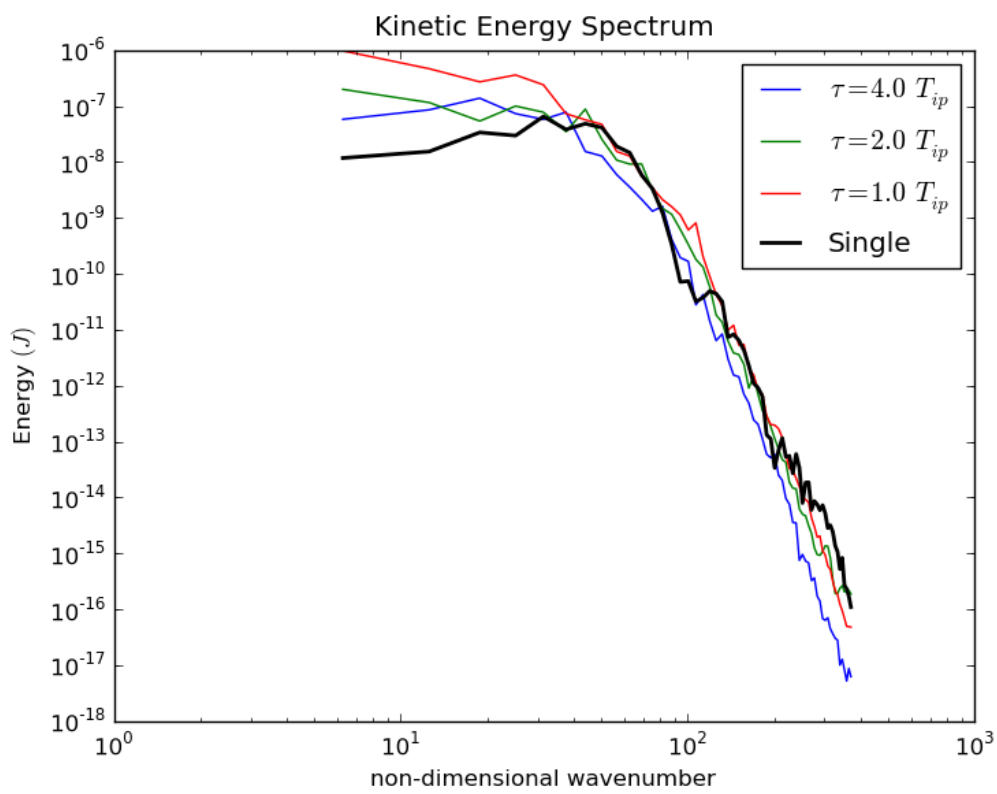


Figure 4.3: Horizontal kinetic energy spectrum at  $800 T_{ip}$  for  $\tau = 4.0 T_{ip}$ ,  $\tau = 2.0 T_{ip}$ , and  $\tau = 1.0 T_{ip}$  compared to the kinetic energy spectrum of a single adjustment vortex in domain with small viscosity at  $20 T_{ip}$ .

Turning to the time evolution of variance of the dye (Figure 4.4), apparent linear growth occurs after  $400 T_{ip}$ . However, when investigating the same plot in a logarithmic frame (Figure 4.5), the fitted growth for the variance is not linear as anticipated. The fitted logarithmic slopes vary from almost linear to almost quadratic,  $\sigma_T^2 = \mathcal{O}(t^{1.195})$ ,  $\sigma_T^2 = \mathcal{O}(t^{1.388})$ , and  $\sigma_T^2 = \mathcal{O}(t^{1.744})$  respectively. Investigating further, the time evolution of the logarithmic slope (algebraic power) of tracer variance evolves over time as well (Figure 4.6). For the  $\tau = 4.0 T_{ip}$  base case, the logarithmic slope  $p(t)$  for  $\sigma_T^2 = \mathcal{O}(t^{p(t)})$  of the variance evolution averages in linear regime,  $p(t) \sim 1.0$ , between  $100 T_{ip}$  and  $400 T_{ip}$ . However, after  $400 T_{ip}$  tracer variance progresses into a more nonlinear regime,  $p(t) > 1.0$ . Conversely, the  $\tau = 1.0$  base case initially disperses the passive tracer in a nonlinear regime  $p(t) \sim 2.0$  before dropping to a more linear regime,  $p(t) \sim 1.5$ , after  $600 T_{ip}$ . Furthermore, for all cases that equilibrate, the power of the dispersion rates settle down to nearly the same level,  $p(t) \sim 1.5$ . This effect is related to the undamped accumulation of barotropic mode kinetic energy reviewed in Section 4.3.3.

#### 4.3.2 Clustered Cases

Turning now to the clustered cases, the same qualities of the simulations for different cluster sizes  $\sigma$  and cluster population  $N$  are examined. As the global rate density of the diffusive forcing is increased with the frequency, it is also increased as the volume is restricted into which the mixing events are introduced. For the base cases, the global rate density increases by factors of 2 as the forcing interval decreased from  $\tau = 4.0$  down to  $\tau = 1.0$ . Likewise, for each decreasing cluster size,  $\sigma = 5$ ,  $\sigma = 2.5$ , and  $\sigma = 0.5$ , the rate density is successively increased by factors of 4.8, 8, and 125 within the standard deviation volume of the Gaussian probability density function above the rate density of the associated base case.

For each of the global frequencies, the clustering had the same general effect on the statistics of the diffusive forcings. For the largest cluster sizes,  $\sigma = 5.0$ , there was very little effect upon the mean diffusive forcing. The mean potential energy for each forcing varied 0.29% to 0.35% from that of their associated base

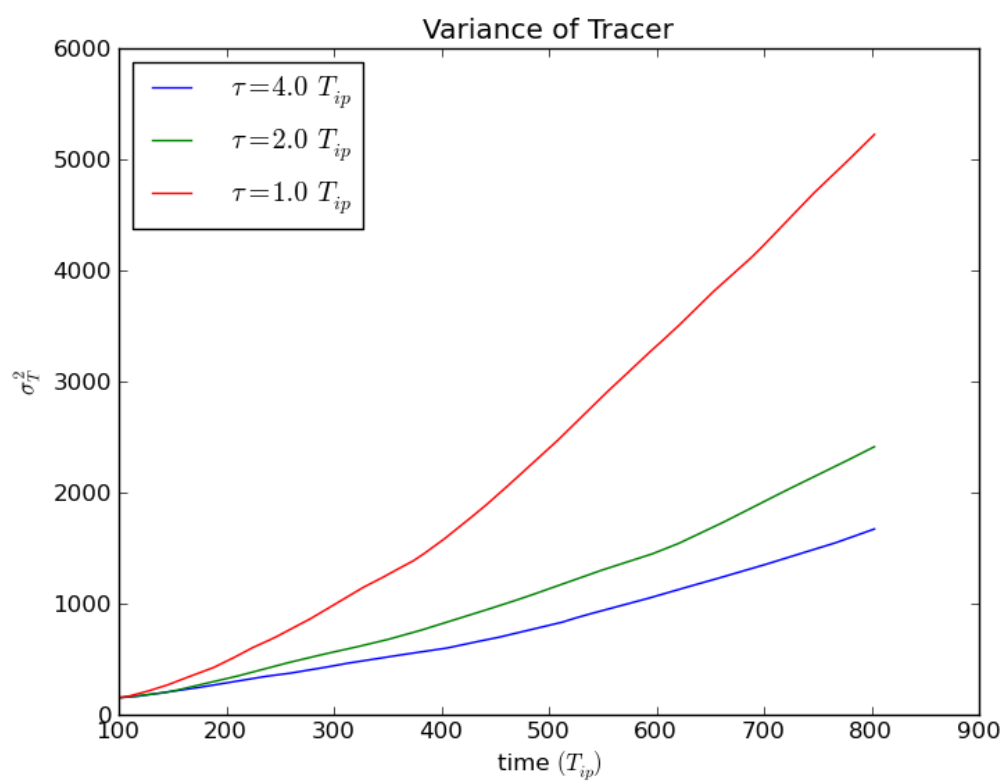


Figure 4.4: Evolution of the variance of a tracer after its introduction at  $100 T_{ip}$ .

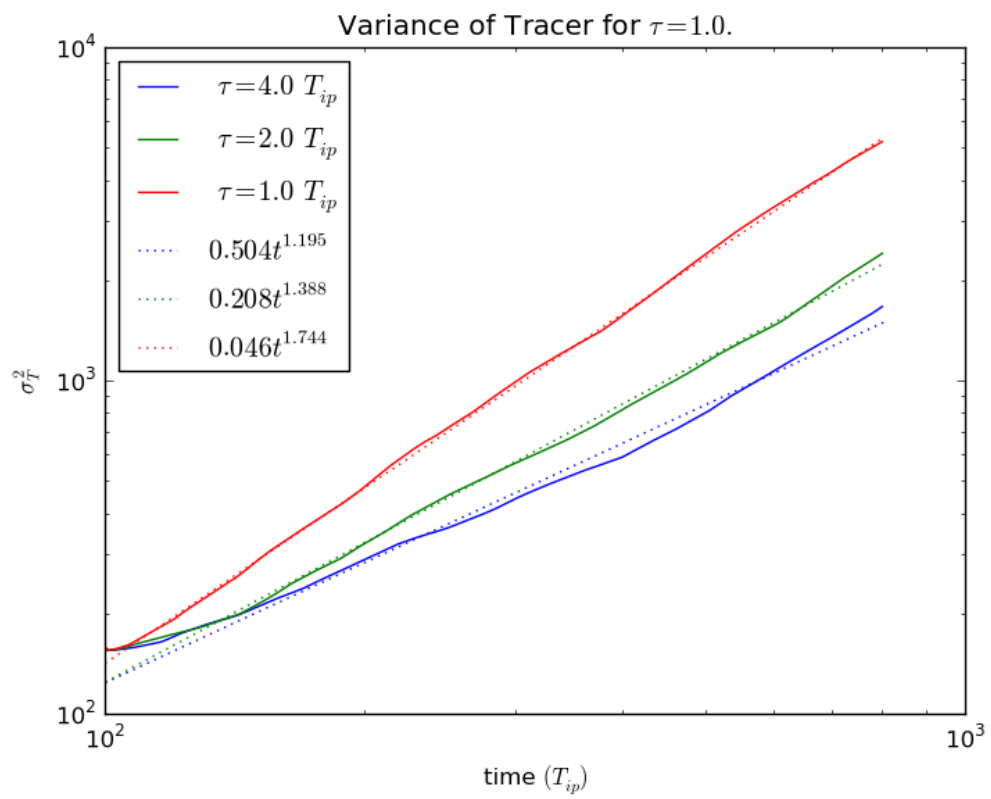


Figure 4.5: Evolution of the variance of a tracer after introduction at  $100 T_{ip}$  in logarithmic scaling.

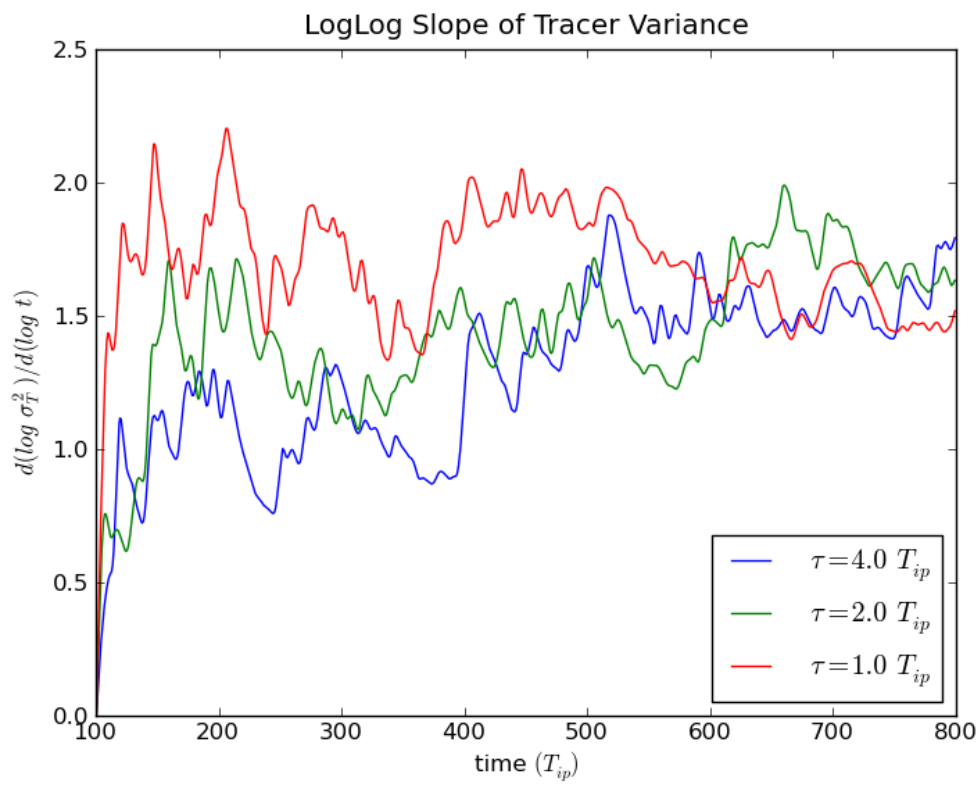


Figure 4.6: Evolution of the variance exponent of a tracer after introduction at  $100 T_{ip}$ .

cases. The standard deviations of the diffusive forcings from this mean ranged from just below that of those for the base cases to about a percentage point (2.6%-3.4%, 4.4%-4.7%, and 6.2%-7.1% respectively). For somewhat smaller cluster sizes,  $\sigma = 2.5$ , the mean of the diffusive forcings varied a bit more, 0.2% to 1.4%, but the standard deviations were greater than the associated base cases (5.9%-6.8%, 7.0%-9.4%, and 14.2%-17.1% respectively). Finally, for the smallest cluster sizes,  $\sigma = 0.5$ , the mean diffusive forcing was 14-39% more than the associated base case, increasing in direct proportion with the cluster population,  $N$ , and only slightly in relation to the associated base frequency. Furthermore, the standard deviations of the forcings were significantly larger than the standard deviations of the base case (13%-15%, 14%-17%, and 15%-19% respectively). These differences in diffusive forcing are illustrated in Figure 4.7 (left bars), for the  $\tau = 4.0 T_{ip}$  cases, along with the associated dissipation of energy between forcings (right bars). Distributions of forcing and dissipation for higher rate densities ( $\tau = 2.0 T_{ip}$ , and  $\tau = 1.0 T_{ip}$ ) had very similar responses to clustering. Finally, the volume average kinetic energy increased in direct relation to increasing rate density (both global and local) and the population of each cluster. For the smallest cluster sizes, kinetic energy of the simulations does not approach equilibration as in simulations with lower overall rate densities.

Additionally, the smallest cluster sizes behaved as a single, larger destratified region. The destratification ratio for a single diffusive forcing is  $\Delta N^2/N^2 = 0.5$  instead of the expected  $\Delta N^2/N^2 = 1.0$  (see Appendix A). The destratification ratio for the smallest clusters,  $\sigma = 0.5$ , is twenty percent more,  $\Delta N^2/N^2 = 0.6$  for the waiting times  $\tau = 1.0 T_{ip}$  and cluster populations  $N = 5$ . This is accompanied by a 10% increase in destratified height and a doubling of horizontal extent. The density profile of the compounded mixed patch was allowed to adjust between clustered diffusive forcings, explaining a smaller ratio between the deformation radius to horizontal scale of the mixed patch. The shape of the compounded mixed patch places the resulting adjustment vortex into a different Burger number regime (Lelong and Sundermeyer, 2005; Brunner-Suzuki et al., 2012). Only simulations

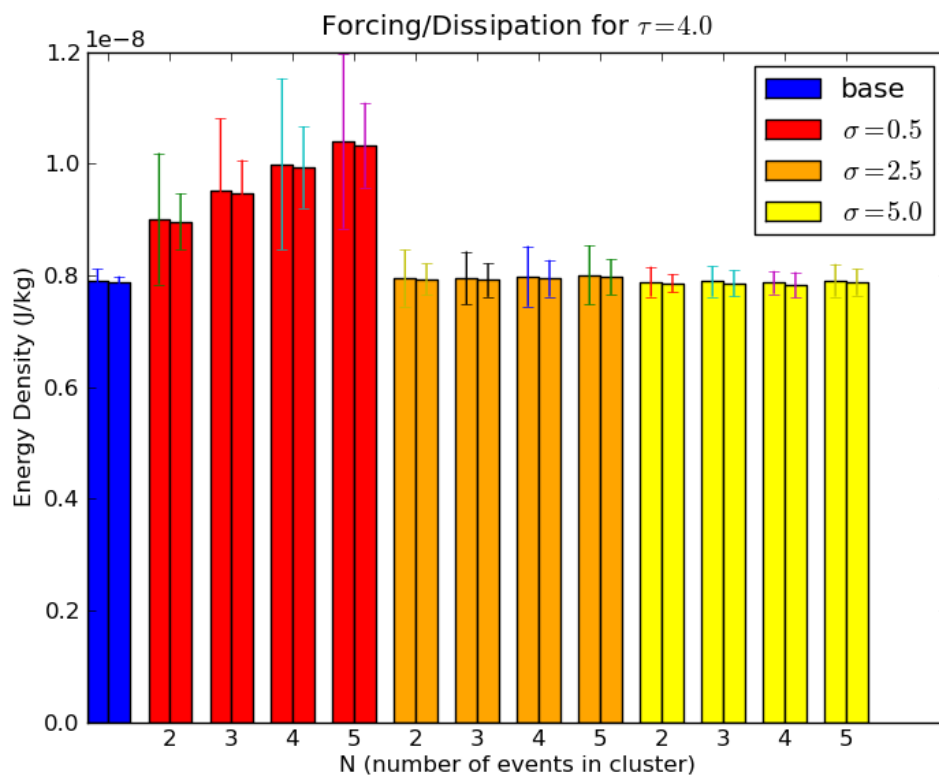


Figure 4.7: Mean and standard deviation of the diffusive forcing and dissipation for simulations with  $\tau = 4.0 T_{ip}$  waiting time.

with the highest rate densities exhibit this kind of behavior. The less tightly clustered cases do not show this behavior and result in separate mixed patches on average.

The above variations in energy and shape produced by clustering are also seen by investigating the horizontal kinetic energy spectrum. For waiting time between forcings of  $\tau = 1.0 T_{ip}$ , the kinetic energy spectrum of the base case is compared to the clustered runs with population  $N = 5$  at different times throughout the simulations (Figures 4.8 - 4.11). At  $10 T_{ip}$  all of the clustered cases have more energy at larger scales than the base case (Figure 4.8). However, the base case has more energy at moderate scales than the  $\sigma = 5.0$  and  $\sigma = 2.5$  cases. This is consistent with the above mean forcing of these cases being close to that of the base case although with larger deviations in the quantity and scale of that forcing. The variability in the quantity and scale of the energy, along with the dissipation of kinetic energy, is enough to reduce the magnitude of large scales in some of the clustered simulations below that of the base case (Figures 4.9,4.10). However, the deviations of forcing around the mean is not enough to diminish the scale and quantity of kinetic energy of the most tightly clustered case below that of the other cases. In general, clustering increases the the amount of large scale energy in the domain. This, in turn, has a direct effect on the dispersion of a passive tracer.

Again, for each of the global rate densities of the diffusive forcings, the clustering had the same general effect on the lateral dispersion of a tracer. Despite having local rate densities almost five times larger than the associated base case, the largest cluster sizes,  $\sigma = 5.0$  showed no more lateral dispersion than the associated base cases. In fact, some cases showed slightly less overall lateral dispersion, especially for the  $\tau = 4.0 T_{ip}$  cases. For somewhat smaller cluster sizes,  $\sigma = 2.5$ , both overall lateral dispersion and the variability in the rate of the lateral dispersion increase. The only exception is the  $\tau = 2.0 T_{ip}$ ,  $N = 5$  case that still shows greater variability in the rate of dispersion. The smallest cluster sizes,  $\sigma = 0.5$ , show the most total lateral dispersion of all cases without exception. However, the kinetic energy for the smallest cluster sizes did not attain statistical equilibrium.

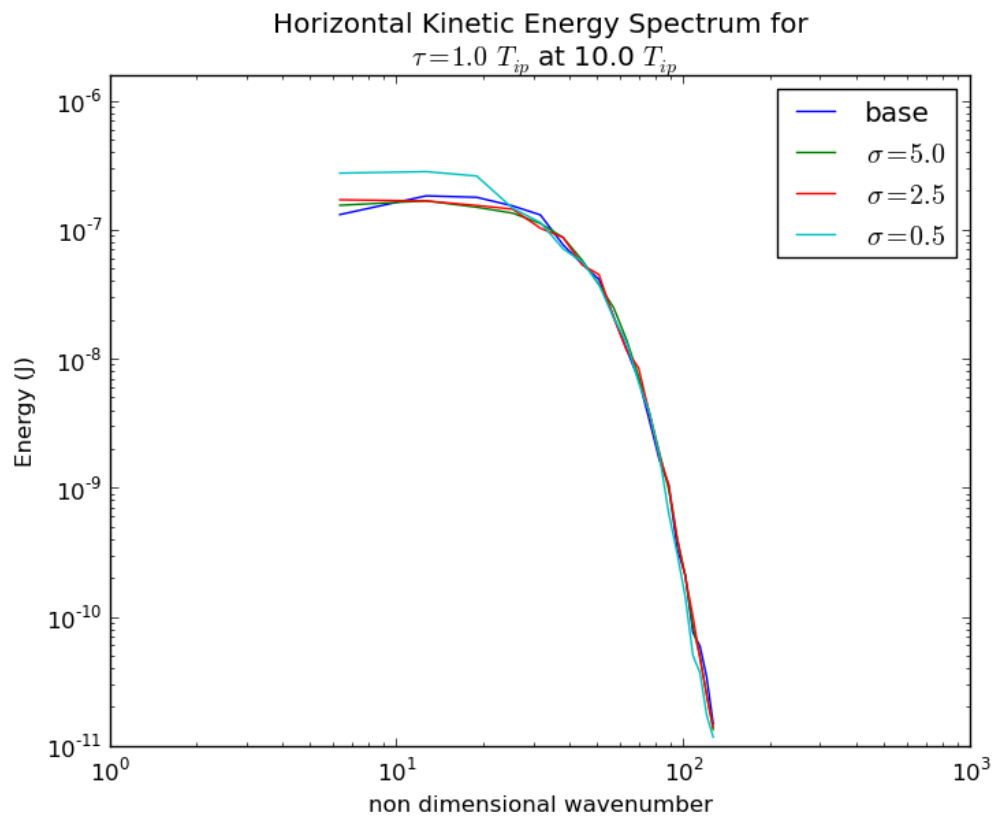


Figure 4.8: Horizontal spectrum of kinetic energy for base case and clustered cases,  $N = 5$ , at  $10 T_{ip}$ . The above shows the general effect of increased large scale energy for clustering.

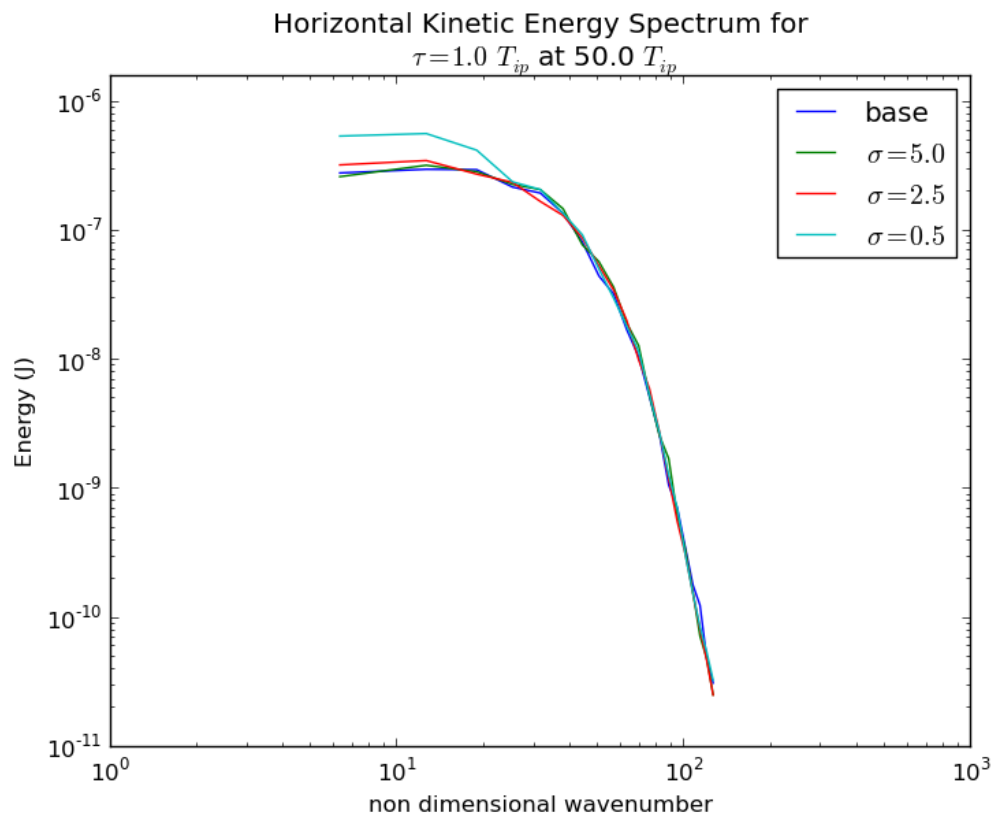


Figure 4.9: Horizontal spectrum of kinetic energy for base case and clustered cases,  $N = 5$ , at  $50 T_{ip}$ . Dissipation and deviations in forcing can cause kinetic energy of the large scales in clustered cases to drop below that of the base case.

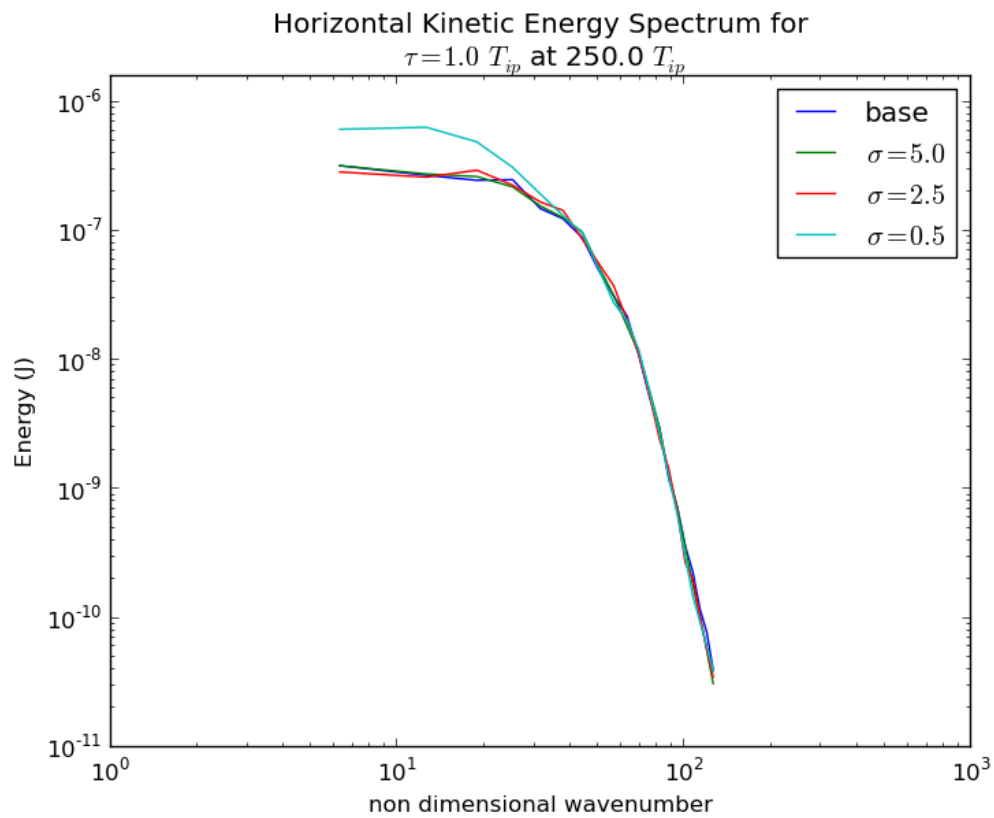


Figure 4.10: Horizontal spectrum of kinetic energy for base case and clustered cases,  $N = 5$ , at  $250 T_{ip}$ . Dissipation and deviations in forcing can cause kinetic energy of the large scales in clustered cases to drop below that of the base case.

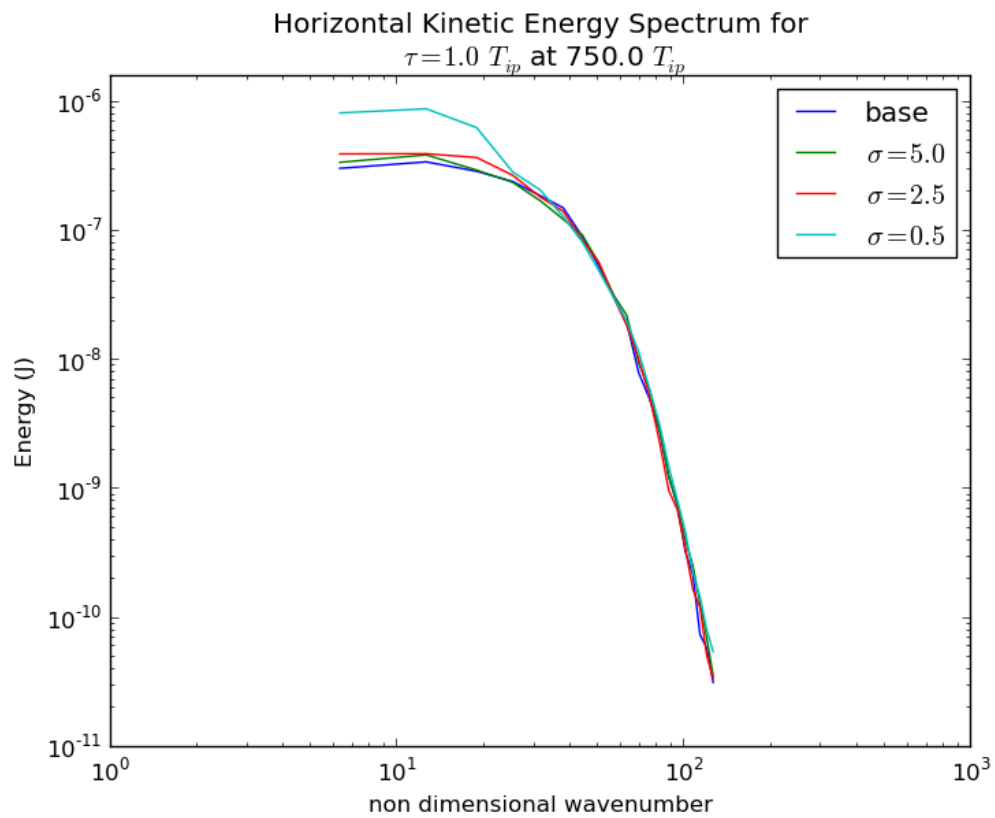


Figure 4.11: Horizontal spectrum of kinetic energy for base case and clustered cases,  $N = 5$ , at  $750 T_{ip}$ . The above shows the general effect of increased large scale energy for clustering.

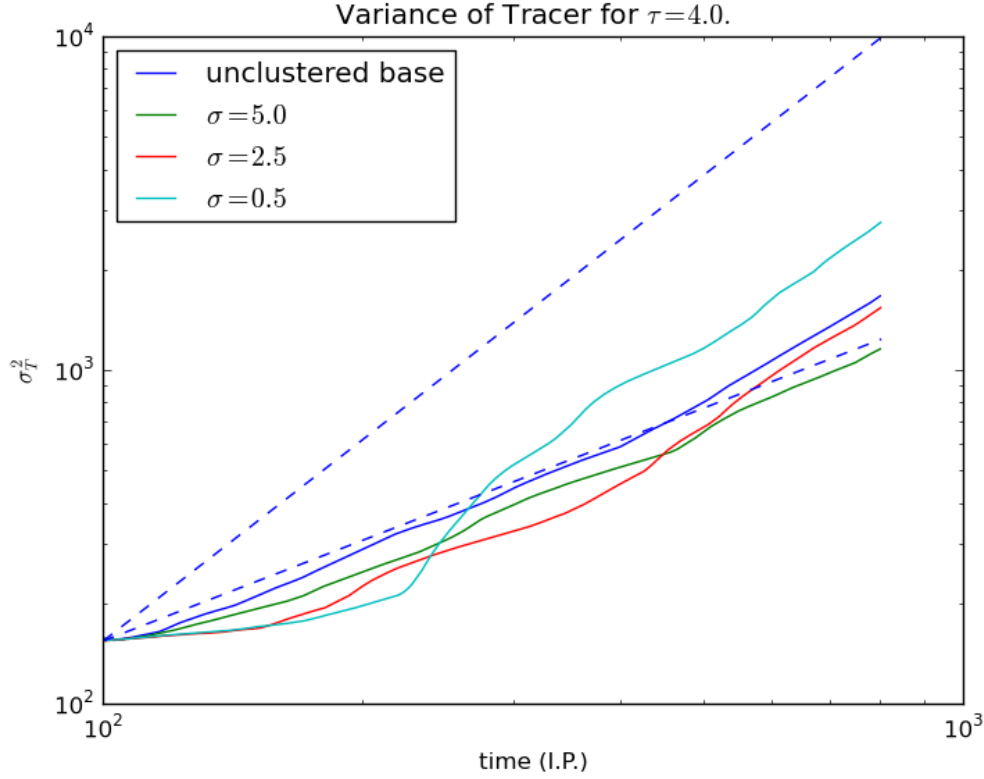


Figure 4.12: Evolution of the variance of a tracer after introduction at  $100 T_{ip}$  for waiting times  $\tau = 4.0 T_{ip}$  with  $N = 5$  and  $\sigma \in \{5.0, 2.5, 0.5\}$  with logarithmic axes. Dashed lines are for comparison with the linear (lower) and the quadratic (upper) rates of dispersion.

For this group of cases, the  $\tau = 1.0 T_{ip}$  simulations show a leveling off of tracer variance toward the end of the simulations due to lateral saturation (horizontal variance of the dye approaching the limiting value of  $\sigma_T^2 = \frac{L_x^2}{12} = 20,833$ ). The effects of the clustering upon the variance of the passive tracer is illustrated in Figures 4.12-4.14 in log-log plots of tracer variance to time.

#### 4.3.3 Influence of the Barotropic Mode

Proceeding, the influence of the barotropic mode on the lateral dispersion of the passive tracer is investigated. The first 7 vertical modes of an unclustered case,  $\tau = 1.0 T_{ip}$ , show the slow accumulation of the barotropic mode kinetic energy with

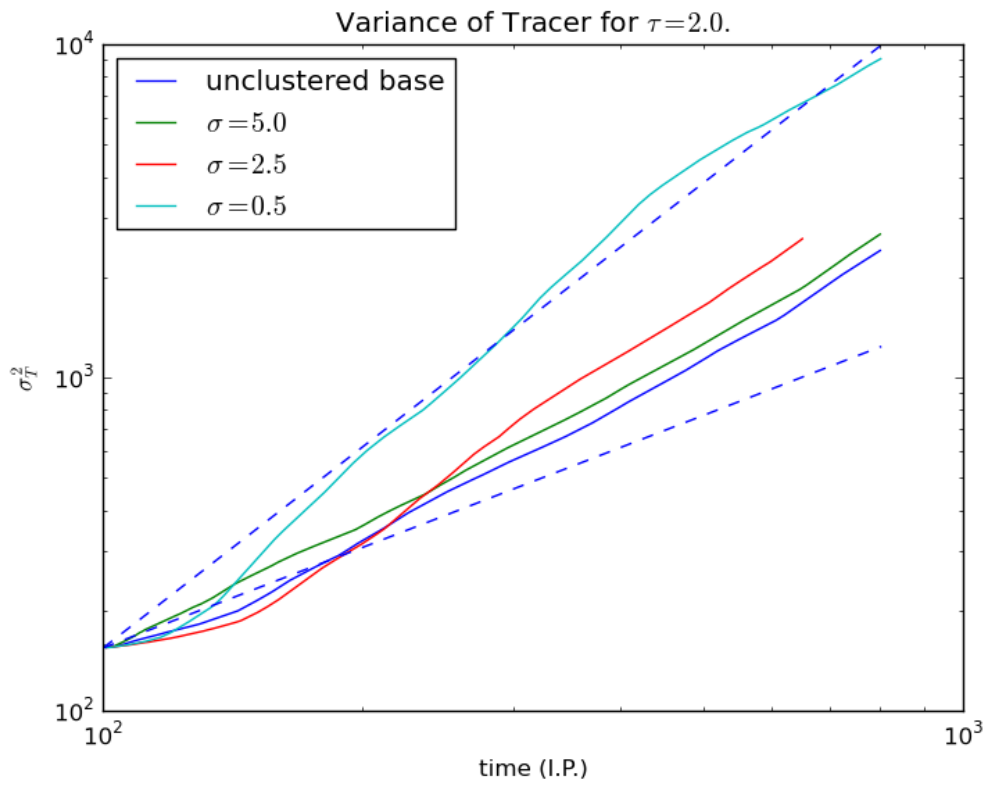


Figure 4.13: Evolution of the tracer variance after introduction at  $100 T_{ip}$  for waiting times  $\tau = 2.0 T_{ip}$ ,  $N = 5$ , and  $\sigma \in \{5.0, 2.5, 0.5\}$  with logarithmic axes. Dashed lines are for comparison with the linear (lower) and the quadratic (upper) rates of dispersion.

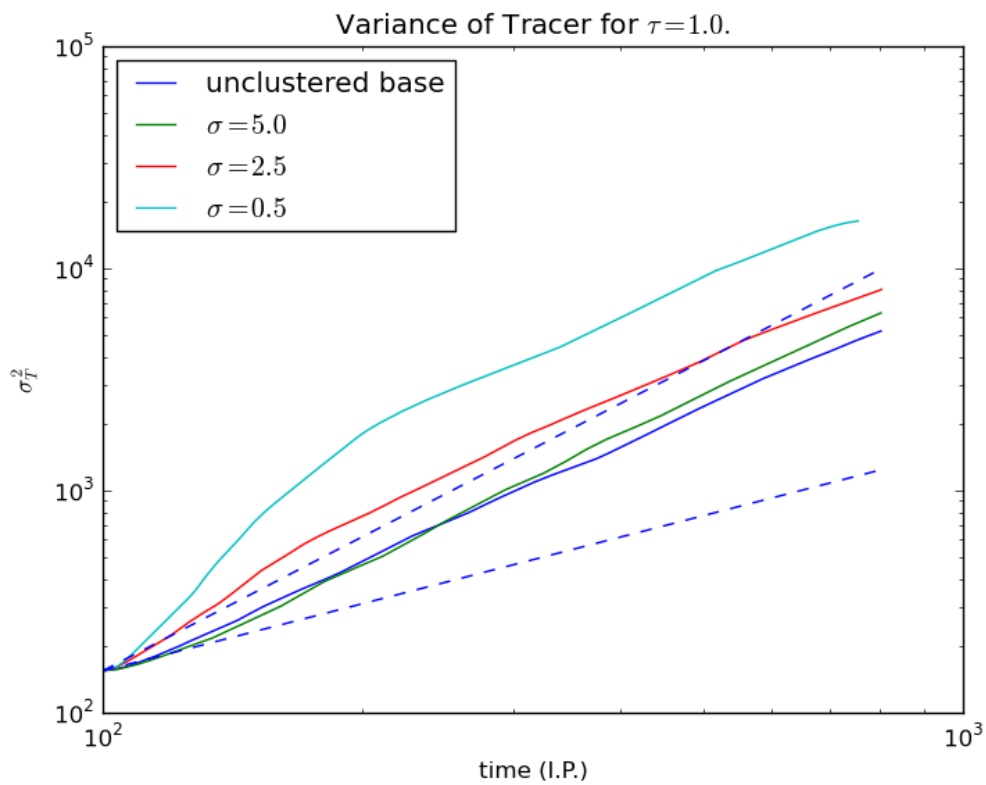


Figure 4.14: Evolution of the variance of a tracer after introduction at  $100 T_{ip}$  for waiting times  $\tau = 1.0 T_{ip}$ ,  $N = 5$ , and  $\sigma \in \{5.0, 2.5, 0.5\}$  with logarithmic axes. Dashed lines are for comparison with the linear (lower) and the quadratic (upper) rates of dispersion.

respect to the relatively equilibrated baroclinic modes (Figure 4.15). The effect on the vertically averaged horizontal modes are shown in Figure 4.16 and Figure 4.17. The accumulation of barotropic mode kinetic energy is nearly linear, scaling with the sum of each adjustment's contribution to the barotropic mode minus the dissipation. It is approximately an order of magnitude weaker ( $5.62 \times 10^{-8}$  J) than the first baroclinic mode ( $3.18 \times 10^{-7}$  J) and reaches a maximum energy level near the fourth baroclinic mode ( $4.95 \times 10^{-8}$  J) near the end of the simulation at  $800 T_{ip}$ . Investigating the two clustered cases of this base frequency,  $\tau = 1.0 T_{ip}$  (not shown), differences in the amount of accumulated barotropic mode kinetic energy are observed. For a moderately clustered case,  $\sigma = 2.5$ , the barotropic mode contains about twice as kinetic energy ( $1.08 \times 10^{-7}$  J) as the unclustered base case, while the first baroclinic energy stays approximately the same ( $3.61 \times 10^{-7}$  J). Striking differences occur for the most tightly clustered case,  $\sigma = 0.5$ , where the barotropic mode kinetic energy ( $5.60 \times 10^{-7}$  J) concludes at a level just greater than all of the baroclinic modes ( $4.37 \times 10^{-7}$  J). Simulations where the barotropic mode kinetic energy remains sub-dominant show dispersion rates that conclude at a near linear state  $\sigma_T^2 = \mathcal{O}(t^{1.5})$ . However, for the unequilibrated clustered simulations, the barotropic mode comes to dominate and the tracer dynamics portray a quadratic evolution  $\sigma_T^2 = \mathcal{O}(t^{2.0})$ . This is due to both the unequilibration and the barotropic dynamics.

As a check, the unclustered base cases are run with a scaled dissipation for the barotropic mode (for the exact form see Chapter 5). First, these simulations equilibrated with near identical global kinetic energy dynamics as the original runs. The exception is that these simulations have less kinetic energy (4.06%, 4.09%, and 4.76% averaged over the last  $100 T_{ip}$ ) than the original runs and they do not have the slight upward drift over the course of the simulation. The barotropic mode does not show unabated growth as it does in the original simulations, equilibrating an order of magnitude weaker than the original base cases ( $1.43 \times 10^{-9}$  J,  $3.1 \times 10^{-9}$  J, and  $6.2 \times 10^{-9}$  J). Furthermore, the total dispersion of the passive tracer is less than or equal to that of the original cases (variances of dye 30.38%, 35.97%, and 50.83%

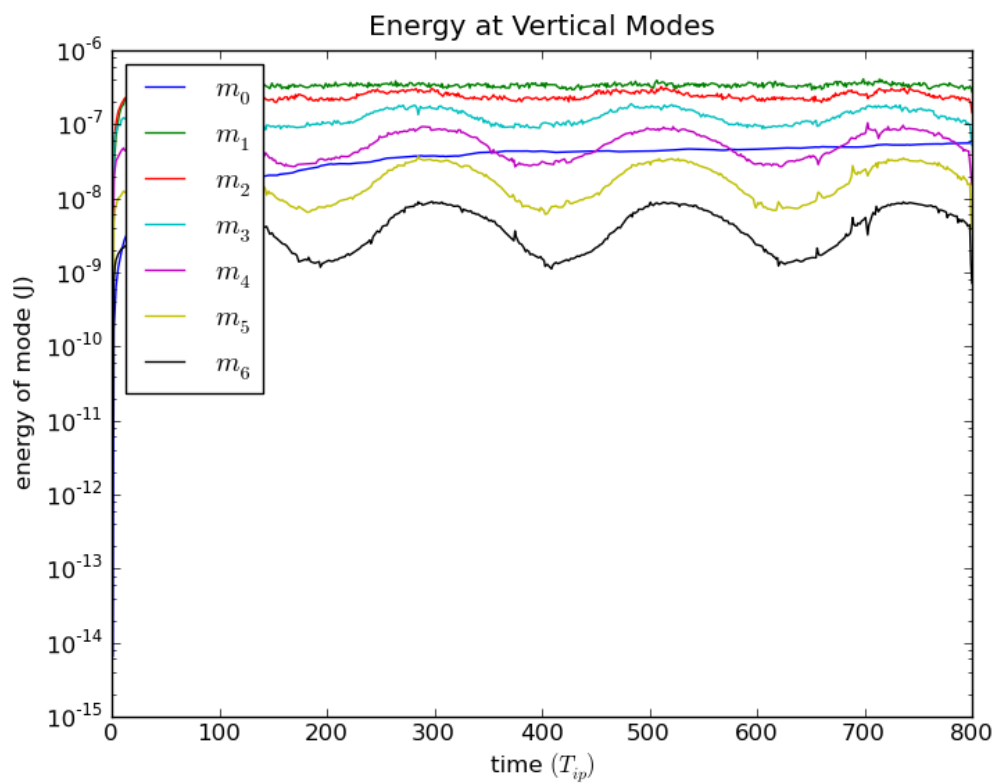


Figure 4.15: Time evolution of the first 6 vertical modes of the  $\tau = 1.0 T_{ip}$  simulation showing the slow accumulation of barotropic mode kinetic energy with respect to the relatively equilibrated baroclinic modes.

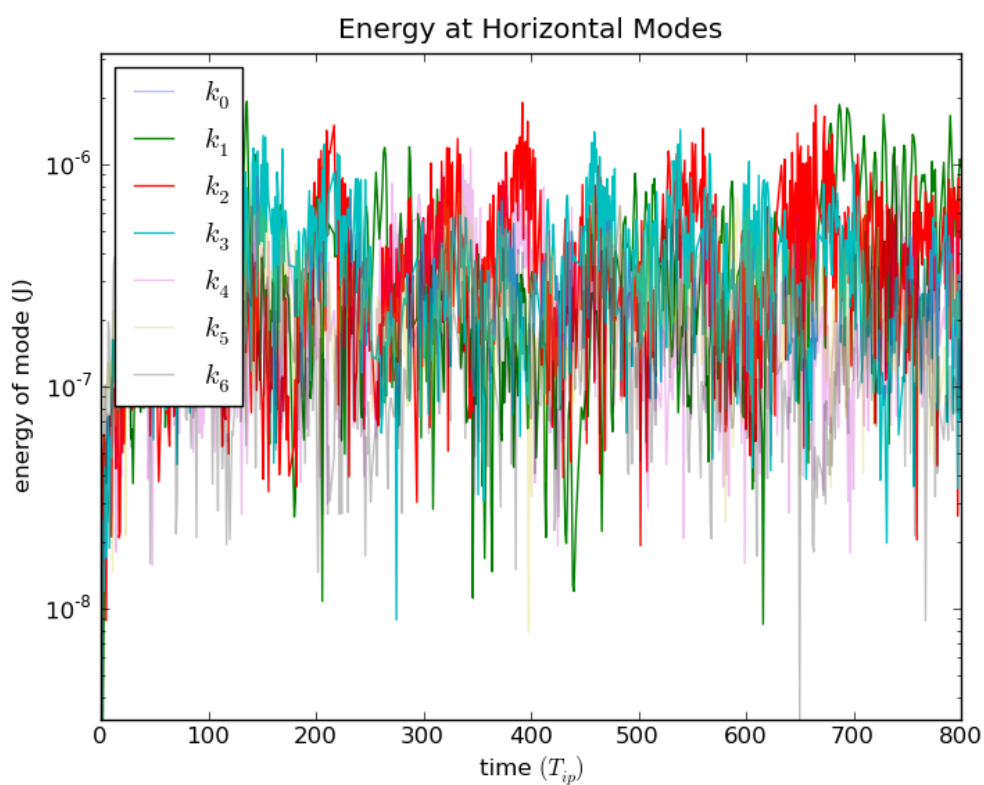


Figure 4.16: Time evolution of the first 6 horizontal modes of the  $\tau = 1.0T_{ip}$  simulation. The first two horizontal modes become persistently dominant after  $700 T_{ip}$ . This is seen more clearly in Figure 4.17.

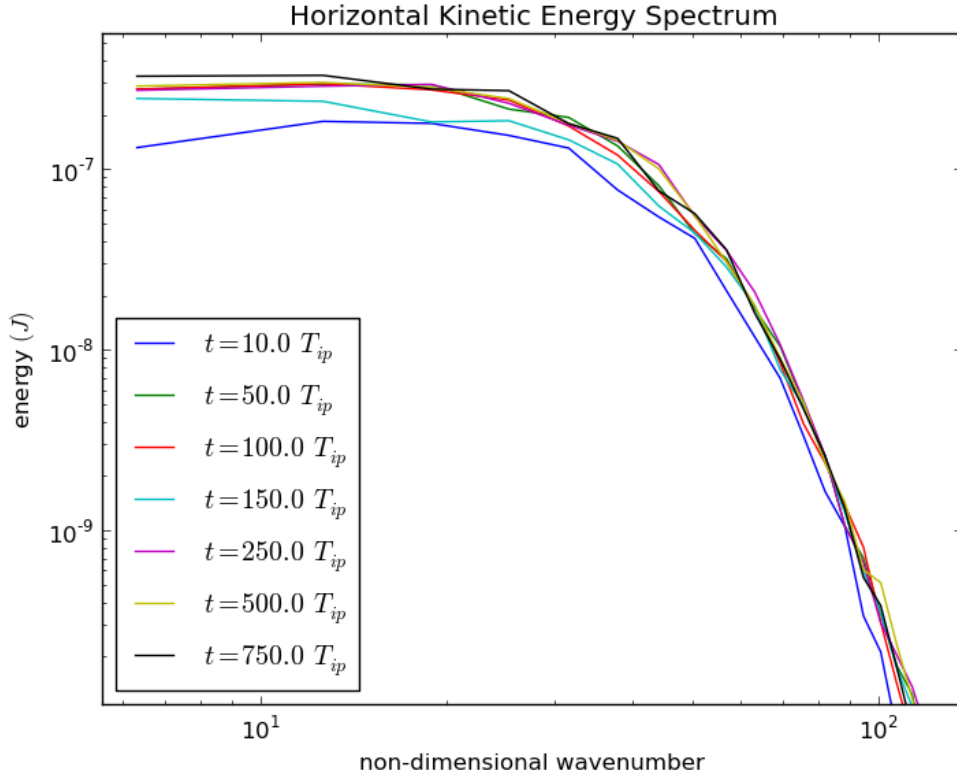


Figure 4.17: Snapshots of horizontal kinetic energy spectrum for the largest scales of the  $\tau = 1.0 T_{ip}$  simulation. The slow accumulation of kinetic energy is seen in at the largest scales.

smaller) (Figure 4.18). The logarithmic slope of the tracer variance eventually averages in the linear regime ( $\sigma_T^2 = \mathcal{O}(t)$ ) after  $600 T_{ip}$  (Figure 4.19). Additionally, comparing the plan views of tracer for the unclustered case for  $\tau = 1.0 T_{ip}$  waiting times, the barotropic mode kinetic energy contributes to large meanders in the dye that are not present when the barotropic damping is applied (Figure 4.20).

#### 4.4 Discussion

Working from a clustering assumption for turbulent mixing events that the adjustment of turbulent mixing events set up conditions for future instabilities and mixing, introduced well-mixed regions are restricted with Gaussian probability density functions of various, scaled sizes. Additionally, varying the population of

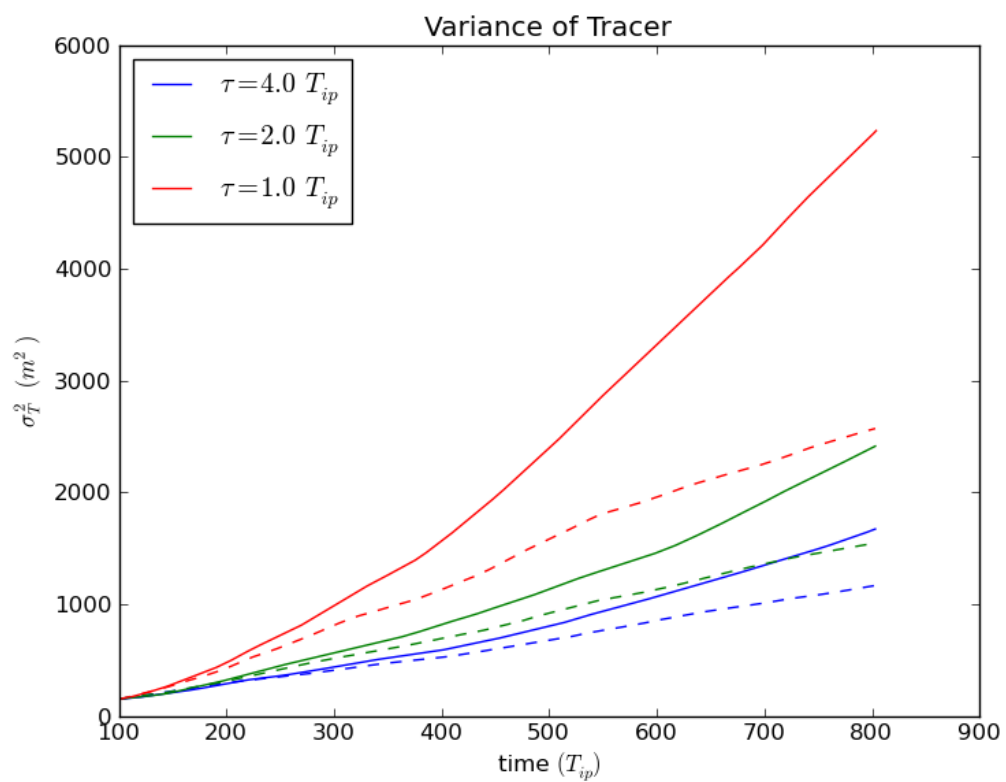


Figure 4.18: Time evolution of the variance of the passive tracer after introduction at  $100 T_{ip}$  for original base cases (solid) compared to base cases with barotropic damping (dashed).

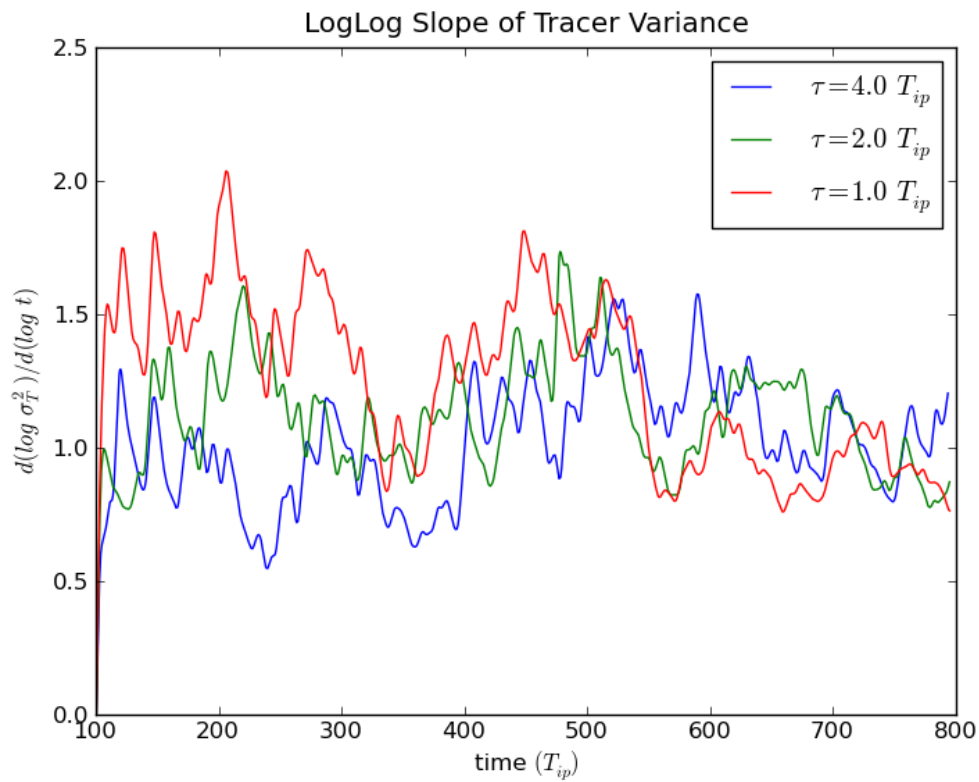


Figure 4.19: Time evolution of the variance exponent of a tracer after introduction at  $100 T_{ip}$  for unclustered simulations with barotropic damping.

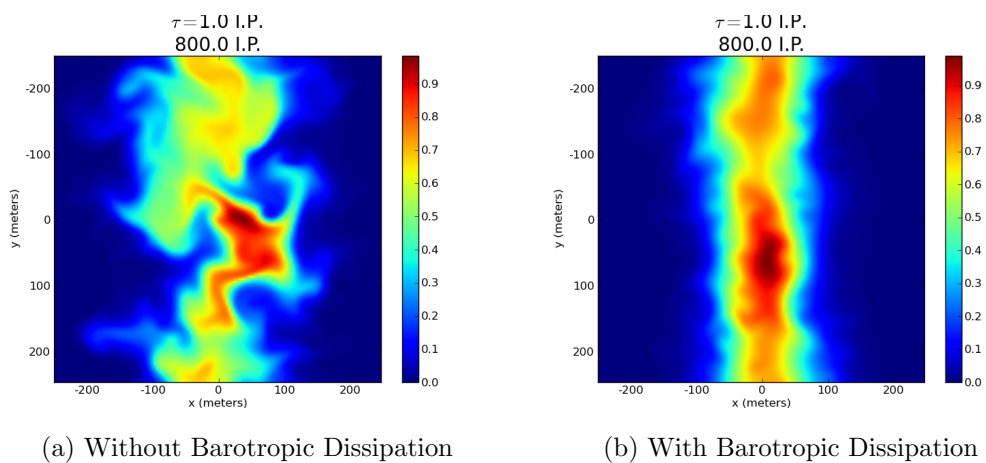


Figure 4.20: Plot of end-time distribution of tracer for simulations, with and without barotropic damping, for waiting time  $\tau = 1.0 T_{ip}$ . The color is scaled by the maximum concentration of the passive tracer in the domain.

each cluster and the waiting time between mixing events, the results of both energetics and passive tracer dispersal to that of unclustered simulations are compared. Both global and local increases in the rate density of the diffusive forcings showed increases in the overall variability of the diffusive forcings themselves. Increases in the scale of kinetic energy came along with increases in global and local rate density of the diffusive forcings. With increasing rate density comes the increase in lateral dispersal and rates of lateral dispersal of a passive tracer. Although some of the rates of dispersion are close to linear, none concluded in a purely, linearly dispersive regime. The accumulating barotropic mode energy is investigated and found to strongly influence the dispersion of the passive tracer. With the barotropic mode kinetic energy damped, the dispersal of the passive tracer is 30% to 50% less and concludes in a linear regime for all simulations.

Increasing the rate density of the diffusive forcing, both globally and locally, increases the likelihood that the forcing overlaps with the remains of previous forcings. It is noted that the dissipative timescale  $T = \nu/h^2$  of the vortices is approximately  $10 T_{ip}$ . This is shorter than most of the timescales of instabilities ( $60 T_{ip} - 200 T_{ip}$ ), dipole pairing ( $5 - 80 T_{ip}$ ), and partial merger ( $15 - 20 T_{ip}$ ) found in Chapter 3 for near inviscid simulations of two proximal adjustment vortices. Although dipole pairing can occur within the dissipation timescale, the rate of the non-linear transfer of kinetic energy is dominated by the dissipation rate. This is easily seen by calculating the Reynolds number  $Re = UL/\nu$ . Using measured quantities of horizontal velocity ( $U = .002$  m/s), vortex radius ( $L = 25$  m), and Laplacian viscosity ( $\nu = 2.5 \times 10^{-5}$  m<sup>2</sup>/s) in the numeric simulations, the Reynolds number ( $Re = 2,000$ ) indicates a near laminar flow. The choice to scale viscosity has the consequence of dissipating vortices before most of the non-linear interactions can occur. Should non-linear interactions result in instabilities or pairing, they are quickly homogenized in the vertical by the strong viscosity. This, in turn, makes the overlapping diffusive forcing as the primary source of scale increasing interactions. It may be that the vertical scale of an adjustment vortex grows sufficiently to participate in other non-linear behavior before dissipation. A doubling

in dissipation time requires a forty percent growth in the height of the adjustment vortex. Simulations with the highest rate densities (and overlapping diffusive forcings) show only a ten percent growth in height over the course of adding additional forcing to the cluster. The most clustered cases have twice the radius and a slightly more thorough destratification than a single mixed patch. The most significant effect on scale and dispersion comes from the barotropic mode kinetic energy.

As noted in Chapter 5, the large scales of the barotropic mode kinetic energy are dissipated four orders of magnitude slower than comparative large scales of the baroclinic modes in an unscaled domain. With forcings that result in small amounts of barotropic mode kinetic energy, undissipated energy tends to accumulate. As is shown, the barotropic mode is the source of virtually all of the unequilibrated kinetic energy. This has a consequence of contributing to the non-linear dispersal of a passive tracer in three major ways. Firstly, the energy is not equilibrated. Though the barotropic mode kinetic energy only amounts to less than five percent of the total kinetic energy, it does not stop growing. Next, large scale, barotropic mode, kinetic energy dissipates at least four orders of magnitude slower than the baroclinic modes and smaller barotropic scales. This allows the larger and slower barotropic scales of a single adjustment vortex to advect the fluid for long times (Lelong and Sundermeyer, 2005). Lastly, the barotropic mode is vertically invariant and is thus a two-dimensional mode. Inverse energy cascades are a known property of two dimensional flows. As a result, scales of motion contributing to the stirring are steadily growing throughout the simulation. For the first, the 4% difference in barotropic kinetic energy is able to produce nearly as much lateral dispersion as doubling the rate of mixing event introduction. This effect alone is not enough to describe the differences. Addressing the third and the second collectively, Chapter 5 shows that for the  $\tau = 1.0 T_{ip}$  unclustered simulation an inverse energy cascade is the most likely way to account for the increase in the scales of kinetic energy in the barotropic mode. However, the unequilibration of kinetic energy will also account for some of this dispersion. The contributions of each have yet to be fully explored.

The scale-dependent dispersion observed for a passive tracer is consistent with observations by both Okubo (1971) and Taylor (1921). In analysis of twenty different sets of field data, Okubo (1971) calculated the apparent diffusion in relation to time of dispersion and radial scale of a dye patch. He found that apparent (or effective) diffusion varied as  $t^{2.3}$  and  $\ell^{1.1}$ , where  $t$  and  $\ell$  are the time and length scales under consideration. With a broad range of kinetic energy scales and associated processes, this is consistent with the theory of Taylor (1921). As presented in Cohen and Kundu (2007), when the scale of a dye patch is less than the mean scale of motion, the effective diffusivity of the dye are nonlinear ( $\sigma_T^2 = \mathcal{O}(t^p)$ ,  $p > 1$ ). However, when the scale of the dye patch exceeds that of the largest vortices, the effective diffusivity approaches a constant Fickian value ( $\sigma_T^2 = \mathcal{O}(t^p)$ ,  $p = 1$ ). As the ocean contains many scales of eddies, the latter regime of dispersion will probably never be achieved.

Yet unaddressed is the effect of the  $N/f$  scaling upon the Reynolds number of the modeled flow. For an anisotropic fluid, the horizontal length scale  $L$  is in proportion to the ratio of buoyancy frequency  $N$  and vertical length scale  $H$  to the Coriolis frequency  $f$ ,  $L = \frac{N}{f}H$ . For a given Ekman number,

$$\begin{aligned}
 Ek &= \nu/(fH^2) = \nu/(fL^2)(N/f)^2, \\
 &= (UL/\nu)^{-1}(U/fL)(N/f)^2, \\
 &= Ro/Re(N/f)^2.
 \end{aligned} \tag{4.5}$$

Solving for the Reynolds number,

$$Re = Ro/Ek(N/f)^2. \tag{4.6}$$

This shows that reducing  $(N/f)$  by an order of magnitude in turn reduces the Reynolds number by two orders of magnitude. Rescaling the Reynolds number in the numerical simulations ( $Re = \mathcal{O}(1,000)$ ) to the oceanic scales ( $Re = \mathcal{O}(100,000)$ ) takes us from a laminar flow to a turbulent flow. The laminar flow of

the  $N/f$ -scaled domain dissipates the baroclinic vortices before non-linear interactions between adjustment vortices can evolve into propagating dipoles observed in Chapter 3. With overly damped baroclinic modes and insufficiently damped barotropic modes, it is doubtful that these simulations are representative of dynamics in the intended oceanic context.

However unrepresentative, it is still likely that the non-linear interactions between proximal adjustment vortices will increase lateral dispersion in the ocean. As is shown in Chapter 3, the close proximity of adjustment vortices to one another precipitate instabilities, dipole pairing, and transient mergers. Furthermore, the  $Re = \mathcal{O}(10,000)$  regime of simulations in Chapter 5, for uniformly distributed mixed patches, show the evolution of multiple non-linear interactions and an inverse energy cascade, although unequilibrated. It may be that higher Reynolds number numerical simulations with single clusters and small populations of mixing events can shed light upon related oceanic processes. The execution and analysis of such numerical simulations is currently underway.

Due to the non-linearity of the dispersion dynamics, a direct comparison with the parameterized scaling of effective diffusivity by Sundermeyer and Lelong (2005) is not yet possible. This linear scaling is not constructed for the variations in energetic scales observed in this current study.

Further work needs to be done to investigate how the barotropic damping may be appropriately applied. It will also be necessary to numerically model a Reynolds number that is more representative of the unscaled dynamics. With both barotropic damping and a more turbulent Reynolds number range, the important non-linear dynamics may be equilibrated and investigated.

#### **4.5 Conclusions**

Although clustering diffusive forcing events increases the lateral dispersion of the tracer, it is not due to the non-linear interactions explored in Chapter 3. The overlapping diffusive forcing and the inverse cascade of kinetic energy in the barotropic mode are the primary drivers of scale increasing interactions. These larger scales

drive the broader dispersal of a tracer and contribute more to an unabated accumulation of barotropic mode kinetic energy. The non-linear interactions are suppressed until the flow is able to become more turbulent, through increased horizontal scales, increased velocity, and the dynamics of a virtually inviscid, barotropic mode. Further work is needed to address the concerns of unequilibrated barotropic mode and the sub-turbulent Reynolds number.

## Chapter 5

**INVERSE CASCADES OF KINETIC ENERGY IN ANISOTROPIC, ROTATING, STRATIFIED DOMAINS**

In this part of the dissertation, the contribution of the anisotropic scaling of the domain to inverse energy cascades of kinetic energy is explored. These inverse cascades of energy have been observed in previous numerical simulations (Sundermeyer and Lelong, 2005).

**5.1 Introduction**

Pseudo-spectral numerical methods involving discrete Fourier transforms have been utilized in investigating diverse phenomena. From quantum mechanics (Kosloff, 1988) to atmospheric fluid dynamics (Bartello, 2010), they provide accurate results that are supported by experimental data. Their precision for periodic phenomena is well known, as are some of their limitations. Presented here are some additional limitations to Fourier methods in the context of investigating the rotating, stratified, flows of anisotropic domains with viscosity.

The inverse cascade of kinetic energy is a well known characteristic of two-dimensional turbulence. Scaling arguments of Kraichnan (1967) predict the inverse kinetic energy cascades and forward cascade of enstrophy. It was also predicted that a similar cascade of energy occurs in three-dimensional, quasi-geostrophic flows, the limit of strong rotation and stratification (Charney, 1971). Recent analysis shows support for both di-polar and bar end states in randomly forced, periodic, two-dimensional flows with small viscosity (Beck and Wayne, 2012). Bar end states of doubly-periodic domains consist of two opposing jets that wrap around the periodic boundary. Many studies of rotating, stratified fluids have used these arguments to explain the inverse energy cascades seen on planetary scales. Examples of these are seen in the merging of Gulf Stream rings Cresswell (1982) and

the large spot on Jupiter.

Rotating, stratified flows experience two antagonistic effects. First, stemming from strong rotation, is the Taylor-Proudman effect. This effect eliminates the vertical gradients of velocity in constant density fluids with strong rotation, thereby stiffening the fluid in the vertical direction and creating a flow that is effectively two-dimensional (Vallis, 2006). The second, stratification, leads to the decoupling of horizontal layers of fluid. When the vertical shear between layers is strong enough to overcome stratification it can inhibit two-dimensional turbulence (Métais and Herring, 1989). From these two effects, it is found that the aspect ratio of many baroclinic vortices scale as  $H/L \sim f/N$ , where  $H$ ,  $L$ ,  $f$ , and  $N$  are the horizontal length scales, vertical length scales, Coriolis parameter, and Brunt-Väisälä frequency. These two effects have been used to show the presence of an inverse kinetic energy cascade in numerical simulations of rotating, stratified flows with minimal dissipation, such as found on large scales in the stratified ocean.

Numerical studies of quasi-geostrophic and Boussinesq fluids have demonstrated inverse energy cascades in anisotropic, spectral domains of rotating stratified fluids. In McWilliams and Weiss (1994) and McWilliams et al. (1994), a triply-periodic, anisotropic, domain displays large coherent vortices emerging from random initial conditions. Spectrally three-dimensional, Gaussian forcings, around a mean scale, of rotating, stratified, triply-periodic domains also display inverse energy cascades (Métais et al., 1996). Using a similar forcing in a Boussinesq fluid, a similar inverse energy cascade was observed (Smith and Waleffe, 1999, 2002). On the contrary, there is a question as to the effect that vertically periodic boundary conditions have upon an inverse cascade. Dritschel and Macaskill (2000) showed that changing the aspect ratio of the domain in relationship to the number and aspect ratio of initial vortices considerably affects the capacity to form coherent two-dimensional vortices.

In this chapter, as in previous chapters, the domain is periodically forced with available potential energy instead of kinetic energy. This available potential energy

takes the form of a well mixed patch of water within the linearly stratified domain. The relaxation and geostrophic adjustment of these well-mixed patches of water is what delivers kinetic energy to the domain. This process, and the oceanic context in which it could occur, is described in more detail in the Introduction, Chapter 2, and Chapter 3. Previous studies have shown that an inverse cascade of kinetic energy can occur as the rate of forcing is increased Sundermeyer and Lelong (2005). It was hypothesized that non-linear interactions between proximal adjustment vortices precipitated this inverse energy cascade.

The close scrutiny of the inverse energy cascades observed in past viscous simulations of a Boussinesq fluid forms the purpose of the present chapter. Deriving a spectral and non-dimensional form of the Boussinesq Navier Stokes equations with dissipation, differences in vertical Fourier modes to take under consideration are presented. I present select numerical simulations where the evolution of the specified vertical Fourier modes portray the expected inverse energy cascade. By applying a scaled damping to the barotropic mode (zeroth vertical Fourier wavenumber), it is shown that the inverse energy cascade can be arrested.

In the Section 5.2, the Boussinesq equations of motion are non dimensionalized with anisotropic scaling, the numerical model used is reviewed, and a method of barotropic dissipation put up for consideration. In the results, the contributions to the barotropic mode kinetic energy of a single adjustment vortex are presented. These contributions are investigated to show that an accumulation of kinetic energy in the barotropic mode together with an inverse energy cascades of kinetic energy for both low and high frequencies of forcing. When the barotropic dissipation is applied, in both cases, the inverse energy cascade is arrested. Potential implications for other work on rotating, stratified flows is considered and future work is proposed in the discussion. I conclude with a summary of the findings.

## **5.2 Methods**

In the sections below, an anisotropic scaling is performed on the Boussinesq equations of motion. The numerical method used to implement the equations are as

described in Section 2.3 and employed in Chapter 3 and Chapter 4. A review of the hyperviscosity is presented in light of the non-dimensional equations. Finally, a method to damp the accumulating kinetic energy in the barotropic mode is presented. The numerical method is employed on a single adjustment vortex and four simulations with periodically introduced mixing events. The simulations are divided into a low frequency forcing, a high frequency forcing, and both frequencies of forcing with a scaled dissipation to the barotropic mode exclusively.

### 5.2.1 Anisotropic Scaling for Boussinesq Equations of Motion with Laplacian Viscosity

The Boussinesq equations are

$$\frac{\partial \mathbf{u}}{\partial t} + \mathbf{u} \cdot \nabla \mathbf{u} + f \mathbf{e}_3 \times \mathbf{u} = -\frac{1}{\rho_0} \nabla p - g \mathbf{e}_3 \frac{\rho}{\rho_0} + \nu_2 \nabla^2 \mathbf{u} + \nu_6 \nabla^6 \mathbf{u}, \quad (5.1)$$

$$\nabla \cdot \mathbf{u} = 0, \quad (5.2)$$

$$\frac{\partial \rho'}{\partial t} + \mathbf{u} \cdot \nabla \rho' + w \frac{d\bar{\rho}}{dz} = \kappa_2 \nabla^2 \rho' + \kappa_6 \nabla^6 \rho', \quad (5.3)$$

The solution variables are, as in (2.19)-(2.21), the velocity vector  $\mathbf{u}$ , pressure perturbation  $p'$ , and density perturbation  $\rho'$ . The remaining parameters are, also as in Section 2.3, the linear density gradient  $d\bar{\rho}/dz$ , the background density  $\rho_0$ , the Coriolis parameter  $f$ , the gravitational acceleration  $g$ , Laplacian viscosity  $\nu_2$ , sixth-order viscosity  $\nu_6$ , Laplacian diffusivity  $\kappa_2$ , sixth-order diffusivity  $\kappa_6$ , and unit vector in the vertical  $\mathbf{e}_3 = [0, 0, 1]^T$ . Together the above set of equations are the momentum equation (5.1), incompressibility condition (5.2), and the advection diffusion equation for density (5.3). The pressure and density perturbations are obtained by removing components related to hydrostatic balance,  $\frac{d\bar{p}(z)}{dz} = -g\bar{\rho}(z)$ , where  $\bar{p}$  and  $\bar{\rho}$  are linearly varying pressure and density.

Using the anisotropic scaling of both length scales and velocity scales ( $L/H \sim N/f$  and  $U/W \sim N/f$  where  $L$ ,  $H$ ,  $U$ , and  $W$  represent horizontal length scale,

vertical length scale, horizontal velocity scale, and vertical velocity scale), as in McWilliams and Weiss (1994), and the following scalings,

$$t = \frac{L}{U} t^\dagger, \quad (5.4)$$

$$p' = U^2 \rho_0 p^\dagger, \quad (5.5)$$

$$\rho' = H \frac{d\bar{\rho}(z)}{dz} \rho^\dagger, \quad (5.6)$$

for time, pressure perturbation, and density perturbation, the non-dimensionalized form of (5.1) is

$$\begin{aligned} \frac{\partial \mathbf{u}}{\partial t} + \mathbf{u} \cdot \nabla \mathbf{u} + \frac{fL}{U} \mathbf{e}_3 \times \mathbf{u} = & -\mathbf{A}^2 \left[ \nabla p' - \mathbf{e}_3 \left( \frac{U}{NH} \right)^{-2} \rho' \right] \\ & + \frac{\nu_2}{UL} (\mathbf{A} \nabla)^2 \mathbf{u} \\ & + \frac{\nu_6}{UL^5} (\mathbf{A} \nabla)^6 \mathbf{u}, \end{aligned} \quad (5.7)$$

where,

$$\mathbf{A} = \begin{bmatrix} 1 & 0 & 0 \\ 0 & 1 & 0 \\ 0 & 0 & (N/f) \end{bmatrix}, \quad (5.8)$$

$$(\mathbf{A} \nabla)^2 = (\mathbf{A} \nabla) \cdot (\mathbf{A} \nabla), \quad (5.9)$$

and all variables are in their non-dimensional forms. With the non-dimensional numbers,

$$Ro = \frac{U}{fL} \text{ (Rossby)}, \quad (5.10)$$

$$Fr = \frac{U}{NH} \text{ (Froude)}, \quad (5.11)$$

$$Re_2 = \frac{UL}{\nu_2} \text{ (second order Reynolds)}, \quad (5.12)$$

$$Re_6 = \frac{UL^5}{\nu_6} \text{ (sixth order Reynolds)}, \quad (5.13)$$

the Fourier transform of (5.7) becomes,

$$\frac{\partial \hat{\mathbf{u}}_k}{\partial t} - T_k + Ro^{-1} \mathbf{e}_3 \times \hat{\mathbf{u}}_k = \mathbf{A}^2 \left[ -\frac{i\mathbf{k}}{\rho_0} \hat{p}'_k + Fr^{-2} \mathbf{e}_3 \hat{\rho}'_k \right] - \frac{1}{2} \mathbb{D}_k \hat{\mathbf{u}}_k, \quad (5.14)$$

with

$$T_k = -(\widehat{\mathbf{u} \cdot \nabla \mathbf{u}})_k, \quad (5.15)$$

$$\mathbb{D}_k = \frac{2}{Re_2} |\mathbf{A}\mathbf{k}|^2 + \frac{2}{Re_6} |\mathbf{A}\mathbf{k}|^6, \quad (5.16)$$

where  $T_k$  is the Fourier transform of the nonlinear term and  $\mathbb{D}_k$  is the spectral dissipation operator. The sixth-order component of spectral dissipation operator  $\mathbb{D}_k$  is updated in Section 5.2.2 to dissipate kinetic energy at selected maximum wavenumbers in each direction with the same rate of decay.

With the spectral form of the incompressibility constraint ( $\mathbf{k} \cdot \hat{\mathbf{u}}_k = 0$ ), the spectral Poisson problem for pressure is solved,

$$\hat{p}_k = \frac{i\mathbf{k}}{|\mathbf{A}\mathbf{k}|^2} \cdot \left( \frac{1}{Ro} \mathbf{e}_3 \times \hat{\mathbf{u}}_k - Fr^{-2} \mathbf{A}^2 \mathbf{e}_3 \hat{\rho}_k - T_k \right). \quad (5.17)$$

Next, to obtain the full spectral, kinetic energy equations, the inner product of (5.14) with the conjugate of the spectral velocity vector,  $\hat{\mathbf{u}}_k^*$ , is taken and the inner product of the velocity vector is taken with the conjugate of (5.14). Finally, adding these products together results in the spectral kinetic energy equations,

$$\frac{\partial |\hat{\mathbf{u}}_k|^2}{\partial t} = \mathbb{T}_k - \mathbb{D}_k |\hat{\mathbf{u}}_k|^2, \quad (5.18)$$

where,

$$\mathbb{T}_k = \hat{\mathbf{u}}_k^* \cdot (T_k - i\mathbf{A}^2 \mathbf{k} \hat{p}_k + Fr^{-2} \mathbf{A}^2 \mathbf{e}_3 \hat{\rho}_k) + c.c., \quad (5.19)$$

where *c.c.* is the complex conjugate of the previous term. The Coriolis term has

been removed by complementary cancellation. This is understandable since it does not add or remove kinetic energy to the domain.

From this point, the differences between the non-dimensional, spectral kinetic energy equations of the baroclinic and barotropic modes in the anisotropic domain are investigated. The baroclinic modes have a nonzero vertical component to the wavenumber vectors ( $\mathbf{k}_{bc} = [k, l, m]^T$ ,  $m \neq 0$ ) where the barotropic terms have a zero vertical component to all wavenumber vectors ( $\mathbf{k}_{bt} = [k, l, 0]^T$ ). This difference in wavenumber vectors affect each term of the non-dimensionalized spectral kinetic energy equation (5.18). Each of these differences are examined in turn.

To begin, the spectral dissipation operator (5.16) and its effect on the evolution of the kinetic energy are examined. To do this, for the moment neglecting  $\mathbb{T}_k$  in (5.18), and reducing the spectral energy evolution equation to an energy diffusion equation,

$$\frac{\partial |\hat{\mathbf{u}}_k|^2}{\partial t} = \mathbb{D}_k |\hat{\mathbf{u}}_k|^2, \quad (5.20)$$

which has solution

$$|\hat{\mathbf{u}}_k(t)|^2 = |\hat{\mathbf{u}}_k(0)|^2 \exp \{-\mathbb{D}_k t\}, \quad (5.21)$$

giving an e-folding dissipation time of

$$\mathcal{T}_k = \frac{1}{\mathbb{D}_k}, \quad (5.22)$$

for wavenumber vector  $\mathbf{k} = [k, l, m]^T$ . Using the full version of the spectral diffusion operator (5.16) for baroclinic wavenumber  $\mathbf{k}_{bc} = [k_1, 0, m_1]^T$ , with  $k_1 = m_1 = 2\pi$  being the smallest non-zero, dimensionless, horizontal and vertical wavenum-

bers for isotropic, dimensionless domain, the e-folding dissipation timescale is

$$\begin{aligned}
\mathcal{T}_{k_{bc}} &= \frac{1}{2Re_2^{-1}(k_1^2 + (N/f)^2 m_1^2) + 2Re_6^{-1}(k_1^2 + (N/f)^2 m_1^2)^3} \\
&= \frac{1}{2Re_2^{-1}(k_1^2 + (N/f)^2 k_1^2) + 2Re_6^{-1}(k_1^2 + (N/f)^2 k_1^2)^3} \\
&= \frac{1}{2Re_2^{-1}(1 + (N/f)^2)k_1^2 + 2Re_6^{-1}(1 + (N/f)^2)^3 k_1^6}. \tag{5.23}
\end{aligned}$$

This yields the dissipation times for the smallest non-zero, baroclinic wavenumber. Depending on the Reynolds numbers,  $Re_2$  and  $Re_6$ , the hyper-viscous term usually becomes much less influential at larger scales than the Laplacian viscous term, yielding dissipation times that can be compared to the smallest, non-zero, barotropic wavenumbers,

$$\begin{aligned}
\mathcal{T}_{k_{bc}} &= \frac{1}{2Re_2^{-1}(1 + (N/f)^2)k_1^2} \\
&= \frac{1}{1 + (N/f)^2} \mathcal{T}_{k_{bt}}. \tag{5.24}
\end{aligned}$$

Depending on the anisotropy of the domain, kinetic energy in the largest baroclinic mode dissipates at a rate of  $1 + (N/f)^2$  faster than its barotropic counterpart. For typical  $N/f = 100$  this represents a four order of magnitude difference. If an  $N/f = 10$  scaling is used, this difference is reduced to two orders of magnitude. However, as reviewed in the discussion, this is not without consequences. Alternatively, if the hyper-viscous terms remain dominant, then a similar analysis follows, but with a difference of  $1 + (N/f)^6$  in dissipation times between large baroclinic and barotropic wavenumbers.

Next, the components of the energy transfer function (5.19) are addressed in turn. Those components are non-dimensional forms of the pressure term (5.17), the buoyancy flux term ( $Fr^{-2} \mathbf{A}^2 \mathbf{e}_3 \hat{\rho}_k$ ), and the nonlinear term (5.15). The spectral pressure term involves the dot product with a wavenumber vector, leading to the elimination of all vertical components of the spectral pressure in the barotropic mode, including the buoyancy term and the vertical component of the nonlinear

term. Simply put, the barotropic perturbation pressure is vertically invariant, contributes nothing to the vertical velocity component, and depends exclusively upon the horizontal velocity.

The next component of the kinetic energy transfer term is the buoyancy flux term  $Fr^{-2}\mathbf{A}^2\mathbf{e}_3\hat{\rho}_k$ . It is noted that the density perturbation, as is the pressure and vertical length scale, is stretched by  $(N/f)^2$ . The buoyancy flux term, as with any other barotropic variable, is vertically invariant. The barotropic density perturbation is only non-zero when the density is no longer stably stratified. With the density stratification assumed to stay stable during the simulations the contribution of this term to the barotropic vertical velocity is zero.

The last component of the energy transfer term to investigate for differences is the non-linear term (5.15). Using a convolution sum for the transfer terms,

$$T_k = \sum_{\mathbf{p}} \hat{\mathbf{u}}_p \cdot \nabla \hat{\mathbf{u}}_{k-p} \quad (5.25)$$

$$= \sum_{\mathbf{p}} \hat{\mathbf{u}}_p \cdot (\mathbf{k} - \mathbf{p}) \hat{\mathbf{u}}_{k-p}. \quad (5.26)$$

The importance of the non-dimensional form is that there is locality in the non-dimensionally isotropic wavenumber space. The relative importance of this term, in the pressure term as well as in the energy equation, is determined by the size of the local Rossby number. This is the only term that can provide forcing for the barotropic mode kinetic energy.

Further differences between the baroclinic and barotropic modes arise from the two-dimensionality of the barotropic mode. All quantities (velocity, pressure, and density) are vertically invariant. For the barotropic mode velocity, the divergence free condition is restricted to the horizontal components,  $\mathbf{k}_{bt} \cdot \mathbf{u}_{k_{bt}} = ku_{k_{bt}} + lv_{k_{bt}} = 0$ . Though this does not exclude vertical velocity in the barotropic mode, or even horizontal variance in the vertical velocity, the lack of forcing in a stably stratified domain make the barotropic vertical velocity zero.

In summary, there are definite differences between the evolution of kinetic energy in the baroclinic and barotropic modes of a strongly anisotropic domain.

If Laplacian viscosity is present, it is more prevalent for the baroclinic modes than the barotropic modes. Unless otherwise adjusted, this effect is also seen in the hyper-viscous term. This is the main difference between isotropic and anisotropic domains that have been spectrally modeled. The pressure term of the barotropic mode arises purely from its need to balance the velocity terms, and not from variations in density. Differences in pressure and density are not limited to anisotropic domains. The only term that can contribute to kinetic energy in the barotropic mode is the nonlinear term (5.15) of the Boussinesq Navier Stokes equation.

### 5.2.2 Hyperviscosity

The methods of hyperviscosity are employed in numerical simulations, as in Section 2.3. However, some details are refined here that provide a representation consistent with the derivation above. The sixth-order hyperviscosity operator is

$$\mathbb{D}_k^{(6)} = \nu'_6 \left[ \left( \frac{k}{k_{max}} \right)^2 + \left( \frac{l}{l_{max}} \right)^2 + \left( \frac{m}{m_{max}} \right)^2 \right]^3, \quad (5.27)$$

where the exponent of (6) on the operator pertains to the order of the dissipation operator and the  $\nu'_6$  parameter represents the inverse dissipation timescale (1/s) at the maximum wavenumbers. Assuming horizontal isotropy,  $k_{max} = l_{max}$ , the horizontal terms are integrated into the viscosity parameter,

$$\mathbb{D}_k^{(6)} = \nu_6 \left[ k^2 + l^2 + \left( \frac{k_{max}}{m_{max}} m \right)^2 \right]^3, \quad (5.28)$$

where  $\nu_6 = \nu'_6/k_{max}^6$  now has the appropriate units ( $m^6 s^{-1}$ ).

Upon review, one quickly notices that the above produces a different hyperviscosity than implied by the dissipation operator in the non-dimensional equations (5.16). Due to the scaling of the numerical domain  $L/H = 40$  and the resolution  $n_x/n_z = 2$ , this changes the effective hyper-dissipation in the vertical direction for

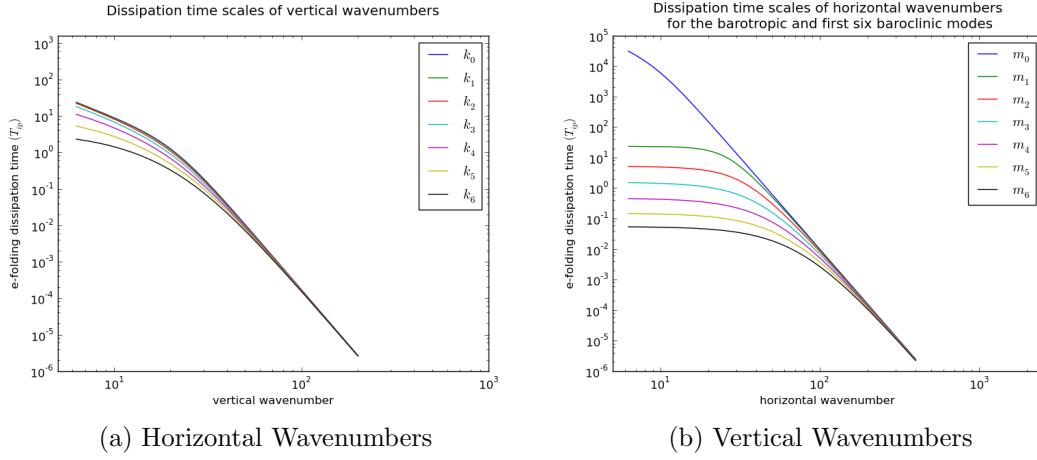


Figure 5.1: E-folding dissipation time scale for kinetic energy at various vertical wavenumbers for given horizontal wavenumber (a) and horizontal wavenumbers for given vertical wavenumber (b). This shows that vertical dissipation dominates horizontal dissipation (a) and that the barotropic mode,  $m_0$ , dissipates kinetic energy four orders of magnitude slower than the first baroclinic mode (b).

the dimensionless equations,

$$\mathbb{D}_k^{(6)} = \nu_6 \left[ k^2 + l^2 + (N/f)^2 \left( \frac{k_{max}}{m_{max}} m \right)^2 \right]^3. \quad (5.29)$$

This amounts to replacing the matrix  $\mathbf{A}$  (5.16) by another matrix,

$$\mathbf{B} = \begin{bmatrix} 1 & 0 & 0 \\ 0 & 1 & 0 \\ 0 & 0 & \frac{1}{2} \end{bmatrix}, \quad (5.30)$$

creating a near isotropic hyper-dissipation parameter for the spectral equation. Without this adjustment, the hyperviscosity would dominate in the vertical spectrum and be barely effective in the horizontal. Allowing for the near isotropy in the hyper-viscosity permits only the first few wavenumbers in each direction to be subject to Laplacian viscosity (Figure 5.1). The value of the hyperviscosity, definition of maximum wavenumber, and the power of the operator can be used to make further refinements to this range.

### 5.2.3 Barotropic Dissipation

The solution for the dimensionless spectral diffusion equation shows us that dissipation timescales are at least two orders of magnitude longer for largest baroclinic scales than for comparative barotropic scales. As is seen, this leads to the accumulation of kinetic energy in the barotropic scales for continuously forced, triply periodic domains that are balanced by dissipation.

The finite periodic domains attempt to emulate a domain with unbounded height in the barotropic mode. It is possible to model the dissipation at the barotropic mode as if it were the first baroclinic mode of a domain twice as high. Implementing this would give a scale appropriate dissipation for the barotropic mode, rather than treating it as fluid at an unbounded vertical extent. Continuity in the wavenumber spectrum near zero would normally imply an unbounded domain (Trefethen, 2000). Though the domain is not unbounded, this idea is used to propose a scaled dissipation for the barotropic mode. The spectral energy diffusion equation for the smallest non-zero, discrete, vertical wavenumber  $m_1$  is:

$$|\hat{u}|_t^2 = -2\nu m_1^2 |\hat{u}|^2. \quad (5.31)$$

It is easy to represent the dissipation at the barotropic mode with a wavenumber of  $m_1/2$ . This gives the barotropic diffusion equation of

$$\begin{aligned} |\hat{u}|_t^2 &= -4\nu \left(\frac{m_1}{2}\right)^2 |\hat{u}|^2 \\ &= -\nu m_1^2 |\hat{u}|^2 \end{aligned} \quad (5.32)$$

where the contributions from positive and negative wavenumbers are taken into account (5.32).

## 5.3 Results

Five numerical simulations are investigated. First, the adjustment of a single mixed patch is examined in a viscous, rotating, stratified domain. This demon-

strates the effects of mode differential dissipation on a single adjustment vortex. Next, numerical simulations are performed with both low and high forcing rates. Finally, the above barotropic dissipation technique is applied to these latter two simulations.

### 5.3.1 *Single Adjustment Vortex*

A single adjustment vortex in a viscous domain is seen to dissipate before any instabilities can occur and change the characteristics of the flow. By contrast, with viscosity reduced by at least an order of magnitude, instabilities become apparent under proper conditions (See Appendix B).

With an adjustment vortex presented into a viscous domain, the adjustment process distributes kinetic energy into various vertical modes. The barotropic mode is forced exclusively by the non-linear term (5.15), which delivers the kinetic energy that is delivered to the baroclinic modes from the buoyancy flux term ( $Fr^{-2}\mathbf{A}^2\mathbf{e}_3\hat{\rho}_k$ ). After kinetic energy is delivered to the barotropic mode it is dissipated at least two orders of magnitude slower than kinetic energy in the baroclinic modes for the  $N/f$ -scaled domain. A physical explanation for this effect is the slumping portion of the adjustment processes is experienced throughout the vertical extent of the periodic domain. These effects are apparent in the time evolution in the first seven modes of the horizontally averaged vertical spectrum (Figure 5.2). The barotropic mode does not visibly decay over the duration of the simulation, whereas the remaining six vertical modes shown have kinetic energy reduced from two to fourteen orders of magnitude. Side view snapshots of vorticity show the detectable evolution to a predominantly barotropic vortex by  $100 T_{ip}$  (Figure 5.3). The velocities of the adjustment vortex peak at 0.002 m/s during adjustment and decay to  $2 \times 10^{-5}$  m/s at  $100 T_{ip}$ .

### 5.3.2 *Persistent Periodic Forcing*

For persistent and periodic forcing by parametrically induced mixing events, simulations of both low and high rates of forcing are presented. In the first, mixing

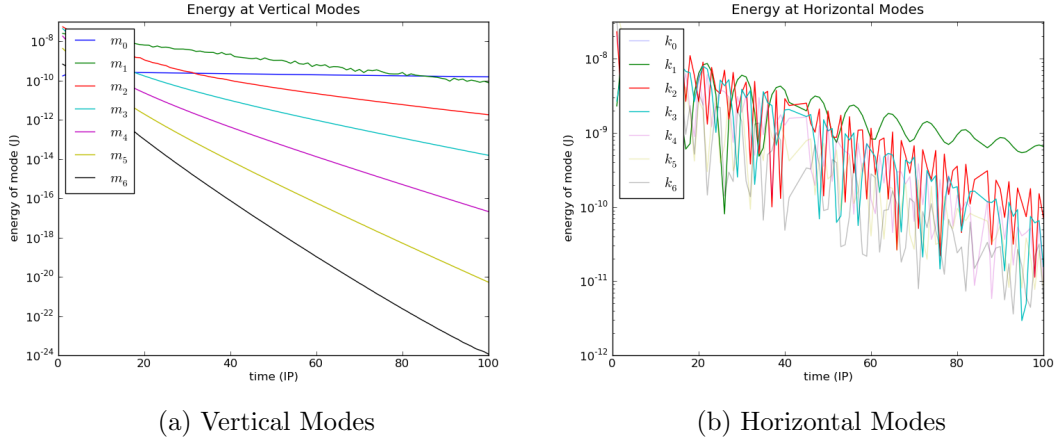


Figure 5.2: Evolution of vertical and horizontal energy by mode number for a single adjustment vortex. For the vertical modes (a), the barotropic mode  $m_0$  shows no appreciable decay over the runtime of the simulation. The first three non-zero modes of (b) are emphasized by dimming the plots of the remaining horizontal wavenumbers.

events are introduced once per inertial period. For the second, mixing events are introduced at a rate of forty per inertial period. In both simulations, the accumulation of barotropic mode kinetic energy and an inverse cascade of kinetic energy is seen.

In the low forcing frequency simulation,  $\tau = 1.0 T_{ip}$ , the domain averaged kinetic energy attains near equilibrium after  $100 T_{ip}$  (Figure 5.4), after which it grows about four percent by the end of the simulation. Investigating the evolution of the first seven modes of the horizontally averaged, vertical kinetic energy spectrum, most of this growth is accounted for in the undissipated accumulation of barotropic mode kinetic energy (Figure 5.5a). As this only accounts for about four percent of the total energy, it does not visibly affect the largest modes of the vertically averaged horizontal spectrum (Figure 5.5b). And, unlike the next simulation, the influence of the barotropic mode kinetic energy is subtle.

To see the subtle influences of the barotropic mode, the vertically averaged (barotropic) vorticity and the horizontal kinetic energy spectrum of the barotropic and baroclinic modes are investigated. Plan views of the barotropic vorticity,

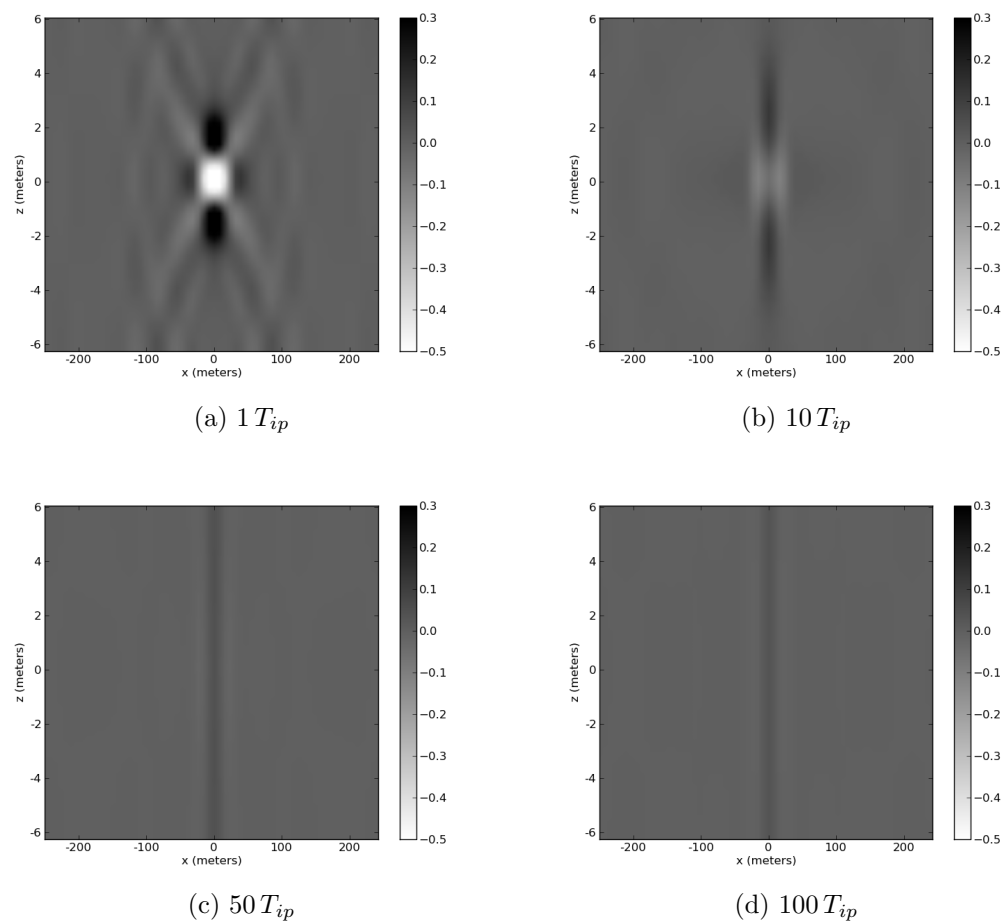


Figure 5.3: Evolution of vorticity for a single adjustment vortex, side view. By  $20 T_{ip}$  (not shown) the cyclones have visibly connected across the vertically periodic boundary. Vorticity is scaled by the Coriolis parameter  $f$ .

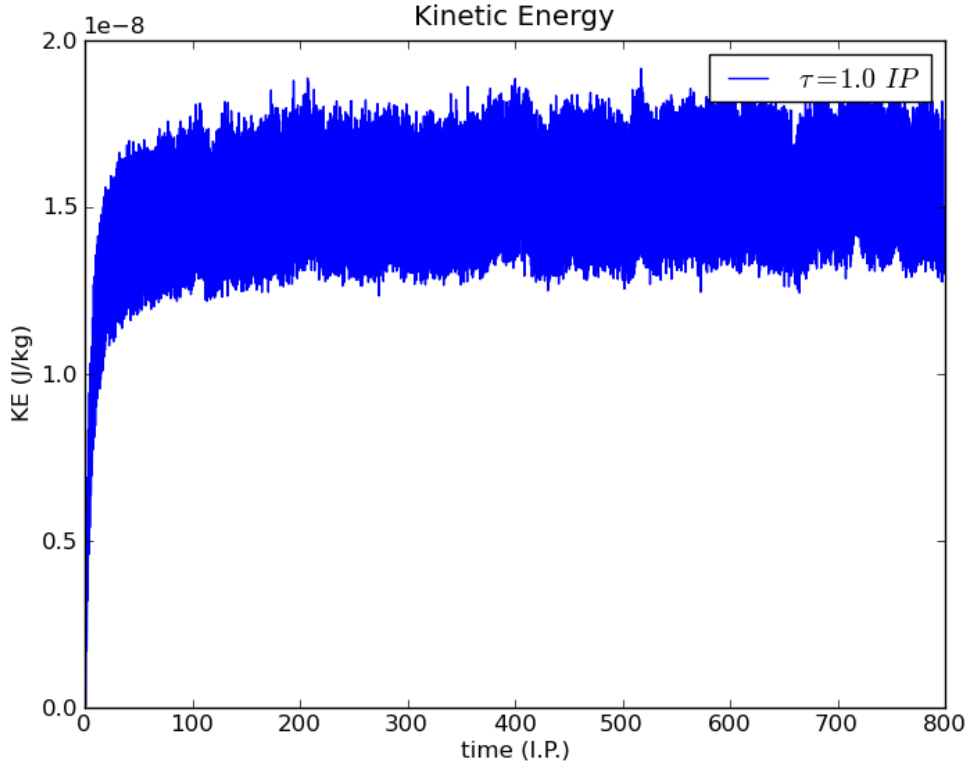


Figure 5.4: Evolution of the domain averaged kinetic energy for  $\tau = 1.0 T_{ip}$  waiting time between adjustment events.

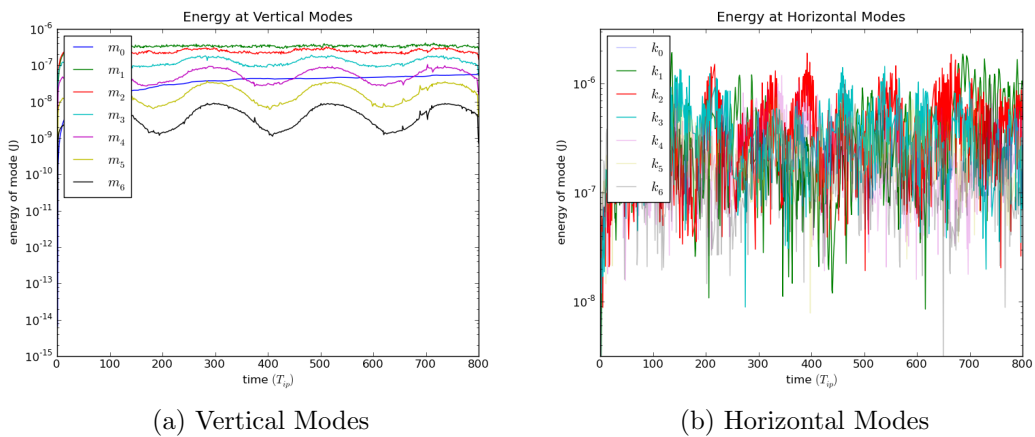


Figure 5.5: Semi-log plots of the horizontally averaged kinetic energy in the barotropic mode,  $m_0$ , and first six baroclinic modes,  $m_1$  to  $m_6$ , (a) and the vertically averaged kinetic energy in the first seven horizontal modes,  $k_0$  to  $k_6$  (b) of the  $\tau = 1.0 T_{ip}$  simulation. The first three non-zero modes of (b) are emphasized by dimming the plots of the remaining horizontal wavenumbers.

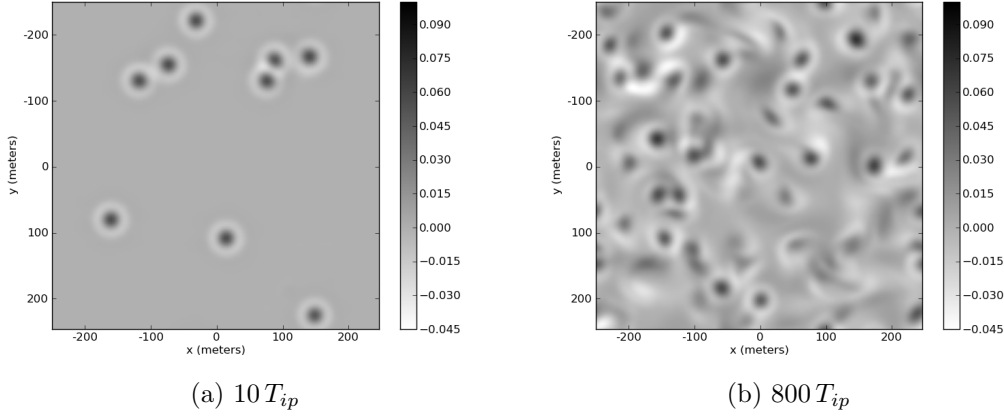


Figure 5.6: Views of the barotropic mode vertical vorticity scaled by the Coriolis parameter,  $f$ , for early (a) and later (b) times of the  $\tau = 1.0 T_{ip}$  simulation.

scaled by  $f$ , show distinct differences between early and late times of the simulation (Figure 5.6). At early times, many distinct, barotropic vortices can be seen with radii close to 25 m. At later times, there are a few vortices that are larger than the forcing scale of the vortices. The horizontal kinetic energy spectrum of the barotropic mode shows a steady increase in scales of energy that are larger than the scale of forcing (Figure 5.7). The scale of the forcing can be seen at  $2 T_{ip}$  in the figure after two forcings. This is a clear indication that there is an inverse energy cascade in the barotropic mode kinetic energy of the simulation with relatively low forcing frequency. However, the first baroclinic mode, along with all other baroclinic modes, do not exhibit the same behavior (Figure 5.8). The horizontal kinetic energy spectrum of the first baroclinic mode shows near equilibration after  $50 T_{ip}$ , with little overall growth in kinetic energy in large scales thereafter.

The second numeric simulation is forced at a rate of forty mixing events per inertial period, or  $\tau = 0.025 T_{ip}$ . Unlike the low forcing simulation, the kinetic energy does not equilibrate at any time during the simulation (Figure 5.9). Again, using the evolution of the first seven modes of the averaged vertical spectrum, the barotropic mode is observed to contain most of this unequilibrated kinetic energy (Figure 5.10a). Likewise, the dominance of the largest horizontal wavenumber

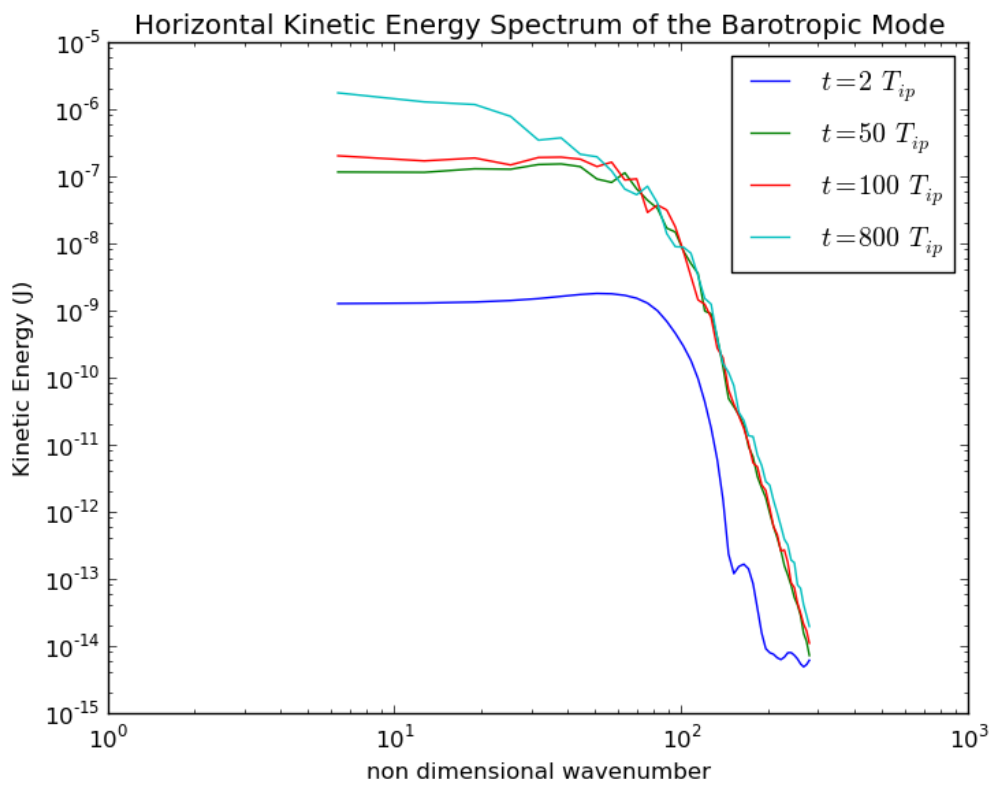


Figure 5.7: Horizontal spectrum of barotropic mode kinetic energy for  $\tau = 1.0 T_{ip}$  case at various times throughout simulation. Later times ( $106 T_{ip}$ ,  $800 T_{ip}$ ), show definite growth in large scale energy over earlier times. The scale of the forcing can be seen after two forcings at  $2 T_{ip}$ .

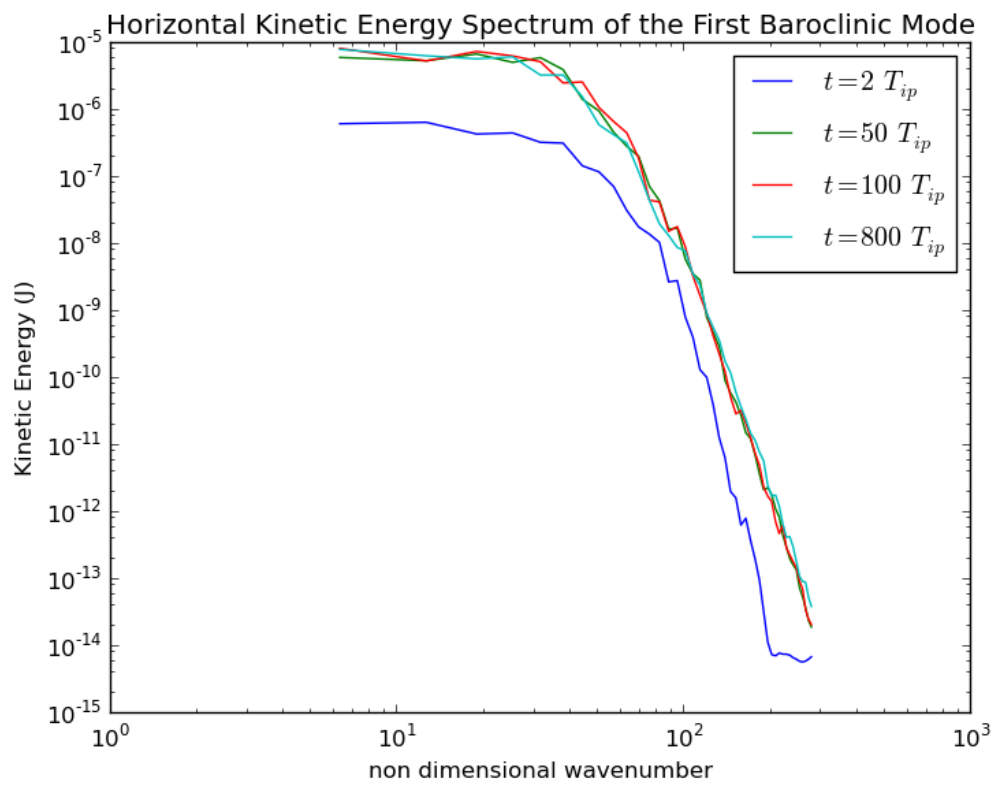


Figure 5.8: Horizontal spectrum of first baroclinic mode kinetic energy for  $\tau = 1.0 T_{ip}$  case at various times throughout simulation. The scales of first baroclinic mode kinetic energy are nearly equilibrated after  $50 T_{ip}$ .

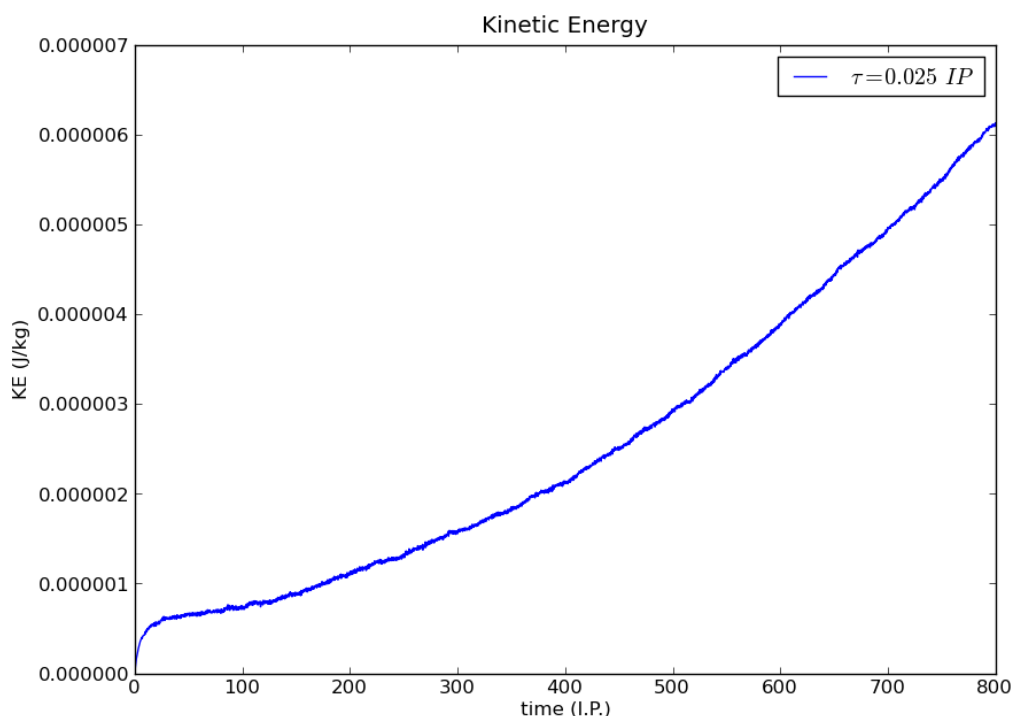


Figure 5.9: Evolution of the domain-averaged kinetic energy for  $\tau = 0.025 T_{ip}$  waiting time between adjustment events.

is observed in the evolution of the first seven modes of the vertically averaged horizontal spectrum (Figure 5.10b). The inverse energy cascade is apparent in plan view plots of the vorticity through the center of the numerical domain (Figure 5.11). In early times, there are many vortices of small size, but at late times there are two counter-rotating vortices that dominate the domain. These two vortices fill the entire vertical extent of the modeled domain. The end velocities of this simulation were approximately 0.01 m/s with vortex radii of approximately 125 m. Furthermore, log-log plots of horizontal kinetic energy spectrum for both barotropic and first baroclinic modes show similar behavior as above (Figures 5.12, 5.13). The barotropic mode kinetic energy experiences growth at large scales while the first baroclinic mode kinetic energy is nearly equilibrated after  $50 T_{ip}$ . The first baroclinic spectrum is reduced to levels lower than at  $50 T_{ip}$  at the end of the simulation, despite high rates of forcing.

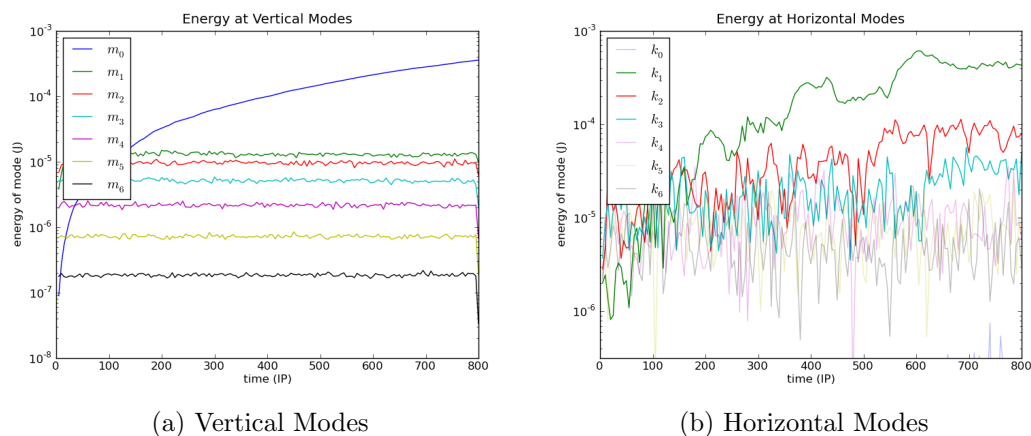


Figure 5.10: Semi-log plots of the horizontally averaged kinetic energy in the barotropic mode,  $m_0$ , and first six baroclinic modes,  $m_1$  to  $m_6$ , (a) and the vertically averaged kinetic energy in the first seven horizontal modes,  $k_0$  to  $k_6$  (b) of the  $\tau = 0.025 T_{ip}$  simulation. The first three non-zero modes of (b) are emphasized by dimming the plots of the remaining horizontal wavenumbers.

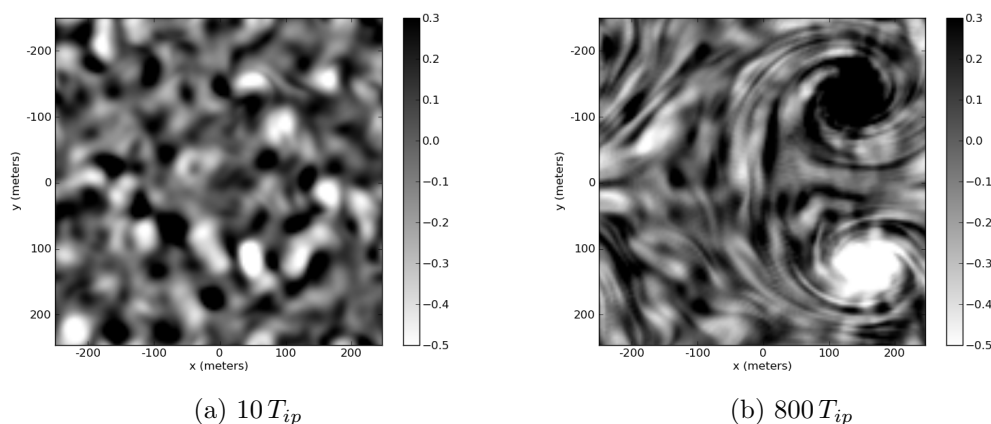


Figure 5.11: Plan views of the vertical vorticity at mid depth, scaled by  $f$ , of the  $\tau = 0.025 T_{ip}$  simulation for early (a) and late (b) times. Much of the vorticity for the late times is vertically invariant.

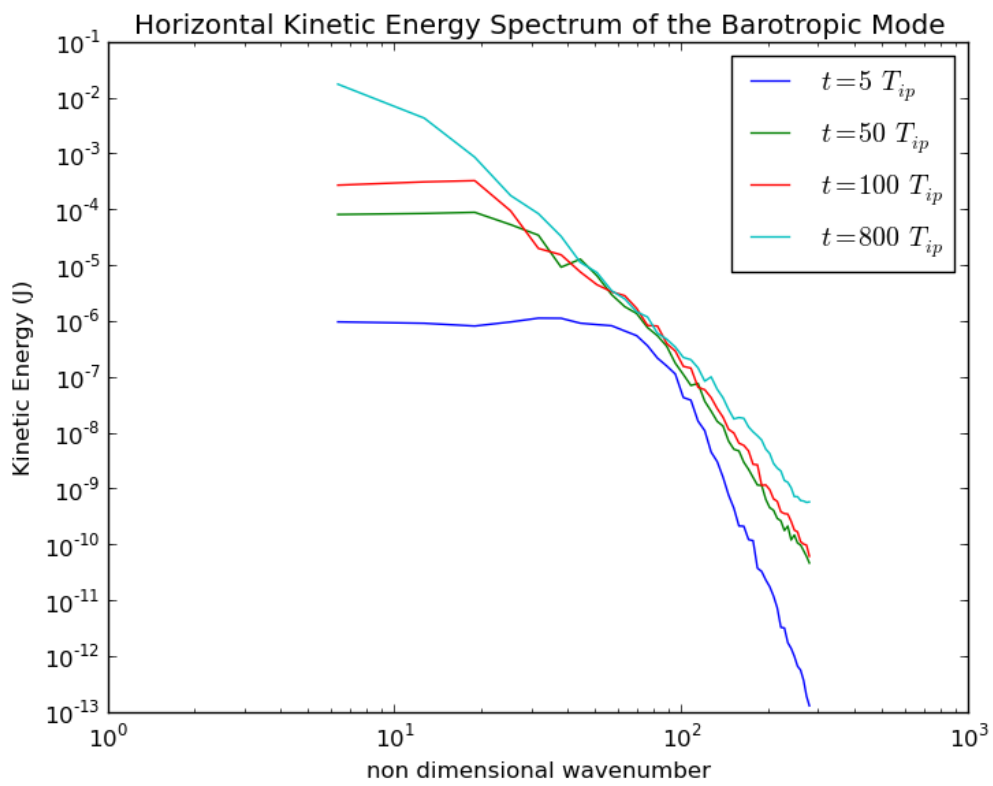


Figure 5.12: Horizontal spectrum of barotropic mode kinetic energy for  $\tau = 0.025 T_{ip}$  case at various times throughout simulation. Growth of kinetic energy at large scales is an indication of an inverse energy cascade.

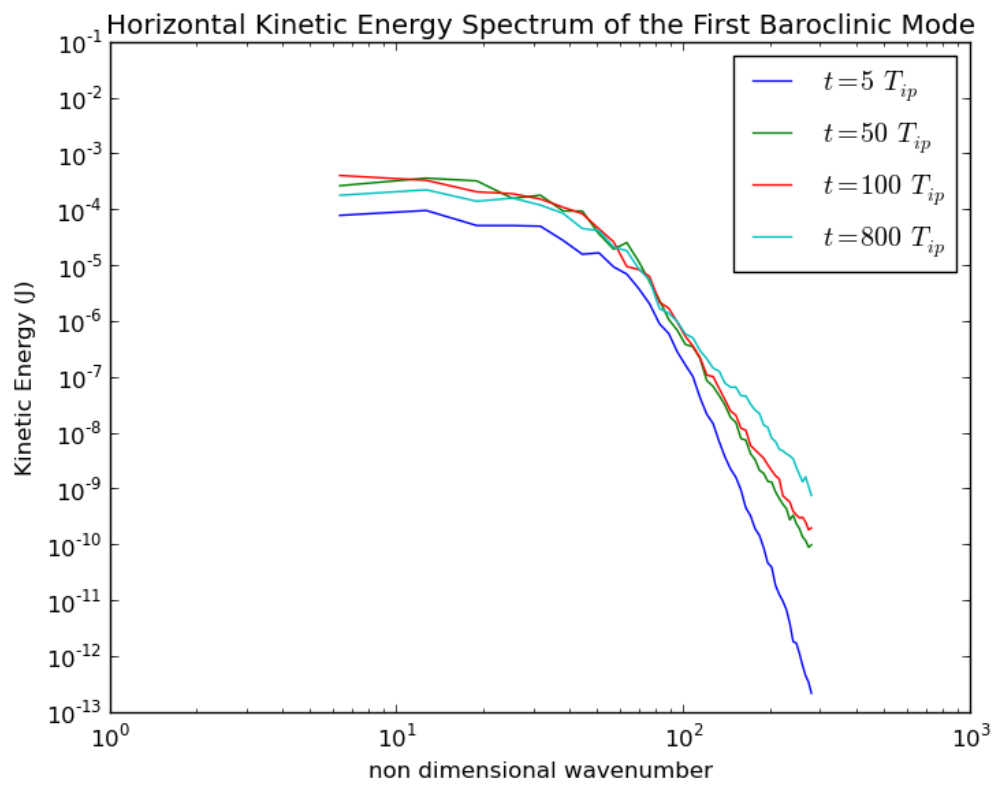


Figure 5.13: Horizontal spectrum of first baroclinic mode kinetic energy for  $\tau = 0.025 T_{ip}$  case at various times throughout simulation. The kinetic energy of the first baroclinic mode shows little variation in scale after  $50 T_{ip}$ .

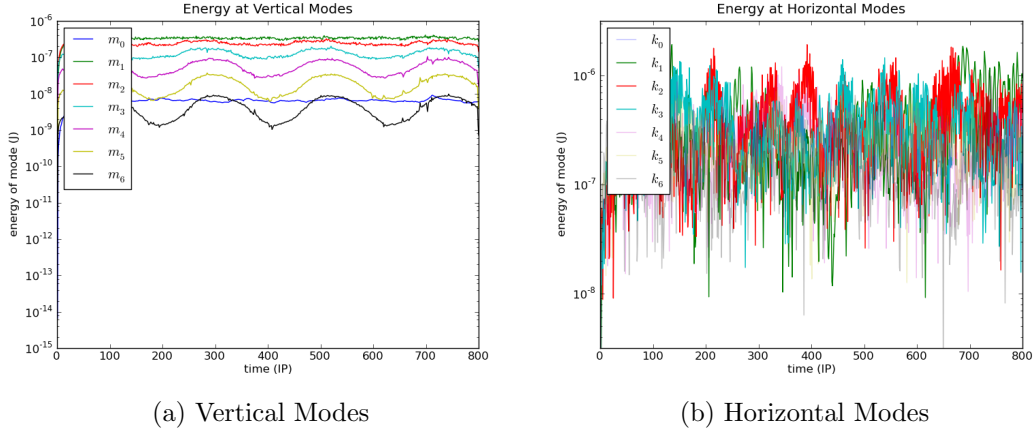


Figure 5.14: Semi-log plots of the horizontally averaged kinetic energy in the barotropic mode,  $m_0$ , and first six baroclinic modes,  $m_1$  to  $m_6$ , (a) and the vertically averaged kinetic energy in the first seven horizontal modes,  $k_0$  to  $k_6$  (b) of the  $\tau = 1.0 T_{ip}$  simulation with scaled barotropic dissipation. The first three non-zero modes of (b) are emphasized by dimming the plots of the remaining horizontal wavenumbers.

Next, applying the scaled barotropic dissipation to the low frequency simulation ( $\tau = 1.0 T_{ip}$ ), definite changes are noticed. The domain averaged kinetic energy no longer grows after equilibration. This simulation has only four percent less total kinetic energy than the simulation without barotropic dissipation at the conclusion of both. These differences are apparent in depictions of the vertical spectrum evolution. The barotropic mode kinetic energy does not accumulate over the entire simulation (Figure 5.14a). Unlike the high frequency simulation, this difference is not detectable in the evolution of the first seven modes of the averaged horizontal spectrum (Figure 5.14b).

Finally, applying scaled barotropic dissipation to the high frequency simulation, the differences are even more striking. The domain averaged kinetic energy equilibrates over the course of the simulation (Figure 5.15), with equilibration of the barotropic mode kinetic energy accounting for almost all of this change (Figure 5.16a). Without this build-up in barotropic mode kinetic energy there is an equilibration in the horizontal modes (Figure 5.16b). Maximum velocities of this

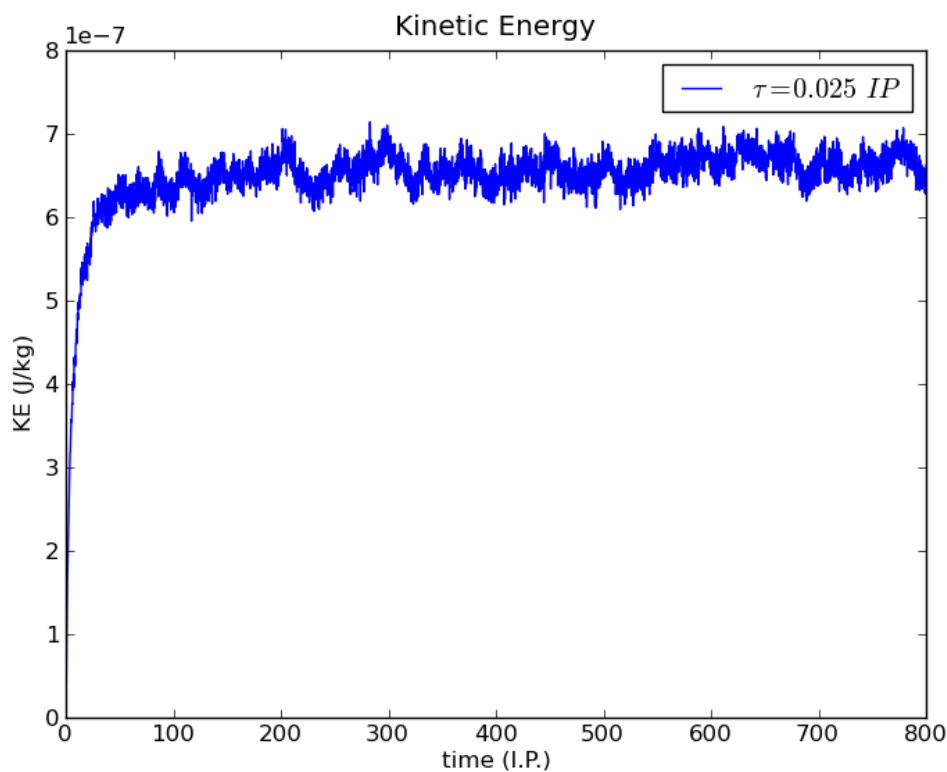


Figure 5.15: Evolution of the domained averaged kinetic energy for  $\tau = 0.025 T_{ip}$  waiting time between adjustment events with scaled barotropic dissipation.

simulation are only approximately 0.003 m/s.

#### 5.4 Discussion

For spectrally modeled, Boussinesq fluids with viscosity in an anisotropic domain, non-dimensional equations that predict large differences in dissipation between the baroclinic and barotropic modes are derived. These differences are shown to have an effect upon the evolution of vortices in a computational model. Presented is the evolution of a single adjustment vortex, low frequency forcings of mixing events, and high frequency forcings that result in an inverse energy cascade in the barotropic mode. Using a scaled barotropic dissipation, this effect can be addressed and an inverse energy cascade arrested.

The non-dimensional equations show kinetic energy enters into the barotropic

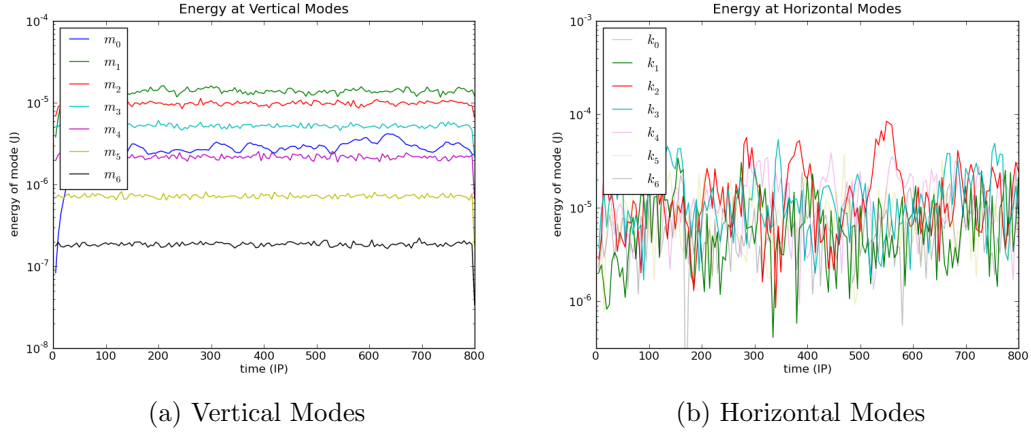


Figure 5.16: Semi-log plots of the horizontally averaged kinetic energy in the barotropic mode,  $m_0$ , and first six baroclinic modes,  $m_1$  to  $m_6$ , (a) and the vertically averaged kinetic energy in the first seven horizontal modes,  $k_0$  to  $k_6$  (b) of the  $\tau = 0.025 T_{ip}$  simulation with scaled barotropic dissipation. The first three non-zero modes of (b) are emphasized by dimming the plots of the remaining horizontal wavenumbers.

mode exclusively through the non-linear interactions (5.15) in a stably stratified fluid. Furthermore, the spectral dissipation operator is demonstrated to damp kinetic energy in the barotropic mode proportionately weaker than in the baroclinic modes. For the adjustment of a single mixing event in a viscous numeric simulation, it is demonstrated that the barotropic mode kinetic energy, though weak, decays at a much slower rate than all baroclinic modes. When simulations are persistently and periodically forced, the barotropic mode accumulates the kinetic energy of each adjustment. The total amount of kinetic energy in the barotropic mode is directly related to the contributions of each adjustment, the contributions of overlapping forcings, additional gains or losses from the non-linear term, and losses from the dissipation of barotropic horizontal scales. Although the dissipation rates in these simulations do not allow the full evolution of the non-linear interactions seen in Chapter 3, the initial phases of these non-linear interactions may deliver kinetic energy to the barotropic mode. In the above numerical simulations, the lack of equilibration of the kinetic energy is exclusively due to the

undissipated accumulation of kinetic energy in the barotropic mode. Simulations with a high rate of forcing accumulate enough kinetic energy in the barotropic mode to participate in an inverse energy cascade. Even though weak, the accumulating barotropic mode kinetic energy in simulations with lower forcing frequencies has been shown to strongly affect the dispersal of a passive tracer (see Chapter 4).

With single adjustment vortices having velocities  $U \sim 0.002$  m/s and radius  $r = 25$  m, the Laplacian Reynolds number is,  $Re_2 = UL/\nu \sim 2,000$ . This is below the Reynolds numbers usually considered turbulent,  $Re \sim 10,000$  (Pope, 2000). Using the non-dimensional equations and the anisotropic scaling for the vertical dissipation this is further reduced to  $(f/N)^2 Re_2 = 20$ . With the final velocities for the simulation with high forcing frequency being  $U \sim 0.01$  m/s and vortex radii of  $r \sim 125$  m the Reynolds number increases to  $Re_2 \sim 50,000$ , being well in the range expected for turbulence, albeit two dimensional. These scaled Reynolds numbers explain the steep spectral slopes,  $k^{-10}$ , of the horizontal kinetic energy spectrum in this and previous work Sundermeyer and Lelong (2005). With sufficiently high Reynolds numbers to ensure turbulent interactions, the kinetic energy spectrum is expected to have logarithmic slope of  $k^{-5/3}$  (Pope, 2000). The difference is due to the rate of non-linear transfer of kinetic energy not being dominated by the rate of viscous dissipation.

Appendix B shows that the instabilities of perturbed adjustment vortices emerge when the Laplacian viscosity is reduced by an order of magnitude. With Ekman number scaling, this is equivalent to increasing the height and length scales of the mixed patch by a factor of three. When the instabilities evolve into sets of propagating dipoles, the energy in the barotropic and first baroclinic modes increase by three and one orders of magnitude respectively. The change in energy is driven by a baroclinic instability that converts the available potential energy to the kinetic energy of the instability. The kinetic energy grows in the first two modes due to a change in structure. The change in structure is from a three-lobed, alternating, vertical structure of the adjustment vortex to a single-lobed, vertical structure of the complementary pairs in a propagating dipole. Whereas

the vertical average of vorticity, and barotropic kinetic energy, in the alternating structure is close to zero, this is not the case for the single-lobed structure. Furthermore, the Fourier transform of a Gaussian profile is another Gaussian profile peaked around wavenumber zero. In pairwise interactions of adjustment vortices in a numeric domain with small viscosity, it is shown that proximal vortices can induce the non-linear behaviors of partial merging, dipole pairing, and instabilities (see Chapter 3). The non-dimensional anisotropic scaling and the numerical simulations predict that the unequilibrated kinetic energy can be accounted for by the accumulation in the barotropic mode. Furthermore, the technique of scaled barotropic damping is akin to Rayleigh damping used in other work to prevent unphysical accumulation of kinetic energy (Bartello, 2010).

As a check, some numerical simulation are done with  $\tau = 1.0 T_{ip}$  waiting time between forcings and viscosity reduced by an order of magnitude below what is implied by the  $N/f$ -scaling. With the Laplacian viscosity at  $\nu = 2.5 \times 10^{-6}$  non-linear interactions are able to fully evolve without being overly damped. Barotropic damping is applied in various degrees to ascertain its effect on the inverse cascade of kinetic energy. With the decreased viscosity, the kinetic energy grows in an unbounded manner and, as above, most of this occurs in the barotropic mode (Figure 5.17a). Characteristics of the inverse cascade of kinetic energy are seen in the time evolution of kinetic energy in horizontal modes (Figure 5.17b). Examining the full horizontal spectrum of kinetic energy at different points in time, it is clear that most of this kinetic energy cascade occurs in the barotropic mode (Figure 5.18). However, growth in the kinetic energy of the first baroclinic mode between  $100 T_{ip}$  and  $300 T_{ip}$  shows a temporary increase in large scales (Figure 5.19). At the end of the simulation, the scale distribution of kinetic settles back down to levels attained at  $100 T_{ip}$ . There are a few different possible causes for this behavior. First, non-linear interactions change the overall structure of vorticity and distribution of energy in the vertical modes. The analysis of Appendix B shows the conversion of available potential energy into the kinetic energy of the evolving instability. Most of the kinetic energy from this conversion is delivered to the barotropic and first

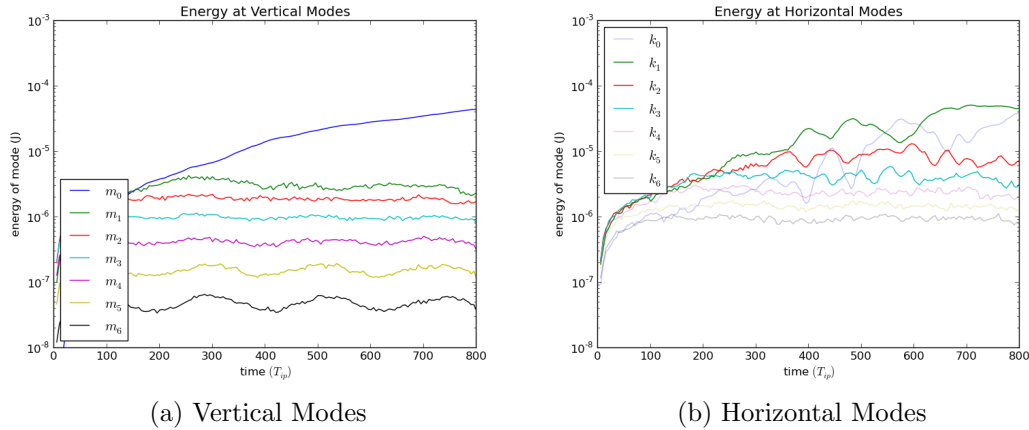


Figure 5.17: Semi-log plots of the horizontally averaged kinetic energy in the barotropic mode,  $m_0$ , and first six baroclinic modes,  $m_1$  to  $m_6$ , (a) and the vertically averaged kinetic energy in the first seven horizontal modes,  $k_0$  to  $k_6$  (b) of the  $\tau = 1.0 T_{ip}$  simulation with  $\nu = 2.5 \times 10^{-6}$ . The first three non-zero modes of (b) are emphasized by dimming the plots of the remaining horizontal wavenumbers.

baroclinic mode. Therefore, it could be the change of vortex structure that is providing kinetic energy to the first baroclinic spectrum of Figure 5.19 between 100  $T_{ip}$  and 400  $T_{ip}$ . Both the equilibration of energy in the first baroclinic mode and the horizontal shear of the barotropic mode could be causing the kinetic energy to equilibrate at a smaller value. Second, the growth in quantity and scale of the first baroclinic mode kinetic energy could be the sign of an inverse cascade of kinetic energy in this vertical mode. Non-linear interactions could be driving horizontal mergers of vortices in the baroclinic mode. These larger structures could then be vertically coupling and continuing to drive the inverse cascade of kinetic energy in the barotropic mode. Careful examination of the physical fields is necessary to determine which possibility may be occurring.

The barotropic damping used above is not sufficient to prevent the inverse cascade of kinetic energy in the barotropic mode. Rates of energy transfer from non-linear interactions are greater than the rate of dissipation. With increased damping in the barotropic mode, the inverse cascade of kinetic energy can be arrested and equilibration can be achieved. However, this does not come with-

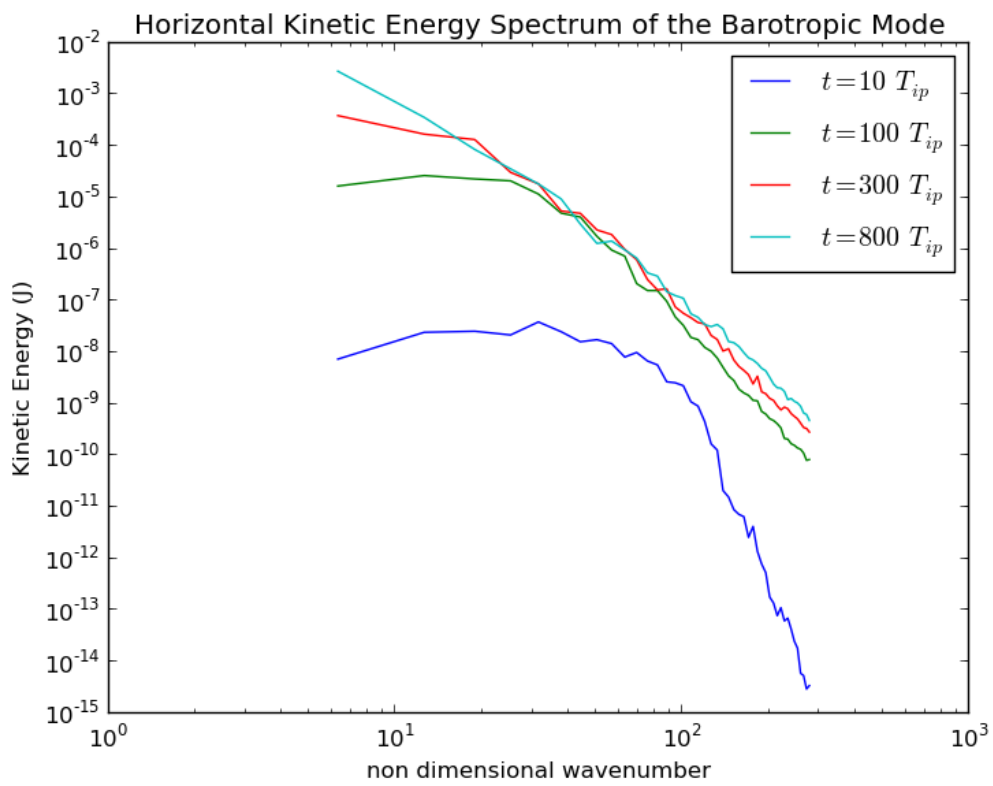


Figure 5.18: Horizontal spectrum of the barotropic mode kinetic energy for the  $\tau = 1.0 T_{ip}$  and  $\nu = 2.5 \times 10^{-6}$  case at various times throughout simulation. An inverse cascade of kinetic energy is apparent in the barotropic mode.

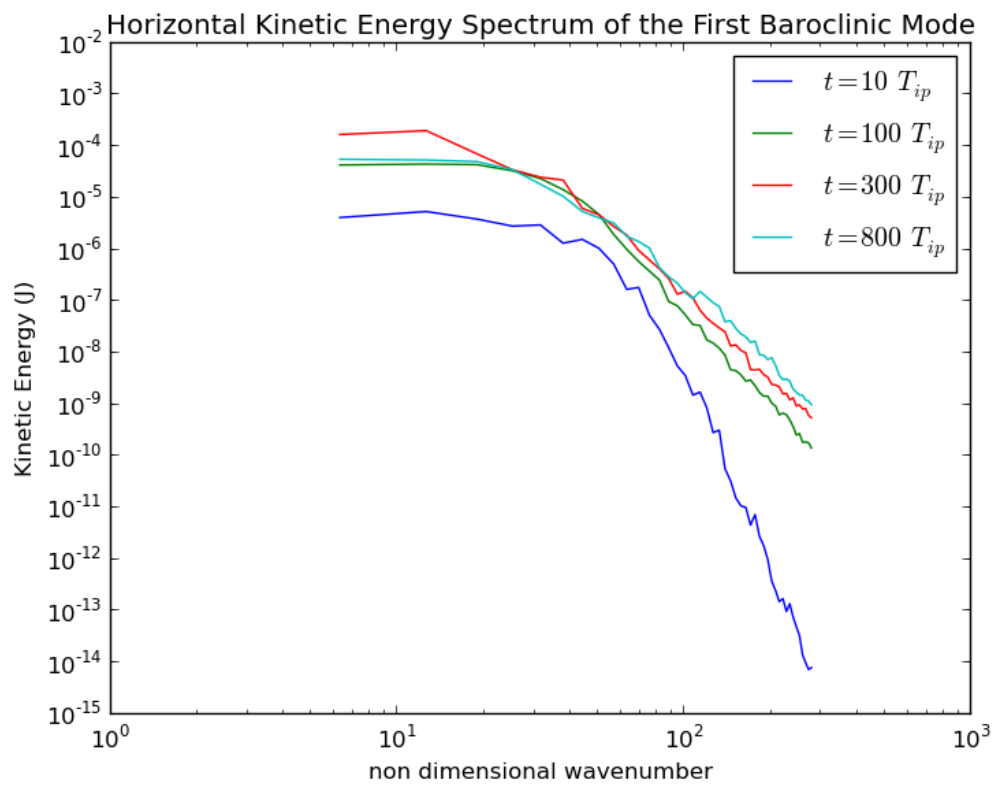


Figure 5.19: Horizontal spectrum of first baroclinic mode kinetic energy for the  $\tau = 1.0 T_{ip}$  and  $\nu = 2.5 \times 10^{-6}$  case at various times throughout simulation. The kinetic energy of the first baroclinic mode shows growth at large scales by  $300 T_{ip}$  before equilibration at later times.

out an additional effect. The structure of the propagating dipoles (see Chapter 3 and Appendix B) requires the kinetic energy of the barotropic mode to be maintained. When the barotropic mode kinetic energy is overly damped, the dipoles are dissipated.

It is apparent, from this last observation, that the barotropic mode is required for the structure of resultant vortices of non-linear interactions and the inverse cascade of kinetic energy observed. How the presence of barotropic mode kinetic energy can be reconciled with the possibility of inverse cascades of kinetic energy in the baroclinic modes is, for the moment, left unexplored. There may exist a balance between the quantities of barotropic kinetic energy required for the structure of propagating dipoles and level that begins to interfere with the quasi-geostrophic dynamics of the baroclinic modes. One means to explore this could entail increasing the vertical scale of the domain from 12.5 m to 50 m or 100 m, without changing grid resolution. This would change the scaling of horizontal to vertical dimension from  $L/H = 40$  to  $L/H = 10$  or  $L/H = 5$ . The effects of dimensional anisotropy would be diminished. The increased resolution of the vertical spectra would allow a more detailed investigation of the transfer of energy between the baroclinic and the barotropic modes. Additionally, strongly damping the largest barotropic modes, in addition to the damping above, may allow equilibration and other dynamics to be observed. This may allow the non-linear evolution of instabilities and interactions that contribute to the lateral dispersion of a tracer. Furthermore, adding new forcings to an already energetic domain on an “as needed”, rather than periodic, basis may provide the statistical equilibration needed for dispersion dynamics. This would entail providing multiple initial forcings and slowly adding more to replace energy lost through dissipation.

## **5.5 Conclusion**

Large disparities in dissipation of kinetic energy are shown to occur for modeled, anisotropic, rotating, stratified fluids with viscosity. Non-dimensional equations and numerical simulations demonstrate the accumulation of barotropic mode ki-

netic energy. In some cases, this leads to an inverse energy cascade. The effects of accumulated barotropic mode kinetic energy can be ameliorated by the application of a scaled barotropic dissipation and the dynamics of a finite domain can be preserved. However, when numerical simulations are performed with a more realistic Reynolds number, barotropic damping can no longer be used to achieve equilibration. Further investigations are needed to explore improvements to this method that yield results representative of oceanic dynamics.

## Chapter 6

### CONCLUSIONS

The purpose of this dissertation is to investigate contributions of non-linear interactions between vortices of geostrophic adjustment to inverse cascades of kinetic energy and the lateral dispersion of a passive tracer. One source of the inverse energy cascade is found to be the barotropic, or purely two-dimensional, mode of the triply-periodic numerical model. The cascade of kinetic energy in the barotropic mode is found to strongly influence the dispersion of a passive tracer at low forcing frequencies. Although weak, large scales continue to disperse the tracer in a non-linear regime. Interactions of two vortices of geostrophic adjustment, in a weakly dissipative domain, show non-linear interactions that are likely to contribute to lateral dispersion in the ocean. The results presented have led to a deeper understanding of the numerical methods used in modeling the oceanic submesoscale. Furthermore, additional mechanisms are observed to occur within the submesoscale as a result of interacting vortices.

The contributions that this dissertation makes to understanding the fluid dynamics of the oceanic submesoscale are as follows. First, interactions between ensembles of adjustment vortices are a likely source for lateral dispersion not previously taken into account or measured. Next, it is found that the continual forcing and excessive dissipation of triply-periodic numerical models will manifest an inverse cascade of kinetic energy that is a consequence of the purely two-dimensional, spectrally barotropic mode. The final contribution is a design of higher-order dissipative terms for ranges of wavenumbers based on the dynamics desired.

The non-linear interactions between adjustment vortices were investigated in Chapter 3. It is shown that proximal adjustment vortices, interacting in a near-inviscid domain, break down into propagating structures. With the multiple scales

of adjusting mixed patches occurring in the ocean, it is believed that these non-linear interactions contribute to the lateral dispersion measured in the oceanic submesoscale. As is elaborated in Appendix A, positioning a new mixing event overlapping with the density perturbation of an existing one introduces varying amounts of available potential energy. The stability of adjustment vortices is more fully explored in Appendix B. The introduction of multiple, periodic diffusive forcings with increased global and local rate density is the subject of Chapter 4. Effects of overlapping diffusive forcing (Appendix A) and the significantly smaller barotropic mode dissipation (Chapter 5) are found to contribute to the lateral dispersion of a passive tracer more than the non-linear effects between adjustment vortices themselves (Chapter 3). Adjustments to viscosity, applied with the method of  $N/f$ -scaling, are shown to damp the non-linear interactions before they can fully evolve. The direct causes for the inverse cascade of kinetic energy, in these dissipative simulations, are shown in Chapter 5. The spectral Boussinesq equations are non-dimensionalized and shown to influence the numerical method used to simulate the processes of interest. The vertically periodic boundary conditions of the anisotropic numerical domains are shown to dissipate barotropic mode kinetic energy four orders of magnitude slower than that of the first baroclinic mode. The accumulated barotropic mode kinetic energy participates in the known process of a two-dimensional inverse energy cascade. A method of barotropic mode damping is applied to arrest this accumulation, arresting the observed inverse energy cascade as well. However, in simulations with more oceanic levels of turbulence, the barotropic damping is unable to arrest the inverse cascade of kinetic energy and statistically equilibrate that kinetic energy. Both inverse cascades of kinetic energy and the lack of statistical equilibration present difficulties in estimating rates of lateral dispersion with the techniques outlined. Both Chapter 4 and Chapter 5 present potential techniques through which this may be addressed.

Additionally, the method of using higher-order dissipation is simplified in Appendix C. Using the power of higher-order dissipation and the dissipation times at selected wavenumbers, the dynamics of interest can be preserved for prede-

terminated ranges of wavenumbers. Preserving intended dynamics for wavenumber ranges brings the spectral slope of these ranges closer to those predicted by theory and confirmed by experiment. These slopes are  $k^{-5/3}$  for forward energy and enstrophy cascades and  $k^{-3}$  for inverse energy cascades.

The results of this dissertation both limit and provide context for numerical models of submesoscale processes. It is shown that triply-periodic numerical methods must take into account the purely two-dimensional effects of the barotropic mode when discussing inverse cascades of kinetic energy. The vortices of geostrophic adjustment, and the products of their non-linear interactions, have different signatures on the vertical spectrum. Adjustment vortices' alternating structure eliminate all but a small contribution to the barotropic mode in a vertically finite domain. However, when a compound vortex no longer has a vertically alternating structure the barotropic mode, by definition, contains the vertically averaged energy. With more kinetic energy in the barotropic mode, the tendency to produce an inverse cascade of kinetic energy is more pronounced. With the damping of the accumulating barotropic mode, statistical equilibration of numeric models can occur sooner, resolution can be increased, and simulation times shortened to better investigate contributions to lateral dispersion with methods presented.

My investigation of adjustment vortices, through numerical methods, has provided insights to understanding lateral dispersion at the submesoscale. Unfortunately, with these insights come limitations to what can be inferred about dynamics of the physical ocean. First, the non-linear behavior of adjustment vortices provide another mechanism through which to explore lateral dispersion at the oceanic submesoscale. However, the barotropic mode dynamics of a triply-periodic model interfere with the capacity to take meaningful statistics of domains with and without oceanic levels of turbulence. It will be the subject of continuing work to address these limitations using a broader range of modeled scales, vortices, and dissipations dynamics.

## BIBLIOGRAPHY

- Acheson, D. (1990). *Elementary fluid dynamics*. New York: Oxford University Press, USA.
- Alford, M. H. and R. Pinkel (2000). Observations of Overturning in the Thermocline: The Context of Ocean Mixing. *Applied Physics* 30(5), 805–832.
- Bambrey, R. R., J. N. Reinaud, and D. G. Dritschel (2007, November). Strong interactions between two corotating quasi-geostrophic vortices. *Journal of Fluid Mechanics* 592, 117–133.
- Bartello, P. (1995). Geostrophic adjustment and inverse cascades in rotating stratified turbulence. *Journal of the Atmospheric Sciences*.
- Bartello, P. (2010). Quasigeostrophic and stratified turbulence in the atmosphere. In D. Dritschel (Ed.), *IUTAM Symposium on Turbulence in the Atmosphere and Oceans*, Volume 28 of *IUTAM Bookseries (closed)*, pp. 117–130. Springer Netherlands.
- Barton, E. and P. Hughes (1982, January). Isolated homogeneous layers over the continental slope off northwest Africa. *Deep Sea Research Part A. Oceanographic Research Papers* 29(1), 135–143.
- Beck, M. and C. E. Wayne (2012). Metastability and rapid convergence to quasi-stationary bar states for the 2d navier-stokes equations. submitted.
- Beckers, M., H. J. H. Clercx, E. Tabak, and R. Verzicco (2003). Evolution and instability of monopolar vortices in a stratified fluid. *Physics of Fluids* 15(4), 1033.

- Beckers, M., H. J. H. Clercx, G. J. F. van Heijst, and R. Verzicco (2002). Dipole formation by two interacting shielded monopoles in a stratified fluid. *Physics of Fluids* 14(2), 704.
- Beckers, M., R. Verzicco, H. Clercx, and G. Van Heijst (2001). Dynamics of pancake-like vortices in a stratified fluid: experiments, model and numerical simulations. *Journal of Fluid Mechanics* 433, 1–27.
- Billant, P. and J.-M. Chomaz (2000, September). Theoretical analysis of the zigzag instability of a vertical columnar vortex pair in a strongly stratified fluid. *Journal of Fluid Mechanics* 419, 29–63.
- Birch, D. A. and M. A. Sundermeyer (2010). Breaking internal wave groups : Mixing and momentum fluxes. *Journal of Physical Oceanography* 23(9).
- Borue, V. and A. Orszag (1995a). Forced Three-Dimensional Homogeneous Turbulence with Hyperviscosity. *Europhys. Lett.* 29(March), 687–692.
- Borue, V. and S. A. Orszag (1995b, February). Self-similar decay of three-dimensional homogeneous turbulence with hyperviscosity. *Physical review. E, Statistical physics, plasmas, fluids, and related interdisciplinary topics* 51(2), R856–R859.
- Brown, G. L., G. Carnevale, and B. R. Sutherland (2008). Beyond ray tracing for internal waves. II. Finite-amplitude effects. *Physics of Fluids* 20(10), 106602.
- Brunner-Suzuki, A.-M. E., M. A. Sundermeyer, and M. P. Lelong (2012). Vortex Stability in a Large-Scale Internal Wave Shear. in press.
- Carnevale, G. and R. C. Kloosterziel (2011). Predicting the aftermath of vortex breakup in rotating flow. *Journal of Fluid* 669, 90–119.
- Carton, X. J. (1992, April). On the Merger of Shielded Vortices. *Europhysics Letters (EPL)* 18(8), 697–703.

- Carton, X. J., G. R. Flierl, and L. M. Polvani (1989, June). The Generation of Tripoles from Unstable Axisymmetric Isolated Vortex Structures. *Europhysics Letters (EPL)* 9(4), 339–344.
- Carton, X. J. and B. Legras (1994, April). The life-cycle of tripoles in two-dimensional incompressible flows. *Journal of Fluid Mechanics* 267, 53.
- Charney, J. G. (1971). Geostrophic Turbulence. *Journal of the Atmospheric Sciences* 28(6), 1087.
- Cohen, I. M. and P. K. Kundu (2007). *Fluid Mechanics* (4th Editio ed.). Boston: Elsevier Academic Press.
- Cresswell, G. R. (1982, January). The coalescence of two East Australian current warm-core eddies. *Science (New York, N.Y.)* 215(4529), 161–4.
- D’Asaro, E. A., C. Lee, L. Rainville, R. Harcourt, and L. Thomas (2011, March). Enhanced Turbulence and Energy Dissipation at Ocean Fronts. *Science (New York, N.Y.)* (March).
- Doney, S., K. Lindsay, and J. Moore (2003). Global ocean carbon cycle modeling. In *Ocean Biogeochemistry: A JGOFS Synthesis*, Chapter 9, pp. 217–238. New York: Springer.
- Dritschel, D. G. and C. Macaskill (2000, November). The role of boundary conditions in the simulation of rotating, stratified turbulence. *Geophysical & Astrophysical Fluid Dynamics* 92(3-4), 233–253.
- Dubosq, S. and A. Viúdez (2007, September). Three-Dimensional Mesoscale Dipole Frontal Collisions. *Journal of Physical Oceanography* 37(9), 2331–2344.
- Flierl, G. R. (1988, April). On the instability of geostrophic vortices. *Journal of Fluid Mechanics* 197, 349.

- Frisch, U., S. Kurien, R. Pandit, W. Pauls, S. Ray, A. Wirth, and J.-Z. Zhu (2008, September). Hyperviscosity, Galerkin Truncation, and Bottlenecks in Turbulence. *Physical Review Letters* 101(14).
- Gent, P. R. and J. C. McWilliams (1986, January). The instability of barotropic circular vortices. *Geophysical & Astrophysical Fluid Dynamics* 35(1-4), 209–233.
- Gill, A. (1982). *Atmosphere-ocean dynamics*. New York: Academic press.
- Gregg, M. C., E. A. D’Asaro, T. J. Shay, and N. Larson (1986, May). Observations of Persistent Mixing and Near-Inertial Internal Waves. *Journal of Physical Oceanography* 16(5), 856–885.
- Griffiths, R. W. and P. F. Linden (1981, April). The stability of vortices in a rotating, stratified fluid. *Journal of Fluid Mechanics* 105, 283.
- Hansen, J., R. Ruedy, M. Sato, and K. Lo (2010, December). Global Surface Temperature Change. *Reviews of Geophysics* 48(4).
- Helfrich, K. and U. Send (1988). Finite-amplitude evolution of two-layer geostrophic vortices. *Journal of Fluid Mechanics* 197, 331–348.
- Helfrich, K. R. and T. M. Battisti (1991). Experiments on Baroclinic Vortex Shedding From Hydrothermal Plumes. *Journal of Geophysical Research* 96(C7), 12511–12518.
- Kloosterziel, R. C. (1994). Emergence and evolution of triangular vortices. 259.
- Kloosterziel, R. C. and G. Carnevale (1999). On the evolution and saturation of instabilities of two-dimensional isolated circular vortices. *Journal of Fluid Mechanics* 388, 217–257.
- Kosloff, R. (1988, April). Time-Dependent Quantum-Mechanical Methods for Molecular Dynamics. *The Journal of Physical Chemistry* 92(8), 2087–2100.
- Kraichnan, R. H. (1967). Inertial ranges in two-dimensional turbulence. *Physics of Fluids* 10(7), 1417–1423.

- Lelong, M. P. and T. J. Dunkerton (1998). Inertia–Gravity Wave Breaking in Three Dimensions. Part II: Convectively Unstable Waves. *Journal of the Atmospheric Sciences* 55(15), 2489–2501.
- Lelong, M. P. and M. A. Sundermeyer (2005). Geostrophic adjustment of an isolated diapycnal mixing event and its implications for small-scale lateral dispersion. *J. Phys. Oceanogr* 35, 2352–2367.
- LeVeque, R. J. (2007, January). *Finite Difference Methods for Ordinary and Partial Differential Equations*. 3600 Market Street, 6th Floor Philadelphia, PA 19104-2688: SIAM.
- Levy, M. (2008). *Transport and Mixing in Geophysical Flows*, Volume 744 of *Lecture Notes in Physics*. Berlin, Heidelberg: Springer Berlin Heidelberg.
- Lighthill, M. J. (1996). *Waves in fluids / James Lighthill*. Cambridge University Press, Cambridge [Eng.] ; New York .:
- Martin, A. (2003, May). Phytoplankton patchiness: the role of lateral stirring and mixing. *Progress In Oceanography* 57(2), 125–174.
- Martin, A. (2012, July). Oceans.The seasonal smorgasbord of the seas. *Science (New York, N.Y.)* 337(6090), 46–7.
- McWilliams, J. C. (1988). Vortex Generation Through Balance Adjustment. *Journal of Physical Oceanography* 18, 1178–1183.
- McWilliams, J. C. (2008, July). Fluid dynamics at the margin of rotational control. *Environmental Fluid Mechanics* 8(5-6), 441–449.
- McWilliams, J. C. and J. B. Weiss (1994, June). Anisotropic geophysical vortices. *Chaos (Woodbury, N.Y.)* 4(2), 305–311.
- McWilliams, J. C., J. B. Weiss, and I. Yavneh (1994, April). Anisotropy and coherent vortex structures in planetary turbulence. *Science (New York, N.Y.)* 264(5157), 410–3.

- Melander, M. V., F. Hussain, and A. Basu (1991). Breakdown of a circular jet into turbulence. In *Eighth Symposium on Turbulent Shear Flows, Technical University of Munich*, University Park, PA (US), pp. 997. Pennsylvania State University.
- Métais, O., P. Bartello, E. Garnier, J. Riley, and M. Lesieur (1996, January). Inverse cascade in stably stratified rotating turbulence. *Dynamics of Atmospheres and Oceans* 23(1-4), 193–203.
- Métais, O. and J. R. Herring (1989, April). Numerical simulations of freely evolving turbulence in stably stratified fluids. *Journal of Fluid Mechanics* 202, 117.
- Morel, Y. and J. C. McWilliams (1997, May). Evolution of Isolated Interior Vortices in the Ocean. *Journal of Physical Oceanography* 27(5), 727–748.
- Okubo, A. (1971). Oceanic diffusion diagrams. *Deep Sea Research and Oceanographic Abstracts* 18(8), 789–802.
- Orszag, S. A. (1972, January). Numerical Simulation of Three-Dimensional Homogeneous Isotropic Turbulence. *Physical Review Letters* 28(2), 76–79.
- Orszag, S. A. and G. S. Patterson (1971). Spectral Calculations of Isotropic Turbulence: Efficient Removal of Aliasing Interactions. *Physics of Fluids* 14(11), 2538.
- Ozugurlu, E., J. N. Reinaud, and D. G. Dritschel (2008, February). Interaction between two quasi-geostrophic vortices of unequal potential vorticity. *Journal of Fluid Mechanics* 597, 395–414.
- Paluszkievicz, T., S. Harper, A. Anis, B. Baschek, E. D’Asaro, R. Ferrari, L. Goodman, E. Kunze, J. Ledwell, P. Lelong, M. Levine, A. Mahadevan, J. Molemaker, S. Smith, M. Sundermeyer, A. Tandon, J. Taylor, and G. Terray (2008). Scalable Lateral Mixing and Coherent Turbulence.

- Polzin, K. L., E. Kunze, J. M. Toole, and R. W. Schmitt (2003, January). The Partition of Finescale Energy into Internal Waves and Subinertial Motions. *Journal of Physical Oceanography* 33(1), 234–248.
- Pope, S. (2000). *Turbulent flows*. New York: Cambridge University Press.
- Prants, S. V., M. Y. Uleysky, and M. V. Budyansky (2011, September). Numerical simulation of propagation of radioactive pollution in the ocean from the Fukushima Dai-ichi nuclear power plant. *Doklady Earth Sciences* 439(2), 1179–1182.
- Reid, R. O., B. A. Elliott, and D. B. Olson (1981, January). Available Potential Energy: A Clarification. *Journal of Physical Oceanography* 11(1), 15–29.
- Reinaud, J. N. and D. G. Dritschel (2002, October). The merger of vertically offset quasi-geostrophic vortices. *Journal of Fluid Mechanics* 469, 287–315.
- Rodríguez-Marroyo, R., A. Viúdez, and S. Ruiz (2011, June). Vortex Merger in Oceanic Tripoles. *Journal of Physical Oceanography* 41(6), 1239–1251.
- Ross, S. (2009). *Introduction to Probability Models* (Ninth ed.). Orlando, FL: Academic Press, Inc.
- Sallée, J.-B., R. J. Matear, S. R. Rintoul, and A. Lenton (2012, July). Localized subduction of anthropogenic carbon dioxide in the Southern Hemisphere oceans. *Nature Geoscience* 5.
- Saunders, P. M. (1973, January). The Instability of a Baroclinic Vortex. *Journal of Physical Oceanography* 3(1), 61–65.
- Schmidt, M. R., M. Beckers, a. H. Nielsen, J. J. Rasmussen, and G. J. F. van Heijst (1998). On the interaction between two oppositely signed, shielded, monopolar vortices. *Physics of Fluids* 10(12), 3099.
- Smetacek, V., C. Klaas, V. H. Strass, P. Assmy, M. Montresor, B. Cisewski, N. Savoye, A. Webb, F. D’Ovidio, J. M. Arrieta, U. Bathmann, R. Bellerby,

- G. M. Berg, P. Croot, S. Gonzalez, J. Henjes, G. J. Herndl, L. J. Hoffmann, H. Leach, M. Losch, M. M. Mills, C. Neill, I. Peeken, R. Röttgers, O. Sachs, E. Sauter, M. M. Schmidt, J. Schwarz, A. Terbrüggen, and D. Wolf-Gladrow (2012, July). Deep carbon export from a Southern Ocean iron-fertilized diatom bloom. *Nature* 487(7407), 313–319.
- Smith, L. M. and F. Waleffe (1999). Transfer of energy to two-dimensional large scales in forced, rotating three-dimensional turbulence. *Physics of Fluids* 11(6), 1608.
- Smith, L. M. and F. Waleffe (2002, January). Generation of slow large scales in forced rotating stratified turbulence. *Journal of Fluid Mechanics* 451, 145–168.
- Smith, S. A. (1997). *Dissipative Closures for Statistical Moments, Fluid Moments, and Subgrid Scales in Plasma Turbulence*. Ph. D. thesis, Princeton University.
- Staquet, C. and J. Sommeria (2002, January). Internal Gravity Waves: From Instabilities to Turbulence. *Annual Review of Fluid Mechanics* 34(1), 559–593.
- Stuart, G. (2011). Laboratory studies of lateral dispersion by the relaxation of diapycnal mixing events. *Journal of Fluid Mechanics*. submitted.
- Sundermeyer, M. A. (1998). *Studies of lateral dispersion in the ocean*. Ph. D. thesis, Massachusetts Institute of Technology Woods Hole Oceanographic Institute.
- Sundermeyer, M. A. and J. R. Ledwell (2001). Lateral Dispersion over the continental shelf: Analysis of dye release experiments. *Journal of Geophysical Research* 106(C5), 9603–9621.
- Sundermeyer, M. A., J. R. Ledwell, N. S. Oakey, and B. J. W. Greenan (2005). Stirring by Small-Scale Vortices Caused by Patchy Mixing. *Journal of Physical Oceanography* 35(7), 1245.
- Sundermeyer, M. A. and M. P. Lelong (2005). Numerical simulations of lateral dispersion by the relaxation of diapycnal mixing events. *Journal of Physical Oceanography* 35(12), 2368–2386.

- Taylor, G. I. (1921). Diffusion by continuous movements. *Proceedings of the London Mathematical Society* 20, 196–211.
- Thomas, L., A. Tandon, and A. Mahadevan (2008). Submesoscale processes and dynamics. In M. W. Hecht and H. Hasumi (Eds.), *Ocean Modeling in an Eddy Regime, Geophysical Monograph Series, Vol. 177*, pp. 17–38. Washington, DC: American Geophysical Union.
- Thorpe, S. A. (2005). *The turbulent ocean*. New York: Cambridge University Press.
- Tóth, G. and G. Házi (2010). Merging of shielded Gaussian vortices and formation of a tripole at low Reynolds numbers. *Physics of Fluids* 22(5), 053101.
- Trefethen, L. N. (2000, January). *Spectral Methods in MATLAB*. Philadelphia, PA: SIAM.
- Tung, K. and W. Orlando (2003). On the differences between 2D and QG turbulence. *Discrete and Continuous Dynamical Systems - Series B* 3(2), 145–162.
- Valcke, S. and J. Verron (1997, April). Interactions of Baroclinic Isolated Vortices: The Dominant Effect of Shielding. *Journal of Physical Oceanography* 27(4), 524–541.
- Vallis, G. (2006). *Atmospheric and oceanic fluid dynamics: fundamentals and large-scale circulation*. New York: Cambridge University Press.
- Vanneste, J. and P. H. Haynes (2000). Intermittent mixing in strongly stratified fluids as a random walk. *Journal of Fluid Mechanics* 411, 165–185.
- Verzicco, R., F. Lalli, and E. Campana (1997). Dynamics of baroclinic vortices in a rotating, stratified fluid: A numerical study. *Physics of Fluids* 9(2), 419.
- Winters, K. B. (1994, April). Three-dimensional wave instability near a critical level. *Journal of Fluid Mechanics* 272, 255–284.

Winters, K. B., J. A. MacKinnon, and B. Mills (2004). A Spectral Model for Process Studies of Rotating, Density-Stratified Flows. *American Meteorological Society* 21(4), 69–94.

## Appendix A

### NONLINEARITY OF DIFFUSIVE FORCING

The method of introducing available potential energy through diffusive forcing of a rotating and stratified domain is reviewed. This method reduces the range of spatial and temporal resolution that would be needed to model both turbulent mixing and geostrophic scales. This method has been found to introduce variable quantities of available potential energy in the numerical model. The sources and consequences of this variability are identified.

#### ***A.1 Introduction***

For all the numerical simulations performed in this dissertation, the following technique is implemented to introduce well mixed patches into a stratified-rotating, fluid domain. This is the same technique that is employed in previous and related work (Lelong and Sundermeyer, 2005; Sundermeyer and Lelong, 2005; Brunner-Suzuki et al., 2012). This technique is used to parameterize turbulent mixing events in a computationally efficient manner. Resolving the physical and temporal scales needed for both small-scale turbulent mixing and large-scale geostrophic adjustment would require orders of magnitude in both spatial scales and time stepping. It would be prohibitive to perform a simulation with multiple adjustments while resolving turbulent mixing. In the following sections I review the method of diffusive forcing, concerns and consequences that this method introduces, and how those consequences are accounted for in simulations. These findings are reviewed in the conclusion.

## A.2 Method

The core of parameterizing a turbulent mixing event (be that from a shear instability, breaking internal wave, or other such process) utilizes a vertical diffusion equation with a strong, localized diffusivity parameter:

$$\frac{\partial \rho}{\partial t} = \frac{\partial}{\partial z} \left( \kappa^*(x, y, z) \frac{\partial \rho}{\partial z} \right), \quad (\text{A.1})$$

with

$$\kappa^*(x, y, z) = \frac{1}{\Delta \hat{t}} \left( \frac{\Delta N^2}{N^2} \right) \sigma_z^2 \exp \left\{ -\frac{1}{2} \left[ \frac{x^2 + y^2}{\sigma_r^2} + \frac{z^2}{\sigma_z^2} \right] \right\}, \quad (\text{A.2})$$

where the density  $\rho$  is the only solution variable. The additional parameters are the spatially varying diffusivity  $\kappa$ , the amount of time to be forced  $\Delta \hat{t}$ , the buoyancy frequency  $N$ , the change in buoyancy frequency desired  $\Delta N$ , radial half-width of mixed patch  $\sigma_r$ , and the vertical half-height of the mixed patch  $\sigma_z$ . The buoyancy frequency  $N$ , also known as the Brunt-Väisälä frequency, is defined by  $N^2 = -g/\rho_0 \frac{\partial \bar{\rho}(z)}{\partial z}$ , with gravitational acceleration  $g$ , background density  $\rho_0$ , and linear density profile  $\bar{\rho}(z)$ . The diffusivity parameter,  $\kappa$ , is further divided into a horizontally varying component,

$$\beta = \exp \left[ -(x^2 + y^2)/(2\sigma_r^2) \right] \quad (\text{A.3})$$

and a vertically varying component,

$$\hat{\kappa}(z) = \kappa(x, y, z)/\beta. \quad (\text{A.4})$$

The  $(x, y, z)$  locations of the diffusivity parameter is adjusted to introduce the strong diffusivity at an arbitrary location  $(x - x_0, y - y_0, z - z_0)$ . Furthermore, the rest of the simulation algorithms use the density perturbation  $\rho'$  of a Reynolds decomposition  $\rho = \bar{\rho}(z) + \rho'$ , to ensure triply periodic boundary conditions needed for the spectrally treated spatial components. Before the diffusive forcing method

is applied, the linear density component is added back to the density perturbation such that it is centered around the vertical location of the mixed patch. This ensures that the diffusive forcing is not being applied over the discontinuous vertical boundary of the complete density profile.

The time stepping of the diffusive forcing routine is performed on each vertical column of the domain using a Forward Euler Finite Difference method,

$$\frac{U_{xy}^{(n+1)} - U_{xy}^{(n)}}{\Delta t} = D_- K D_+ U_{xy}^{(n)}, \quad (\text{A.5})$$

where the discrete density profile  $U_{xy}^{(n)}$  at time step  $n$ , the time step  $\Delta t$ , the diagonalization of the diffusivity parameter  $K$ , right sided differentiation matrix  $D_-$  and left sided differentiation matrix  $D_+$ . Each of the finite differences for spatial derivatives are left and right first-order methods,

$$\begin{aligned} \frac{\partial \rho(x, y, z_m)}{\partial z} &\approx \frac{\rho(x, y, z_m) - \rho(x, y, z_{m-1})}{h}, \\ \frac{\partial \rho(x, y, z_m)}{\partial z} &\approx \frac{\rho(x, y, z_{m+1}) - \rho(x, y, z_m)}{h}, \end{aligned} \quad (\text{A.6})$$

where  $z_m = m \cdot h = m \Delta z$ . Dirichlet boundary conditions are imposed from the values of the original full density. Solving (A.5) for  $U_{xy}^{(n+1)}$  gives,

$$U_{xy}^{(n+1)} = (I + \Delta t D_- K D_+) U_{xy}^{(n)}, \quad (\text{A.7})$$

$$= (I + \Delta t D_- K D_+)^n U_{xy}^{(0)}, \quad (\text{A.8})$$

where  $U_{xy}^{(0)}$  is the initial condition of density in a vertical column of fluid at coordinates  $(x, y)$ .

To account for the horizontally varying component of the diffusivity parameter,  $\beta(x, y)$ , powers of two are added to the spatial component of the above method to yield sixty-four distinct differentiation matrices,

$$A_i = (I + 2^{-i} \Delta t D_- K D_+)^n, \quad i \in \{0, 1, 2, \dots, 63\}. \quad (\text{A.9})$$

This is and applied to yield,

$$U_{xy}^{(n+1)} = \left( \prod_{i=0}^{63} a_i A_i \right) U_{xy}^{(0)} \quad (\text{A.10})$$

where each  $a_i \in \{0, 1\}$  is successively chosen such that  $\sum_{i=0}^{63} a_i 2^{-i} \leq \beta(x, y)$  is the largest sum that meets this condition.

The numerical stability of the above method can be ensured by investigating the stability of  $u_t = \lambda u$ , where  $\lambda$  is an eigenvalue of  $A_0$ . The stability region of a forward Euler method is the unit circle in the complex plane centered at  $Z = -1$ . The matrix  $D_- K D_+$  is symmetric and negative definite with real and negative eigenvalues. With the diagonal elements of  $K$  enumerated  $k_1, k_2, \dots, k_n$ , each interior row of  $D_- K D_+$  is  $a_i = [0 \dots 0 k_i - k_i - k_{i+1} k_{i+1} 0 \dots 0 / \Delta z^2]$ , where  $a_i$  is the  $i^{\text{th}}$  row. According to Gershgorin's Circle Theorem, every eigenvalue will lie within a Gershgorin disc around the diagonal element. For the given row  $a_i$ , all eigenvalues will lie within a  $(|k_i| + |k_{i+1}|) / \Delta z^2$  distance from  $-k_i - k_{i+1}$ . With  $\sigma_z^2$  as the maximum element of the diagonal matrix  $K$ , all eigenvalues of  $D_- K D_+$  will satisfy  $\lambda_p \geq -4\sigma_z / \Delta z^2$ . For the above method to be stable, the condition  $\Delta t \lambda_p \in (-2, 0)$  must be met. With Gershgorin's Circle Theorem this is bounded as  $\Delta t 4\sigma_z^2 \lambda_q \in (-2, 0)$ . Using a CFL-like condition for the heat equation (LeVeque, 2007, Pg. 223), the condition for stability reduces to,

$$\frac{4\sigma_z^2 \Delta t}{\Delta z^2} \leq 2 \quad (\text{A.11})$$

or

$$\Delta t \leq \frac{1}{2} \left( \frac{\Delta z}{\sigma_z} \right)^2. \quad (\text{A.12})$$

For refinements in vertical resolution, appropriately modifying the time step size  $\Delta t$ , and implementing for a total of  $1.0 / \Delta t$  time steps, gives the desired and stable result.

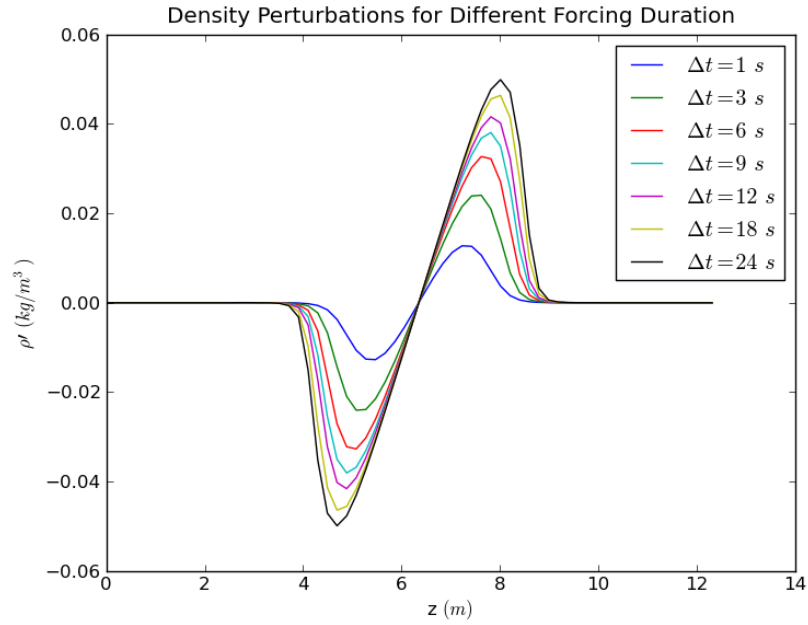
Improvements to the above method are possible. Implementing a Crank-

Nicolson method may be more efficient. Although each time step must be applied multiple times, the time steps themselves can be larger and still maintain stability. The Crank-Nicolson method is implicit and can be solved with order  $n$  tri-diagonal solver. Depending on the time step taken, this may be more efficient than the above method.

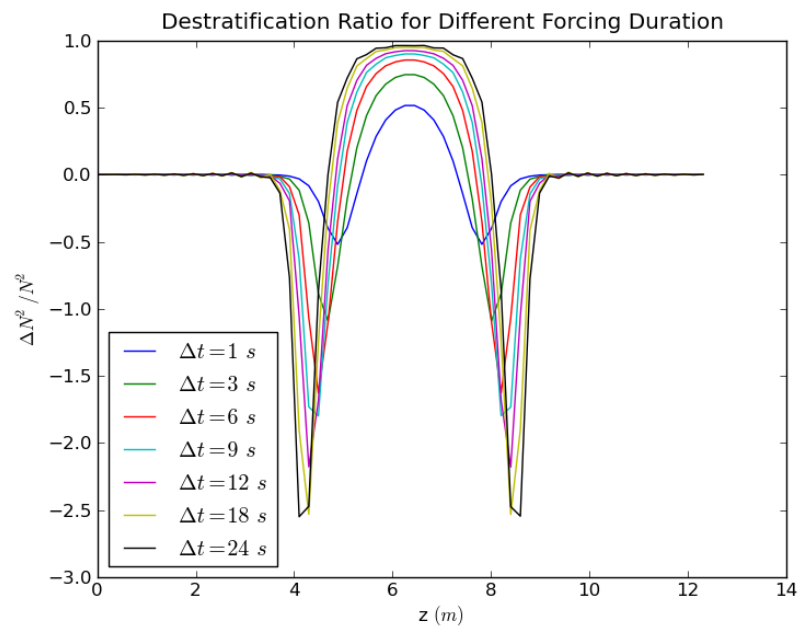
### ***A.3 Consequences of Diffusive Forcing in a Numeric Domain***

In practice, the above method does not give a completely destratified region for  $\Delta N^2/N^2 = 1.0$ . Rather it gives a partial destratification after applying the method for a duration of one second. This can be seen in Figure A.1b, where the  $\Delta N/N \approx 0.71$ , which leads to a destratification ratio of  $\Delta N^2/N^2 = 0.5$ . In the same figure, the diffusion is applied with increasing durations. Though this gives a more complete destratification in the center of the patch, the density gradients at the vertical extremities of the density perturbation are too sharp to be accurately resolved with Fourier methods. This leads to the inability to proceed with the numerical simulation due to unstable time stepping.

Another consequence of the method involves diffusive forcings interacting with a perturbed density field. When the density field is no longer completely linear, the diffusive forcing method can introduce varying amounts of potential energy into the stratified fluid. The dynamics of the original diffusion equation (A.1) act to reduce density gradients that are in the scope of the diffusivity parameter (A.2). If applied in the vertical center of a mixed patch, this has both the effect of increasingly homogenizing the fluid in the vertical center and of steepening the gradients at the vertical extents. The steep vertical density gradients at the boundary of the mixed patch start to drive the diffusion for an arbitrarily small, but non-zero, diffusivity parameter. Taken to an extreme, this effect would drive an increasingly large region of destratification, with the introduced available potential energy approaching a fixed value (Figure A.2). If the diffusive forcing is applied in the steep density gradient of a mixed patch, it tends to reduce that stratification, reducing the size of the previous mixed patch, create a mixed patch that is off-



(a) density perturbation



(b) destratification ratio

Figure A.1: Density perturbation (a) and destratification ratio ( $\Delta N^2 / N^2$ ) (b) for seven increasing durations of diffusive forcing at the same location.

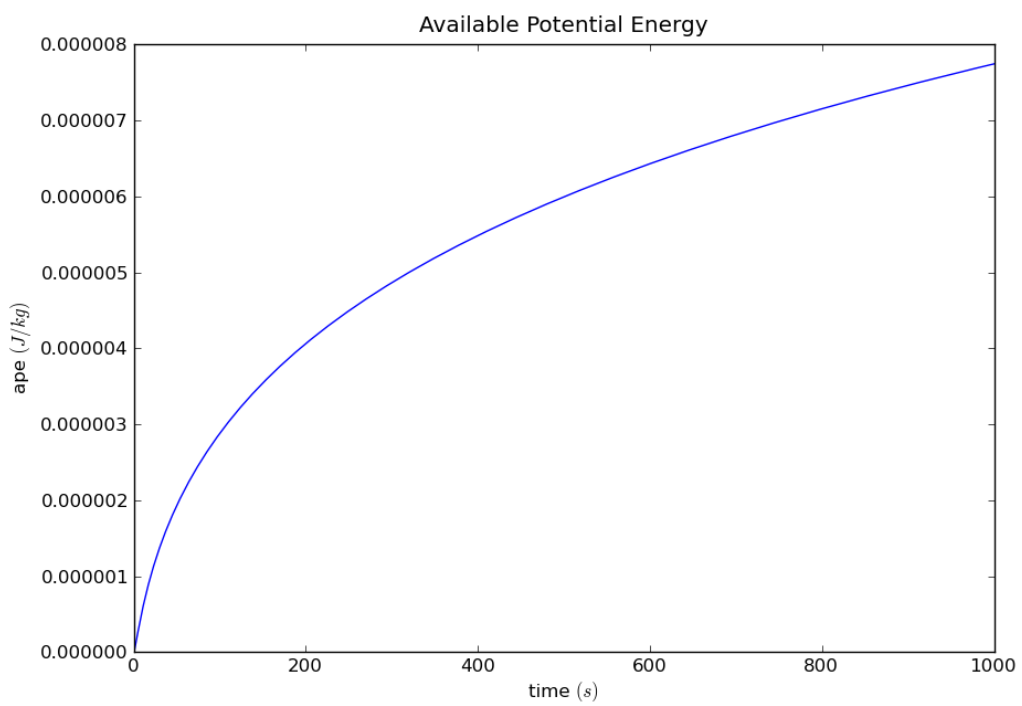


Figure A.2: Available potential energy for continuously forcing a mixing event for 1,000 seconds.

centered with the mean density of its surroundings, and introducing less available potential energy. The vertical asymmetry results in more energy radiated away in internal waves and smaller vortices. With two subsequent diffusive forcings separated by one inertial period in the full simulation, the potential energy of the latter forcing can vary by 40% (Chapter 3). In simulations with persistent forcings, this has the consequence of introducing vortices with a broader range of scales and energy content than originally intended (Chapter 4).

#### ***A.4 Detecting Differences in Diffusive Forcing***

In simulations with increases in local and global rate density of diffusive forcings, regions of new forcings overlap with old mixed patches of fluid. Depending on the density gradient where diffusive forcings are introduced, they will introduce varying amounts of available potential energy in the form of mixed regions of different symmetries. We can readily observe these differences in available potential energy throughout simulations that diffusively force multiple mixing events. In a simulation that introduces a mixing event every two inertial periods, these differences are readily apparent (Figure A.3). A sharp rise in the total energy of the domain provide a means to measure how much energy is delivered by the forcing. Likewise, the more gradual decline of energy after the forcing provides a means to measure the dissipation of that energy. Investigating the amount of energy delivered by each event over the course of a simulation provide us with relevant statistics (Figure A.4). For the simulation shown, the forcings deliver a mean energy of  $1.029 \times 10^{-8} J/kg$  with a standard deviation of  $1.91 \times 10^{-9}$ , or nearly a 19% variation in delivered energy in one standard deviation around the mean. In Chapters 3 and 4 of this dissertation, it is shown that these overlapping diffusive forcings can create a broader range of energetic scales than is initially intended. The larger scales of adjustment vortices persist longer in the domain, making them more likely to encounter an overlapping forcing. Furthermore, when events locally occur in quick succession, a single mixed patch can result in increases of vertical extent, horizontal extent, and destratification. These larger adjustment vortices

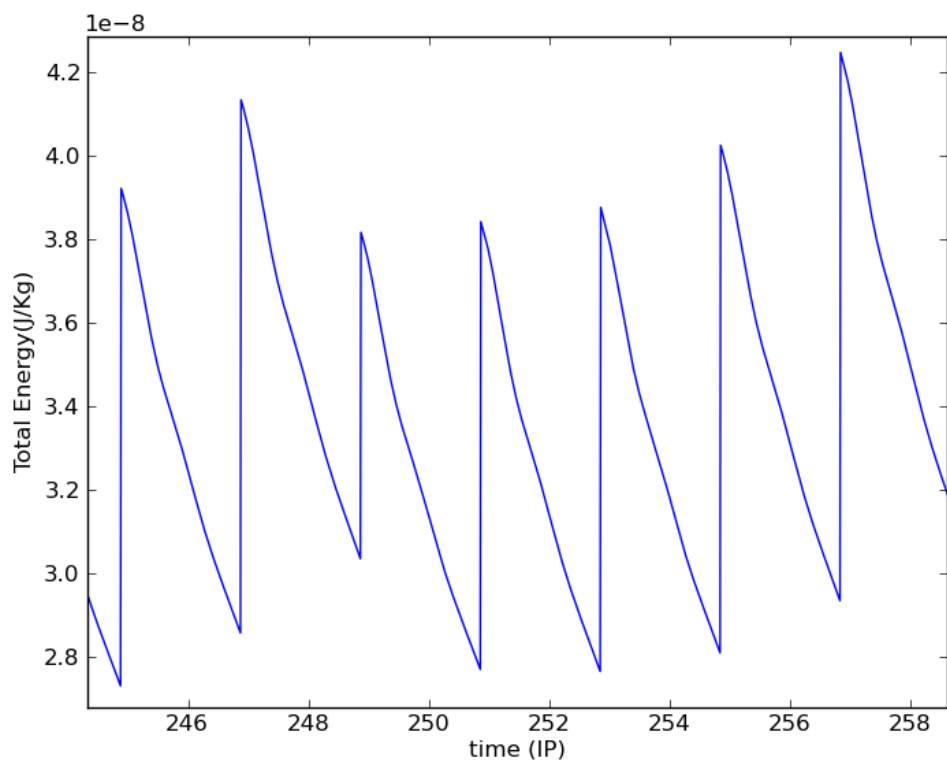


Figure A.3: Details of changes in total domain energy as several parameterized mixing events are introduced. The sudden jump in energy is the forcing while the more gradual decline afterwards is the dissipation of that energy.

also have an increased signature in the barotropic Fourier mode and will tend to contribute more to an inverse cascade of kinetic energy, as seen in Chapter 5.

### **A.5 Conclusion**

The technique of diffusively forcing simulations of rotating, stratified, incompressible fluids has proven to be useful in creating adjustment vortices, but it is not without concerns. When the location of a diffusive forcing coincides with a previously destratified and geostrophically adjusted region, variation in introduced energy and physical qualities can occur. Though this variation may be more representative of oceanic properties, barotropic dynamics (Chapter 5) interfere with the capacity to infer useful dispersion statistics after long times. Some attempts

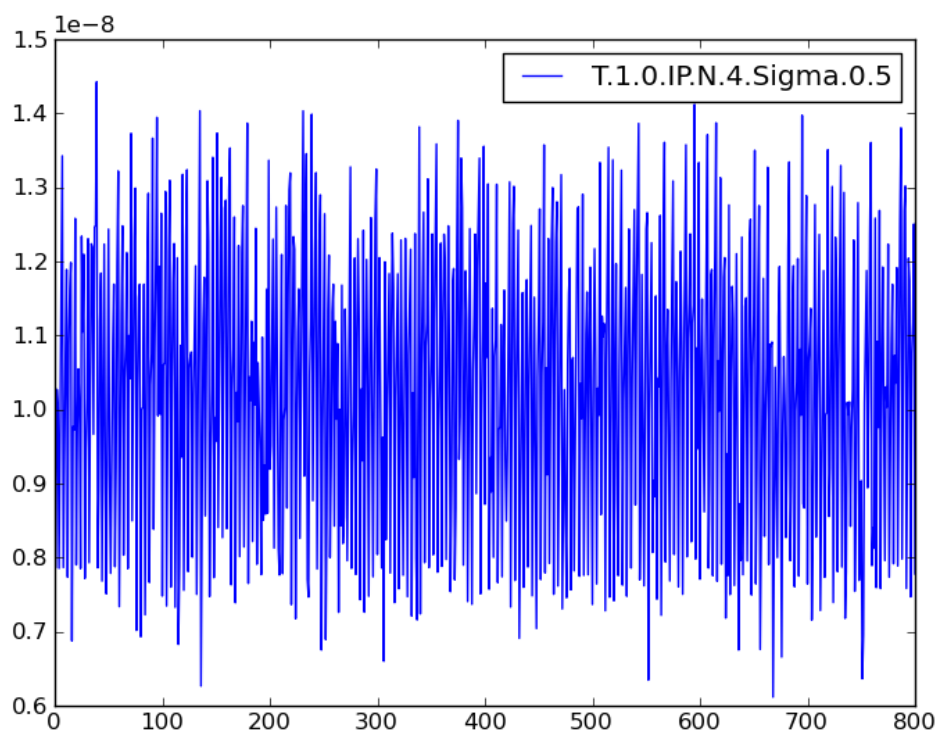


Figure A.4: The energy delivered by each forcing, for a particular simulation, is plotted with respects to time. The mean and standard deviation of the forcings are correlated with variations in kinetic energy scale in simulations.

have been made to vertically diffuse momentum as well as density. As of yet, these techniques do not guarantee that the incompressibility constraint is met. For the numerical simulations presented in this dissertation, little difference is seen when vertically diffusing momentum.

## Appendix B

### STABILITY OF ADJUSTMENT VORTICES

The stability of adjustment vortices is compared to the stability of known two-dimensional structures. These two-dimensional instabilities are reviewed from the literature. Techniques for the analysis of full three-dimensional perturbations to an adjustment vortex are not yet considered.

#### ***B.1 Introduction***

The adjustment vortices of this dissertation have been found to be unstable to perturbations, commented on in Chapter 3. These instabilities were first noticed in Brunner-Suzuki et al. (2012). In this document we address the stability of these vortices more thoroughly. Though adjustment vortices are fully three-dimensional structures, they have sufficient similarities to two-dimensional vortices to warrant comparison. The evolution of instabilities in adjustment vortices are compared to similar stages in the evolution of instabilities in two-dimensional vortices.

The stability of two-dimensional vortices has received a thorough treatment. The foundation for much of what is known is laid down in Reid et al. (1981). In this book, the one dimensional mean flow (azimuthal velocity varying only in the radial direction) is perturbed by three-dimensional variations from the mean flow. Simplifications to these perturbations lead to different classes of instabilities. In (Gent and McWilliams, 1986) the perturbed azimuthal velocity profile  $V_\theta(r) = -2r \exp^{-r^2}$  is investigated for stability properties for the quasi-geostrophic, potential vorticity conservation equation. The mean flow is perturbed by azimuthal modes  $\ell$  and vertical modes  $m$  of vertical structure functions  $F(z)$  that satisfy

$$f^2(F_z/N^2)_z + m^2 F = 0. \quad (\text{B.1})$$

The fastest growing vertical modes  $m$  were found for the azimuthal wavenumbers  $\ell \in \{1, 2\}$ . Purely two dimensional perturbations to different profiles are examined by Carton et al. (1989). For an azimuthal velocity profile,  $V_\theta(r) = \frac{1}{2}re^{-r^\alpha}$ , azimuthal wavenumber  $\ell = 2$  is found to be the fastest growing mode for the steepness parameter  $\alpha > 1.85$ . This profile for velocity represents a “shielded vortex”, where the horizontal integral of vorticity over the entire domain, or circulation, is zero. Instabilities are found to develop in stages of linear growth, non-linear amplification, and non-linear saturation or breakdown (Carton and Legras, 1994). In the first stage, linear growth of unstable modes draws energy from the mean flow. In the next stage, non-linear amplification, satellite vortices emerge from the separation of vorticity in the “shield”. Lastly, there is finite-amplitude saturation or breakdown. The finite-amplitude saturation results in a stable tripole structure (a core with two satellites). The breakdown that occurs for  $\alpha > 3.5$  results in a set of dipole pairs propagating away from the site of the original vortex. Further work developed the growth rates for individual azimuthal modes depending on the steepness parameter  $\alpha$  (Kloosterziel, 1994; Kloosterziel and Carnevale, 1999). For  $\alpha \in (1.85, 6)$  the second azimuthal mode,  $\ell = 2$ , was found to be the fastest growing. For  $\alpha > 6$ , the third azimuthal mode becomes dominant. Additionally, centrifugal instabilities were found to be more influential than barotropic instabilities for  $\alpha < 1.85$  (Carnevale and Kloosterziel, 2011).

Whereas the above analysis of two-dimensional mean flows gives insight into the barotropic instabilities of vortices in two-dimensional fluids, perturbations of mean flows with vertical variations also give us insight into our problem. Contour dynamics were used to analyze the stability for

$$q = \begin{cases} q_1(z) + q_2(z), & r < 1 + \eta(z), \\ q_b(z), & 1 + \eta(z) < r < b + \tau(z) \quad , \\ 0, & b + \tau(z) < r \end{cases} \quad (\text{B.2})$$

with potential vorticity  $q$ , non-dimensional radial coordinate  $r$ , non-dimensional vertical coordinate  $z$ , vertically varying perturbation to inner extent  $\eta$  ( $r = 1$ ),

and vertically varying perturbation to the outer extent  $\tau$  ( $r = b$ ) for the vortex defined in a piecewise manner. When the structure is purely two-dimensional ( $q$ ,  $\eta$  and  $\tau$  do not vary in  $z$ ), the structure of the vortex is shown to be unstable when the thickness of the outer extent  $b$  as compared to the ratio of the inner and outer potential vorticity  $\Delta = q_b/(q_1 + q_b)$  is in the appropriate range. When taken to two layers, counter-rotating vortices spawn propagating pairs of layer-separated vortices whose number are in direct relation to the azimuthal mode perturbed (Helfrich and Send, 1988). A mode two perturbation would yield two propagating pairs and, likewise, a mode three perturbation would yield three propagating pairs.

Furthermore, where the analysis of continuous vertical variations in a stratified, non-rotating fluid becomes prohibitive, numerical simulations have provided additional insight. In Beckers et al. (2001, 2003) numerical simulations of isolated mono-polar vortices are used to examine and extend observations of physical experiments. Where Beckers et al. (2001) present a method to numerically simulate these vortices and compare them to physical experiments, Beckers et al. (2003) use numeric simulations to investigate the stability of these vortices in relation to steepness parameter, viscous effects, and stratification ( $\alpha$ , Reynolds number  $Re$ , and Froude number  $Fr$ ). The method by Beckers et al. (2001, 2003) defines a horizontal structure for velocity with a shielded profile and a Gaussian structure to define its vertical extent

$$v_{\theta,\alpha}(r, z; t = 0) = \frac{1}{\Lambda\sqrt{2\pi}}e^{-(1/2)(z/\Lambda)^2} \times \frac{1}{2}re^{-r^\alpha}. \quad (\text{B.3})$$

Cyclostrophic balance is used to define an initial condition for the density perturbation. Like what has been seen in Carton and Legras (1994), these vortices can undergo instabilities that result in stable tripole structures or propagating dipoles, depending on steepness. Unlike the two-dimensional, quasi-geostrophic vortices described above, the instabilities of these vortices can draw energy from the conversion of the available potential energy in the density perturbations to kinetic energy when the Froude number is sufficiently large,  $Fr > 0.6$ . These

instabilities are classified as baroclinic, rather than barotropic instabilities that draw energy mainly from the mean flow.

In subsequent sections of this appendix the instabilities of an adjustment vortex are addressed. In Section 2, the techniques used in previous work to analyze the stability of two-dimensional vortices are reviewed. In Section 3, these techniques are applied to an analytical representation of adjustment vortex mean flow with perturbations. The difficulties in solving for growth rates are briefly discussed. In Section 4, a numerical simulation of a single adjustment vortex is shown to produce mode two azimuthal instabilities from model specific perturbations. The evolution of instabilities is compared to instabilities evolving in two-dimensional vortices. In Section 5, a technique to numerically explore the instabilities of these vortices is presented. As in Beckers et al. (2003), dependencies on Reynolds, Froude, and perturbation amplitude need to be explored. However, unlike previous work, additional concerns of Rossby number will come into play. Also, with the steepness parameter set by the adjustment process, it is unlikely that we can explore ranges of this parameter in numerical simulations.

## B.2 The Stability of Two-Dimensional Vortices

To explore the two-dimensional instabilities of barotropic vortices, we will start by simplifying the cylindrical Navier-Stokes equations (Cohen and Kundu, 2007),

$$\frac{\partial u}{\partial t} + (\mathbf{u} \cdot \nabla)u - fv - \frac{v^2}{r} = -\frac{1}{\rho_0} \frac{\partial p}{\partial r} + \nu \left( \nabla^2 u - \frac{u}{2} - \frac{2}{r^2} \frac{\partial v}{\partial \theta} \right), \quad (\text{B.4})$$

$$\frac{\partial v}{\partial t} + (\mathbf{u} \cdot \nabla)v + fu + \frac{uv}{r} = -\frac{1}{\rho_0 r} \frac{\partial p}{\partial \theta} + \nu \left( \nabla^2 v + \frac{2}{r^2} \frac{\partial u}{\partial \theta} - \frac{v}{r^2} \right), \quad (\text{B.5})$$

$$\frac{\partial w}{\partial t} + (\mathbf{u} \cdot \nabla)w = -\frac{1}{\rho_0} \frac{\partial p}{\partial z} - g \frac{\rho}{\rho_0} + \nu \nabla^2 w, \quad (\text{B.6})$$

$$\frac{\partial \rho}{\partial t} + \nabla \cdot (\rho \mathbf{u}) = \kappa \nabla^2 \rho, \quad (\text{B.7})$$

$$\frac{1}{r} \frac{\partial}{\partial r} (r v_r) + \frac{1}{r} \frac{\partial v_\theta}{\partial \theta} + \frac{\partial v_z}{\partial z} = 0, \quad (\text{B.8})$$

to their two-dimensional, inviscid form,

$$\frac{\partial u}{\partial t} + (\mathbf{u} \cdot \nabla)u - fv - \frac{v^2}{r} = -\frac{1}{\rho_0} \frac{\partial p}{\partial r}, \quad (\text{B.9})$$

$$\frac{\partial v}{\partial t} + (\mathbf{u} \cdot \nabla)v + fu + \frac{uv}{r} = -\frac{1}{\rho_0 r} \frac{\partial p}{\partial \theta}, \quad (\text{B.10})$$

$$\frac{1}{r} \frac{\partial}{\partial r}(rv_r) + \frac{1}{r} \frac{\partial v_\theta}{\partial \theta} = 0. \quad (\text{B.11})$$

In the above equations, the solution variables are the horizontal velocity parallel to the x-axis  $u$ , the horizontal velocity parallel to the x-axis  $v$ , the vertical velocity  $w$ , the pressure  $p$ , and the density  $\rho$ . Other constant parameters are the mean density  $\rho_0$ , the viscosity  $\nu$ , the diffusivity  $\kappa$ , the gravitational acceleration  $g$ , and the Coriolis parameter  $f$ . The vertical velocity is eliminated as is the density equation due to the constant density of the two-dimensional flow. Next we assume a mean flow that is in steady-state, hydrostatic, and gradient wind balance,

$$fV_\theta + \frac{V_\theta^2}{r} = \frac{1}{\rho_0} \frac{\partial P}{\partial r}, \quad (\text{B.12})$$

$$\frac{\partial p}{\partial z} = -\rho g, \quad (\text{B.13})$$

$$\frac{\partial V_\theta}{\partial \theta} = 0. \quad (\text{B.14})$$

The two-dimensional, cylindrical Navier-Stokes equations is expressed as a perturbation around the above mean flow:

$$\frac{\partial u}{\partial t} + \frac{V_\theta}{r} \frac{\partial u}{\partial \theta} - fv - \frac{V_\theta v}{r} = -\frac{1}{\rho_0} \frac{\partial p}{\partial r}, \quad (\text{B.15})$$

$$\frac{\partial v}{\partial t} + u \frac{\partial V_\theta}{\partial r} + \frac{V_\theta}{r} \frac{\partial v}{\partial \theta} + fu + \frac{V_\theta u}{r} = -\frac{1}{\rho_0 r} \frac{\partial p}{\partial \theta}, \quad (\text{B.16})$$

$$\frac{1}{r} \frac{\partial}{\partial r}(rv_r) + \frac{1}{r} \frac{\partial v_\theta}{\partial \theta} = 0, \quad (\text{B.17})$$

where all lower case variables are perturbations around the mean flow  $V_\theta$ . Terms in gradient wind balance or terms that contain the product of perturbations have been removed.

At this point the stream function,

$$\psi = \phi(r)e^{i(\ell\theta - \omega t)}, \quad (\text{B.18})$$

is introduced such that the horizontal velocity components can be expressed by

$$u = \frac{1}{r} \frac{\partial \psi}{\partial \theta} = \frac{i\ell}{r} \phi(r) e^{i(\ell\theta - \omega t)}, \quad (\text{B.19})$$

$$v = -\frac{\partial \psi}{\partial r} = -\phi'(r) e^{i(\ell\theta - \omega t)}. \quad (\text{B.20})$$

Furthermore, to assist in the simplification of the equations, the pressure perturbation term is also expressed as  $p = \hat{p}(r)e^{i(\ell\theta - \omega t)}$ .

Substituting the above expressions for velocity and pressure and removing the exponential term yields

$$\frac{\omega\ell}{r} \phi - \frac{\ell^2}{r^2} V_\theta \phi + f\phi' + \frac{V_\theta}{r} \phi' = -\frac{1}{\rho_0} \hat{p}', \quad (\text{B.21})$$

$$(i\omega)\phi' + \frac{i\ell}{r} V_\theta' \phi - (i\ell) \frac{V_\theta}{r} \phi' + f \frac{i\ell}{r} \phi + \frac{V_\theta}{r} \frac{i\ell}{r} \phi = -\frac{i\ell}{\rho_0 r} \hat{p}. \quad (\text{B.22})$$

From reorganizing (B.22), taking the radial derivative, setting equal to the previous equation, and simplifying, we arrive at,

$$(cr - V_\theta) \left( \phi'' + \frac{1}{r} \phi' - \frac{\ell^2}{r^2} \phi \right) + \frac{\partial}{\partial r} \left[ \frac{1}{r} \frac{\partial(rV_\theta)}{\partial r} \right] \phi = 0. \quad (\text{B.23})$$

This is the Rayleigh equation derived in Reid et al. (1981), Gent and McWilliams (1986), and Carton and Legras (1994). The technique for solving for the growth rate  $c$  of azimuthal mode  $\ell$  presented in Carton and Legras (1994) is as follows. For a velocity profile defined,

$$V_\theta(r) = \frac{1}{2} r e^{-r^\alpha}, \quad (\text{B.24})$$

the vertical vorticity is,

$$\begin{aligned} Q(r) &= \frac{1}{r} \frac{d(rV_\theta)}{dr}, \\ &= \left(1 - \frac{\alpha}{2} r^\alpha\right) e^{-r^\alpha}. \end{aligned} \quad (\text{B.25})$$

The above velocity profile is constructed in a piecewise continuous manner,

$$\begin{aligned} 0 < r < a, \quad V_\theta(r) &= \frac{r}{2}, & Q(r) &= 1, \\ a < r < b, \quad V_\theta(r) &= \frac{a^2}{2r}, & Q(r) &= 0, \\ b < r < 1, \quad V_\theta(r) &= \frac{a^2}{2(1-b^2)} \left(\frac{1}{r} - r\right), & Q(r) &= \frac{a^2}{1-b^2}, \\ 1 < r, \quad V_\theta(r) &= 0, & Q(r) &= 0, \end{aligned}$$

at predetermined points  $0 < a < b < 1$ . As a consequence, the derivative of vorticity is zero on all intervals and does not exist over the boundaries between intervals.

With the above definition for vorticity, the Rayleigh equation above becomes

$$(cr - V_\theta) \left( \frac{d^2\varphi}{dr^2} + \frac{1}{r} \frac{d\varphi}{dr} - \frac{\ell^2}{r^2} \varphi \right) + \varphi \frac{dQ}{dr} = 0. \quad (\text{B.26})$$

On sections of the interval where  $Q$  is constant,  $\varphi$  must satisfy the Euler equations.

Therefore,

$$\begin{aligned} 0 < r < a, \quad \varphi(r) &= a_1 r^\ell, \\ a < r < b, \quad \varphi(r) &= a_2 r^\ell + b_2 r^{-\ell}, \\ b < r < 1, \quad \varphi(r) &= a_3 r^\ell + b_3 r^{-\ell}, \\ 1 < r, \quad \varphi(r) &= b_4 r^{-\ell}, \end{aligned}$$

where the constants  $a_i$  and  $b_i$  are attained by enforcing continuity constraints for  $\varphi$  and integrating across the discontinuities of (B.26),

$$\frac{d^2\varphi}{dr^2} + \frac{1}{r} \frac{d\varphi}{dr} - \frac{\ell^2}{r^2}\varphi = -\frac{\varphi \frac{dQ}{dr}}{(r\hat{c} - V)}, \quad (\text{B.27})$$

$$\int_{a-\epsilon}^{a+\epsilon} \left( \frac{d^2\varphi}{dr^2} + \frac{1}{r} \frac{d\varphi}{dr} - \frac{\ell^2}{r^2}\varphi \right) = -\int_{a-\epsilon}^{a+\epsilon} \frac{\varphi \frac{dQ}{dr}}{(r\hat{c} - V)}, \quad (\text{B.28})$$

$$\frac{d\varphi}{dr} \Big|_{a-\epsilon}^{a+\epsilon} + \frac{\varphi}{r} \Big|_{a-\epsilon}^{a+\epsilon} - \int_{a-\epsilon}^{a+\epsilon} \frac{\ell^2}{r^2}\varphi dr = -\frac{\varphi Q}{(r\hat{c} - V)} \Big|_{a-\epsilon}^{a+\epsilon} + (\text{IBP}), \quad (\text{B.29})$$

where (IBP) represents integration by parts. In the limit as  $\epsilon \rightarrow 0$  and with continuity of  $\varphi$ , the second and third terms on the right hand side vanish, as do all (IBP) terms, resulting in,

$$(r\hat{c} - V) \frac{d\varphi}{dr} \Big|_{a-\epsilon}^{a+\epsilon} = -\varphi Q \Big|_{a-\epsilon}^{a+\epsilon}, \quad (\text{B.30})$$

$$\ell \left( \hat{c} - \frac{1}{2} \right) ((a_2 - a_1)a^\ell - b_2 a^{-\ell}) = a_1 a^\ell. \quad (\text{B.31})$$

Repeating this for the other points of discontinuity gives us the system of equations,

$$a^\ell a_1 = a^\ell a_2 + a^{-\ell} b_2, \quad (\text{B.32})$$

$$b^\ell a_2 a_2 + b^{-\ell} b_2 = b^\ell a_3 + b^{-\ell} b_3, \quad (\text{B.33})$$

$$a_3 + b_3 = b_4, \quad (\text{B.34})$$

$$\ell \left( \hat{c} - \frac{1}{2} \right) ((a_2 - a_1)a^\ell - b_2 a^{-\ell}) = a_1 a^\ell, \quad (\text{B.35})$$

$$\ell \left( c - \frac{a^2}{2b^2} \right) (b^\ell (a_3 - a_2) + b^{-\ell} (b_2 - b_3)) = Q(b^\ell a_3 + b^{-\ell} b_3), \quad (\text{B.36})$$

$$\ell c (b_4 - b_3 + a_3) = Q b_4, \quad (\text{B.37})$$

where the first three equations pertain to the continuity of  $\varphi$  and the latter three come from the above process of integrating over the discontinuities.

In order to admit non-trivial solutions for the vector  $\mathbf{b} = [a_1, a_2, a_3, b_2, b_3, b_4]^T$ , the determinant of the above system must be zero. This yields a dispersion relation

for  $c$ . Setting  $\ell = 2$ , the determinant of the system is

$$64b^4c^3 - 16b^2(2a^2 + b^2)c^2 + 4a^2(2b^2 - a^4(1 + b^2) + a^2b^2(2 + b^2))c + a^8 - a^4b^2(b^2 + 2) = 0. \quad (\text{B.38})$$

Thus the growth rate of azimuthal instabilities can be calculated for velocity profiles (B.24) with different steepness parameters. By refining the number of points between which the velocity profile is piecewise constant, refinements to this algorithm have been made to predict growth rates (Kloosterziel and Carnevale, 1999).

### ***B.3 An Eigenvalue Problem for an Approximated Adjustment Vortex***

To analyze the instabilities of a perturbed adjustment vortex, an analytic representation of a balanced adjustment vortex is substituted for a mean flow. Instead of creating an adjustment vortex from a resting state with perturbed density, the structure of a developed adjustment vortex is used as a guide for an analytic description. As in Beckers et al. (2001, 2003), three dimensional structure functions for the velocity profile in a stratified fluid are introduced. Assuming hydrostatic and gradient wind balance, it is possible to derive an equation for the density perturbation that would exactly balance the structure of the velocity.

In the horizontal, the adjustment vortex most resembles the shielded monopolar vortices proposed by Carton and Legras (1994). These take the form of

$$G(\hat{r}) = \frac{1}{2}\hat{r}e^{-\hat{r}^\alpha}, \quad (\text{B.39})$$

where  $\hat{r} = r/\sigma_r$  is the nondimensional radius scaled by  $\sigma_r$ , the dimensional radius. In the vertical, a tri-lobed structure is needed, thus the form of

$$H(\hat{z}) = (1 - \beta\hat{z}^\beta)e^{-\hat{z}^\beta}, \quad (\text{B.40})$$

where  $\hat{z} = z/\sigma_z$  is the nondimensional height scaled by  $\sigma_z$ , the dimensional height.

Combined with the amplitude  $A$  these two structure functions compose the azimuthal velocity of an adjustment vortex in cylindrical coordinates:

$$V_\theta(\hat{r}, \hat{z}) = AG(\hat{r})H(\hat{z}). \quad (\text{B.41})$$

For non-dimensional variables  $\hat{r}$  and  $\hat{z}$ , the vertical vorticity is zero when either of them is one. Furthermore, the azimuthal velocity is at a maximum when  $\hat{r} = 1$  and is zero when  $\hat{z} = 1$ .

To construct the density perturbations required for gradient wind (B.12) and hydrostatic balance (B.13), an equation similar to the thermal wind equation (Vallis, 2006) is derived,

$$f \frac{\partial V_\theta}{\partial z} + \frac{2V_\theta}{r} \frac{\partial V_\theta}{\partial z} = -\frac{g}{\rho_0} \frac{\partial \varrho'}{\partial r}, \quad (\text{B.42})$$

where  $\varrho'$  is the density perturbation required for gradient wind balance. Assuming that  $\varrho' \rightarrow 0$  as  $r \rightarrow \infty$  the following gives us a solution to  $\varrho'$  in terms of the structure functions above,

$$\varrho'(r, z) = -\frac{\rho_0}{g} \int \frac{\partial V_\theta}{\partial z} \left( f + 2\frac{V_\theta}{R} \right) dR, \quad (\text{B.43})$$

$$= -\frac{\rho_0}{g} A \int H'(z)G(R) \left( f + 2A\frac{H(z)G(R)}{R} \right) dR, \quad (\text{B.44})$$

$$= -\frac{\rho_0}{g} A H'(z) \left[ f \int G(R) dR + 2AH(z) \int \frac{(G(R))^2}{R} dR \right]. \quad (\text{B.45})$$

A similar technique, using only cyclostrophic and hydrostatic balance, was used by Beckers et al. (2001) and Beckers et al. (2003).

By examining the velocity and vorticity profiles of an adjustment vortex derived from a mixed patch, the above parameters can be chosen to closely match. The choices  $A = 6.6e - 3$ ,  $\sigma_r = 27.0$ ,  $\sigma_z = 1.35$ ,  $\alpha = 2.0$ , and  $\beta = 2.4$  provide close matching of velocity, vorticity, and perturbation density to a vortex derived purely from adjustment (Figures B.1, B.2, and B.3). Numerical simulations have shown that this structure function approximation of an adjustment vortex behaves in

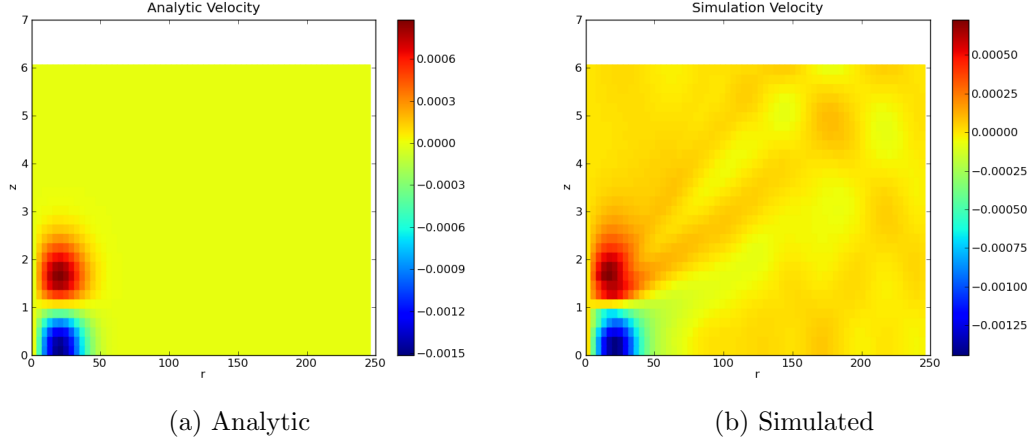


Figure B.1: Comparison between the Analytic and the Simulated velocity fields

much the same way as one produced by the adjustment process itself. The most notable exception is that the energy in the internal wave field is two orders of magnitude less than created in a vortex from adjustment. The structure functions for velocity and density perturbations assume an infinite domain. That they are truncated to a finite and triply-periodic domain is a likely cause for further adjustment and the production of internal waves.

Using the derived solution above as a steady state, it is possible to construct an eigenvalue problem from perturbations to this steady state. The variables of velocity, pressure, and density are represented as perturbations to that steady state,

$$\mathbf{v} = \bar{\mathbf{v}} + \mathbf{v}' = \langle 0, V_\theta, 0 \rangle + \langle u, v, w \rangle, \quad (\text{B.46})$$

$$p = \bar{p} + \tilde{p} + p', \quad (\text{B.47})$$

$$\rho = \bar{\rho} + \varrho' + \rho', \quad (\text{B.48})$$

with  $u$ ,  $v$ , and  $w$  the velocity perturbations from the mean azimuthal velocity  $V_\theta$ ;  $p'$  the perturbation pressure from the gradient wind pressure  $\tilde{p}$  and hydrostatic pressure  $\bar{p}$ ; and  $\rho'$  the perturbed density from the gradient wind perturbation density  $\varrho'$  and the linear density gradient  $\bar{\rho}$ . When these variables are used in

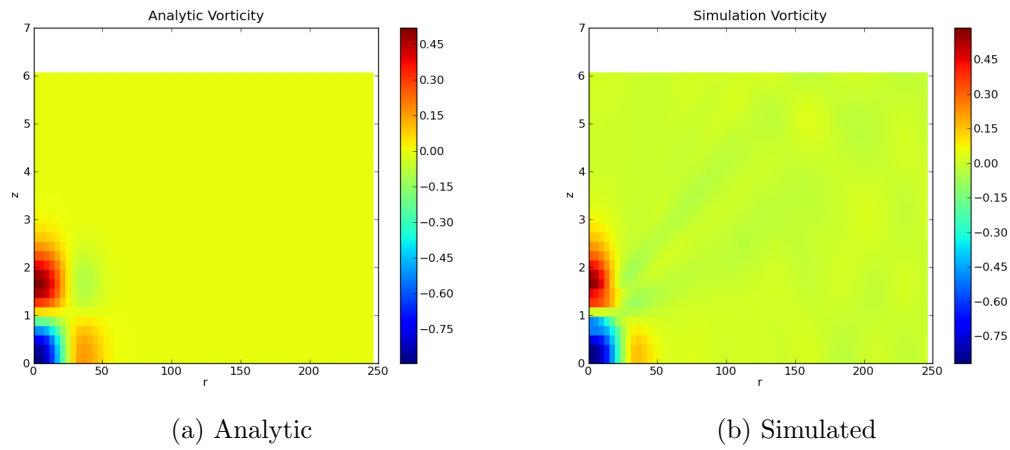


Figure B.2: Comparison between the Analytic and the Simulated vorticity fields

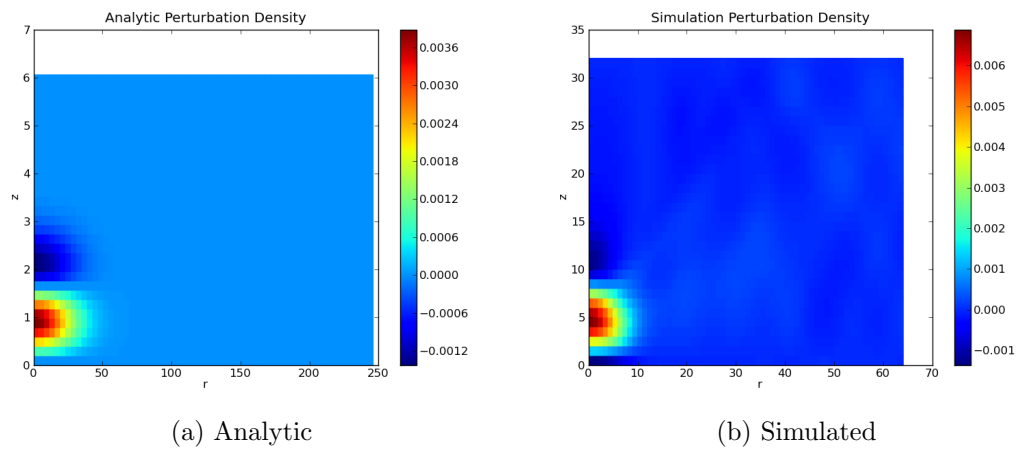


Figure B.3: Comparison between the Analytic and the Simulated perturbation density fields

the inviscid version of the cylindrical Navier-Stokes equations (B.4)-(B.8), the components pertaining to gradient wind and hydrostatic balance can immediately be eliminated. For linearization, products of perturbations are removed, resulting in,

$$\frac{\partial u}{\partial t} + \frac{V_\theta}{r} \frac{\partial u}{\partial \theta} - fv - V_\theta v = -\frac{1}{\rho_0} \frac{\partial p}{\partial r}, \quad (\text{B.49})$$

$$\frac{\partial v}{\partial t} + \frac{V_\theta}{r} \frac{\partial v}{\partial \theta} + fu + \frac{uV_\theta}{r} = -\frac{1}{\rho_0 r} \frac{\partial p}{\partial \theta}, \quad (\text{B.50})$$

$$\frac{\partial w}{\partial t} + ur \frac{\partial V_\theta}{\partial r} + \frac{V_\theta}{r} \frac{\partial w}{\partial \theta} = -\frac{1}{\rho_0} \frac{\partial p}{\partial z} - g \frac{\rho}{\rho_0}, \quad (\text{B.51})$$

$$\frac{\partial \rho}{\partial t} + \left( u \frac{\partial \hat{\rho}}{\partial r} + \frac{V_\theta}{r} \frac{\partial \rho}{\partial \theta} + w \frac{\partial \rho'}{\partial z} \right) + \rho' \nabla \cdot \mathbf{v} = 0, \quad (\text{B.52})$$

$$\frac{1}{r} \frac{\partial}{\partial r} (rv_r) + \frac{1}{r} \frac{\partial v_\theta}{\partial \theta} + \frac{\partial v_z}{\partial z} = 0, \quad (\text{B.53})$$

where all lower-case variables are perturbations from the mean state, unless otherwise noted.

Where the analysis of two-dimensional instabilities allows for the removal of all but radial variable dependence (B.22), the vertical dependence of both the mean state and the perturbation variables prohibit a simple Fourier component analysis. While it may be possible to remove the vertical dependence in the perturbation variables, analysis of the instabilities of a simulated vortex from adjustment does not support this. The instabilities of an adjustment vortex are fully three-dimensional. Analyzing this space for solutions may be possible with numeric techniques not yet considered.

#### **B.4 Evolution of a Single Adjustment Vortex**

Using the numerical codes of Winters et al. (2004), a well mixed region is introduced into a rotating stratified fluid. It develops the form of the adjustment vortex after one inertial period (defined as  $T_{ip} = 2\pi/f$ , where  $f$  is the Coriolis parameter). After one inertial period, the structure of the adjustment vortex can be seen in contours of the vertical component of the vorticity vector ( $\zeta = [\nabla \times \mathbf{u}]_z = dv/dx - du/dy$ ), or vertical vorticity (Fig.B.4a). Though other

components of the vorticity vector are present, the vertical vorticity is the one that is investigated for azimuthal instabilities. The growing mode 2 instability first becomes apparent after about 170 inertial periods (see Fig.B.5b) though this is not visible in the 3D view until after about 180 inertial periods (Fig. B.4b). Though not pronounced in the 3D evolution (Fig.B.4), the mode 2 instabilities growing in the top and bottom components of the adjustment vortex are almost 90 degrees out of phase from the central structure. This effect is seen in Helfrich and Send (1988), where counter-rotating vortices in separate layers develop instabilities. As the mode 2 instabilities grow in strength, the annular rings of each core aggregate into satellite vortices. This is much like the non-linear amplification stage seen by Carton and Legras (1994). By 210 inertial periods (Fig. B.4c), the layers of vorticity have ceased to be separate. The like signed vorticity of each layer has merged with the like signed vorticity of the adjacent layers. I believe It is this merging that gives strength to the respective satellite vortices to tear the structure apart at less than the horizontal steepness required in Carton and Legras (1994) ( $\alpha \geq 3.2$ ). The results of this break up is seen after 250 inertial periods (Fig. B.4d) in the form of propagating dipoles. The resolution of the simulation makes the straining of the vorticity seem discontinuous.

To explore the evolution of the azimuthal and vertical structure of the adjustment vortex, a projection onto cylindrical coordinates is made (Fig. B.5,B.6). In Figure B.5, a horizontal cross section through the middle of the central anticyclone is taken. The evolution of the second mode and break up into propagating structures is easily seen. In Figure B.6, the merging of like signed vorticity across previously isolated layers is apparent. A Fourier transform is taken of the vertical vorticity seen in Figure B.4 and volumetrically averaged. The evolution of the first six azimuthal modes is shown in Figure B.7 and compared to a similar method used by Carton and Legras (1994). Both figures show the growth of a dominant azimuthal mode two instability.

The source of the instabilities for an isolated adjustment vortex in these codes is not yet fully understood. It is suspected that internal waves that are reentrant

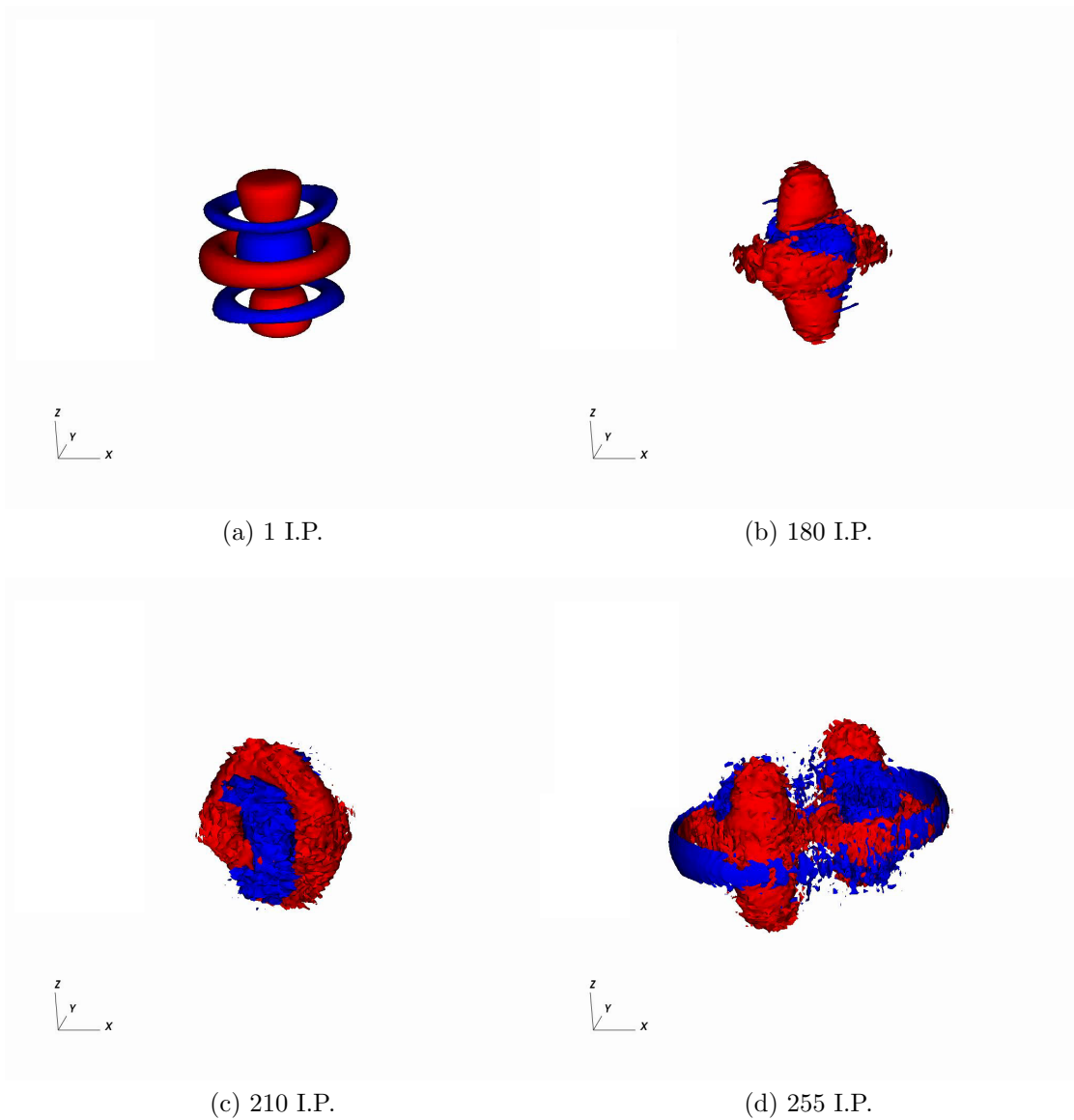


Figure B.4: The evolution of instabilities of a single adjustment vortex. Red denotes cyclonic vorticity and blue anticyclonic vorticity. Contours of vertical vorticity, scaled by the Coriolis parameter, shown are  $\zeta = -0.4 f$  (blue) and  $\zeta = 0.4 f$  (red).

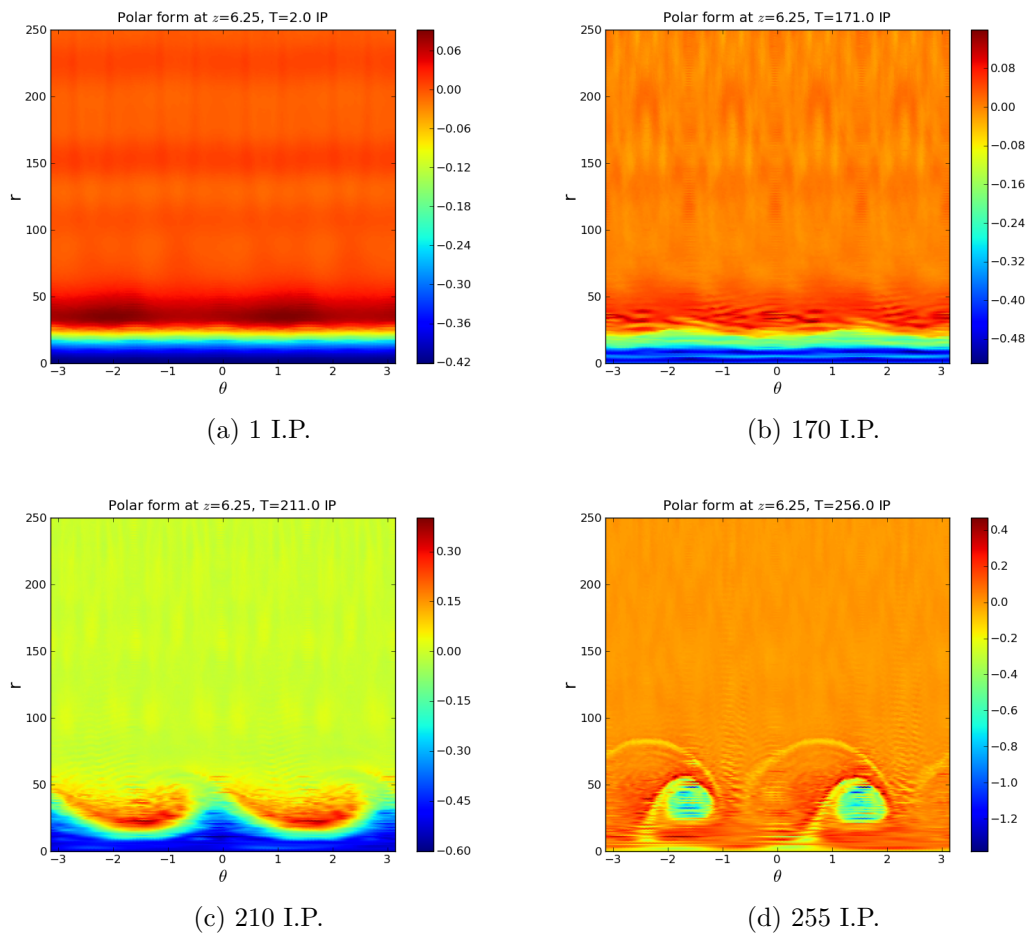


Figure B.5: The polar evolution of instabilities of a single adjustment vortex through the center of the anticyclonic core.

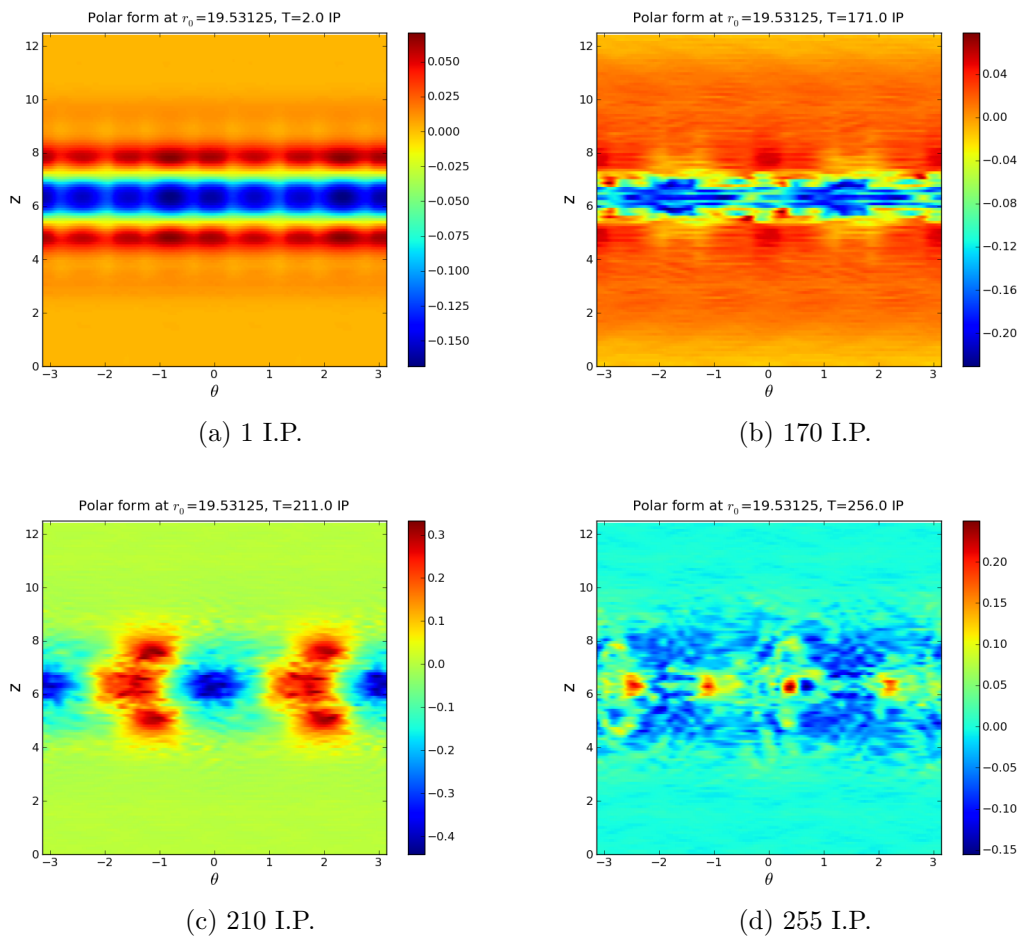


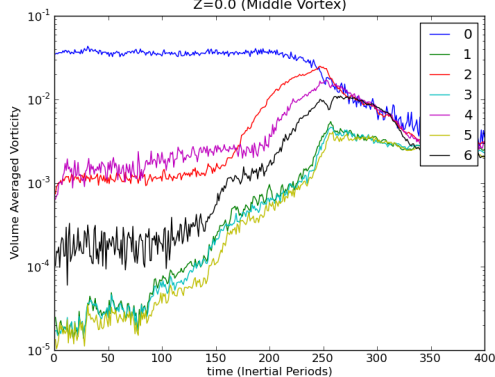
Figure B.6: The cylindrical evolution of instabilities of a single adjustment vortex through a radial section within the cores ( $r = 20 m$ ).

into the triply-periodic, Cartesian domain could induce the azimuthal mode 4 (and harmonics) perturbations. Instabilities of mode 4, and harmonics, have affected simulations of circular jet flows in periodic Cartesian domains (Melander et al., 1991). This potential source is also supported by the instabilities developing twice as fast when two distant, well-mixed regions are introduced into a domain (Chapter 3). To eliminate this source for instabilities of a vortex, a cylindrical Navier-Stokes solver was used to evaluate the stabilities of baroclinic, cyclostrophic vortices (Beckers et al., 2003). Another cause could be low level numeric noise present through the time stepping of the numerical method.

For a single adjustment vortex we can characterize some of the non-dimensional numbers based on data from the physical fields. With  $U = 0.002$  m/s,  $L = 25$  m,  $h = 1.25$  m,  $f = 9.5 \times 10^{-4}$  s $^{-1}$ ,  $N = 0.01885$  s $^{-1}$ , and  $\nu = 2.5 \times 10^{-10}$  m $^2$ /s being the maximum horizontal velocity, radius of the mixed patch, height of the mixed patch, Coriolis parameter, buoyancy frequency, and viscosity; the Reynolds ( $Re = UL/\nu$ ), Ekman ( $Ek = \nu/h^2f$ ), Rossby ( $Ro = U/fL$ ), and Froude ( $Fr = U/Nh$ ) numbers are investigated. The Reynolds number for the low viscosity simulation is well in the range for turbulence,  $Re = 2 \times 10^8$ , as is apparent by the development of instabilities. The Ekman number is small,  $Ek = 1.68 \times 10^{-7}$ , indicating the relative importance of viscosity to inertial effects. The Rossby number is also small,  $Ro = 0.0842$ , indicating the importance of planetary rotation in the balance equations. Lastly, the Froude number is again small,  $Fr = 0.0848$ , indicating importance of stratification over vertical shear instabilities. If we unconventionally take  $N$  to be the actual measure of stratification in the center of the mixed patch,  $N = 5.655 \times 10^{-3}$ , we get a larger Froude number,  $Fr = 0.2829$ . This change may help examine the type of instability that is found to evolve.

For isolated shielded vortices in a stratified, non-rotating fluid the azimuthal instabilities were baroclinic for  $Fr = 0.80$ , while they were barotropic for  $Fr = 0.16$  (Beckers et al., 2003). The baroclinic azimuthal instabilities draw kinetic energy from the conversion of available potential energy in the density field, while barotropic azimuthal instabilities draw kinetic energy from the kinetic energy of

Development of Azimuthal Instabilities for a Single Adjusted Mixing Event  
Z=0.0 (Middle Vortex)



(a) Adjustment vortex

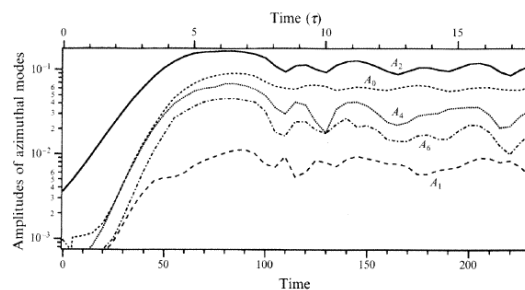


FIGURE 4. Evolution of the main components of the azimuthal mode decomposition of the perturbation. See definition of the amplitude  $A_i$  in the text.

(b) Vortex from Carton and Legras (1994)

Figure B.7: Comparison of the growth of azimuthal modes of an adjustment vortex and in Carton and Legras (1994). Both show the growth of azimuthal mode two being the dominant instability. The azimuthal mode two is the fastest growing mode for an adjustment vortex from  $150 T_{ip}$  to  $220 T_{ip}$ .

the mean flow. However, for rotating stratified flows the azimuthal instabilities may be primarily baroclinic (Saunders, 1973; Griffiths and Linden, 1981; Verzicco et al., 1997). The strongest instabilities for an adjustment vortex have characteristics of a baroclinic instability.

Investigating the evolution of a single adjustment vortex, the relative strength of the azimuthal modes (Figure B.7) grow in direct relationship to the exchange of available potential energy to the kinetic energy of the vortex (Figure B.8). Furthermore, the barotropic and first baroclinic modes (zeroth and first vertical Fourier modes) see the most gain in kinetic energy, without relative gains in the other baroclinic modes (Figure B.9). This change can be seen to be related both to the conversion of vortex potential energy to vortex kinetic energy and a change in the structure of the vorticity itself. During the initial stable phase, an adjustment vortex has three vortex cores with vertically alternating sign. This three-lobed, alternating structure virtually eliminates the vertical average of velocity, giving the barotropic mode near zero kinetic energy. After the development of instabilities and breakdown of the vortices into dipole pairs, the vorticity structures vertically have one lobe of vorticity or two lobes of tightly coupled vorticity of the same sign.

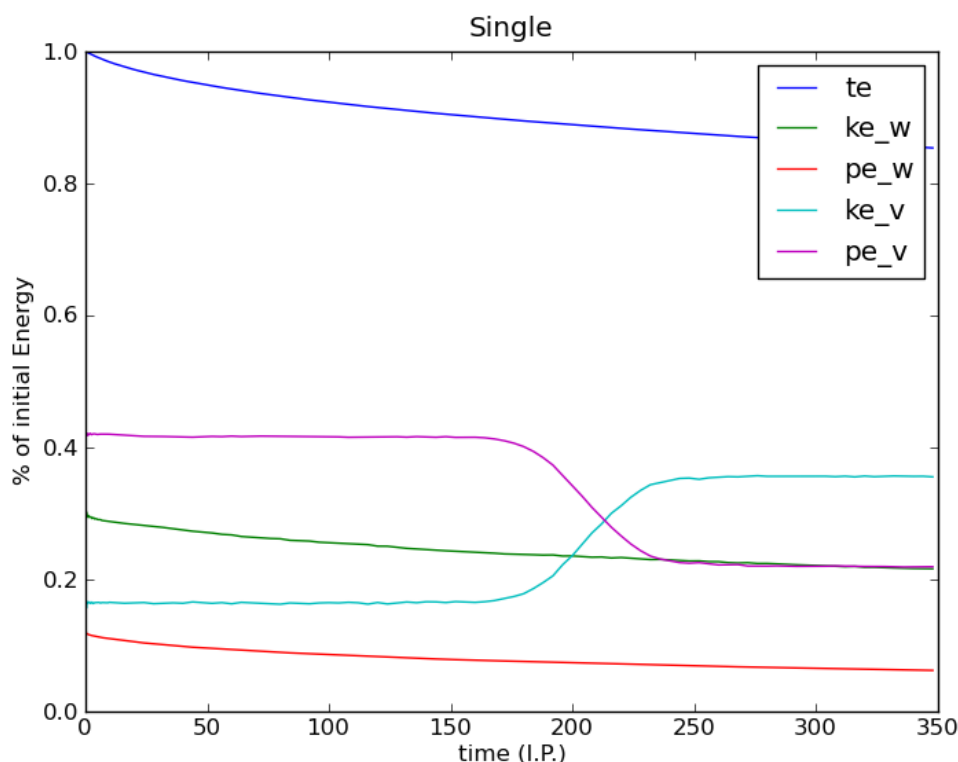


Figure B.8: Wave-vortex decomposition for the evolution of a single adjustment vortex. Exchanges of vortex available potential energy to vortex kinetic energy indicates baroclinic instability.

As the Fourier transform of a Gaussian structure is itself a Gaussian in spectral space, the vertically single-lobed structures will have a strong peak in the lower Fourier modes. That the barotropic mode is not completely dominant at later times may be the consequence of the wave field or smaller vortical structures.

For simulations of multiple adjustment vortices in a triply-periodic and viscous domain, the existence of the barotropic mode can induce an inverse cascade of kinetic energy (see Chapters 4 and 5). This is primarily due to the much smaller dissipation of the accumulated barotropic mode kinetic energy of each adjustment vortex. When the viscosity is small,  $\nu = 2.5 \times 10^{-10}$ , the above instabilities can evolve by proximal effects (see Chapter 3). For simulations of multiple adjustment vortices with small viscosity, inverse cascade of kinetic energy occur more read-

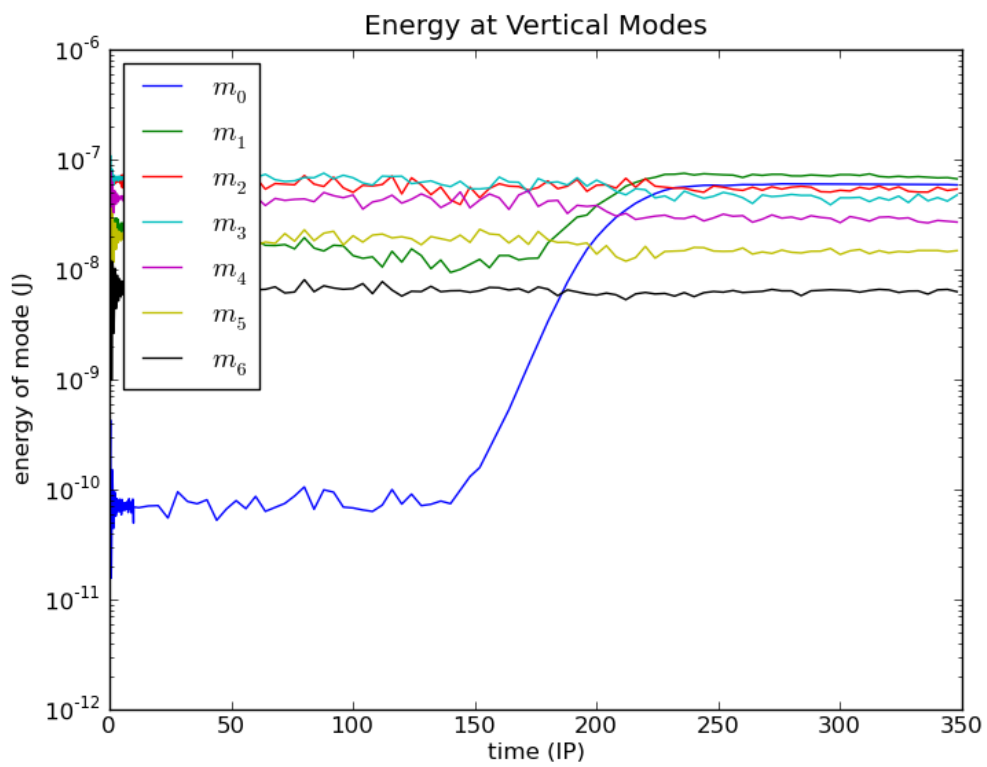


Figure B.9: The evolution of kinetic energy in the first seven modes of horizontally averaged, vertical kinetic energy spectrum. The barotropic mode  $m_0$  kinetic energy increases by three orders of magnitude, while the first baroclinic mode  $m_1$  kinetic energy increases less than an order of magnitude.

ily with the increase in barotropic mode kinetic energy provided by developing instabilities.

### ***B.5 Proposed Numerical Study***

In all the previous studies of the geostrophic adjustment of mixed patches there has been little done to explore the effects of varying non-dimensional number ranges upon stability. In microstructure field study by Gregg et al. (1986), most mixed patches were found to be vertically small ( $< 1 m$ ) and transient. Taller destratified regions were seen to persist for days, potentially indicating the persistence of an adjustment vortex. All the mixed patches in this dissertation, and in previous numerical studies, have mixed patch height of  $1.25 m$ , close to what is called “transient puffs” by Gregg et al. (1986). Lelong and Sundermeyer (2005) investigated varying the Burger number,  $Bu = (R/L)^2$  ( $R$  the internal deformation radius and  $L$  being the radius of the mixed patch), on the effectiveness of converting the potential energy of the mixed patch into the kinetic energy of a vortex. These simulations were done in a triply-periodic domain with small viscosity for relatively short times ( $< 20 T_{ip}$ ) as compared to instability times. Reducing the viscosity increases the Reynolds number and reduces the Ekman number. Equivalent Ekman dynamics are achieved by increasing the vertical scale of the vortex proportional to the root of decrease in viscosity scale. Changes in viscosity do not change the Rossby, Froude, or Burger number of the mixed patches, although changes in radius and vertical height will. Changes in the height of the mixed patch will be translated into changes of radius as the patch adjusts towards its deformation radius.

Instead of exploring all five ( $Ro$ ,  $Fr$ ,  $Re$ ,  $Ek$ ,  $Bu$ ) dimensionless numbers, a few are chosen to be investigated at a time, although changes in some will invariably affect the others. One such dependence, with  $N/f$ -scaling, is  $Re = Ro/Ek(N/f)^2$ . For anisotropic domains, the Reynolds number is directionally dependent, with the effectiveness depending on the gradients of velocity in each direction (see Chapter 5). Numerical simulations have been started that vary the viscosity, azimuthal

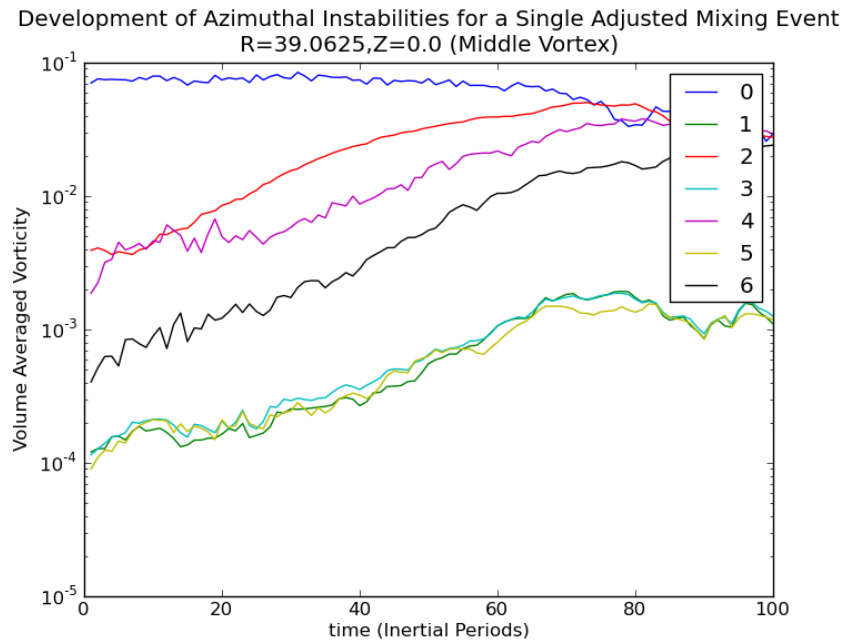


Figure B.10: The first six azimuthal modes of an elliptical mixing event that is perturbed by a mode-two azimuthal instability with amplitude 10% of the mean flow.

wavenumber, amplitude of perturbation, and the radius of the mixed patch. The change in viscosity affects the Reynolds numbers and Ekman numbers exclusively, while the change in patch radius affects Reynolds, Burger, and Rossby numbers. Changes to Froude number may play an important role in stability dynamics and cascades of kinetic energy independent of those solely due to barotropic effects. The quasi-geostrophic approximation is known to drive inverse cascades of kinetic energy in the limit of small Rossby and Froude numbers (Charney, 1971).

Preliminary results show an order of magnitude reduction in viscosity, from  $\nu = 2.5 \times 10^{-5}$  to  $\nu = 2.5 \times 10^{-6}$ , is enough to allow instabilities to evolve. A 10% perturbation to azimuthal mode 2 is sufficient to display instability growth, non-linear saturation, and breakdown within  $80 T_{ip}$  (Figure B.10). Variations in azimuthal mode 2 amplitude show some stabilizing effects, resulting in three-dimensional, horizontal, tri-pole structures similar to the two-dimensional tripole structures in Carton and Legras (1994) and Kloosterziel (1994). Other azimuthal

modes and variations in Burger number have yet to be performed.

## Appendix C

### HYPERVISCOSITY SIMPLIFIED

The use of higher-order dissipation has been employed to ensure numerical stability in many kinds of models. None of the references that utilize higher-order dissipation have presented sufficient rationale for the parameters they use. Lacking adequate rationale has led to extensive experimentation to find suitable parameters for the desired dynamics. In the following, I offer a simplified method of higher-order dissipation that addresses this.

#### ***C.1 Introduction***

Numeric simulations of the Navier-Stokes equations are inherently limited in the range of scales that they can effectively model. Laplacian viscosity dissipates velocity primarily at centimeter to millimeter scales. However, to be computationally tractable, large scale simulations do not simultaneously model the virtually-inviscid, larger scales and the dissipative small scales. For simulations with turbulent forward cascades of energy and enstrophy, this can lead to the build up of kinetic energy and enstrophy at the smallest resolved scales. To address this potential for numeric instability, a higher order dissipative term, or hyperviscosity, has often been employed.

Hyperviscosity has been used in many studies to maintain inertial dynamics for a broad range of scales, while strongly dissipating kinetic energy at the smallest resolved scales. Fourth order dissipative terms,  $-\nu\nabla^4$ , were used to model large coherent vortices emerging from random initial conditions in an anisotropic and quasi-geostrophic triply-periodic numerical models (McWilliams and Weiss, 1994; McWilliams et al., 1994). For triply-periodic, Boussinesq simulations spectrally forced around a mean scale, a sixteenth-order dissipative term was used,  $(-1)^{p+1} \times$

$\nu(\nabla^2)^p \mathbf{u}$  with  $p = 8$  in place of the normal viscosity term  $\nu \nabla^2 \mathbf{u}$  (Smith and Waleffe, 1999, 2002). Throughout this dissertation, and in all related work (Lelong and Sundermeyer, 2005; Sundermeyer and Lelong, 2005; Brunner-Suzuki et al., 2012), both Laplacian viscosity and a sixth-order hyperviscosity was used in conjunction with a wavenumber truncation method (Orszag and Patterson, 1971).

Though many numerical models allow for the use of hyperviscosity, the rationale for the magnitude and power is not yet consistent in the literature. The following sections present an alternative perspective on the hyperviscosity presented in previous work.

## C.2 Dissipation Time Scales

To begin with, we start with the momentum components of the Navier-Stokes equations. These are,

$$\frac{\partial \mathbf{u}}{\partial t} + \mathbf{u} \cdot \nabla \mathbf{u} + \mathbf{f} \times \mathbf{u} = -\frac{1}{\rho_0} \nabla p - \mathbf{g} \frac{\rho}{\rho_0} + \nu_2 \nabla^2 \mathbf{u} + (-1)^{p/2+1} \nu_p \nabla^p \mathbf{u}, \quad (\text{C.1})$$

where the solutions variables, as in (2.19), are the velocity vector  $\mathbf{u}$ , perturbation pressure  $p'$ , and perturbation density  $\rho'$ . Also, as in (2.19), the additional parameters are the background density  $\rho_0$ , the Coriolis vector  $\mathbf{f} = [0, 0, f]^T$ , gravitational acceleration  $\mathbf{g} = [0, 0, g]^T$ , Laplacian viscosity  $\nu_2$ , and hyper-viscosity  $\nu_p$  ( $p$  even). Using the anisotropic scaling of  $N/f$  for both length scales and velocity scales ( $L/H \sim N/f$  and  $U/W \sim N/f$  where  $L$ ,  $H$ ,  $U$ , and  $W$  represent horizontal length scale, vertical length scale, horizontal velocity scale, and vertical velocity scale), as in McWilliams and Weiss (1994), and the following scalings,

$$t = \frac{L}{U} t^\dagger, \quad (\text{C.2})$$

$$p' = U^2 \rho_0 p^\dagger, \quad (\text{C.3})$$

$$\rho' = H \frac{d\bar{\rho}(z)}{dz} \rho^\dagger, \quad (\text{C.4})$$

for time, pressure perturbation, and density perturbation, we non-dimensionalize with parameters,

$$Ro = \frac{U}{fL} \text{ (Rossby)}, \quad (\text{C.5})$$

$$Fr = \frac{U}{NH} \text{ (Froude)}, \quad (\text{C.6})$$

$$Re_2 = \frac{UL}{\nu_2} \text{ (second order Reynolds)}, \quad (\text{C.7})$$

$$Re_p = \frac{UL^{p-1}}{\nu_p} \text{ (} p\text{-th order Reynolds)}. \quad (\text{C.8})$$

The dimensionless equations are converted to spectral space by the use of Fourier transforms,

$$\frac{\partial \hat{\mathbf{u}}_k}{\partial t} - T_k + Ro^{-1} \mathbf{e}_3 \times \hat{\mathbf{u}}_k = \mathbf{A}^2 \left[ -\frac{i\mathbf{k}}{\rho_0} \hat{p}'_k + Fr^{-2} \mathbf{e}_3 \hat{\rho}'_k \right] - \frac{1}{2} \mathbb{D}_k \hat{\mathbf{u}}_k \quad (\text{C.9})$$

with

$$T_k = -(\widehat{\mathbf{u} \cdot \nabla \mathbf{u}})_k, \quad (\text{C.10})$$

$$\mathbb{D}_k = \frac{2}{Re_2} |\mathbf{A}\mathbf{k}|^2 + (-1)^{p/2+1} \frac{2}{Re_p} |\mathbf{A}\mathbf{k}|^p, \quad (\text{C.11})$$

where  $T_k$  is the Fourier transform of the nonlinear term and  $\mathbb{D}_k$  is the spectral dissipation operator.

A single adjustment is needed to allow the Laplacian dissipation dynamics to influence vertical gradients of velocity rather than having them dominated by the hyper-dissipation. This change also makes the higher-order dissipation nearly isotropic in wavenumber space for the anisotropic scaling. To provide additional insight into this, the hyperviscosity is constructed such that the dissipation timescale, or e-folding timescale, is constant on the surface of an ellipsoid defined by

$$\left( \frac{k}{k_{max}} \right)^2 + \left( \frac{l}{l_{max}} \right)^2 + \left( \frac{m}{m_{max}} \right)^2 \approx 1,$$

where  $\mathbf{k} = [k, l, m]^T$  is the wavenumber vector and  $\mathbf{k}_{max} = [k_{max}, l_{max}, m_{max}]^T$  is

the maximum retained wavenumber in each direction, defined by truncating the largest 1/9 of the wavenumbers in each direction. Integrating this into a spectral hyper-dissipation operator,

$$\mathbb{D}_k^{(p)} = (-1)^{p/2+1} 2\nu'_p \left[ \left( \frac{k}{k_{max}} \right)^2 + \left( \frac{l}{l_{max}} \right)^2 + \left( \frac{m}{m_{max}} \right)^2 \right]^{p/2}, \quad (\text{C.12})$$

where the exponent of  $(p)$  on the operator pertains to the order of the dissipation operator and the  $\nu'_p = 1/T_{max}$  parameter represents the inverse dissipation timescale (1/s) at the maximum defined wavenumbers. Absorbing isotropic horizontal terms, assuming that  $k_{max} = l_{max}$ , into the hyper-viscosity operator yields

$$\mathbb{D}_k^{(p)} = (-1)^{p/2+1} 2\nu_p \left[ k^2 + l^2 + \left( \frac{k_{max}}{m_{max}} m \right)^2 \right]^{p/2}, \quad (\text{C.13})$$

where  $\nu_p = \nu'_p / k_{max}^p$  now has the appropriate units ( $m^p s^{-1}$ ). With the scaling of our numerical domain  $L_x/L_z = 40$  and the resolution  $n_x/n_z = 2$ , this will change the effective hyper-dissipation in the vertical direction for the dimensionless equations,

$$\mathbb{D}_k^{(p)} = (-1)^{p/2+1} \frac{2}{Re_p} \left[ k^2 + l^2 + (N/f)^2 \left( \frac{k_{max}}{m_{max}} m \right)^2 \right]^{p/2}. \quad (\text{C.14})$$

This amounts to replacing the matrix  $\mathbf{A}$  in (C.11), for the higher-order terms, by another matrix,

$$\mathbf{B} = \begin{bmatrix} 1 & 0 & 0 \\ 0 & 1 & 0 \\ 0 & 0 & 12 \end{bmatrix}, \quad (\text{C.15})$$

creating a near isotropic hyper-dissipation parameter for our spectral equation. For domain scaling as  $L_x/L_z = N/f$  and equal numbers of grid points in horizontal and vertical directions,  $n_x/n_z = 1$ , this matrix will be the identity  $\mathbf{B} = \mathbf{I}$ .

Eliminating all but the time derivative and the dissipation terms in (C.1),

taking the Fourier transform, and multiplying by the conjugate of the spectral velocity vector,  $\hat{\mathbf{u}}_k^*$ , gives the kinetic energy diffusion equation,

$$\frac{\partial |\hat{\mathbf{u}}_k|^2}{\partial t} = -\mathbb{D}_k |\hat{\mathbf{u}}_k|^2. \quad (\text{C.16})$$

Solving (C.16) yields the solution,

$$|\hat{\mathbf{u}}_k(t)|^2 = |\hat{\mathbf{u}}_k(0)|^2 \exp \{-\mathbb{D}_k t\}, \quad (\text{C.17})$$

with e-folding dissipation time of,

$$\mathcal{T}_k = \frac{1}{\mathbb{D}_k}, \quad (\text{C.18})$$

for the kinetic energy at wavenumber vector  $\mathbf{k} = [k, l, m]^T$ . This decomposition makes it possible to investigate dissipation time scales for ranges of wavenumbers.

For simulations in this dissertation and related work, parameters influencing dissipation time scales have been set as follows: The length scales,  $L_x = L_y = 40L_z = 500 m$ , number of grid points,  $n_x = n_y = 2n_z = 128$ , Laplacian viscosity,  $\nu_2 = 2.5 \times 10^{-5} m^2/s$ , and the sixth-order dissipation inverse timescale,  $\nu'_6 = 48 s^{-1}$ . Dissipation time scales are displayed for the complete horizontal wavenumber spans of vertical wavenumbers (Figure C.1a) and complete vertical wavenumber spans of the first seven horizontal wavenumbers (Figure C.1b). What is immediately noticeable is the effect of anisotropy on the distribution of timescales for various wavenumber. The first seven vertical modes have decreasing dissipation timescales that are a product of strong Laplacian dissipation for vertical wavenumbers. As was more thoroughly discussed in Chapter 5, dissipation timescales for the barotropic mode is four orders of magnitude longer than for the first baroclinic mode. Furthermore, the sixth-order dissipation is seen to dominate the range of wavenumbers, leaving only a narrow range for Laplacian dynamics at larger scales. If the rate of energy transfer through non-linear interactions is

significantly slower than the dissipation rate of kinetic energy, the kinetic energy spectrum will have a steeper spectral slope than  $k^{-5/3}$  predicted by theory.

### C.3 Defining the Higher-Order Dissipation Range

The above dynamics limit the Laplacian dissipation dynamics to a small range for the smallest wavenumbers in each direction. Higher-order dissipation was originally intended to remove strong velocity gradients at the largest wavenumbers. To define a desired effective range for higher-order dissipation, a further simplification to the dissipation timescale is made. With a zero vertical wavenumber, the dissipation timescale becomes,

$$\mathcal{T}_k = \frac{1}{\nu k^2 + \nu'_p (k/k_{max})^p}. \quad (\text{C.19})$$

The wavenumber for which the higher-order term has equivalent influence as the Laplacian term can be solved for by

$$\nu'_p \left( \frac{k_e}{k_{max}} \right)^p - \nu_2 k_e^2 = 0. \quad (\text{C.20})$$

Solving this equation for the positive real root gives,

$$k_e = \left( k_{max}^p \frac{\nu_2}{\nu'_p} \right)^{1/(p-2)}, \quad (\text{C.21})$$

$$= (k_{max}^p \nu_2 T_{max})^{1/(p-2)}, \quad (\text{C.22})$$

where  $k_e$  and  $T_{max}$  are the equivalence wavenumber and dissipation timescale at the maximum wavenumber. If a certain ratio of the wavenumbers is desired to have Laplacian dynamics, we can express  $P_e = k_e/k_n$ , with  $k_n = 2\pi n_x/L_x$  being the Nyquist wavenumber. Wavenumbers less than  $k_e$  will be primarily influenced by Laplacian dynamics, with the rest influenced by the higher-order dissipation. We can now solve for the necessary order  $p$  of the higher-order dissipation,

$$p = \frac{\ln(P_e^2 k_n^2 \nu_2 T_{max})}{\ln(P_e k_n / k_{max})}, \quad (\text{C.23})$$

and round it to the closest even number.

For the above settings for length scales, resolution, and viscosity parameters,  $p = 26$  gives the higher-order dissipation that allows for  $P_e = 0.50$  of the wavenumbers to experience Laplacian dynamics (Figure C.2).

Alternatively, if the effect of the Laplacian dynamics are negligible, one can define the desired percentage of wavenumbers to experience an e-folding timescale over the length of the simulation, or any other useful timescale. Solving (C.19) for the dissipation timescale without Laplacian dynamics yields,

$$P_{sim}k_n = k_{sim} = k_{max} (\nu_p T_{sim})^{-1/p}, \quad (\text{C.24})$$

were  $P_{sim}$  is the ratio of wavenumbers,  $k_{sim}/k_n$ , with dissipation timescales greater than the simulation time,  $T_{sim}$ . With the same parameters,  $p = 30$  gives the higher-order dissipations that allows for  $P_{sim} = 0.50$  of the wavenumbers to have a longer dissipation timescale than the simulation time,  $T_{sim} = 800 T_{ip}$  (Figure C.3).

The power of hyperviscosity for the above estimates are much higher than has been commonly used in the literature. In the limit of very high powers of hyperviscosity a ‘‘bottleneck’’ effect can occur before the dissipative subrange (Frisch et al., 2008). This consists of a build up of kinetic energy from non-linear transfers that occurs before dissipation is dominant. A value of  $p = 16$  is considered to be a moderately high setting (Borue and Orszag, 1995a; Smith, 1997). A couple of minor adjustments can be made to the above parameters to bring the power of hyperviscosity down into this range. First, changing the dissipation timescale at the maximum defined wavenumber to half that of the simulation time step,  $T_{max} = 1/\nu'_p = \Delta t/2 = 15 s$ , reduces the power of the first to  $p = 16$ . Next, changing the representative dissipation timescale from that of the length of the simulation to that of the instability timescale,  $T_{sim} = 50 T_{ip}$ , also brings down the power of the second example to  $p = 16$ .

Both of these modifications will be effective in maintaining numeric stability and creating representative subranges on two conditions. The first condition is

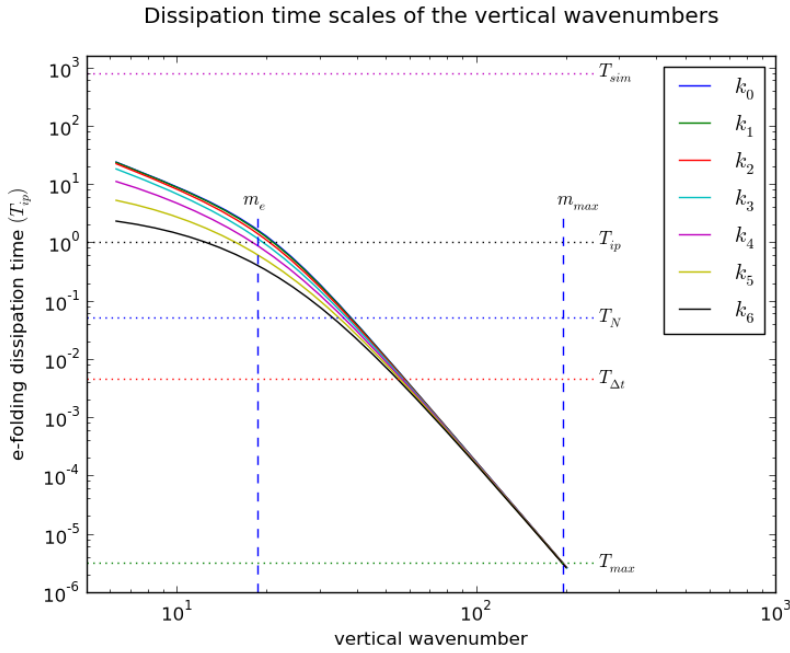
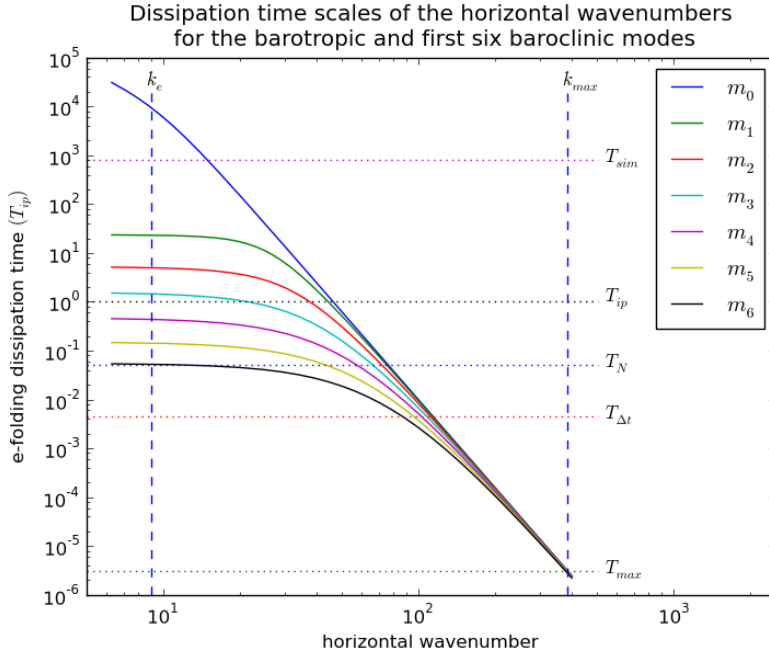


Figure C.1: Dissipation timescales for the first seven vertical (a) and horizontal (b) wavenumbers with  $L_x = L_y = 40L_z = 500 \text{ m}$ ,  $\nu_2 = 2.5 \times 10^{-5} \text{ m}^2/\text{s}$ , and  $\nu'_6 = 48 \text{ s}^{-1}$ .  $T_{sim}$ ,  $T_{ip}$ ,  $T_N$ ,  $T_{\Delta t}$ , and  $T_{max}$  are the simulation timescale, inertial timescale, buoyancy timescale, simulation time step, and dissipation time at the maximum defined wavenumber ( $k_{max}$  or  $m_{max}$ ). Also,  $k_e$  and  $m_e$  are the wavenumbers for which the Laplacian and higher-order dissipation have an equivalent effect for the respective zeroth wavenumber.

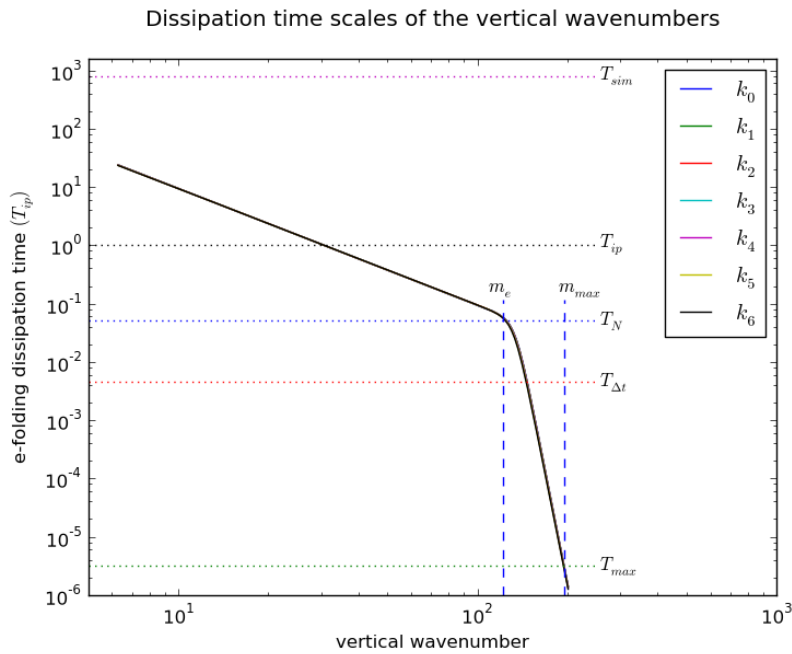
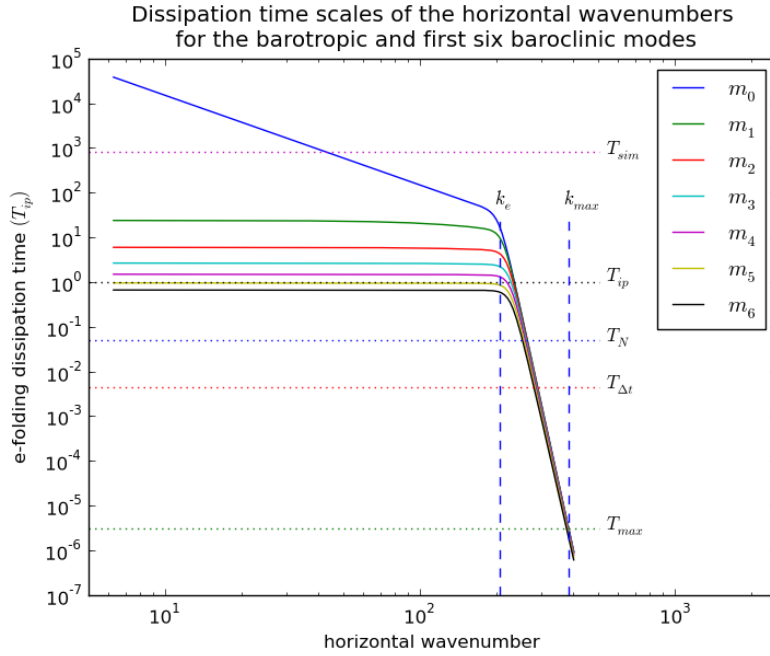


Figure C.2: Dissipation timescales for the first seven vertical (a) and horizontal (b) wavenumbers with  $L_x = L_y = 40L_z = 500 \text{ m}$ ,  $\nu_2 = 2.5 \times 10^{-5} \text{ m}^2/\text{s}$ , and  $\nu'_{26} = 48 \text{ s}^{-1}$ .

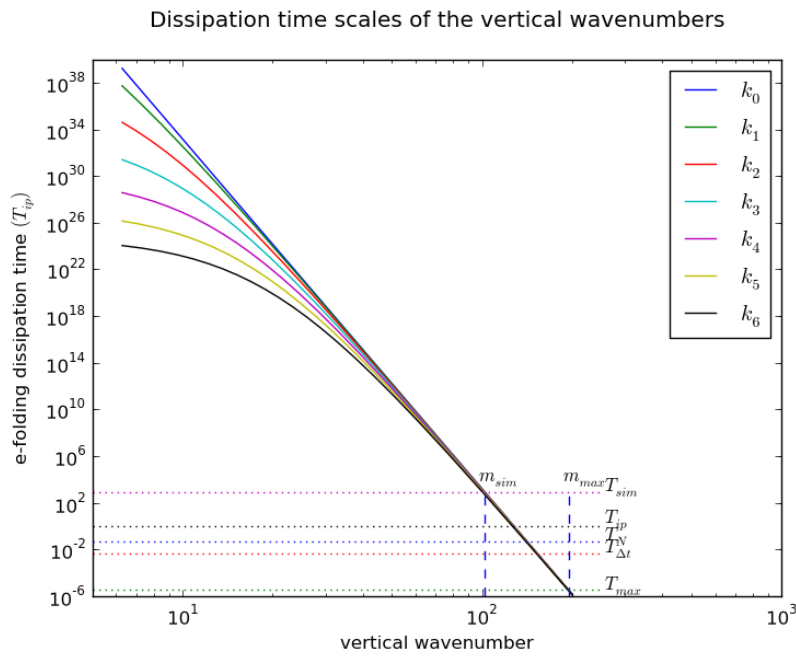
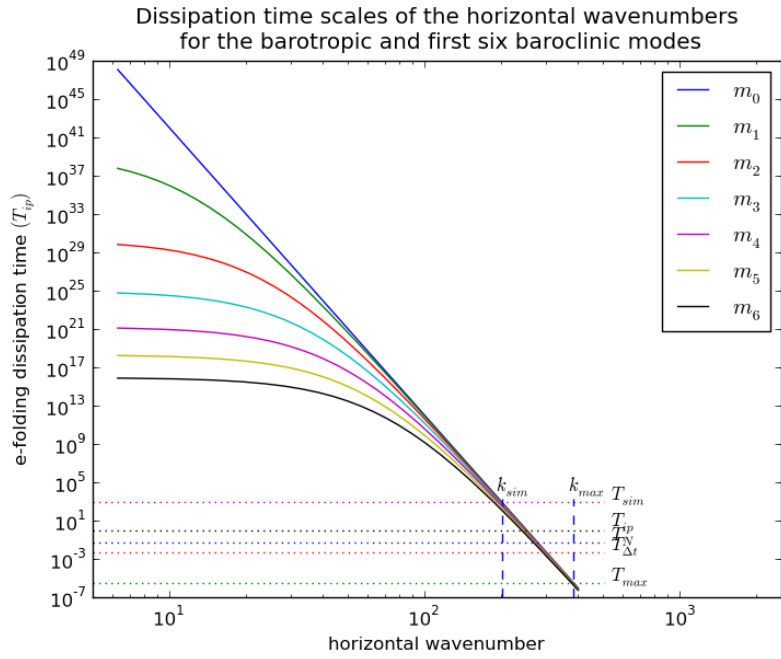


Figure C.3: Dissipation timescales for the first seven vertical (a) and horizontal (b) wavenumbers with  $L_x = L_y = 40L_z = 500 \text{ m}$ ,  $\nu_2 = 0 \text{ m}^2/\text{s}$ , and  $\nu'_{30} = 48 \text{ s}^{-1}$ .

that they prevent the build up of energy at the smallest scales. And secondly, that the non-linear transfer of energy to smaller scales is faster than dissipation for the defined inertial subranges.

One concern of this technique is that it would lead to insufficient thermalization of the energy at small scales. Higher order dissipation is seen to lead to this "bottleneck" effect in some numerical simulations (Frisch et al., 2008). With the bottleneck effect, there is a build up of energy at small scales due to the lack of energy at the smallest scales to provide an eddy viscosity. A few numerical simulations with very high orders confirm that this will remain a concern.

#### ***C.4 Conclusion***

The capacity to set higher-order dissipation according to dynamics desired for ranges of wavenumbers is presented. For Laplacian dynamics, it has been shown that an equivalent scale can be set according to the ratio of wavenumbers to have Laplacian dynamics. With negligible Laplacian dynamics for a simulation, it is possible to set the order of dissipation according to the required level of dissipation at two different timescales. It is further noted that the scaling of the maximum wavenumber in each direction for the higher-order dissipation can be set without the need to be integer multiples of some minimum, non-zero wavenumber. It would also be possible to reduce the dissipation to zero for a range of smaller wavenumbers, thereby making cascades to dissipative wavenumbers the only way energy could get out of the inertial range of wavenumbers. Furthermore, the rate at which energy is dissipated at the selected maximum wavenumbers may be set to be at or greater than the rate of energy transfer from larger scales through nonlinear interactions. The rate of energy dissipation presented for the selected maximum wavenumbers is most likely to be unnecessarily high. These rates may be set more appropriately and help prevent the bottleneck effect discussed above.

Though this technique is presented for an anisotropic, stratified, rotating domain it could also be useful in isotropic models that use higher-order dissipative terms. These models will not be limited to those that simulate fluid dynamics.

Higher-order dissipative terms have been used in other areas with mixed success and would benefit from a more effective design.

## CURRICULUM VITAE

JOSHUA JACOBS

---

### ADDRESS

Department of Applied Mathematics  
University of Washington  
Guggenheim Hall #414  
Box 352420  
Seattle, WA 98195-2420  
Phone: (206)963-0897  
Fax: (206)685-1440  
Email: joshier@uw.edu

---

### EDUCATION

9/2006 – 8/2012 PhD student at University of Washington

9/2003 – 6/2005 M.A. in Applied Mathematics at University of Minnesota Duluth

1989 – 1996 B.A. Mathematics at Winona State University

---

## PUBLICATIONS

- unpublished     Jacobs, Joshua, M. P. Lelong, M. A. Sundermeyer. “Effects of Spatially Correlated Vortices of Geostrophic Adjustment on Oceanic Lateral Dispersion”
- unpublished     Jacobs, Joshua, M. P. Lelong, M. A. Sundermeyer. “Instability, Dipole Formation, and Merging of Two Vortices of Geostrophic Adjustment”
- 2010             Heath, Daniel and Joshua Jacobs. “Geometry Playground” , Loci (September 2010), DOI: 10.4169/loci003567
- 2005             Jacobs, Joshua. “Factor Group Transformations on Escher Patterns”, Proceedings of the Bridges Conference, August 2005

---

## CONFERENCES ATTENDED

- 4/10/2010       Annual PNW MAA Meeting, Seattle, WA, Presented
- 2/26/2010       AGU Ocean Sciences Meeting, Portland,OR, Presented
- 8/31/2009       IEEE Cluster 2009, New Orleans, LA
- 7/13/2008       SciDAC 2008, Seattle WA

---

## SOFTWARE DEVELOPMENT

- 4/1/2011       Contributions to clawpack, enabling binary file input/output in netCDF format.

- 5/1/2010 “For studying the definition of the derivative”, Written with Dr. Daniel Heath, PLU, and purchased by Plato Learning
- 5/1/2010 “Riemann Sums”, Written with Dr. Daniel Heath, PLU, and purchased by Plato Learning
- 1/1/2010 “Geometry Playground”, Written with Dr. Daniel Heath, PLU, an Open Source compass and ruler application in 6 different geometries and ten languages.

## EXPERIENCE

### *C.4.1 Research Experience*

3/2012 – 6/2012 Research Assistant for the Kristing Swanson Lab, mathematically modeling glioblastoma multiforma.

7/2008 – 6/2001 Research Assistant funded by the National Science Foundation (NSF B807 MPLBELL)

Research Focus: Lateral Dispersion in Density Stratified Fluids.

### *C.4.2 Teaching Experience*

9/2011 – 3/2012 Teaching Assistant for graduate applied mathematics courses at University of Washington

6/2011 – 8/2011 Instructor for “Applied Linear Algebra and Numerical Analysis”

9/2006 – 6/2008 Teaching Assistant for undergraduate mathematics courses at University of Washington

9/2005 – 6/2006 Instructor of Mathematics at University of Minnesota Duluth

9/2003 – 6/2005 Teaching Assistant for Calculus II courses at University of Minnesota Duluth

#### *C.4.3 Work Experience*

2011 – Present Parallel programming assistance for the Kirsten Swanson Lab, mathematically modeling glioblastoma multiforme.

#### 1998 – 2003 **Contract Programming**

Providing programming, database services, and technical expertise for the following clients:

**Badger Foundry** – database integration

**Alumnae Association of the College of Saint Teresa** – database and technical support

**RBI Ltd** – database integration

**Omni Engineering Services** – Database Application Programming

1996 – 1998 **Riverwise Inc.** – Database Design, Development, and Deployment through online interfaces